2012

Numerical simulations of fracture propagation and sealing: implications for wellbore strengthening

Saeed Salehi

Department: Geosciences and Geological and Petroleum Engineering

NUMERICAL SIMULATIONS OF FRACTURE PROPAGATION AND SEALING: IMPLICATIONS FOR WELLBORE STRENGTHENING

by

SAEED SALEHI

A DISSERTATION

Presented to the Faculty of the Graduate School of the

MISSOURI UNIVERSITY OF SCIENCE AND TECHNOLOGY

In Partial Fulfillment of the Requirements for the Degree

DOCTOR OF PHILOSOPHY

in

PETROLEUM ENGINEERING

2012

Approved

Dr. Runar Nygaard, Advisor

Dr. Shari Dunn-Norman

Dr. Baojun Bai

Dr. Andreas Eckert

Mr. Keith Morton

ABSTRACT

To mitigate the small tolerance between pore pressure and fracture gradients an engineering practice referred to as "*wellbore strengthening*" is conducted to increase the fracture gradient. The method relies on propping and/or sealing the fractures with specially designed materials. Different competing theories exist for physical wellbore strengthening mechanisms which can be categorized into two groups. The first group explains that strengthening happens as a result of increasing wellbore hoop stress when fractures are sealed while the second group emphasis is on fracture tip isolation with suitable materials and enhancing fracture propagation pressure. The numerical models and lab experiments in previous studies have not fully replicated the operational phenomenon of wellbore strengthening.

This study presents three-dimensional poro-elastic finite-element simulation's results for hydraulic fracture's initiation, propagation and sealing in the near wellbore region. The main objective of these simulations was to investigate the hypothesis of wellbore hoop stress increases when fractures are wedged and/or sealed during lost circulation control. To further support the numerical simulations' results, relevant field case studies, near wellbore fracture experiments and analytical models were also used.

This study demonstrates that fracture sealing is not able to increase wellbore hoop stress more than its ideal state where no fracture exists, however, it helps to restore part or all of the wellbore hoop stress lost during fracture propagation. Field cases reveal the importance of connecting wellbore hoop stress restoration with leak off test's (LOT) interpretation and how wellbore condition can affect initial fracture gradient.

ACKNOWLEDGMENTS

I would like to thank my advisor Dr. Runar Nygaard for accepting me as his graduate student in this program. He was not only an excellent advisor but also a mentor and a friend, who has taught me lessons which will always be important to me in my professional career. In addition, I will always be indebted to Dr. Nygaard for supporting my studies and recognizing my potential, without him, this work could not have been possible. In addition, I would like thank my committee members, Dr. Shari Dunn-Norman, Dr. Bajoun Bai, Dr. Andreas Eckert form Missouri S&T Petroleum Engineering program and Mr. Keith Morton from Chevron Corporation for their valuable feedback and support. Dr. Eckert was my instructor for Finite Element Analysis and his comments on Finite-element models were invaluable. Furthermore, I would like to thank the graduate students who have helped me to conduct the experimental work in my research. Especially, Mr. Aaron Blue for constructing the fracturing cell and set up in the laboratory. I would also like to thank Mr. Max Liberman for running the fracture experiments. On a personal note, I would like to express my gratitude to my best friend and lovely wife Elham for her encouragement and undying devotion and my daughter Nahal who has given me every reason to make her proud. I will always be indebted to my parents without whom none of the opportunities in my life would have ever been possible. Finally, I would like also to thank my other colleagues and the GSE department staff, especially Ms. Paula Cochran and Mr. Ahmad Aladasani who, their memories will always remain dear to me. This work was partially funded by Chevron Corporation.

TABLE OF CONTENTS

LIST OF ILLUSTRATIONS

LIST OF TABLES

NOMENCLATURE

Symbol	Description
A	Borehole Pressurization Rate
c	Diffusion Coefficient
E	Young's Modulus
G	Fracture Energy
G_C	Critical Fracture Energy
G_n^C	Fracture Energy in Normal Direction
G_s^C	Fracture Energy in First Shear Direction
G_S	Total of Fracture Energy in First and Second Shear Directions
G_T	Total of Fracture Energy in Shear and Normal Directions
J	Material Parameter
H	Total Fracture Height
$h_{1/2}$	Half Fracture Length
K_c	Rock Fracture Toughness
K_{ss}	Pseudo Fracture Toughness
k	Volumetric Viscosity Coefficient
L_t	Cohesive Elastic Stiffness
l_C	Cohesive Zone Length
L	Fracture Length
P_p	Pore Pressure
P_w	Wellbore Pressure (Mud Weight)
P_{fp}	Fracture Propagation Pressure
P_{frac}	Fracture Breakdown Pressure
P_n	Net Fracture Pressure
R1	Fracture Invaded Zone
R	Fracture Length (Diameter)
r	Radial Distance from Wellbore

r_w	Wellbore Radius
S	Strain Rate Operator
T_0	Rock Tensile Stress
t_0	Cohesive Element Thickness
V	Velocity Vector
V_c	Velocity Coefficient
σ_h	Minimum Horizontal Stress
σ_H	Maximum Horizontal Stress
σ_V	Overburden Stress
σ_{rr}	Radial Stress
$\sigma_{\theta\theta}$	Hoop Stress or Tangential Stress
σ_{zz}	Vertical Stress at Wellbore Wall in Cylindrical Coordinates
σ_{xx}	Normal Stress at Wellbore Wall in x Direction in Cartesian Coordinates
σ_{yy}	Normal Stress at Wellbore Wall in y Direction in Cartesian Coordinates
σ_z	Normal Stress at Wellbore Wall in z Direction in Cartesian Coordinates
$\tau_{xy}, \tau_{yz}, \tau_{xz}$	Shear Stresses at Wellbore Wall in Cartesian Coordinates
$\tau_{r\theta}, \tau_{\theta z}, \tau_{rz}$	Shear Stresses at Wellbore Wall in Cylindrical Coordinates
θ	Angle of borehole circumference Measured from Max Horizontal Stress Direction
λ	Sealing Efficiency Factor
β	Deviation Angle
η	Barrier Efficiency Factor
w_c	Critical Fracture Width
υ	Poisson's Ratio
γ_s	Surface Energy per Unit Area
σ_f	Fracture Stress
w_m	Maximum Fracture Width, inch
δ_{ij}	Kronecker Delta
$\dot{\varepsilon}$	Strain Rate

τ_{ij}	Deviatoric Stress
μ	Dynamic Viscosity
λ	Lame Notation
α	Biot's Coefficient
σ_n	Nominal Traction Stress in Normal Direction
σ_s	Nominal Traction Stress in First Shear Direction
σ_t	Nominal Traction Stress in Second Shear Direction
δ^f	Final Displacement
δ_n	Displacement in Normal Direction
δ_s	Displacement in First Shear Direction
δ_t	Displacement in Second Shear Direction
ζ	Dimensionless Borehole Pressurization Rate
OCR	Overconsolidation Ratio
UCS	Uniaxial Compressive Strength

1. INTRODUCTION

1.1. MOTIVATION

The complexity of modern oil and gas exploitation requires a better understanding of the geomechanical behavior of rocks at depth. This ranges from understanding large scale geology features like fault behavior and salt diapirs to near wellbore issues such as the integrity of the wellbore wall. Most important among these is the integrity of the wellbore wall from either tensile failure causing mud losses and stuck pipe or too low mud weight causing borehole collapse. Both mechanisms often result in hindering further drilling; however, tensile failure occurs more frequently and has more severe consequences. The extent of tensile failure is increased when drilling in deep offshore basins, depleted formations, or when planning highly deviated wellbores. One major concern in these situations is the shrinkage of the safe mud weight window between pore and fracture pressure which is a crucial factor in well design. Total overburden density decreases in deep offshore basins since the uppermost interval is water, which has considerably less density than rock. This can be described by the following equation for total overburden stress:

$$\begin{aligned}\sigma_{ob} &= \sigma_{ob(water)} + \sigma_{ob(formation)} \\ &= g\int_0^{D_w} \rho_w dD + g\int_{D_w}^{D} \rho_b dD\end{aligned} \tag{1.1}$$

The equation shows the overburden stress is the sum of the water weight plus the weight of the formation's rocks to the depth of interest; so as the water depth increases, the overburden stress decreases at a given depth. A direct consequence of reduction in overburden stress is decrease in the formation fracture gradient which narrows the operational window (Figure 1.1).

A similar scenario is illustrated in Figure 1.1, where fracture gradient decreases with wellbore deviation (assuming isotropic stresses and drilling in minimum horizontal stress orientation). For deviated wellbores, the fracture gradient ($P_{frac\text{-}deviated}$) can simply be estimated based on the vertical fracture gradient ($P_{frac\text{-}vert}$) and the wellbore inclination (β) as follows (Aadnoy and Chenevert, 1987).

$$P_{frac-deviated} = P_{frac-vert} + \frac{1}{3}(P_P - 16)\sin(\beta) \tag{1.2}$$

The equation shows that tensile fractures and possible mud losses will occur at lower pressures in deviated wells compared to vertical wells. Although creating fractures is favorable during hydrofrac operations, in drilling operations this can lead to loss of mud which is the main safety control inside the wellbore. Severe mud loss might also lead to wellbore kicks and blowouts which cost the industry millions of dollars.

Another condition is drilling through depleted formations in which operational mud weight window shifts and thus increases the risk of lost circulation as well as kicks and blowouts. In depleted formations, formation pore pressure will drop causing reduction in the formation total stress. At the same time, shale layers (above or below the reservoir) might have maintained their pore pressure, which increases the risk of lost circulation when drilling the depleted (Figure 1.1). Drilling problems in depleted reservoirs are reported in both offshore and onshore sedimentary basins. For instance, Gulf of Mexico deep water wells are complicated by presence of high geo-pressures and relatively low fracture gradients leading to very small margins (van Oort, 2009). In McAllen and Pharr fields onshore Texas (Montilva et al., 2010) complex fault regime caused over pressured virgin reservoir compartments to exist between severe depleted zones. The complex fault regime in this field made pore pressure and fracture gradient prediction difficult. Infill drilling in these fields was accompanied by excessive lost circulation and well control events.

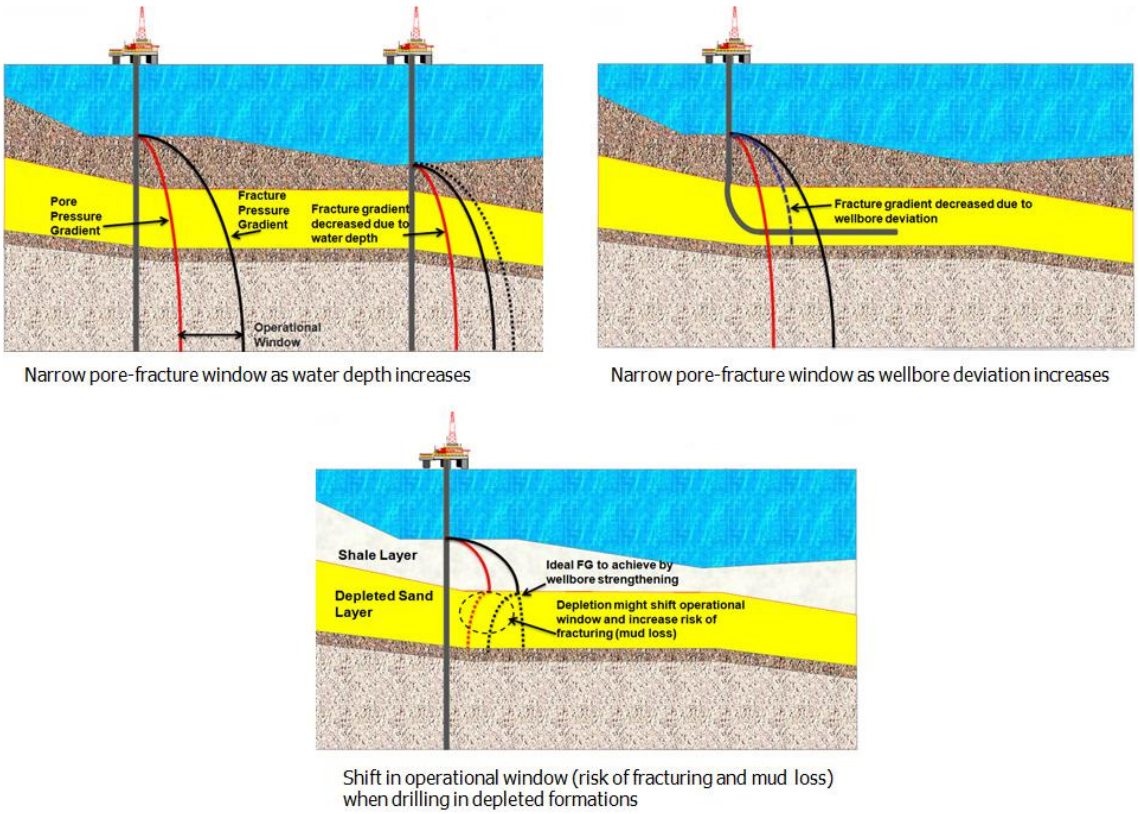

Figure 1.1. Motivation to increase the current limit of the fracture gradient by using wellbore strengthening technology

The three major geomechanical problems caused by a narrow operational window can be listed as:

- Lost circulation
- Wellbore breathing
- Kicks and blowouts

Lost circulation is one of the largest contributors to down time in drilling operations and is ranked first in the top ten concerns in deep offshore wells (Zamora et al., 2000). In the Gulf of Mexico only, it is estimated that more than 12% of NPT (Non-productive Time) is related to lost circulation problems (Wang et al., 2009). To stop mud losses into the formation, lost circulation materials (LCM's) are added to the mud system

to fill the fractures which are created while drilling or fractures or vugs already naturally occurring in the formation. Although using these materials decreases the loss rate, the method does not give consistent results, and materials are selected by trial and error (Alberty and Mclean, 2004). Further, it is not clear to what extent loss rate can be decreased and how long LCM's are stable and effective for a given loss zone. Often the only remedy that works when encountering losses is to set a cement plug and drill a sidetrack (Zamora et al., 2000).

Wellbore breathing (ballooning) is a common loss/gain phenomenon in which slow mud losses are observed while drilling accompanied by mud returns afterwards when the pumps are off. This is normally severe when losses happen in a tight pore-fracture pressure window. Typical reasons that are mentioned for borehole breathing effect include opening and closing of the natural fractures, deformation of the borehole wall, and temperature variations of drilling muds (Lavrov and Tronvoll, 2005)

Opening and closing of fractures occur when fractures are opened when annular pressure is applied to the wellbore and the fracture fills with drilling fluid. The fracture closes when the pressure is dropped and makes the fluid return.

Static wellbore conditions at higher well depth heighten the temperature in the drilling fluid and expands its volume which misguides the observer to be fluid gain. The temperature decrease from circulation causes drilling fluid to contract and to be incorrectly interpreted as fluid loss

Wellbore kick and blowout is another consequence of a tight operational window which typically is related to lost circulation. The Maconda well incident is a recent example for which the current report of investigation mentioned lost circulation as one of the major "well control problems" leading to disaster (DOI, 2011).

Distinguishing between real kicks and wellbore breathing is another challenging issue. Incorrect interpretation of wellbore breathing as fluid influx may lead to unwarranted well control procedures and increasing the mud weight which creates new fractures and lost circulation problem consequently. On the other hand, ignoring fluid returns and kick indictors as wellbore breathing may also lead to pressure rise in the wellbore and a potential blow out.

Wellbore strengthening is defined as “a set of techniques used to efficiently plug and seal induced fractures while drilling to deliberately enhance the fracture gradient and widen the operational window”. This technology has the potential to mitigate the lost circulation problem, and improve wellbore integrity to avoid well control disasters. In addition, it might reduce the number of casing strings required to drill deep water wells.

Developing wellbore strengthening techniques with the potential to manage well control disasters is an important aspect of this technology. Linking wellbore strengthening technology with operational practices can be beneficial from both economical and environmental aspects.

1.2. BACKGROUND AND LITERATURE SURVEY

The objective of this section is to review previous experimental work and numerical models investigating wellbore strengthening and lost circulation. First the experimental work of DEA-13 fracturing experiments conducted in the 1980s and GPRI joint industry project accomplished in late 1990s are presented. Then, numerical models including a summary of a barrier design system based on an elastic-plastic fracture model as well as numerical models conducted for wellbore strengthening studies are investigated. Finally, the important distinguishing of the two operational strategies of proactive and corrective wellbore strengthening is addressed.

1.2.1. DEA-13 Fracturing Experiments (Drilling Engineering Association-13). These experiments were the early industrial efforts looking closely at the loss circulation phenomenon based on rock fracturing experiments (Morita et al., 1990). Hydraulic fracturing experiments performed in predrilled boreholes with 10-lbm/gal and 16-lbm/gal density oil and water based mud on Berea and Torrey Buff sandstones and Mancos shale showed that fracture reopening pressure depends upon the amount of mud cake left on wellbore wall (Morita et al., 1990, Onyia, 1994 Morita et al., 1996a, and Morita et al., 1996b). Solids in the drilling fluid formed a bridge in the fracture aperture which caused this effect. Since water-based mud develops a larger mud cake, it will normally have higher reopening pressure than oil-based mud as observed in the experiments. Although, no significant difference was observed in the fracture initiation pressures for water and oil-based muds (Figure 1.2).

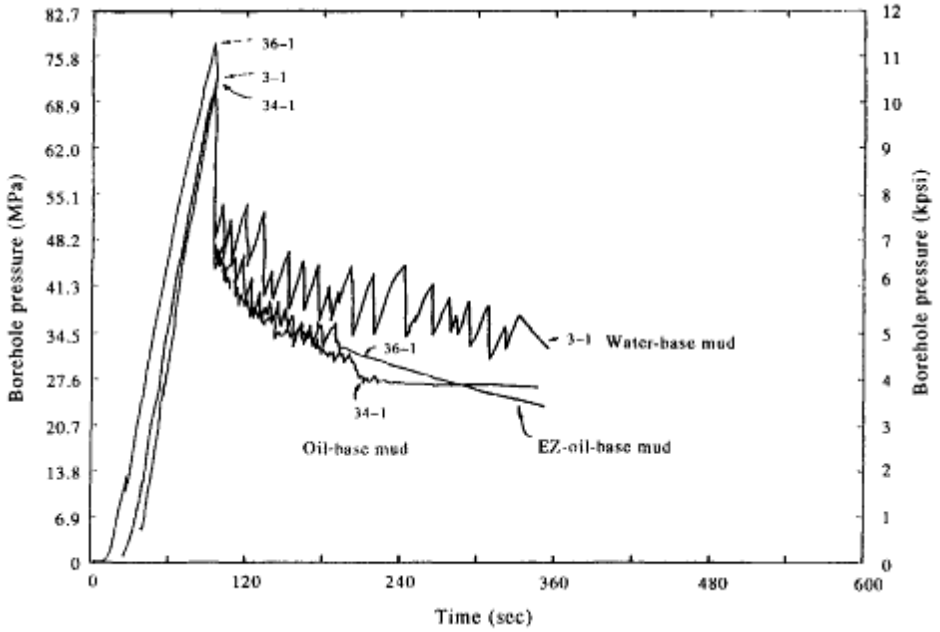

Figure 1.2. No significant difference was observed in fracture breakdown pressure using water and oil-based muds (Taken from Morita et al., 1996)

The observations from the split samples (Figure 1.3) indicated three distinctive zones:

- (1) non-invaded zone; drilling fluid cannot penetrate this zone
- (2) mud dehydrated zone; high solid concentration was observed in this zone
- (3) fractured zone; this zone mostly filled with fresh mud

The important observation was that dehydrated zone length changed with different drilling fluids. Water-based muds have a significantly larger dehydrated zone compared with non-aqueous drilling fluids.

The first order affecting the break down pressure and creating the initial fracture were Young's modulus, wellbore size, mud solids bridging, and degree of dehydration. Secondary effects were thermal cooling, hole inclination, and pore pressure build up. Laboratory experiments conducted by Fuh et al. (1992) showed that certain loss circulation materials can be used to increase the fracture propagation pressure above what was seen with untreated drilling mud.

Figure 1.3. Split rock sample after hydraulic fracturing DEA experiments (Wang, 2007b)

Fuh et al., (1992) concluded that they were able to isolate the induced fracture tip and increase fracture propagation in the range of 3 lbm/gal to 6 lbm/gal in field trials.

1.2.2. GPRI Joint Industry Project (JIP). This project was carried out in the late 1990's with the aim to replicate DEA-13 experiments in smaller scales (Dudley et al., 2001 and Van Oort, 2009). The main focus of the project was to investigate the effectiveness of different lost circulation materials (LCM's). It was found that the fracturing pressure can be significantly enhanced by using synthetic graphites of specific types and sizes, where these materials are able to effectively enter the fracture and seal it (Figure 1.4). It was also found that WBM (Water-Based-Muds) are more effective in increasing the fracture propagation pressure compared to SBM (Synthetic-Based-Muds). Effect of hydraulically conductive fractures on fracture re-opening pressure was also investigated during these experiments. It was also found that hydraulically conductive fractures can lower ideal fracture re-opening pressure close to the confining pressure or minimum horizontal stress.

1.2.3. Stress Cage Model. Alberty and Mclean (2004) presented a physical model of wellbore strengthening based on a linear elastic fracture mechanics model. They allowed small fractures to form in the wellbore wall and keep the fracture surfaces apart by using bridging materials near the fracture mouth. If the fracture is successfully bridged at the wellbore wall or close to it, the hoop stress around the wellbore increases (Figure 1.5).

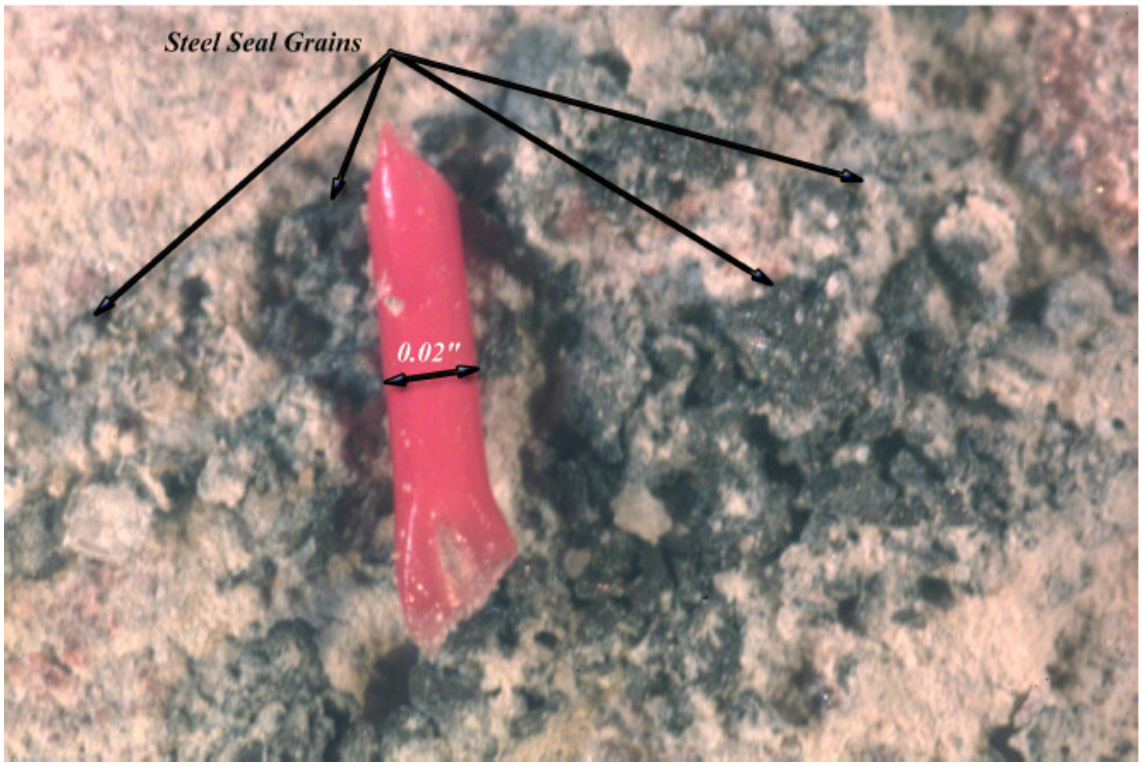

Figure 1.4. LCM particles effectively enter the fracture and seal it (Wang, 2007b)

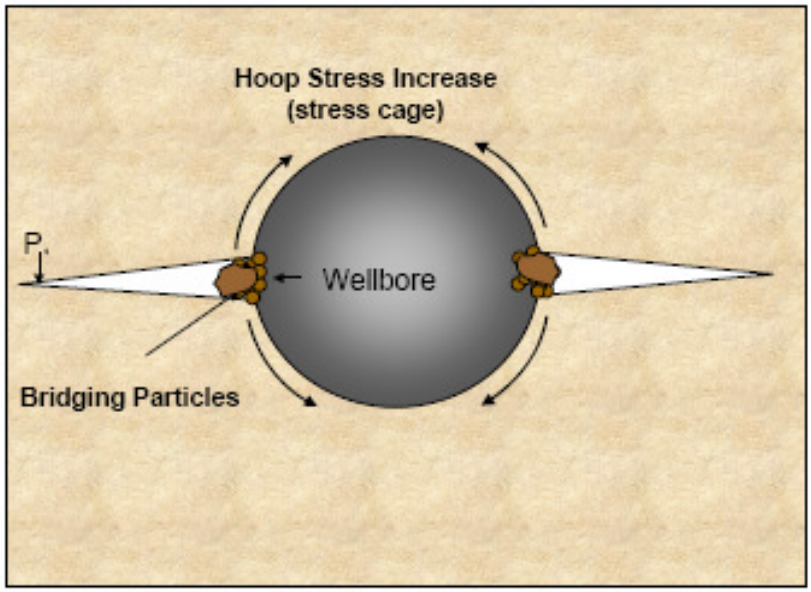

Figure 1.5. Development of a "Stress Cage" by filling a fracture which will increase the hoop stresses around the wellbore (Aston et al., 2007)

They investigated fracture sealing using hollow cylinder rock samples, hydraulically fractured with drilling fluid. The study pointed out that calcium carbonates and graphite blends are the best materials to reduce mud losses into fractures.

A two-dimensional finite-element model was used for simulating Stress Cage around the wellbore. Figure 1.6 illustrates the published FEM model. However, even this was a major step in further investigating wellbore strengthening their publication does not reveal specific detail about their numerical model, its boundary conditions, or loading procedure.

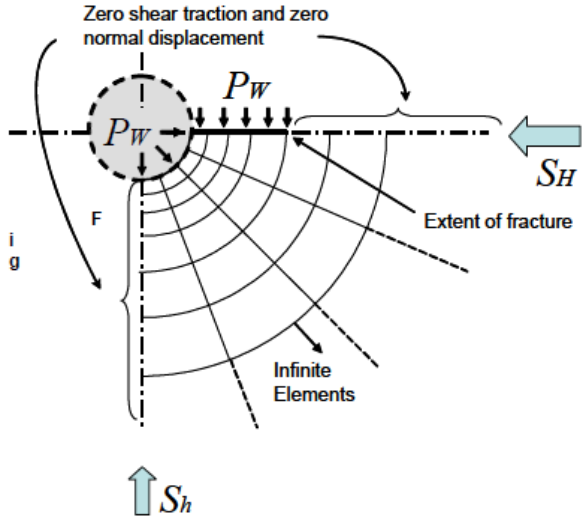

Figure 1.6. 2D FEM model used for Stress Cage simulations (Taken from Alberty and Mclean, 2004)

1.2.4. Fracture Closure Stress (FCS) Model. Dupriest (2005) introduced fracture closure stress (FCS) as an alternative explanation of how the fracture gradient is increased by remediation. Fracture closure stress is defined as the normal stress on the fracture plane keeping the fracture faces in contact. Fracture closure stress is increased by

widening the fracture which then compresses the adjacent rock (Figure 1.7). This method requires the fracture tip to be sealed to create a higher fracture gradient.

It seems that both the FCS approach and the Stress Cage follow the same mechanism in enhancing the fracture gradient by changing the near wellbore hoop stress, but there are some differences when applying the two methods. In the FCS approach, tip isolation is very crucial for a successful operation and also bridging can take place anywhere inside the fracture; but in the Stress Cage, tip isolation is not reported to be an essential part and also it is very important to keep the bridging materials close to the fracture mouth. Surprisingly, Dupriest (2005) states that lost circulation material size and type are relatively unimportant which contradicts previous studies (Fuh et al., 1992, and Alberty and Mclean, 2004).

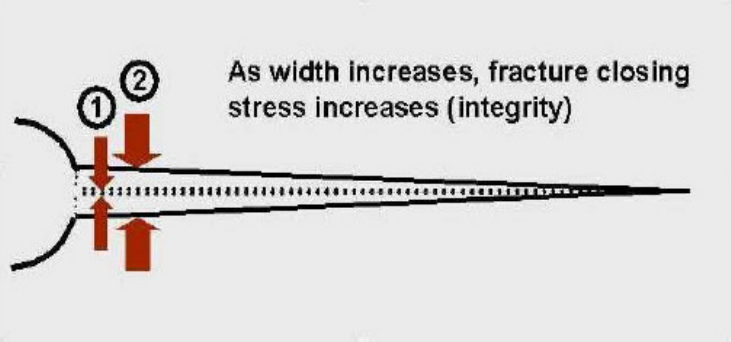

Figure 1.7. Schematic of how increasing the fracture width increases the fracture closing stress (Dupriest, 2005)

1.2.5. Elastic-Plastic Fracture Model. Aadnoy and Belayneh (2004) presented a third alternative explanation of how fracture gradient can be increased above the theoretical Kirsch model value. Based on both continuum mechanics and fracture mechanics they introduced a well barrier design approach developed by using an elastic-plastic fracture model. Their laboratory experiments on low permeable formations

demonstrated that fracturing resistance can be significantly improved by changing mud composition. According to them, the reason for the higher fracture pressure is that when a fracture opens, the mud cake does not split up but deforms plastically, maintaining a barrier (Figure 1.8). The elastic-plastic model assumes a deforming mud cake normally does not occur in low permeability formations. Therefore the connection between their theoretical study and laboratory experiments was not fully developed.

Contradictory to the other mentioned studies, Aadnoy and Belayneh (2004) recommended using materials and additives with higher mechanical strength in the mud design instead of polymer type particles which are not sufficiently strong. It was also concluded that there will be a significant variation in the magnitude of the fracture breakdown pressure with a small amount of changes in the particle content. Their experimental data on different samples confirmed that there is a significant difference in both initial fracturing pressure and reopening pressure mainly because of changing bridging materials and also effectively placing the barrier.

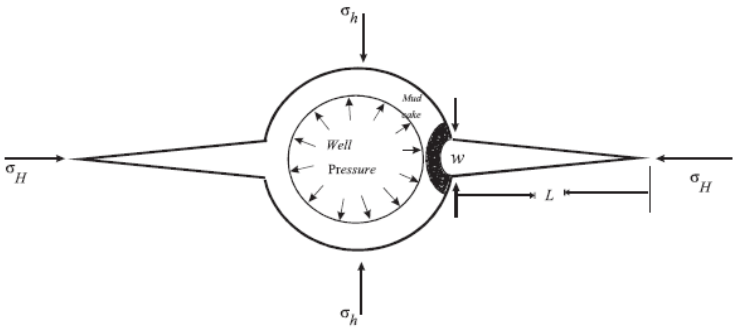

Figure 1.8. A schematic of Aadnoy's elasto-plastic borehole fracture model (Aadnoy and Belayneh, 2004)

1.2.6. Wang's BEA (Boundary Element Analysis). Wang (2007) investigated physical mechanisms of wellbore strengthening using Boundary Element Analysis (BEA). According to his results, fracture sealing can significantly increase the hoop stress beyond the theoretical limit. Figure 1.9 illustrates Wang's results for wellbore hoop stress increase when conducting Stress Cage. Figure 1.9 shows depending on stress anisotropy, hoop stress can be increased up to 20000 Psi (137 MPa) via Stress Cage.

Wang et al., (2009) conducted a parametric study in which parameters affects hoop stress using a boundary element method for a fractured wellbore. He concluded that stress anisotropy and Young's module have significant effect on hoop stress and fracture width, while Poisson's ratio and fracture strength have a less effect. Figure 1.10 illustrates the effect of changing Young Modulus and stress anisotropy on wellbore hoop stress.

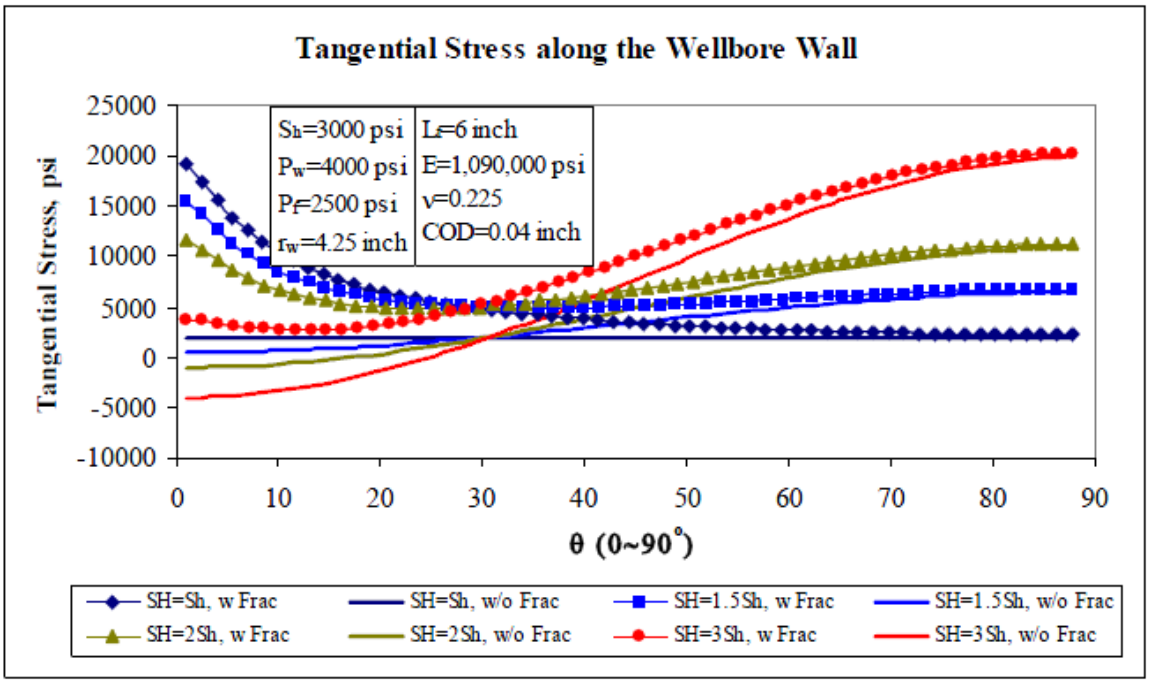

Figure 1.9. Wellbore hoop stress significantly increased when using Stress Cage method (From Wang, 2007)

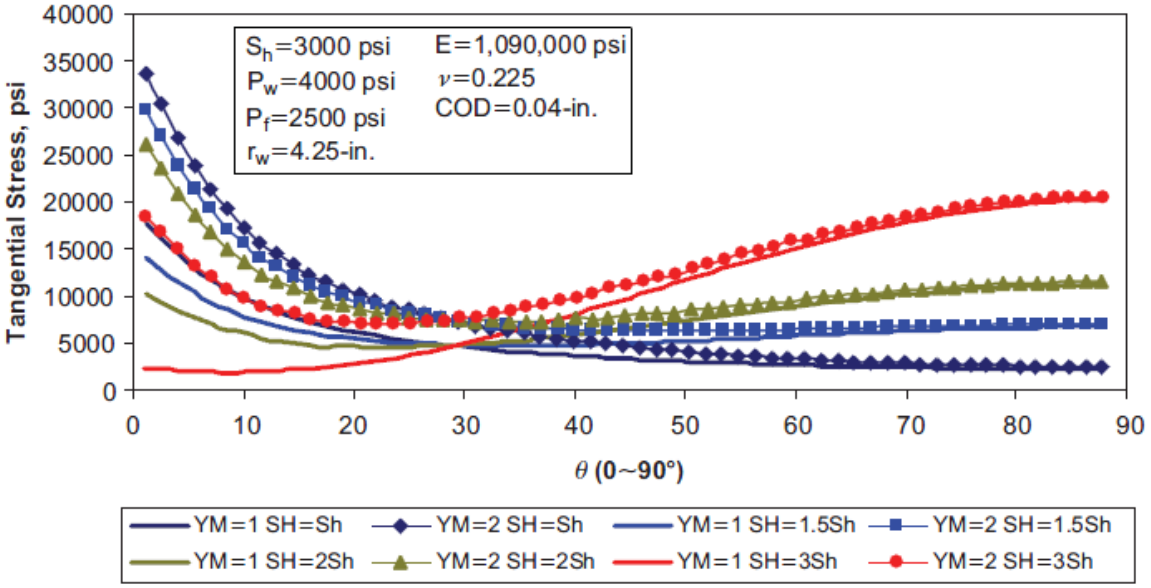

Figure 1.10. Wellbore hoop stress affected by Young's modulus and stress anisotropy (From Wang et al., 2009)

Wang's analysis is the only parametric study done in the literature on "wellbore strengthening", however, the model used for BEA study is an initially fractured wellbore with a predetermined fracture width and length. As a result, simulations based on sealing predetermined fractures are not truly replicating the same phenomenon applied in the field. Both fracture initiation and propagation change the state of stress around the wellbore; and for this reason, any change in hoop stress after fracture sealing must be compared with intact wellbore without any fracture.

1.2.7. Proactive and Corrective Wellbore Strengthening. Proactive and corrective remediation are the two operational strategies used for wellbore strengthening (Wang et al., 2007a, 2009; Fuh et al., 2007). The proactive approach is based on isolating the fracture tip to stop fracture propagation. The pressure improvement from this approach relies on the fracture length and decreases significantly when fracture length is increased. In order to implement this approach effectively it is very important to arrest the fracture as quickly as possible as to stop fracture propagation. Sealing micro cracks and short fractures are one of the steps applied in industry for proactive strengthening. In

a normal drilling there would be several micro fractures created or they might exist as natural fractures or caused by depletion. When these fractures are open and conduct fluid, any wellbore pressure exceeding the minimum horizontal stress will extend these fractures. This phenomenon also confirmed by Onya (1994) with the laboratory results for pre-fractured samples showing much lower breakdown pressures compared with intact and un-fractured samples. Dudley et al., (2001) experiments on fracture-reopening pressure confirmed that when resilient graphite materials were added to the base mud, the fracture opening pressure improved significantly. Wellbore breakdown pressure with the higher value of the Kirsch hoop-stress equation was also reported in the same study, indicating that materials play a major role in borehole strengthening where higher pressure than ideal may be observed in successful operations.

Corrective borehole strengthening can be achieved by widening the fracture width and increasing the compressive strength or fracture closure stress as mentioned previously by Dupriest (2005). By creating an appropriate fracture width and propping it by the bridging material, an increase in fracture closure stress will be achieved if the material isolates the tip effectively and no drilling fluid bypass to the propagation zone. Deformable, Viscous and Cohesive (DVC) materials have been proved to be useful in wellbore strengthening applications in the field (Traugott et al., 2007; Wang et al., 2007a). These materials can deform under pressure or stress. When fracture width increases with wellbore pressure, the seal body maintains the seal by deforming.

1.2.8. Alternative Wellbore Strengthening Methods. Additional alternative explanations of wellbore strengthening proposed in the literature are summarized in Table 1.1. Internal filter-cake bridging and time-dependent wellbore strengthening is based on gaining a wellbore strengthening effect when an impermeable filter cake is formed inside the fracture which increases fracture resistance (Abousoleiman et al., 2007, Benaissa et al., 2006, Reid and Santos, 2006; Santos et al., 2006). Changing the wettability of the filter cake in Non-aqueous fluid (NAF) from oil-wet to water-wet increases the fracture healing of the mud (Brege et al., 2010). This approach has the potential to improve the effectiveness of these fluids and to improve their LCM hold and further increase the fracture propagation pressure by changing wettability.

Thermal effects can play an important role on wellbore strengthening technology. These thermal effects can be created by various operational means which might change near-wellbore fracture gradient. For instance, by increasing mud and thereby wellbore temperature, it is possible to increase effective fracture gradient and/or avoid unnecessary losses (Gonzalez et al., 2010; I.Gill et al., 2006).

Although the above wellbore strengthening approaches are novel, to this date no successful field application has been reported to support these mechanisms.

Table 1.1. A summary of alternative wellbore strengthening approaches

Alternative Wellbore Strengthening Approaches	**Authors**
Internal filter-cake bridging Filter-cake wettability alteration Time dependant wellbore strengthening Chemical wellbore strengthening	Abousleiman et al., 2007; Benaissa et al., 2006; Reid and Santos, 2006; Santos et al, 2006; Brege et al., 2010
Temperature related wellbore strengthening	Gonzalez et al., 2004; I.Gill et al., 2006

1.2.9. Lost Circulation Problem and Practical Mitigation. As mentioned earlier in this section, the main objective for wellbore strengthening is to mitigate lost circulation by increasing the fracture gradient. Lost circulation means loss of drilling fluid, however, the type, severity, and root cause of the problem will be different. The operational procedures to cure losses while drilling, tripping and/or cementing might also

be different. In recent years, field practices, studies and new technologies such as wellbore strengthening have helped to attain great success in mitigating the loss circulation problem (Mclean et al., 2010). However, the problem still lacks a satisfactory solution especially when the results of using the new methods are inconsistent. Poor understanding of wellbore strengthening physics or mechanisms and unavailability of an advanced diagnostic procedure to identify the root cause in advance are the main obstacles to develop new mitigation technologies.

Lost circulation can happen either by pressure induced fractures or through encountering naturally existing fractures and/or vugs. The first type of the lost circulation can happen as results of a narrow pore-fracture window, tight casing/hole clearances and negative impacts of pressure and temperature on rheological properties. Different techniques and LCM types are applied to mitigate lost circulation problem. Figure 1.11 summarizes the most applied lost circulation remedy techniques by industry for both pressure induced type of loss and losses occurred as a result of vugs and natural fractures. Although using these techniques resulted in tremendous NPT reduction, they are not always effective and their results are not consistent (Alberty and Mclean, 2004).

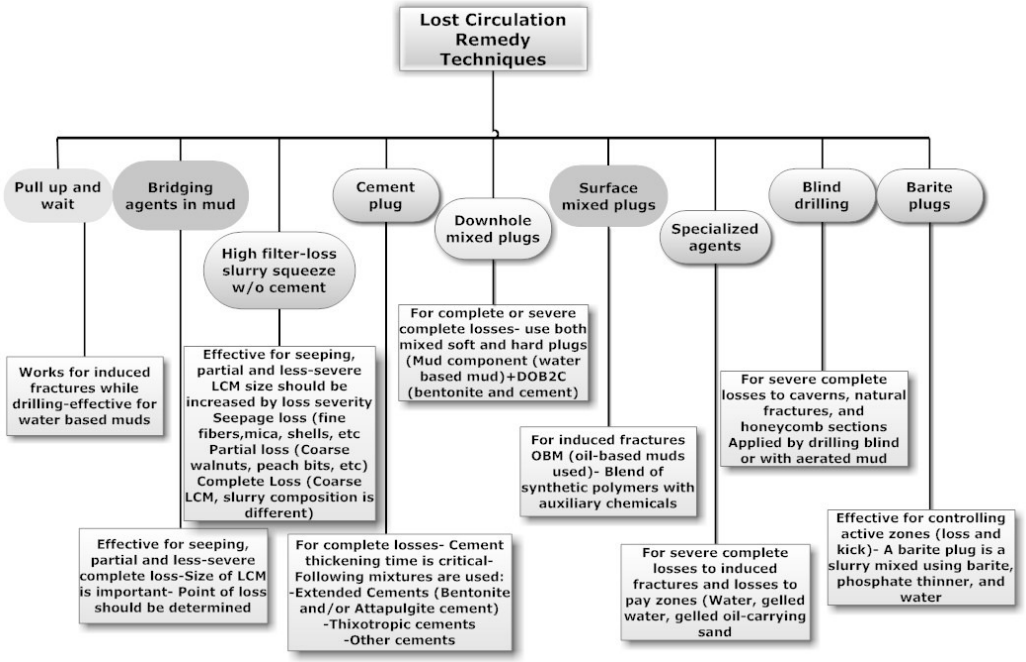

Figure 1.11. A summary of lost circulation remedy techniques

Table 1.2 shows the typical lost circulation material used which are mostly granular, fiber and flake shaped. The data in Figure 1.11 further demonstrate the relationships between the largest particles the bridging agent contains and the largest fracture it would seal.

Table 1.2. Typical lost circulation materials used

Lost Circulation Material	**Type**	**Additional Information**
Nutshells, Calcium Carbonate, Sized Salt, Hard Rubber, Asphalt, Gilsonite, Plastic, Limestone, Sulfur, Expanded Perlite	Granular	
Cellulose Fibers, Saw Dust, Shredded Paper, Hay, Rice, Husks, Bark, Shredded Wood	Fiber-shaped	
Mica, Cellulose, Cottonseed Hulls, Wood Chips, Laminated Plastic, Graphite, Calcium Carbonate	Flake Shaped	
Commercial blends		A blend of two or three different materials to cover a range of sizes and shapes, e.g. combining granular, fibrous and flaked in one sack

It can be concluded from Figure 1.12 that both the bridging agent size and concentration in the drilling fluid determine the largest fracture it will seal. Of these, size

is more critical. To seal a loss zone effectively, the bridging agent must have particles matching the width of the lost zone (Messenger, 1981).

One main challenge in using the referred techniques and materials is to avoid formation damage when losses occur in the pay zone. Most often LCM treatment does not bridge off at the face of the fracture. Instead, it is forced into the formation. It can damage the permeability or be lost entirely to the formation. Because of this, LCM materials are often acid-soluble so that any damage caused when operating in producing intervals can be rectified.

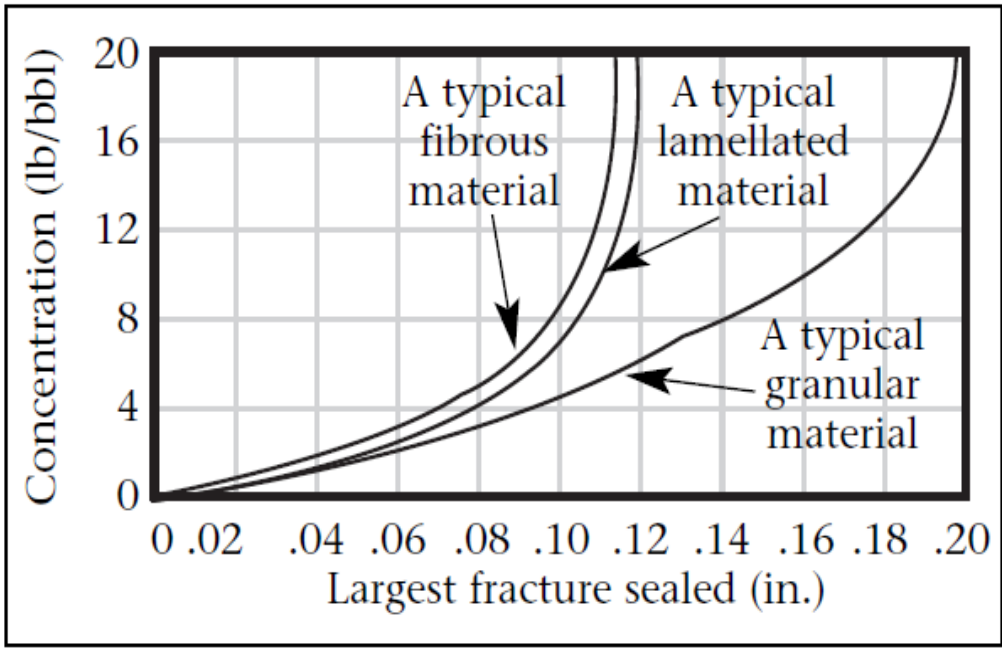

Figure 1.12. Effect of concentration and type of LCM on sealing fractures (After Howard and Scott, 1951)

1.3. SUMMARY AND CRITICAL REVIEW OF THE LITERATURE

The literature study of wellbore strengthening revealed that the DEA-13 and GPRI were the two main laboratory scale experiments conducted to investigate lost circulation. The prominent outcome of these tests was the ability to increase fracture reopening pressure using a specific type and size of materials in the drilling fluid system. Investigating the physical mechanism that enhances the fracture gradient was not truly feasible using these experiments. Therefore, a clear understanding regarding the effect of material properties (size, type and strength) of the actual sealing mechanism was never achieved.

The two main theories, Stress Cage (SC) and FCS (Fracture Closure Stress) were repeatedly mentioned for strengthening boreholes based on increasing hoop stress around the wellbore. To investigate this effect, numerical linear elastic modeling (Finite element and Boundary element methods) were formulated to see the effect of fracture sealing and/or propping on the wellbore hoop stress. Poro-elastic effects, rock and fracture permeability parameters were not considered in these studies.

Most recently, a fracture propagation resistance (FPR) explanation was proposed by Van Oort et al., 2009. This theory is mostly based on DEA-13 fracturing experiments results in which fracture gradient increase are relied on enhancing the fracture propagation pressure. Some field observations in the Gulf of Mexico and lab test results were presented to support the case by focusing mostly on using synthetic and oil-based muds. Van Oort's results are consistent with Fuh et al., 1992, where their study confirmed significant increase of fracturing pressure in the field trials with having filtrate loss to cause tip screen-out. However, this effect is not present in shales and another limitation is that it is only effective for high Young modulus rocks and when induced fracture size is small.

Although some successful field applications for "wellbore strengthening" have been reported, it is still not understood to what extent we can enhance the fracturing pressure in a wellbore. There are contradicting results on which parameters are affecting this phenomena and which physical model describes this phenomena (Table 1.3).

Table 1.3. Summary of wellbore strengthening literature

Author	Materials	Material Size	Material Strength	Tip Isolation	Rock Stress	Method	Field Applications
Fuh et al., 1992	LPM	Important	Selected Strength	Required	Not Changing	Fracture Pressure Inhibitor	California (Ventura)/ Oklahoma (Newkirk)
Alberty and McLean, 2004	Calcium Carbonate	Important	Important	Not Required	Changing	Stress Cage (SC)	Gulf of Mexico
Dupriest, 2008	DSF	Unimportant	Unimportant	Required	Changing	Fracture Closure Stress(FCS)	Malaysia (Jerneh field)/ East Texas (Trawick field)
Wang et al., 2007a, 2007b	DVCS	Important	Important		Changing	Stress Cage (SC)	Gulf of Mexico/ South Texas
Van Oort et al., 2009		Important	Unimportant	Required	Not Changing	Fracture Propagation Resistance (FPR)	Gulf of Mexico
Aadnoy and Belayneh, 2008	High Strength Materials	Important	Very Important		Not Changing	Fracture Healing	North Sea

Table 1.3 summarizes the wellbore strengthening methodologies, whereby some of them differentiate in the mechanism involved, material type and strength to be used plus the necessity for tip isolation.

Several important questions around fracturing a wellbore are still not answered. First, to what extend are we able to change the near wellbore stresses of the rock, or are we just healing the fractures and not necessarily altering the rock stress? Second, how important are mud properties and mud additive properties such as material size, type, and strength? As discussed above, some results support that the technique is successful only

when specially selected size materials are used. Some others report successful field applications regardless of material properties. For instance, different materials system, forming gels by cross-linked polymers (Aston et al., 2007), calcium carbonates (Alberty and Mclean, 2004; Fuh et al., 2007), DVCS sealant (Traugott et al., 2007; Wang et al., 2008), DSF (Drill and Stress Fluid) water-based systems (Dupriest et al., 2008) to materials with higher mechanical strength (Aadnoy et al., 2008) were reported for wellbore strengthening applications. Although some authors (Aadnoy et al., 2008) reported poor experimental results using calcium carbonate and polymer based mud systems, successful field applications with significant increase of fracture gradient were reported when these materials were used in the mud system (Fuh et al., 2007; Aston et al., 2007).

Another important issue is the application of this technique for different rocks. All reported "wellbore strengthening" operations were conducted in the hard and consolidated rocks and no significant results were achieved for implementing this technology in soft sediments. Although the methodology seems to be applicable in soft rocks, is it possible to keep the bridges stable when the formation is weak? Or what can be done with the new opened fractures while creating a cage for previously opened fractures?

Another issue is the upper bound for fracture gradient increase. Is the fracturing pressure being increased beyond what is given by the Kirsch solution? Aadnoy et al., (2008) verified that it is possible to increase fracture pressure by designing a better mud. However, a detailed leak off test of including initial fracture breakdown pressure and fracture reopening pressure when the fractures sealed has not been published yet.

Using simple linear-elastic formulations to study wellbore strengthening mechanisms is a very simplistic approach. These models are very convenient and easy to implement; however, when the outcomes compared with related experiments, it revealed that linear elastic deformation simplifies the results to a great extent. The presence of a freely moving fluid in a porous rock modifies its mechanical behavior and makes the rock to respond poro-elastically (Detournay and Cheng, 1993). This study aims to replicate the wellbore strengthening as close as possible to the real behavior of the rocks based on using porous-elastic models.

Another limitation in the wellbore strengthening literature is the limit focus on rock fracture mechanics principles. Rock fracture mechanics can give a better explanation of fracture initiation and propagation characteristics. These include the idea of micro-fracturing in rocks, fracture toughness measurement, heterogeneous and anisotropic nature of the rocks and changes in their resistance curves. One of the main objectives of this dissertation is to investigate these concepts in the context of wellbore strengthening.

1.4. PROBLEM STATEMENT AND DISSERTATION OUTLINE

As summarized, the current understanding of wellbore strengthening and the mechanisms behind it is still under debate. A common theme in all wellbore strengthening theories is that the strengthening effect is achieved by adding a blend of engineered materials to the mud system; however, the main difference is on the actual mechanism how these materials impart strengthening effect on the wellbore. Intensive numerical simulations followed by laboratory experiments and field trials are required to study those mechanisms. The laboratory setup used to date simply is not designed to impose those mechanisms. Most have only replicated a parallel plate or natural fracture experiment (Kaggeson-Loe et al., 2008). As well as for numerical simulations, pore-elastic behavior of the rock has often been ignored which has a prominent impact on stress changes when fracturing occurs.

The main objective of this dissertation is to conducting numerical simulations to understand the physical mechanisms behind wellbore strengthening. In addition, analytical models, field case studies, and lab experiments are used to further understand these mechanisms and also to support results obtained from the simulations.

Three-dimensional poro-elastic finite element simulations are carried out in this study in order to simulate fracture's initiation, propagation and sealing. Cohesive modeling is used as the primary methodology to initiate fractures which is based on non-linear fracture behavior of the rocks.

This dissertation is summarized into seven sections. **Section 1** presents an overview of wellbore strengthening, motivation and literature survey.

Section 2 reviews some fundamental concepts in fracture mechanics starting with linear elastic fracture mechanics, reviewing non-linear behavior of the fracture in rocks and finally introducing other strengthening mechanisms from fracture mechanics literature. The aim here is present a clear definition of fundamental concepts such as fracture toughness, fracture energy and fracture propagation which are used in other sections for building numerical models.

Section 3 presents an overview of stress analysis and wellbore failure mechanisms. Since the near wellbore stresses especially hoop stress plays an important role in this study, a clear understanding of these stresses is required. In addition, this section includes the Kirsch solution for near wellbore stresses and analytical solutions to predict fracture pressure in penetrating and non-penetrating situations.

Section 4 introduces the main hypothesis and methodology of the dissertation. Details on the finite-element model, analytical models for predicting fracture propagation pressure, and laboratory fracture experiments are presented. The aim of this section is to provide a deep insight on the methods and analysis used in this study.

Section 5 presents the results for the finite-element model, the analytical model, field case studies and fracture experiments. Finite-element model results include fracture width determination, parametric studies of fractures, and hoop stress results for fracture initiation, propagation and sealing. For field case studies, several field cases worldwide have been reviewed with tight pore-fracture pressure window or severe lost circulation problems. And then numerical model and analytical equations were used to predict new fracture gradient if successful wellbore strengthening operation applied. Finally, fracture experimental results are presented which have been used for calibrating finite-element model.

Section 6 discusses common misconceptions about wellbore strengthening. This can be explained better by reviewing the link between leak off tests and wellbore hoop stress. Further, two field case studies of wellbore strengthening in the Gulf of Mexico are critically reviewed.

Section 7 presents main conclusions and recommendations from this work and recommendation for future research.

2. FUNDAMENTALS OF FRACTURE MECHANICS

To investigate the fundamentals of fracture mechanics, this section is divided into two sections where the first section reviews fundamental concepts in fracture mechanics especially linear elastic fracture mechanics and the second section covers fracture strengthening in materials. The terms described in this section are the basis for the numerical simulations in future sections.

An overview of non-linear fracture behavior and subcritical fracture growth which governs the fracture pattern in rocks is explained. This is an important concept existing in fracture mechanic's literature regarding fracture patterns in rocks, because although rocks are considered as brittle materials, they are actually quasibrittle which typically show strain softening behavior (Anderson, 2005). **This behavior in rock when they fracture is the foundation to develop cohesive zone models for fracture modeling.** These models have been used for fracture simulations in this dissertation which will be explained in the next section.

Different modes of fractures are also explained. Simulations in this work only assume Mode-I fracturing which forms a classical two wing fracture. Furthermore, concept of resistance curves is also presented. This is a critical parameter in understanding how fracture toughness can be increased in materials. It is noted that rocks posses a rising resistance curve due to their non-linear fracture propagation behavior.

The objective for the second section is to review *strengthening* approaches in other materials such as ceramics. Techniques and procedures to increase fracture toughness has existed (since 1965) in ceramic's engineering literature (Evans, 1987). Different mechanisms, procedures and materials are explained to increase fracture toughness whereby some of them sound very analog to what was reviewed as wellbore strengthening mechanisms.

Various models have been developed to explain fracture closure and arrest in steel by fracture wedging. Effect of wedge location, thickness, stiffness and when to insert the wedge have been studied for steels.

2.1. ROCK FRACTURE MECHANICS

Knowledge of fracture mechanics is required to understand how rock fails during mechanical excavation processes, such as drilling, mining and fragmentation. Rock fracture applications range from energy-related areas such as drilling and hydraulic fracturing to mining, underground storage, earthquake and tectonic studies (Table 2.1). The mechanics and terminology of rock fracture is sedimentary basins are shared among geologists, petroleum, and geological engineers.

Table 2.1. Rock fracture mechanics energy applications (Modified from Swanson, 1984)

Energy Related Applications	Drilling (Oil and Gas) and Hydraulic Fracturing
	CO2 sequestration
	Geothermal
	Coal Gasification and Oil Shale Rubbilization
Mining and Other Geotechnical	Breakage
	Long-Term Stability
Underground Storage	Nuclear and Toxic-Waste Repositories
	Compressed-Gas Storage
	Solar-Heat Reservoir
Earthquake and Tectonic studies	Earthquake Prediction and Control
	Crustal-Stress Measurement
	Magma fracture and Stress Indication

The study of rock fractures has its roots in earlier work to understand the failure of the metals, and glasses; and more recently, ceramics. However, the existence of the

heterogeneity which is a physical non-uniformity of the material (Whittaker et al., 1992, page1) and the anisotropy which refers to directional properties of a material make the study of the rock fractures requiring additional terms and mechanisms to explain rock failure.

Figure 2.1 shows a sample of Berea sandstone which has several types of grain-scale heterogeneity, including heterogeneity in the size and shape of the grains, the type and geometry of grain contacts, the grain mineralogy and the amount of weathering. This indicates that even the sample assumed to be a uniform rock has different heterogeneities at grain scale which affects fracture propagation behavior and its path (Blair and Cook, 1998). Figure 2.1 also shows a section of the hydrofracture with a torturous path due to grain scale heterogeneity.

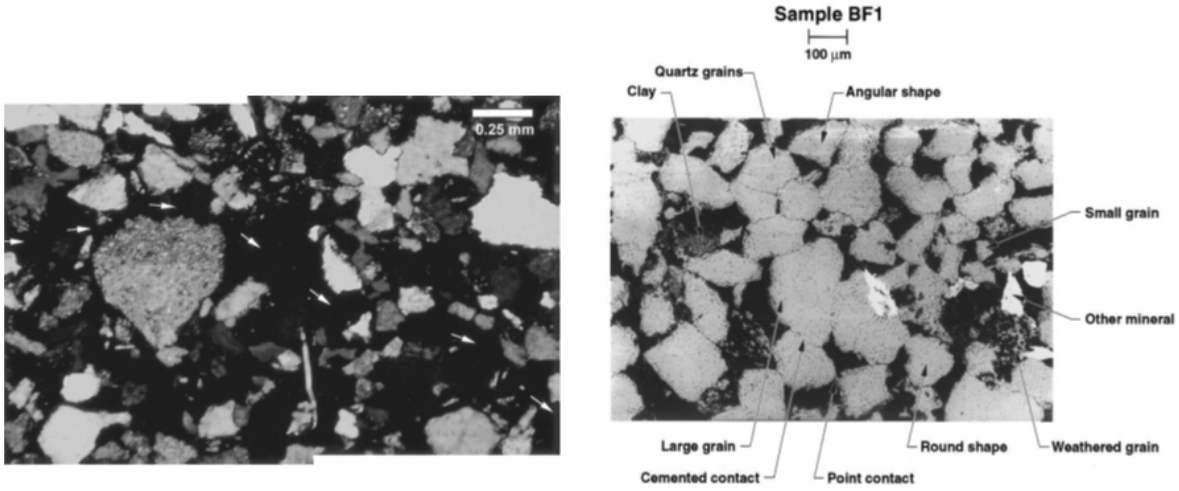

Figure 2.1. Right: Cross section of Berea sandstone, showing different types of heterogeneity in rock at grain scale (From Blair and Cook, 1998), Left: Torturous fracture path due to grain-scale heterogeneity (From Song et al., 2001)

In addition, mineral variations, in type and size, make fracture behavior different for rocks than other materials both for small and large scales. In terms of anisotropic

properties, for instance orientation of minerals, rock behaves differently to the same stress in different orientations.

Existence of initial flaws or initial fractures plays a prominent role in rocks. These fractures impact mechanical behavior of the rock masses, since existing fractures provide planes of weakness on which further deformation can more readily occur (Jaeger et al., 2007, page 365).

2.1.1. Linear Elastic Fracture Mechanics. Linear elastic fracture mechanics (LEFM) is an important fundamental concept for fracturing in rocks. A solid background in LEFM is required for understanding advanced concepts in fracture mechanics.

Leonardo da Vinci was the first man who approached the root cause of the fracture. He measured the strength of iron wires and found that the fracture strength was not a constant similar to yield strength but rather varied inversely with wire length, implying that flaws in the material controlled the strength (E.Launey and Ritchie, 2009). A connection between size of the flaw and fracture stress was later published by Griffith (1920). Griffith developed a relationship among fracture shape, material properties and the external force needed for fracture propagation. According to Griffith, the fracture stress for a penny-shaped crack in a material is (Anderson, 1995):

$$\sigma_f = \left(\frac{\pi E \gamma_s}{2(1-\upsilon^2)a}\right)^{\frac{1}{2}} \tag{2.1}$$

Where a is the crack radius, E and v are material Young's modulus and Poisson's ratio describing the material deformation with stress and γ_s is the surface energy per unit area that is equal to one half of the fracture energy, because two surfaces are created when a material fractures. Following Griffith, another approach for crack modeling was introduced by Irwin (1954) that is almost equivalent to the Griffith model but is more convenient when used in engineering applications:

$$G = \frac{\pi \sigma^2 a}{E} \tag{2.2}$$

Where G is the energy release rate which is the amount of energy for an increment of crack extension (Anderson, 1995). The Griffith theory for the critical

condition in fracture initiation becomes as given by the following equation (Whittaker et al., 1992):

$$G = G_C \tag{2.3}$$

Where G_C is the critical strain energy release rate. Sometimes it is also named fracture toughness which is a characteristic property of a material. Fracture toughness is a quantitative way of expressing a material's resistance to brittle fracture. Since the initiation of the fracture depends highly on fracture toughness value, the determination of this parameter appears to be very important. Extensive laboratory work has been done on determination of fracture toughness in various rocks where different types of specimen configurations have been used (Clifton et al., 1976).

2.1.1.1. Crack tip displacement modes. Assuming an ideal flat and sharp crack, there are three modes of crack displacement (Atkinson, 1987). Different loading at crack tips including normal, in-plane shear and out of the plane shear generates the following modes (Figure 2.2):

Mode I or opening mode: In this mode the tip of the crack is subjected to normal stress which separates the crack faces symmetrically regarding to the crack front so that the displacements of the crack surfaces are perpendicular to the crack plane (Whittaker et al., 1992).

Mode II or in-plane shearing mode (sliding mode): An in-plane shear stress affects the crack tip which makes the crack faces slide relative to each other so that the displacements of the crack surfaces are in the crack plane and perpendicular to the crack front.

Mode III or out-of-plane mode (tearing mode) is the case where an anti-plane shear stress affects the crack tip. In this mode, the crack faces move relative to each other so that the displacements of the crack surfaces are in the crack planes but parallel to the crack front.

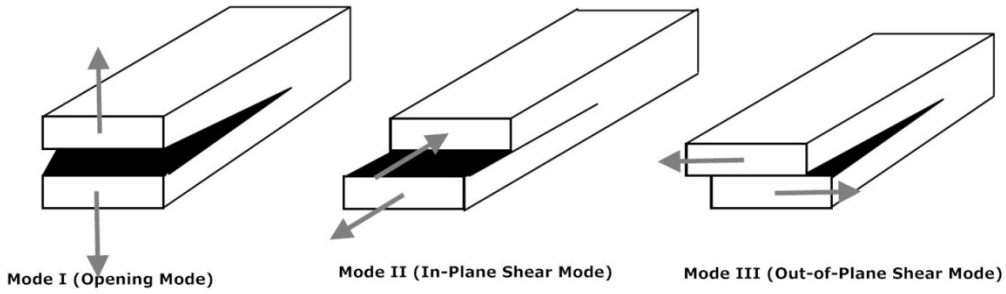

Figure 2.2. Three modes of crack tip displacement

Mode I is the most important loading case in the majority of the scientific and engineering applications. For this reason, most of the fracture mechanics work has concentrated on the Mode I stress intensity factor and fracture toughness in rock fractures (Atkinson, 1987).

2.1.1.2. Stress intensity analysis. Assuming isotropic linear elastic material model, it is feasible to derive a closed-form solution for the stresses in certain cracks. This will be valid if the non-linear region be negligibly small. It is believed, however, that non-linear behavior is involved at crack tips in many materials. Figure 2.3 shows the polar coordinate axis with the origin at the crack tip. Each of the loading produces stresses near the tip proportional to $\frac{1}{r^2}$ which r is the distance from the crack tip. The stress intensity factor, K_I, is the magnitude of the crack tip stress field for a particular mode in a homogeneous linear elastic material. Stress fields ahead of the crack tip in Mode I and Mode II are shown in the Table 2.2.

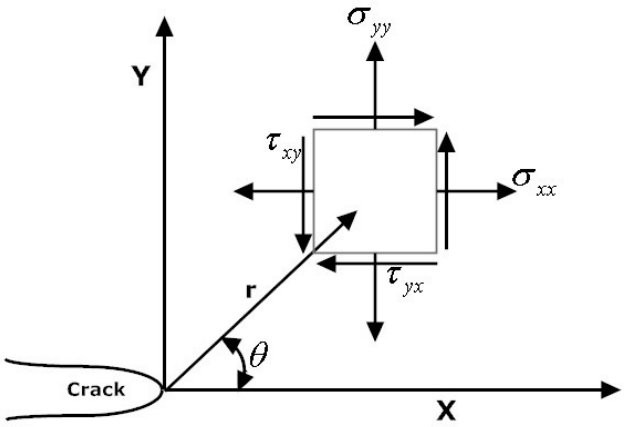

Figure 2.3. Stresses at the crack tip based on linear-elastic model

Table 2.2. Stresses ahead of the crack tip for opening and in-plane shear modes (Anderson, 2005)

	Mode I	Mode II
σ_{xx}	$\frac{K_I}{\sqrt{2\pi r}}\cos(\frac{\theta}{2})[1-\sin(\frac{\theta}{2})\sin(\frac{3\theta}{2})]$	$-\frac{K_{II}}{\sqrt{2\pi r}}\sin(\frac{\theta}{2})[2+\cos(\frac{\theta}{2})\cos(\frac{3\theta}{2})]$
σ_{yy}	$\frac{K_I}{\sqrt{2\pi r}}\cos(\frac{\theta}{2})[1+\sin(\frac{\theta}{2})\sin(\frac{3\theta}{2})]$	$\frac{K_{II}}{\sqrt{2\pi r}}\sin(\frac{\theta}{2})\cos(\frac{\theta}{2})\cos(\frac{3\theta}{2})$
τ_{xy}	$\frac{K_{II}}{\sqrt{2\pi r}}\cos(\frac{\theta}{2})\cos(\frac{\theta}{2})\cos(\frac{3\theta}{2})$	$\frac{K_I}{\sqrt{2\pi r}}\cos(\frac{\theta}{2})[1-\sin(\frac{\theta}{2})\sin(\frac{3\theta}{2})]$
σ_{zz}	0 (Plane Stress) $\upsilon(\sigma_{xx}+\sigma_{yy})$ (Plane Strain)	0 (Plane Stress) $\upsilon(\sigma_{xx}+\sigma_{yy})$ (Plane Strain)
τ_{xz}, τ_{yz}	0	0

2.1.1.3 Unstable cracks and R curve. According to Griffith, the fracture starts initiating when $G = G_C$. To distinguish stable from unstable crack growth, R is replaced by G_C, which is the material resistance to crack propagation. A plot of R versus crack extension is called crack resistance curve or R curve (Anderson, 1995). Driving force curve is given as the plot of G versus crack extension.

To distinguish between the flat R-curve and increasing R- curve consider Figures 2.4 and 2.5. In the flat R-curve, the material resistance is constant with crack growth; so that a single value of the toughness characterizes the material. When the stress reaches σ_1 the crack stays stable; but once the crack reaches σ_2, the crack extension will become unstable. This is due to increase in driving force with crack growth while the material resistance remains constant. In materials with a rising R-curve, stable crack growth occurs. In these materials, there is no single value of toughness that characterizes the material as the driving force for unstable crack propagation depends on the extent of crack growth. As illustrated in Figure 2.5, the crack grows a small amount when the stress reaches σ_2 but cannot grow unless the stress increases. The conditions for stable crack growth can be expressed as follows (Anderson, 1995):

$$\text{G=R and } \frac{dG}{da} \leq \frac{dR}{da} \tag{2.4}$$

Unstable crack growth occurs when:

$$\frac{dG}{da} \succ \frac{dR}{da} \tag{2.5}$$

According to Equations 4 and 5, a material fails when the driving force is tangent to the R-curve.

Material behavior is a dominant factor on shape of the R-curve. For instance, in ideal brittle materials the R-curve is flat. The material R curve will change once non-linear material behavior affects fracture. Existence of ductile materials or a zone of elastic-plastic will result in a rising R curve.

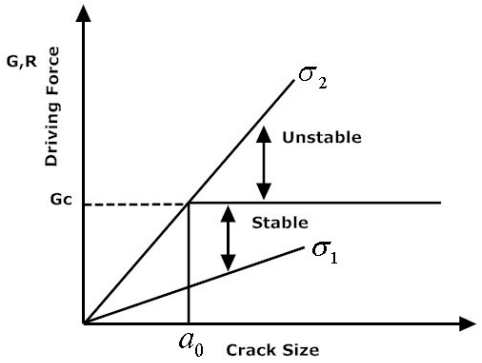

Figure 2.4. Driving force/flat R-curve diagram

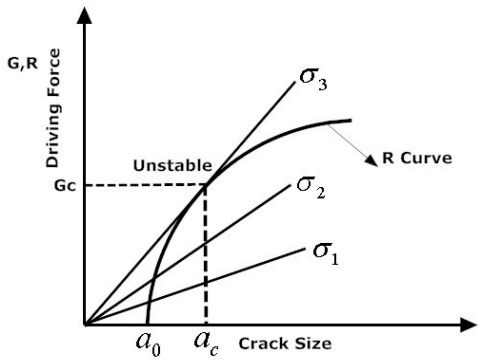

Figure 2.5. Driving force/rising R-curve diagram

The driving force must be increased for crack propagation in materials having a rising R curve. Geometry and size of the cracked structure can also have some effects on the shape of R curve. A crack in the thick sheet will produce a different R curve than a plate in a thin sheet, because conditions in front of the crack tip in the thin sheet will be plane stress while in the thick plate it is loaded in plain strain.

The advantage of using R curve approach is that it will be compared with the appropriate crack extension force or curves of the specimen. The unique K curve that develops tangency with the R curve defines the critical load that will cause forming of unstable fracturing. The R curve method has been employed to describe material fracture toughness variation beyond the slow stable crack initiation portion. This approach is used when fractures are initiated in rocks because the existence of R curves in rocks has been well observed (Ouchterlony, 1982a and b).

2.1.2. Subcritical Fracture Growth: A Common Phenomenon in Rocks, Glass, Metals and Ceramics. Subcritical crack growth is another characteristic that makes the rocks have non-linear and time-dependent crack growth (Swanson, 1984). Although it is often assumed that the rocks behave as brittle materials which obey LEFM (Linear-Elastic Fracture Mechanics) in reality they act more like quasibrittle materials. This behavior is better described using non-linear fracture mechanics. The non-linear behavior has the form of microcracking in the fracture zone which continues until

ultimate failure (Figure 2.6). The subcritical crack growth which is the main reason for the microcracking was first observed in the glass by Grenet (1899);
"*This fact was appreciated by French champagne makers of the time who never used the same bottle twice, although bottles were expensive, thus saving many a good bottle of wine from destruction*"

Later similar fracture behavior was seen in other materials such as rocks, metals and ceramics. In metals, fatigue crack growth happens at a significant lower stress intensity values than the fracture toughness. The reason is the accumulation of damage from the cyclic plastic deformation in the plastic zone at the crack tip. An example of this delayed failure in metals was observed in World-War II, when "at least nine T-2 tankers and seven liberty ships suddenly broke completely in two by brittle fracture" (Rolf and Barsorm, 1977). This phenomenon also leads to very complex fracture propagation in rocks which often requires intensive studies for the prediction of fracture parameters. Environmental chemical effects on rock destruction is one of the factors that have mostly been ignored by the majority of researchers compared to other mechanical effects such as pore pressure and swelling (Torfs and Van Grieken, 1997). Today, knowledge of subcritical fracture growth is of great significance in rock fracture mechanics which catastrophic fracture propagation is often observed (Anderson, 1995). It is also essential to know the long-term response of the pre-existing fractures in deep sedimentary basins which are the targets of drilling for hydrocarbons. Time-dependent behavior of fault reactivations and earthquake processes are better explained with subcritical fracture growth (Lockner and M. Beeler, 2002).

Investigating non-linear region ahead of fracture tip can help to understand variations in fracture toughness with different parameters. This region is a governing factor in fracture mechanics, because it controls important aspects such as stress and strain distribution, fracture mechanics parameters, and in particular, the fracture toughness (Whittaker et al., 1992). The nature of non-linearity is quite different in rocks and metallic materials. In metals, shearing is the main producer of the crack tip plastic zone. For this reason, shape and size of the plastic zone can be well described by classical yield criterion (Whittaker et al., 1992, Atkinson, 1987).

In rocks, opening of the existing and newly formed microcracks is the main cause of producing a non-linear region. When the microcracks initiate and propagate, they will form a microcrack zone ahead of the crack tip (Figure 2.6). Development of this zone finally leads to a macrocrack extension and this keeps the fracture propagating. Most rocks frequently exhibit highly non-linear behavior prior to significant macroscopic propagation (Atkinson, 1987, Anderson, 2005).

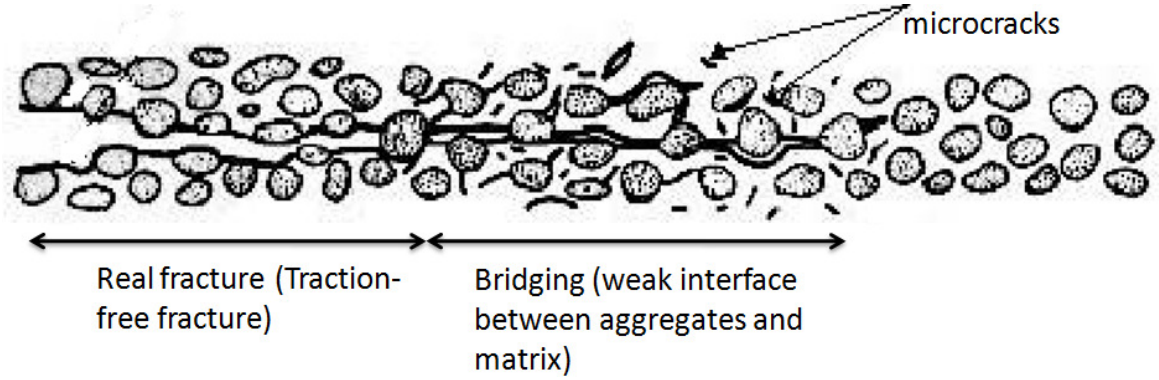

Figure 2.6. Fracture propagation in rocks, microcracks form ahead of a macroscopic fracture, bridged zone exists directly behind the tip (Modified from Anderson, 1995)

Measured laboratory values of subcritical crack propagation have a range starting from 10^{-2} to 10^{-8} (m/s). Under these rates, it would take around 30 seconds to one-year for a crack to propagate equal to the length of a sheet of paper (Swanson, 1984). This time-dependant crack propagation behavior is observed in various materials such as metals, concrete and rocks. It is believed this behavior is not only a property of the material but also affected by environmental conditions. For instance, moisture is recognized as one of the factors responsible for time-dependant subcritical growth in glass (Freiman et al., 2009).

Subcritical fracture growth can be a significant factor for rocks in tectonically active regions. It has been shown that fracture aperture and connectivity can be controlled

by this process (Olson et al., 2001). An empirical equation has been derived to correlate subcritical fracture velocity and the stress intensity factor (Gale et al., 2007):

$$V = k_0 (\frac{K_I}{K_{IC}})^n = AP^n \quad (2.6)$$

where n is the subcritical fracture index, K_I is the stress intensity factor and K_{IC} is the critical stress intensity factor or fracture toughness, P is the applied load and, A and K_0 are constants. Table 2.3 reports subcritical crack index with other rock mechanical properties for different shales and chalks.

Table 2.3. Reported subcritical index and rock mechanical properties for shales and chalks (From Gale et al., 2007)

Lithology	**Young Modulus (GPa)**	**Poisson's Ratio**	**Subcritical crack index (n)**
Barnett Shale	33	0.2-0.3	109-326
Other Shales	4.5-61	0.03-0.3	No data
Austin Chalk	48	0.1-0.4	95-124
Other Chalks	25.6-65	0.24	No data

When planning hydraulic fracturing operations, it is required to have knowledge of the subcritical fracture index to characterize fracture patterns such as their spacing, size, sealing and orientation to bed thickness (Gale et al., 2007).

2.1.3. Hydraulic Fracture Models. There have been numerous theories proposed for hydraulic fracturing in rocks (Harrison et al., 1954, Hubbert and Willis, 1957 and Economides, 1995). Traditionally, Griffith-Sneddon formed the basis of most fracture geometry models (Economides, 1995). Their work then was expanded by Perkins and

Kern (1961). Later on Nordgren (1972) modified the PK model to include the effects of fluid loss into formation. Khristianovic and Zheltov (1955) and Greetsma and de Klerk (1969) developed another fracturing model, assuming horizontal plane strain condition often referred to as the KGD geometry (Figure 2.7).

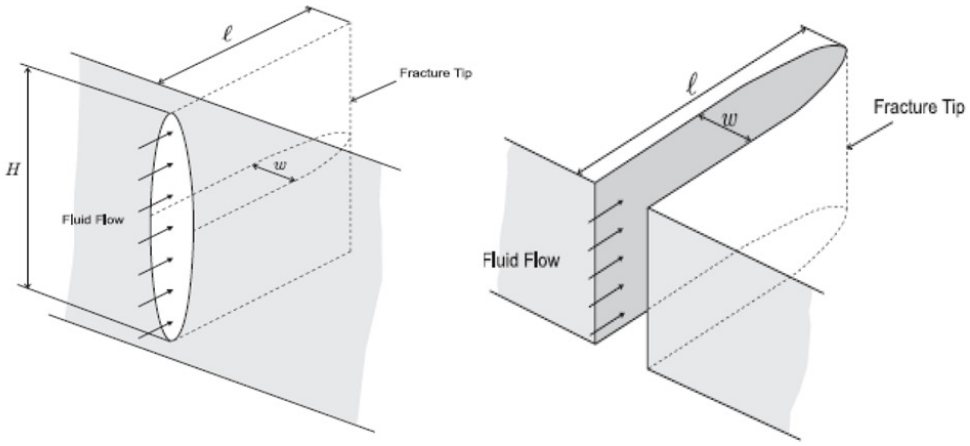

Figure 2.7. PKN and GDK 2D fracture geometry models (Taken from Adachi et al., 2007)

The maximum fracture width (w_m) occurs at the borehole wall in both models and for the PKN model:

$$w_m = \frac{2(1-\upsilon^2)Hp_n}{E} \tag{2.7}$$

And for the KGD model, the Equation 2.8 is used.

In the Equation 2.8, L is fracture length, E is the Young's modulus of formation, and v is the formation Poisson's ratio.

$$w_m = \frac{4(1-\upsilon^2)Lp_n}{E} \tag{2.8}$$

H is the total fracture height and L is fracture half length, and p_n is the net fracture pressure (which is the fluid pressure inside the fracture subtracted by the smallest in-situ stress, Fjaer et al. 2009).

The main difference in two models is that the PKN model assumes plane strain in the vertical direction and the KGD model assumes plane strain in the horizontal direction. Fractures in formations are bound at the top and bottom by lithologies; and thereby, a limited fracture height is better approximated by the PKN model. Small fracture treatments or uncontrolled fracture height are better approximated by the KGD model (Valco and Economides, 1995). Another important difference is that in the PKN model the effect of the fracture tip is not considered; wherein the KGD model, the tip area plays an important role.

Although using these models has led to successful hydraulic frac operations, it has been found that when dealing with complex geomechanical fields or when drilling in unconsolidated formations, these models cannot predict fracture geometry accurately (Fett et al., 2008). The main reason is the complexity of the hydraulic fracturing process such as, coupling exists between mechanical deformation, fluid flow inside fractures and fracture propagation. If stress anisotropy and rock heterogeneities added to those processes, then the problem needs more investigation regarding the effects of new parameters added.

PKN and KGD modified models were not applicable to layered reservoirs where the fracture growth is dependent upon changes in the formations confining stress. These models were frequently used until the 1990s and sometimes used today, but they have been replaced by pseudo-3D models as well as advanced finite-element models (Adachi et al., 2007, Advani and Lee, 1992 and Stolarska et al., 2000).

Finite-element models have the capability of considering geomechanical properties of the formation and are widely used today to predict fracture geometry in hydraulic fracturing operations. One advantage of using these techniques is their ability to consider different couplings involved in the fracturing process. Wherein, the existing analytical solutions cannot accurately predict fracture behavior due to non-linearity of the process and complex boundary conditions.

2.2. FRACTURE TOUGHENING (STRENGTHENING) IN ADVANCED MATERIALS

As mentioned in the introduction section, increasing fracture resistance by improving rock fracture pseudo-toughness is one of the primary wellbore strengthening mechanisms. This can normally be done by shielding the fracture tip using appropriate fracture filling materials.

Although the term "strengthening" is a new phrase in the drilling industry for enhancing fracture gradient, it has existed in other branches of engineering as *fracture strengthening* or *toughening* (Evans, 1990, Ohiji et al., 1998). This approach has applications in different materials including ceramics, bones, polymers and steels. For this reason, the aim of this section is to review existing mechanisms for fracture toughness improvement in the fracture mechanic's literature.

Improving fracture resistance (fracture toughness) is often referred to as *fracture toughening* which sometimes is also called fracture *strengthening* in different materials including ceramics, bones, polymers and steels (Ohiji et al., 1998).

Fracture strengthening mechanisms help to develop and formulate appropriate materials to enhance fracture resistance for various non-metallic materials such as ceramics. Ceramics are used in engineering applications due to their hardness and wear resistivity as well as their chemical and environmental durability. However, the brittle nature of these materials caused by weak ionic bonds and low fracture resistance resulted in catastrophic failure under a low stress level in some applications (Cao and Sakai, 1996). To increase ceramic's toughness and resistance, they were fiber and glass reinforced. Reinforcement of ceramics was demonstrated as early as 1972 (Evans, 1990). However, extensive research on increasing ceramics toughness was not pursued until 1983 when SIC-fiber-reinforced glass ceramics were introduced. Toughening Al_2O_3 with SiC (Silicate Carbonates) whiskers was also a step forward in developing the concepts of toughening brittle materials.

Increasing the fracture toughness in epoxy systems (Cardwell and Yee. 1998) and bioceramics for replacement of human bones (Peterlik et al., 2006) were also introduced. Experimental results in the last two decades on increasing the fracture toughness by

orders of magnitudes attracted a great deal of attention on the mechanisms involved (Warner et al., 1991; Niihara, 1991).

Different mechanisms were identified for causing the material toughening. These mechanisms target either the zone ahead of the fracture which is sometimes referred to as intrinsic toughening (intrinsic strengthening) or the zone behind the crack tip which is called extrinsic toughening (extrinsic strengthening, E.Launey and Ritchie, 2009; Ritchie et al., 2000; Ritchie, 1999).

Figure 2.8 illustrates the difference between these two toughening mechanisms. Intrinsic strengthening mechanisms are an inherent property of the material which are normally active irrelevant to crack size and geometry.

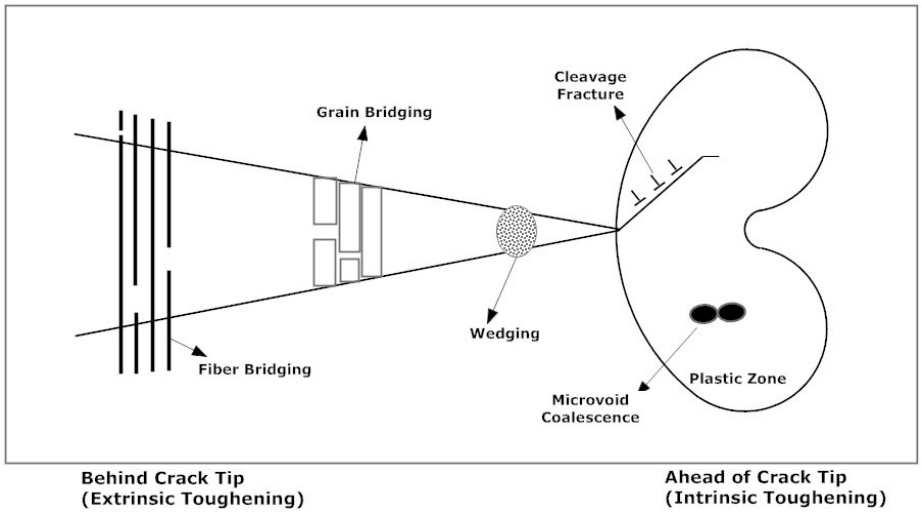

Figure 2.8. Extrinsic strengthening mechanism (Fiber Bridging, Grain Bridging, and Wedging) acting behind crack tip versus intrinsic strengthening mechanisms acting ahead of crack tip (Modified form E.Launey and Ritchie, 2009)

Intrinsic strengthening is normally active in metals where dislocation pile-ups or interface decohesion lead to failures by cleavage and intergranular cracking (Ritchie, 1999).

Extrinsic strengthening reduces the crack-driving force. This sometimes is referred to as crack-tip shielding by introducing materials into the fracture. Both intrinsic and extrinsic mechanisms reduce the crack extension driving force as the crack grows. Sometimes a steeper resistance curve can be achieved when these mechanisms are applied. For instance, bridging mechanism in alumina-silicon carbide nanocomposites creates a steeper R-Curve compared to monolithic alumina polycrystals (Figure 2.9).

The advantage of a steep increase in fracture resistance is that it leads directly to high fracture strength which is the main goal in ceramic nanocomposites.

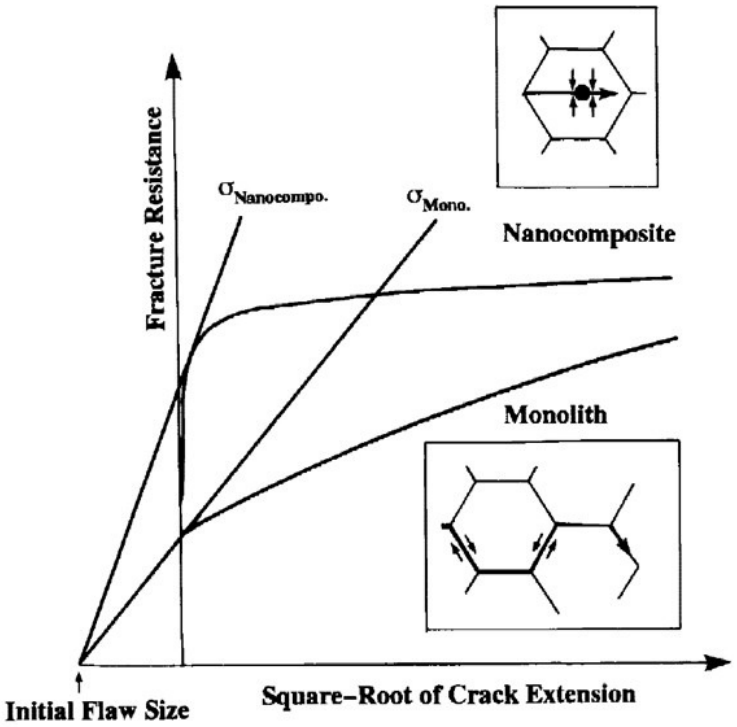

Figure 2.9. Fracture resistance-curves of the alumina-silicon carbide nanocomposite and the monolithic alumina polycrystal, fracture resistance steeply increases with particle bridging (Taken from Ohiji et al., 1998)

2.2.1. Toughening Mechanisms in Ceramics. Several micromechanisms are proposed to be responsible for increasing the fracture resistance in ceramics (Anderson, 1995). The micromechansims proposed are given in Table 2.4.

Microcrack toughening is to release the strain energy by formation of microcracks in or near the second-phase particles. The main problem with this mechanism is a need for a rising R curve behavior, because stable microcrack growth does not usually occur in a brittle solid. Initial flaws in these materials force the crack to propagate unstably, that leads it to the final failure. Generally, this mechanism is relatively ineffective which only a few number of multiphase ceramic materials were being toughened by the microcrack toughening mechanism. Table 2.5 summarizes the toughness achieved by different mechanisms.

Table 2.4. Proposed micro mechanisms and their description

Proposed micromechanism	**Description**
Microcrack toughening	Releasing energy by forming microcracks
Transformation toughening	Building a non-linear zone near the crack tip
Ductile phase toughening	Bridging and absorbing near fracture tip
Fiber toughening	High strength fibers to increase fracture resistance
Whisker toughening	Increasing Fracture Toughness

The main idea in the transforming toughening mechanism is to transform particles near the crack tip which results in a non-linear process zone. Crack tip shielding is a common alternative definition where the local driving force decreased at the crack tip.

Table 2.5. Ceramics with toughening mechanisms (Modified from Anderson, 1995)

Toughening Mechanism	Material	Maximum Toughness, MPa$\sqrt{m}$
Fiber reinforced	LAS/SiC	~20
	Glass/C	~20
	SiC/SiC	~20
Whisker reinforced	Al_2O_3/SiC	10
	Si_3N_4/SiC	14
Ductile network	Al_2O_3/Al	12
	B_4C/Al	14
	WC/Co	20
Transformation toughened	PSZ	18
	TZP	16
	ZTA	10
Microcrack toughened	ZTA	7
	Si_3N_4/SiC	7

Using nanocomposites in modern ceramics lead to a steep R curve behavior for ceramic materials which results in increasing fracture toughness incredibly as demonstrated in Figure 2.10. For instance, the fracture toughness of a magnesia-silicon carbide nanocomposite improved from 1.2 MPa.m$^{1/2}$ to 4.5 MPa.m$^{1/2}$, followed by strength increase from 340 MPa to 700 MPa (Niihara, K. 1991).

The main mechanism in ductile phase toughening is to have ductile materials in the fracture zone which can do both bridging and process zone toughening (Figure 2.11). Ductile materials increase the fracture resistance of the materials by plastically deforming to bridge the faces of a propagation crack and absorbing its energy through applying closure stress in the crack tip region.

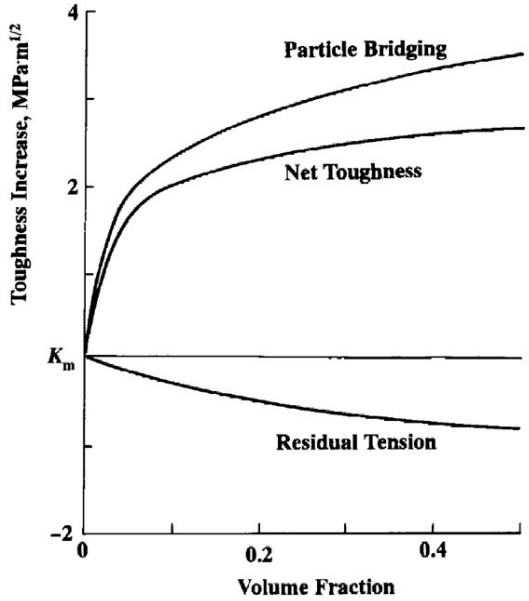

Figure 2.10. Fracture toughness curves in alumina-silicon carbide nanocomposite, fracture toughness increased as a result of particle bridging (Taken from Ohiji et al., 1998)

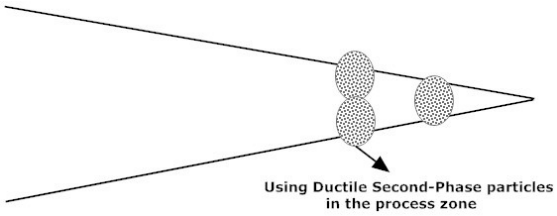

Figure 2.11. Ductile phase toughening, ductile second-phase particles increase the ceramic fracture resistance by plastic deformation in the fracture zone

This mechanism has applications in bioceramics. For instance, hydroxyapatites with low fracture toughness were strengthened using ductile platinum particles. The

experimental observation also confirms the role of using ductile particles within the ceramics matrix (Sigl et al., 1981; Rubinstein and Wang, 1998; Bannister et al., 1992; Biner, 1994).

Similar results were observed with the addition of thermoplastic second phase materials in epoxy blends (Cardwell and Yee, 1998). Presence of the thermoplastic phase significantly increased the fracture toughness of the epoxy matrix materials with a very small decrease in compressive modulus and yield strength.

2.2.2. Calculation of Fracture Toughness Increase by Using Ductile Particles. The work of fracture per unit area of the crack face is given by (Bannister et al., 1992):

$$\Delta G_{ss} = V_f \int_0^{u_{\max}} \sigma(u)du \tag{2.9}$$

V_f is the volume fraction of the ductile materials and $\sigma(u)$ is the nominal stress required to stretch the a ductile particle by u. $U_{\max}$ is the failure displacement. The crack displacement in the case of a small bridging zone can be calculated by the following equation:

$$u(x) = \frac{8(1-\upsilon^2)}{\sqrt{2\pi}} \frac{K_c}{E} \sqrt{x} \tag{2.10}$$

Where x is the distance from the crack tip, K_0 , E and υ are the fracture toughness, Young's modulus and Poisson's ratio of the material. Using ductile particles in the fracture zone increases the fracture toughness of ceramic by the Equation 2.11.

In the Equation 2.11, K_{ss} is steady-state resistance of the toughened material when ductile particles are used. The equation indicates that material Young's modulus and Poisson's Ratio play a prominent role in strengthening the material using ductile particles.

$$K_{ss} = \{K_c^2 + \frac{E}{(1-\upsilon^2)} \Delta G_{SS}\}^{1/2} \tag{2.11}$$

2.2.3. Toughening Materials by Fiber and Whisker. Using fibers in ceramics proved to be one of the effective mechanisms in ceramic toughening. The bond between the matrix and fibers is the key point resulting in fracture toughness increase. As shown in Figure 2.12, the behavior is linear elastic up to $\sigma_{\max}$ which the steady-state cracking initiates in the ceramic matrix. Once the crack initiates in the matrix, the load is carried

by fibers. The fibers do not fail simultaneously, because the fibers in between have a very high strength. As a result, the material behaves in a quasiductile way, where damage accumulates gradually until final failure. Figure 2.13 shows how fibers increased the overall material's fracture toughness.

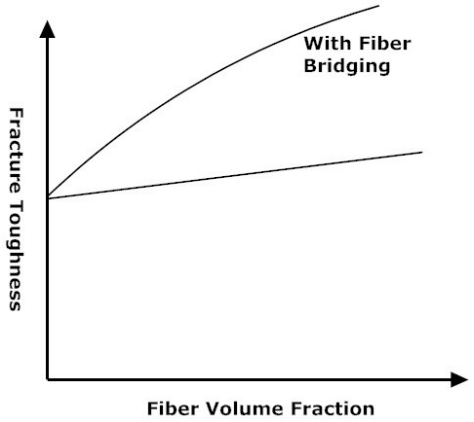

Figure 2.12. Fiber-bridging increases fracture toughness (modified from Anderson, 1995)

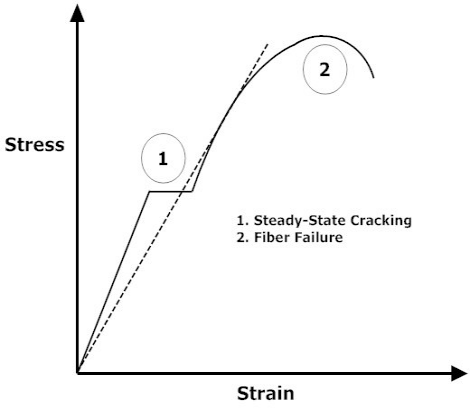

Figure 2.13. Stress-strain behavior with fiber bridging mechanism

2.2.4. Toughening Mechanism in Bones. As in ceramics, similar strengthening mechanisms were identified in bones which includes viscoplastic flow, microcracking and crazing, crack bridging and crack deflection that are illustrated in Figure 2.14.

Fibers of collagen are assembled into the structure of a mature bone. These fibers act as bridging agents when the initial fracture starts to propagate in the bone. And like polymers, viscoplastic flow is an active mechanism in which collagen needs time to re-form after pulling.

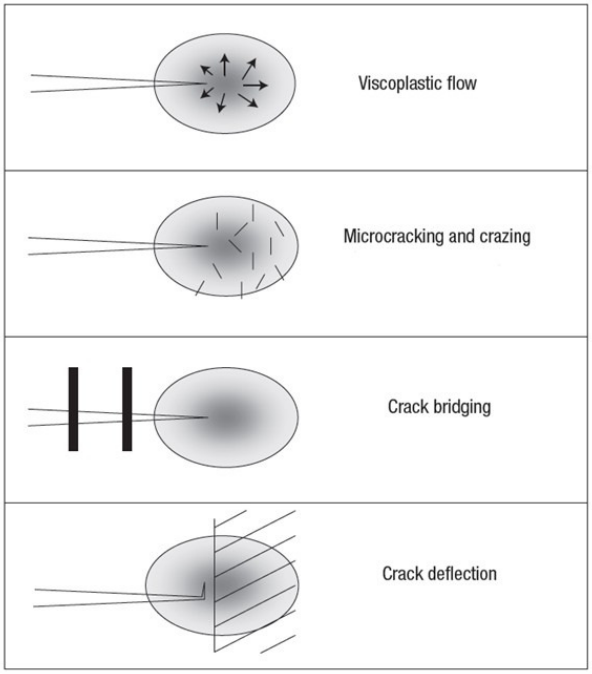

Figure 2.14. Effective toughening mechanisms in bone (Taken from Peterlik et al., 2005)

Formation of microcracks in a fracture zone also help to reduce the stress intensity factor near the crack tip. Crack bridging is the effective mechanism in bones when intact ligaments inside the crack reduce the fracture driving force.

2.2.5. Toughening Mechanism in Steel and Polymers (Fatigue Crack Retardation). One of the key failures in structural materials is fatigue which demands specific devotion to develop procedures to stop fatigue crack propagation. The process of fatigue failure itself includes several other processes which involve initial cyclic damage, crack initiation, crack propagation and final failure (Ritchie, 1999).

The mechanism of mitigating fatigue-crack propagation is quite similar to corresponding toughening mechanisms in brittle materials such as intermetallics and ceramics. One of effective procedures to stop this is by shielding the crack tip which reduces the stress intensity factor near the crack tip and results in the fracture resistance increase (Maiti and Geubelle, 2006).

Infiltration of appropriate materials inside the crack shows that it helps to bring additional crack closure and stop subsequent crack propagation (Sin and Cai, 2000). The successfulness of this procedure depends on the properties of the sealant and how to effectively keep it inside the crack.

Various models have been developed to explain the crack closure and arrest effect in this approach (Shin and Cai, 2000; Ur-Rehman and Thomason, 1993; Yanyan et al., 1993). In one of these models (Ur-Rehman and Thomason, 1993), a rigid body wedge was considered inside the crack while others discussed that the wedge must be modeled using elastoplastic material behavior in order to arrest the fracture (Sin and Cai, 2000). An important finding in their studies was that "A higher sealant Young's Modulus increases the amount of induced crack closure; however, the modulus should be above a certain value in order to have a significant closure effect."

Another key factor in fatigue crack retardation is the distance the wedge has from the crack tip (Ur-Rehman and Thomason, 1993). Figure 2.15 is a result of elasto-plastic finite element studies of non-linear fractures where the wedge is inserted at different distances from the crack tip (Maiti and Geubelle, 2006). It demonstrates that the shielding effect is reduced as the distance between the bridge and the crack tip increased.

Results regarding change in the bridge thickness indicate as the thickness increases, the stress intensity factor also increases and this results in a higher closure effect (Figure 2.16).

Demonstrated results on the effect of bridging time confirm that the sooner the bridge is inserted, the more effective the bridging mechanism becomes (Figure 2.17).

Finally, when the bridge behaves as a rigid body, it is very effective in influencing closure. Figure 2.18 shows that the rigid wedge arrests the crack growth; and once the crack starts propagation again, the rate of propagation is significantly lower than in other cases.

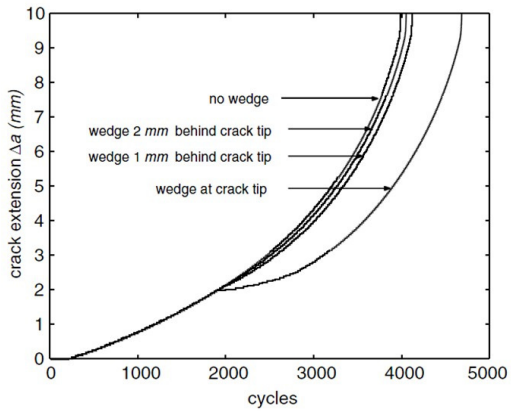

Figure 2.15. Effect of wedge location at different distances from the crack tip (Taken from Maiti and Geubelle, 2006)

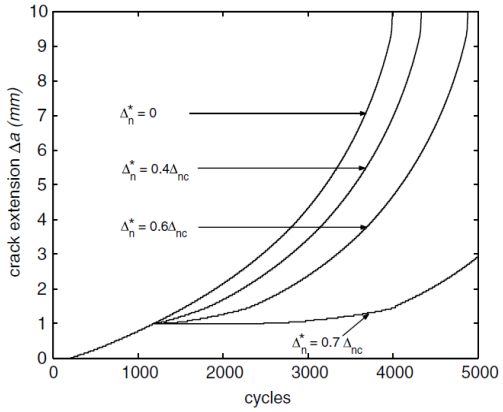

Figure 2.16. Effect of wedge thickness on the crack propagation, Δ_{nc} is the displacement jump of the fracture and Δ^{*}_{nc} is the wedge thickness (Taken from Maiti and Geubelle, 2006)

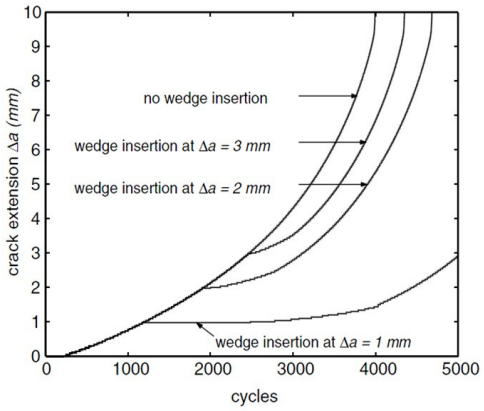

Figure 2.17. Effect of wedge insertion behind the crack tip after the crack has propagated by 1, 2, 3 and 4 mm (Taken from Maiti and Geubelle, 2006)

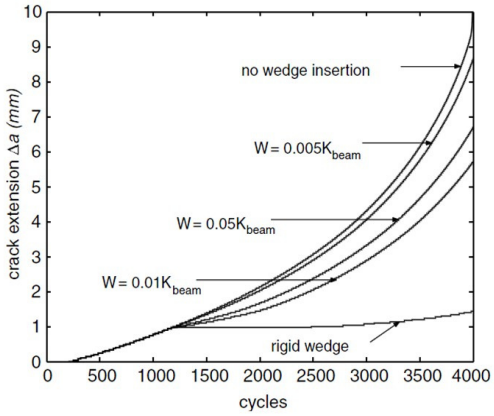

Figure 2.18. Evaluation of crack propagation by changing wedge stiffness (Taken from Maiti and Geubelle, 2006)

2.3. SUMMARY

Fracturing is reported to be a key problem in all engineering aspects. Substantial efforts have been made to investigate the mechanisms involved in fracture initiation and propagation that mainly relies on the Griffith work on the linear elastic fracture mechanics (LEFM).

In order to comprehend and formulate the fracture behavior in rocks, special characteristics of the rocks must be considered. Rocks often have heterogeneities and anisotropies that are associated with having different mineral and layering under various loadings and geological conditions. In addition, subcritical fracture growth that is a common phenomenon in rocks must be considered when formulating rock fracture mechanics (Swanson, 1984). Time-dependency fracture behavior and delayed failure is observed in the rocks to classify them under non-linear fracture mechanics or as quasi-brittle materials.

Fracture toughness is a crucial parameter in fracture propagation of all materials. Usually, this parameter can only define the propagation behavior but also the demonstration of the fracture driving force with its extension which is referred to as fracture resistance curve or simply fracture R-Curve (Anderson, 1995). In materials with the rising R-curve, the resistance of the materials to fracturing increases when fracture propagates. The implication here is that toughness is often developed primarily during fracture propagation and not fracture initiation.

The concept of R-Curve behavior paved the way for fracture mechanics researchers to develop high strength materials. This approach is called strengthening or toughening and have applications in ceramics, and bioceramics in medical applications; such as bone replacement, and metals in structural engineering (Evans, 1990, Ohiji et al., 1998). Strengthening is often grouped into two categories; intrinsic strengthening that target ahead of the fracture tip and extrinsic strengthening that target behind the fracture tip. Fracture bridging, shielding through using high strength fibers, wedges and ductile particles are examples of extrinsic strengthening. Although the mechanism involved in each approach is different than the other, the main goal is to give the material R-Curve behavior or steepen the fracture resistance curve. For instance, significant increase of

ceramics strength has been reported by using nano-composite materials in which the mechanism led to a very steep R-Curve (Niihara et al., 1991).

Extrinsic strengthening methods have also been used in metals in which inserting the wedge in the fracture made it possible to mitigate fatigue-crack propagation. Results of the related studies revealed that proximity of the wedge to the fracture tip is a major factor in stopping the fracture propagation. It was also concluded that the mechanism becomes more effective when the wedge is inserted early into the fracture (Maiti and Geubelle, 2006). Using a rigid wedge also resulted in a higher closure effect of the fracture. The rigid wedge arrests the fracture growth more deliberately; and once the fracture starts propagation again, its rate is significantly lower than in other cases.

3. STRESS ANALYSIS AND WELLBORE FAILURE MECHANISMS

There are two sets of principal stresses important in the analysis of wellbore stability: Near wellbore stresses and far-field stresses. Near wellbore stresses can be categorized as radial and tangential stresses. The tangential stress, often called the hoop stress, is the most critical near wellbore stress for wellbore stability analysis. Far field stresses exist in the formation far away from the wellbore and are not affected by the wellbore (Aadnoy, 2009). Near wellbore stresses are controlled by mud density and/or corresponding ECD (equivalent circulating density) when in dynamic conditions.

Equations defining stresses around wellbore were initially derived by the Kirsch in 1898. Since these equations are used in the following sections for mesh sensitivity analysis and results discussion, the equations are explained below. Since near wellbore stresses are linked to other subsurface stresses such as overburden, maximum and minimum horizontal stresses, these will be explained first. Finally, wellbore failure mechanisms (tensile and shear failures) are discussed.

3.1. IN-SITU STRESS REGIMES

Underground formations are always in a stressed state and can be described by the three orthogonal subsurface stresses (Fjaer et al., 2008). These three stresses include overburden stress in the vertical direction (σ_V), maximum horizontal stress (σ_H) and minimum horizontal stress in horizontal directions (σ_h). There are three geological conditions related to these stresses that are often called fault systems:

i. Normal faulting; $\sigma_V > \sigma_H > \sigma_h$

ii. Strike slip faulting : $\sigma_H > \sigma_V > \sigma_h$

iii. Reverse faulting: $\sigma_H > \sigma_h > \sigma_H$

The term normal fault is simply used to define the relative order for the stress magnitudes regardless of the normal fault being present or not (Aadnoy et al., 2009). The other faulting regimes might happen in tectonically active areas where one or both of the horizontals stresses can be greater than overburden stresses.

The stress regimes described above are based on assuming the vertical stress as one of the principle stresses which can be reasonable for most sedimentary basins. However, this can change in complex basins such as around salt bodies where the principle stresses might be rotated out of the vertical and horizontal planes (Aadnoy et al., 2009).

The difference in horizontal stress fields is referred to as stress anisotropy. Stress anisotropy represents the difference in the magnitude of the horizontal stresses (maximum and minimum). To maximize wellbore stability, stress anisotropy should be minimized through optimizing the direction and inclination of the well path (Mitchell, 2001). In addition, having knowledge on the magnitude of far field stresses (subsurface stresses) is very critical for any wellbore stability related studies. One simple source for calculating overburden stress is using the following equation:

$$\sigma_V = \int_0^D \rho(z) g dz \tag{3.1}$$

Where σ_v is vertical stress, $\rho(z)$ is bulk density of overburden formations and an eventual water column for offshore situations, and dz is depth increment. Assuming the surface is flat, the vertical stress will be one of the principle stress directions. There are special cases where other factors affect the overburden stress such that it cannot be easily calculated based on density integration; for instance, areas of stress arching above depleted and compacted reservoirs or around salt domes (Aadnoy, 2009).

As mentioned above, any stress state in the subsurface will consist of three principle stresses 90 degrees apart. Therefore, any stress in the subsurface can be expressed as the function of vertical stress and two horizontal stresses. Assuming linear elastic behavior, the relationship between vertical and horizontal stresses will be expressed solely on Poisson's ratio, and the minimum horizontal stress can be determined by:

$$\sigma_h = \frac{\upsilon}{1-\upsilon}\sigma_v \tag{3.2}$$

The above equation is valid for geologically relaxed areas and when assuming rock behaves as a linear elastic material which is undergoing one-dimensional compression. The above equation is based on total stresses.

In porous rocks, pore fluids carry some of the load and deformations in the subsurface are caused by effective stresses, defined as total stresses subtracted pore pressure (Terzaghi's effective stress discussed in section 4).

It is also possible to estimate minimum horizontal stress magnitude from other sources like LOT (Leak-off tests) and/or XLOT (Extended LOT). It is not straight forward to determine maximum horizontal stress magnitude. Data from logs such as caliper or image logs can be used to determine maximum horizontal stress direction (Fjaer et al., 2008). It is also possible to estimate the magnitude from an analytical equation when input data on fracture breakdown pressure is available through LOT and/or XLOT.

3.2. STRESS DISTRIBUTION IN THE NEAR WELLBORE

When a well is drilled, the rock stress imposed by the three orthogonal stresses is removed and replaced by drilling mud pressure. However, this mud pressure does not exactly match the stresses removed, so it causes stress concentration around the wellbore.

The problem of deriving stresses outside a circular hole in an infinite elastic solid, with a uniform state of stress far from the hole, was first solved by Kirsch (1898), then it was modified by others (Deiley and Owens, 1969; Bradley, 1979; Aadnoy, 1988; Aadnoy et al., 1987).

Assuming linear-elastic conditions, the stress distribution around the wellbore in cylindrical coordinates is illustrated in Figure 3.1 and the following equations can be defined.

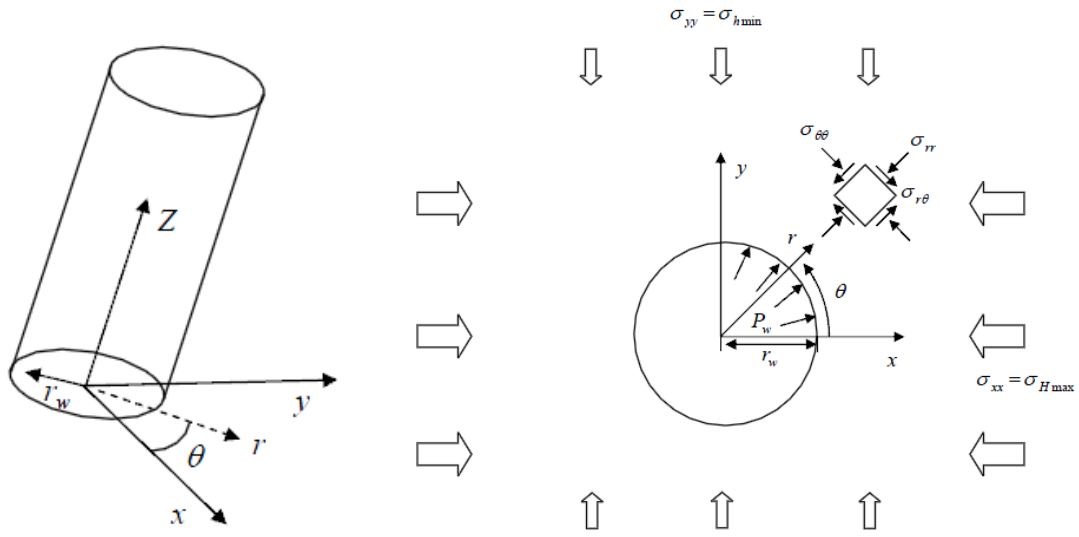

Figure 3.1. An arbitrary oriented wellbore under in-situ stress system (Modified from Park, 2006).

$$\sigma_{\theta\theta} = \frac{\sigma_{xx}+\sigma_{yy}}{2}(1+\frac{r_w^2}{r^2}) - \frac{\sigma_{xx}-\sigma_{yy}}{2}(1+3\frac{r_w^4}{r^4})\cos 2\theta - \tau_{xy}(1+3\frac{r_w^4}{r^4})\sin 2\theta - p_w\frac{r_w^2}{r^2} \tag{3.3}$$

$$\sigma_{\theta\theta} = \frac{\sigma_{xx}+\sigma_{yy}}{2}(1+\frac{r_w^2}{r^2}) - \frac{\sigma_{xx}-\sigma_{yy}}{2}(1+3\frac{r_w^4}{r^4})\cos 2\theta - \tau_{xy}(1+3\frac{r_w^4}{r^4})\sin 2\theta - p_w\frac{r_w^2}{r^2} \tag{3.4}$$

$$\begin{aligned}
\sigma_{ZZ} &= \sigma_Z - \upsilon[2(\sigma_{xx}-\sigma_{yy})\frac{r_w^2}{r^2}\cos 2\theta + 4\tau_{xy}\frac{r_w^2}{r^2}\sin 2\theta] \\
\tau_{r\theta} &= \frac{\sigma_{yy}-\sigma_{xx}}{2}(1-3\frac{r_w^4}{r^4}+2\frac{r_w^2}{r^2})\sin 2\theta + \tau_{xy}(1-3\frac{r_w^4}{r^4}+2\frac{r_w^2}{r^2})\cos 2\theta \\
\tau_{\theta Z} &= (-\tau_{xz}\sin\theta + \tau_{yz}\cos\theta)(1+\frac{r_w^2}{r^2}) \\
\tau_{rz} &= (\tau_{xz}\cos 2\theta + \tau_{yz}\sin\theta)(1-\frac{r_w^2}{r^2})
\end{aligned} \tag{3.5}$$

For a hole along a principle stress direction, the above equations will simplify. In the case of a vertical borehole with far field stresses of maximum and minimum horizontal stresses (σ_H, σ_h) and angle θ measured from maximum horizontal stress:

$$\sigma_{rr} = \frac{\sigma_H + \sigma_h}{2}(1 - \frac{r_w^2}{r^2}) + \frac{\sigma_H - \sigma_h}{2}(1 + 3\frac{r_w^4}{r^4} - 4\frac{r_w^2}{r^2})\cos 2\theta + p_w \frac{r_w^2}{r^2} \tag{3.6}$$

$$\sigma_{\theta\theta} = \frac{\sigma_H + \sigma_h}{2}(1 + \frac{r_w^2}{r^2}) - \frac{\sigma_H - \sigma_h}{2}(1 + 3\frac{r_w^4}{r^4})\cos 2\theta - p_w \frac{r_w^2}{r^2} \tag{3.7}$$

$$\sigma_{ZZ} = \sigma_V - 2\upsilon(\sigma_H - \sigma_h)\frac{r_w^2}{r^2}\cos 2\theta$$

$$\tau_{r\theta} = -\frac{\sigma_H - \sigma_h}{2}(1 - 3\frac{r_w^4}{r^4} + 2\frac{r_w^2}{r^2})\sin 2\theta \tag{3.8}$$

$$\tau_{\theta Z} = \tau_{rz} = 0$$

At the borehole wall:

$$\sigma_{rr} = p_w \tag{3.9}$$

$$\sigma_{\theta\theta} = \sigma_H + \sigma_h - 2(\sigma_H - \sigma_h)\cos 2\theta - p_w \tag{3.10}$$

$$\sigma_{ZZ} = \sigma_V - 2\upsilon(\sigma_H - \sigma_h)\cos 2\theta$$

$$\tau_{r\theta} = -\frac{\sigma_H - \sigma_h}{2}(1 - 3\frac{r_w^4}{r^4} + 2\frac{r_w^2}{r^2})\sin 2\theta \tag{3.11}$$

$$\tau_{\theta Z} = \tau_{rz} = \tau_{r\theta} = 0$$

Important implications from the above equations are that the maximum and minimum hoop stresses at borehole wall occur at minimum horizontal stress and maximum horizontal stress, respectively:

$$\sigma_{\theta\theta\max} = 3\sigma_h - \sigma_H - P_w - P_p \tag{3.12}$$

$$\sigma_{\theta\theta\max} = 3\sigma_H - \sigma_h - P_w - P_p \tag{3.13}$$

The above equations assume an impermeable borehole wall (non-penetrating case). For penetrating drilling fluid, have the following set of equations can be defined:

$$\sigma_{rr} = P_w - P_p \tag{3.14}$$

$$\sigma_{\theta\theta\min} = 3\sigma_h - \sigma_H - P_w + \alpha(\frac{1-2\upsilon}{1-\upsilon})(P_w - P_p) \tag{3.15}$$

$$\sigma_{\theta\theta\max} = 3\sigma_H - \sigma_h - P_w + \alpha(\frac{1-2\upsilon}{1-\upsilon})(P_w - P_p) \tag{3.16}$$

Where α is Biot's coefficient, the poro-elastic property of the rocks given as:

$$\alpha = 1 - \left(\frac{K_{bulk}}{K_{grain}} \right) \tag{3.17}$$

where K_{bulk} is the bulk compressibility modulus and K_{grain} is the grain compressibility modulus assuming hydrostatic stress and linear elastic material condition, will be in the range of $0 < \alpha \leq 1$. For sedimentary rocks with significant porosity where the compressibility of the rock is much larger than the grain compressibility, the compressibility can normally be assumed to be unity. This formulation of the wellbore stresses also assumes there is no fluid pressure drop over any potential mud-cake in the hole.

Figure 3.2 shows the effective hoop and radial stress by the ratio of the distance over the wellbore radius. As seen in Figure 3.2, the hoop stresses are highest closer to the wellbore wall and then is reduces until it reaches the far field stresses just a few wellbore radius away from the wellbore. Figure 3.3 shows the compressive hoop stress around the wellbore. Minimum horizontal stress orientation is at zero degree and maximum horizontal stress orientation is at 90 degrees.

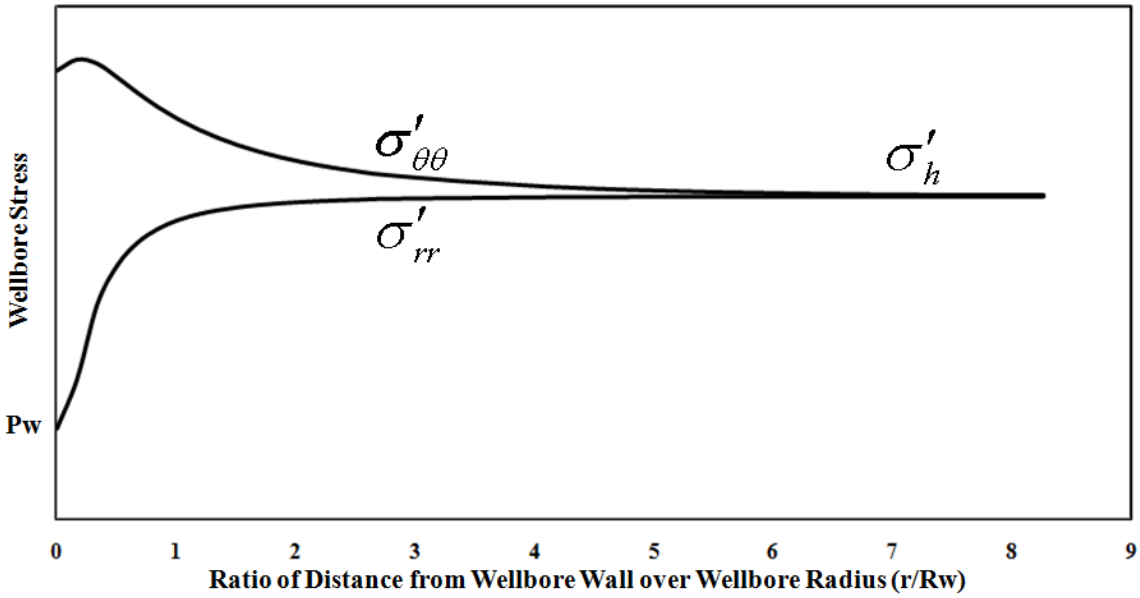

Figure 3.2. Effective radial and hoop stress by ratio of distance from wellbore wall over wellbore radius

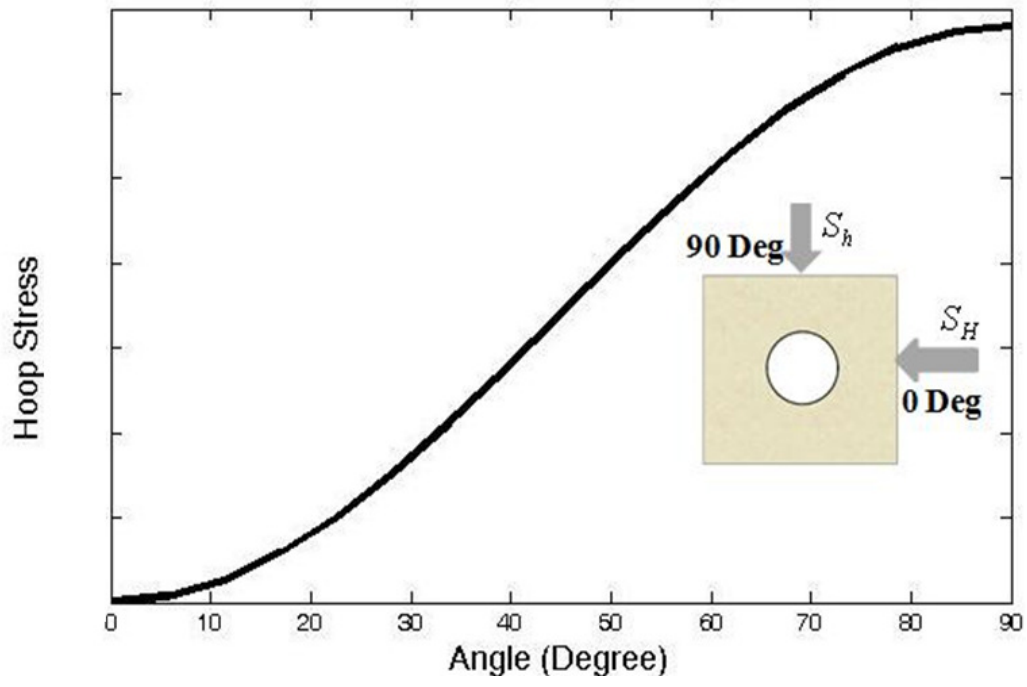

Figure 3.3. Hoop stress around the wellbore

3.3. MECHANICS OF WELLBORE FAILURE IN INTACT ROCKS

As noticed before, drilling fluid pressure (mud weight) is used to balance the removed stresses from the borehole while drilling. It is often hard to keep the fluid pressure in balanced mode which does not go above the state of tensile stress or below the state of compressive stress. In some cases, this state of imbalance leads to wellbore tensile failure or compressive failure.

Generally, tensile failure occurs when the effective tensile stress across a plane in the sample exceeds a critical limit (Fjaer, 2008). This limit is called tensile strength. The tensile strength is a characteristic property of the rock; and in most sedimentary basins, it has a very small value around a few MPa, if any.

The failure criterion, which specifies the stress condition when tensile failure occurs in a principle stress space, can be written as:

$$\sigma' = -T_0 \tag{3.18}$$

$$\sigma_3' = -T_0 \tag{3.19}$$

Where σ' is the effective principle stress in the failure plane and T_0 is the formation tensile strength. For isotropic rocks, the condition for tensile failure will be fulfilled for lowest principal stress first.

In the wellbore, the tensile criteria will be fulfilled when the effective tangential stress at the wellbore wall reaches the formation tensile strength. This happens when mud weight increases excessively which results in tensile failure risk of lost circulation and subsequent well control issues (Figure 3.4). Compressive or shear failure occurs when the drilling fluid density is too low. This results in brittle shear fracturing and caving of the wellbore referred to as borehole breakouts. Several criteria have been proposed for compressive (shear) failure. The most commonly used one is Mohr-Coulomb criterion. More details on these criteria can be found in Jaeger et al., (2007) and Fjaer et al., 2008.

The upper limit of drilling fluid density has to be controlled to prevent tensile failure at the wellbore wall and subsequent breakdown of the formation. Fracture breakdown pressure is defined as the wellbore pressure necessary to induce hydraulic fractures at the wellbore wall.

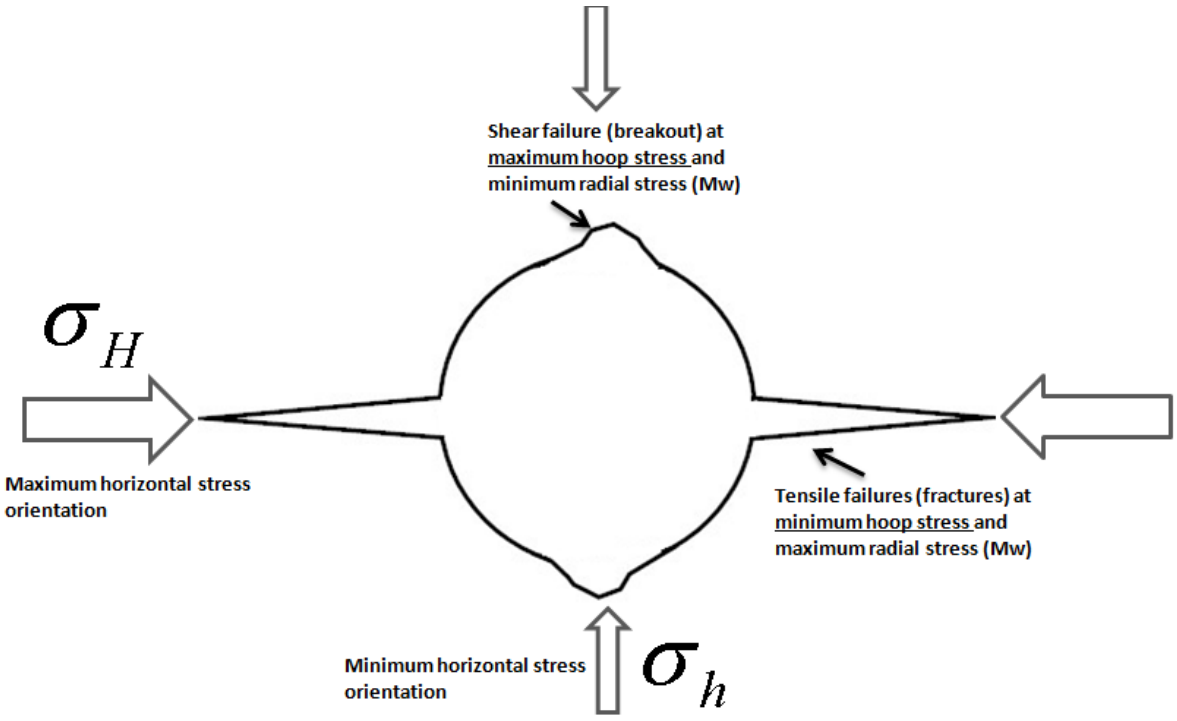

Figure 3.4. Schematic of near wellbore stresses and wellbore failure mechanisms

For a vertical wellbore in a normal stressed regime, a vertical fracture will develop parallel to the maximum horizontal stress direction where the hoop stress around the wellbore wall is minimum. Furthermore, there are two conditions to evaluate: a non-penetrating and a penetrating case. For the non-penetrating case where there is an impermeable filter cake around the vertical wellbore, the fracture breakdown pressure (P_{frac}) can be determined by solving Equation 3.18 along the minimum hoop stress orientation given as:

$$P_{frac} = 3\sigma_h - \sigma_H - P_p + T_0 \tag{3.20}$$

P_{frac} is then equal to the maximum mudweight pressure (P_w) in Equation 3.12. Equation 3.20 gives an upper limit for fracture breakdown pressure. In the poro-elastic case (penetrating case) in which the pore pressure at the vicinity of the wellbore is increased this will decrease the effective stress around the borehole. This pressure is

referred to as poro-elastic fracture breakdown pressure or lower bound pressure (Valko and Economides, 1995):

$$P_{frac,poroelastic} = \frac{3\sigma_h - \sigma_H - \frac{\alpha(1-2\upsilon)}{(1-\upsilon)} P_p + T_0}{2 - \frac{\alpha(1-2\upsilon)}{(1-\upsilon)}} \tag{3.21}$$

If Biot's coefficient assumed to be one, the equation can be simplified to:

$$P_{frac} = 2(1-\upsilon)\sigma_h - (1-2\upsilon)P_p + (1-\upsilon)\sigma_t \tag{3.22}$$

In a real situation, the fracture pressure fluctuates between the upper and lower limit and depends on several factors (Fjaer, 2008):

- Initial cracks and flaws at the borehole wall, in which the effective tensile strength will be zero
- Time-dependant effects of pressure transfer from the borehole wall into the formation (permeability effects)

In the case of a wellbore with conductive micro-fractures, the following empirical equation has been proposed (Abou-Seyed et al., 1978):

$$P_{frac} = \frac{(3\sigma_h - \sigma_H + T_0)}{2} \tag{3.23}$$

In order to use this equation, the fracture length should be smaller than 10% of the wellbore radius. Formation tensile strength reduces as the fracture length increases. The equation clearly shows that fracture pressure can be significantly lower when conductive micro-fractures exist around the wellbore. With the assumption of isotropic stresses ($\sigma_H = \sigma_h$) and zero tensile strength, we have:

$$P_{frac} = \sigma_h \tag{3.24}$$

This shows that the fracture breakdown pressure can be very close to the minimum horizontal stress when conductive micro-fractures exist around the wellbore.

Regarding the permeability effects, there is no clear distinction between permeable and impermeable rocks (Song et al., 2001). Permeability can vary from one rock to another, and it is confusing whether to use an upper limit or lower limit equation

to calculate fracture pressure. To include the effect of pressurization rate, Detournay and Cheng (1992) modified the equation to:

$$P_{frac} = \frac{3\sigma_h - \sigma_H - \frac{\alpha(1-2\upsilon)}{(1-\upsilon)} P_p + \sigma_t}{1 + (1 - \frac{\alpha(1-2\upsilon)}{(1-\upsilon)})h(\zeta)} \tag{3.25}$$

where ζ is a dimensionless pressurization rate given by:

$$\zeta = \frac{A\chi^2}{4cS}, 0 \le \zeta \le \infty \tag{3.26}$$

where A, χ and c are borehole pressurization rates, micro-crack length scale and diffusion coefficient, respectively, and S is defined as stress quantity:

$$S = 3\sigma_h - \sigma_H - P_p + T_0 \tag{3.27}$$

$h(\zeta)$ can be derived from the diffusion equation representing pore pressure distribution in the vicinity of the wellbore (Song et al., 2001). The new criteria implies that tensile failure condition depends also on wellbore pressurization rate in addition to permeability effects.

In addition to effect of pressurization effect, Poison's ratio can also affect wellbore breakdown pressure when injecting into the wellbore. This has not been considered in the conventional Kirsch solution; but later on, added to the equation as Poisson's ratio scaling factor. The equation shows the modified Kirsch solution when taking effect of Poisson's ratio (Aadnoy and Belayneh, 2009):

$$P_{wf} = \frac{(1+\upsilon)(1-\upsilon^2)}{3\upsilon(1-2\upsilon) + (1+\upsilon)^2}[3\sigma_h - \sigma_H - 2P_p] + P_p \tag{3.28}$$

The first term in the equation above is called Poisson's ratio scaling factor. The scaling factor increases as Poisson's ratio decreases. The maximum number for the scaling factor is 1 which occurs when Poisson's ratio drops to zero which is an unrealistic number. For rocks with an average 0.25 Poisson's ratio, the scaling factor is around 0.6.

4. RESEARCH METHODOLOGY

This section outlines the research methodology and the tasks performed to address the study objectives. First, the main hypothesis of this research and objectives are presented. Second, a general summary of finite-element modeling is provided which is followed up by the numerical description and the main steps conducted.

After the numerical method description, research methodology for predicting fracture propagation pressure, when fractures sealed, is presented. Finally, details of laboratory experiments including workflow and set up are explained.

4.1. RESEARCH HYPOTHESIS

The main objective of this research is to investigate the physical mechanisms for wellbore strengthening. In order to reach this objective, two hypotheses are initiated:

- Wellbore strengthening causes wellbore hoop stress to increase
- Wellbore strengthening causes fracture resistance to increase

As outlined in Section 1, several competing theories have been reported to explain wellbore strengthening. According to Wang et al., (2008b), the mechanisms behind the various theories proposed and used for increasing the fracture gradient are still debated and not fully understood. However, the wellbore strengthening physical mechanisms can be classified into two major categories or it can be a combination of both. The first mechanism is based on creating fractures around the wellbore while drilling and sealing them with specially designed particles to increase wellbore hoop stress. The second mechanism states that fracture sealing helps to initiate a non-invaded zone inside the fracture which will increases fracture propagation pressure.

In order to test the above hypotheses, the following objectives are intended:

- Hoop stress increase by numerical models
- Fracture resistance increase by analytical model
- Laboratory verification of numerical and analytical models

- Field investigation

The first objective was achieved by numerical simulations to model the fracture's initiation, propagation and sealing (Figure 4.1). Results for wellbore hoop stress are recorded after each step of the simulation to test the first hypothesis. Regarding the second hypothesis, analytical equations were investigated to predict fracture propagation pressure when fractures are sealed. Furthermore, to verify results from numerical and analytical methods, near wellbore fracture experiments are conducted. In addition, the proposed methodologies were used to investigate relevant field cases having a severe lost circulation history.

4.2. RESEARCH METHODOLOGY DESCRIPTION

Figure 4.1 is a schematic of the detailed tasks followed for this research. As illustrated in Figure 4.1, finite-element analysis was used to model fractures. Before explaining modeling details, a short summary of finite-element formulation is required.

4.2.1. Research Methodology for Task 1-Investigation of Hoop Stress Increase. The finite element method is a numerical technique which gives approximate solutions to differential equations that model problems arising in physics and engineering. The finite element method was first applied to problems of structural related problems like stress analysis; and has since, due to its versatility, been applied to other problems of continua. In all applications, the analyst seeks to calculate a field quantity. In stress analysis, it is the displacement field or stress field. In thermal analysis it is the temperature field or the heat flux. In fluid flow, it is the stream function or the velocity potential function. FE analysis does not produce a formula as a solution, nor does it solve a class of problems. Also the solution is approximate unless the problem is so simple that the stiffness matrix can be solved explicitly.

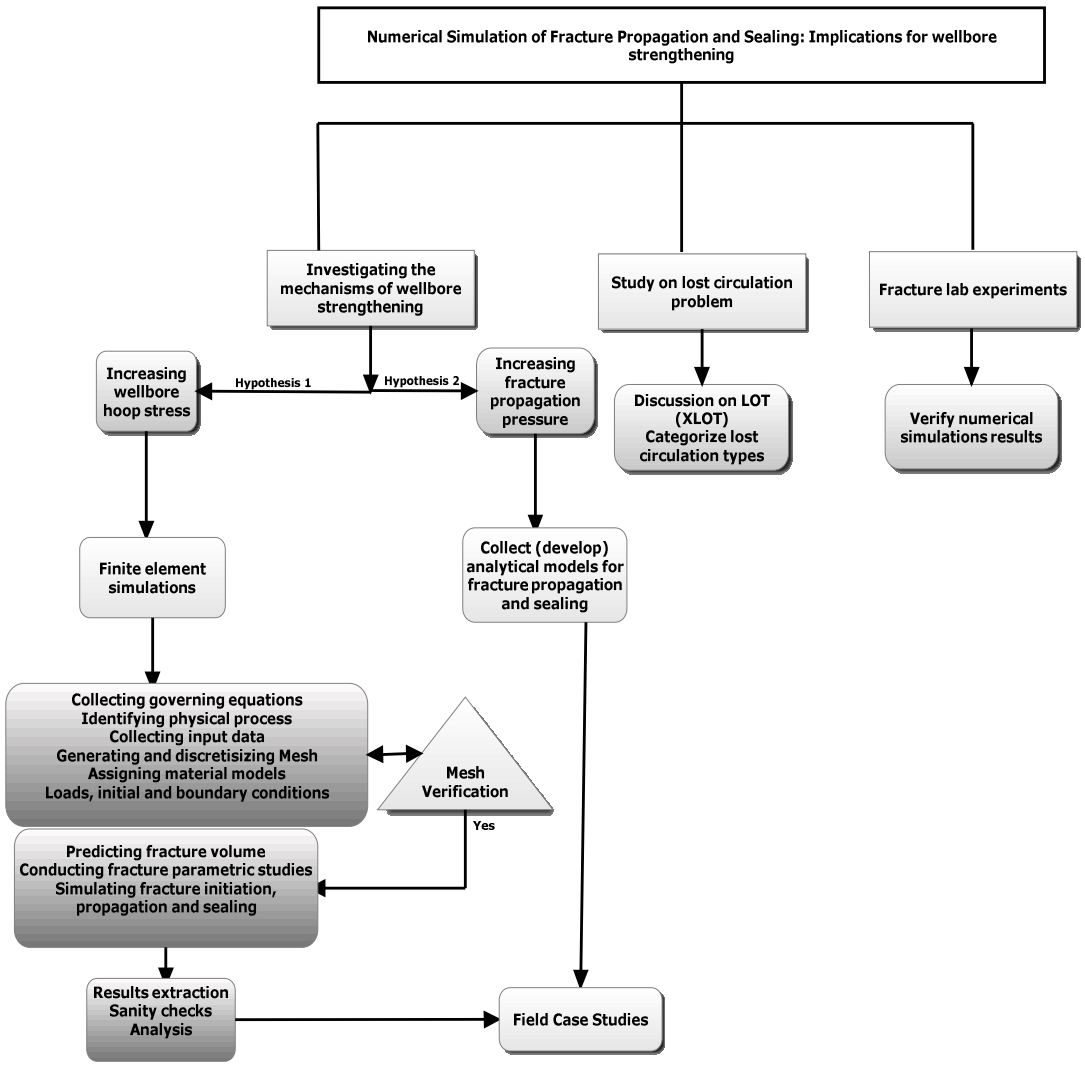

Figure 4.1. A schematic of major steps and workflows followed up for this research

A simple description of the FE method is that it involves cutting a structure into several elements (piece of structure), describing the behavior of each element in a simple way, and then reconnecting elements at "nodes" (Figure 4.2).

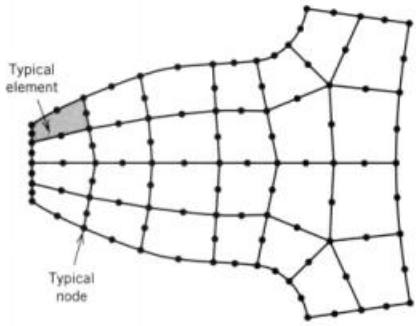

Figure 4.2. Typical finite element mesh consisting of elements and nodes (Taken from Cook, R.D., 1995)

This process results in a set of simultaneous algebraic equations. In stress analysis these equations are equilibrium equations of the nodes. In order to accomplish the FE analysis, these set of equations need to be solved by computer.

Generally, a FE method solves a problem through piecewise polynomial interpolation. That is, over an element, a field quantity such as displacement is interpolated from the values of the field quantity at nodes. By connecting elements together, the field quantity becomes interpolated over the entire structure in piecewise fashion. The minimization process generates a set of simultaneous algebraic equations for values of the field quantity at nodes. Matrix symbolism for this set of equations is:

$$KU=F \tag{4.1}$$

Where U is the vector of unknowns (values of the field quantity at the nodes), F is a vector of unknown loads, and K is a matrix of unknown constants. In stress analysis, K is known as a "stiffness matrix".

Finite-element methods (FEMs) have been used previously to simulate fractures in the rocks and these methods have yielded satisfactory results agree with field cases and lab experiments (Dixon and Strannigan, 1972; Woo and Kuruppu; 1992; Sepehr and Stimpson; 1988).

Most hydraulic fracturing simulations are based on the assumptions of specific fracture geometry. For instance, symmetrical fractures (Nordgern, 1972) and planar fractures were frequently used to model hydraulic fractures in the wellbore. However,

since conditions in front of the crack are neither plane strain or plane stress (Anderson, 1995), this work relied on three-dimensional numerical models. The three dimensional models used in this dissertation are designed to study the entire fracture process of Mode-I fracturing.

In order to formulate a finite-element model, it is required to follow several steps before model can be run. These steps can be summarized as:

- Collecting governing equations
- Physical process identification and description
- Input data collection
- Mesh generation, discretization and verification
- Material model assignment
- Initial loads and boundary conditions
- Simulations run
- Results extraction, analysis and verification

4.2.1.1. Governing equations. Since this research has modeled liquid flow through a porous medium, it is required to review the basic governing equations behind finite element modeling before explaining details on mesh creation and numerical procedure.

The governing equations for solids are very similar in many aspects to the governing equations for fluids. There is, however, some differences, such as fluids cannot support any deviatoric stress when not in motion (Zienkiewicz et al., 2006). Therefore, fluids at rest can only have mean compressive stress or pressure applied. If deviatoric stresses applied, fluid start to move and such fluid motion is the main interest of fluid dynamics. The main difference between the governing equations of fluid flow and solid mechanics is that the velocity vector (v) replaces the displacement vector:

$$v_i, i = 1,2,3 \text{ or } v = [v_1 \quad v_2 \quad v_3]^T \tag{4.2}$$

This will replace the displacement variable in solid mechanics. Strain rates are primary causes of general stresses, and these can be defined as:

$$\dot{\varepsilon}_{ij} = \frac{1}{2}\left(\frac{\delta v_i}{\delta x_j} + \frac{\delta v_j}{\delta x_i}\right) \tag{4.3}$$

The relationship for strain rate vector can be as follow:

$$\dot{\varepsilon} = Sv \tag{4.4}$$

Where **S** is known as the strain rate operator, and **v** is the velocity given in the equation.

To define stress and strain relationships for linear isotropic fluid, it is required to define deviatoric stress and pressure. The deviatoric stress can be defined as:

$$\tau_{ij} \equiv \sigma_{ij} - \frac{1}{3}\delta_{ij}\sigma_{kk} = 2\mu\left(\dot{\varepsilon}_{ij} - \frac{1}{3}\delta_{ij}\dot{\varepsilon}_{kk}\right) \tag{4.5}$$

In the above equation, τ_{ij} is the deviatoric stress, μ is dynamic (shear) viscosity which is analogous to shear modulus G in the linear elasticity. The quantity in parentheses describes the deviatoric strain rate, δ_{ij} is the Kronecker delta and also:

$$\dot{\varepsilon}_{kk} \equiv \dot{\varepsilon}_{11} + \dot{\varepsilon}_{22} + \dot{\varepsilon}_{33} \tag{4.6}$$

$$\sigma_{kk} \equiv \sigma_{11} + \sigma_{22} + \sigma_{33} \tag{4.7}$$

The pressure relationship for fluid flow can then be written as:

$$p = -\frac{1}{3}\sigma_{kk} = -k\dot{\varepsilon}_{kk} + p_0 \tag{4.8}$$

Where k is a volumetric viscosity coefficient which is analogous to bulk modulus K in solid mechanics, and p_0 is the initial hydrostatic pressure. Combining equations gives the following:

$$\sigma_{ij} = \tau_{ij} - \frac{1}{3}\delta_{ij}\dot{\varepsilon}_{kk} + k\delta_{ij}\dot{\varepsilon}_{kk} - \delta_{ij}p_0 \tag{4.9}$$

$$\sigma_{ij} = 2\mu\dot{\varepsilon}_{ij} + \delta_{ij}\left(k - \frac{2}{3}\mu\right)\dot{\varepsilon}_{kk} - \delta_{ij}p_0 \tag{4.10}$$

The lame notation can be defined as:

$$\lambda = k - \frac{2}{3}\mu \tag{4.11}$$

Ignoring compressibility and volumetric viscosity of the fluid, the final equation has the following form:

$$\sigma_{ij} = 2\mu(\dot{\varepsilon}_{ij} - \frac{1}{3}\delta_{ij}\dot{\varepsilon}_{kk}) = \mu[(\frac{\delta u_i}{\delta x_j} + \frac{\delta u_j}{\delta x_j}) - \frac{2}{3}\delta_{ij}\frac{\delta u_k}{\delta x_k}] \quad (4.12)$$

The above equation is identical to the equation in linear elasticity if compressibility is ignored. There is no anisotropy for fluids, so it is always purely isotropic behavior.

4.2.1.1.1. Fluids mass conservations. In order to consider conversion principles, it is required to write the equations for fluid dynamics. In fluid dynamics, a control volume is used to write mathematical models of a physical process. Figure 4.3 illustrates a control volume in a three-dimensional coordinate system of X (x1), Y (x2) and Z (x3). The mass transfer equation for fluid leaving and entering the control volume (Figure 4.3) can be written as:

$$\frac{\delta\rho}{\delta t} + \frac{\delta}{\delta x_i}(\rho v_i) \equiv \frac{\delta\rho}{\delta t} + [\frac{\delta}{\delta x_1} + \frac{\delta}{\delta x_2} + \frac{\delta}{\delta x_3}](\rho v) = 0 \quad (4.13)$$

Where ρ is fluid density, and ρv_i is mass flow.

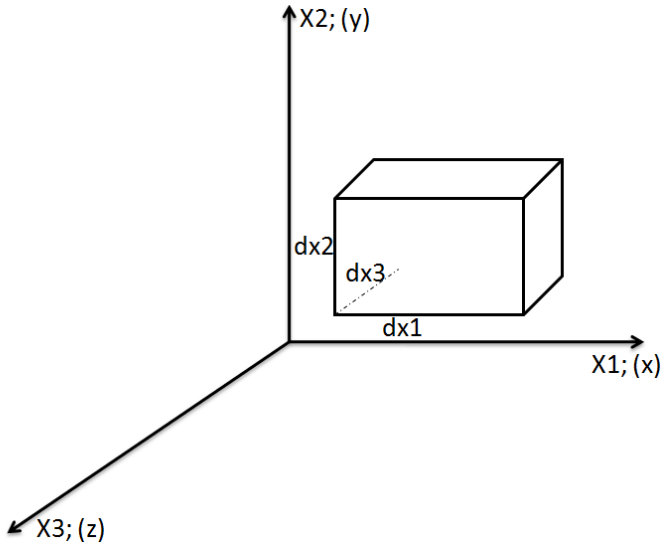

Figure 4.3. Control volume used for mass and momentum conversions

4.2.1.1.2. Momentum conservations. The momentum balance transfer equation describes the conservation of momentum leaving and entering the control volume and can be summarized as:

$$\frac{\delta(\rho v_j)}{\delta t} + \frac{\delta}{\delta x_i}[(\rho v_j)v_i] - \frac{\delta}{\delta x_i}(\sigma_{ij}) - \rho g_j = 0 \tag{4.14}$$

where ρg_j represents the body forces.

The equilibrium expressed by writing the principle of the virtual work for the volume under consideration for a given time can be expressed as:

$$\int_V \sigma_{ij}\delta\varepsilon d_V = \int_S t.\delta v dS + \int_V \hat{f}.\delta v dV \tag{4.15}$$

Where;

t: surface tractions per unit area

$\hat{f}$: Body forces per unit volume

u_i : Displacement of the solid skeleton

ρ_w : Density of the wetting liquid

g: Gravitational acceleration

δv : Virtual velocity field

$\delta\varepsilon$: Virtual rate of deformation

n: porosity

$\hat{f}$ will often include the weight of the wetting liquid which can be shown as;

$$f_w = (sn + n_t)\rho_w g \tag{4.16}$$

For simplicity, the loading can be considered explicitly so that any other gravitational term in $\hat{f}$ is associated with the weight of the dry porous medium; therefore, the virtual work equation can be modified as:

$$\int_V \sigma_{ij}\delta\varepsilon d_V = \int_S t.\delta v dS + \int_V f.\delta v dV + \int_V (sn + n_t)\rho_w g\delta v dV \quad (4.17)$$

$$\int_V \sigma_{ij}\delta\varepsilon d_V = \int_S t.\delta v dS + \int_V f.\delta v dV + \int_V (sn + n_t)\rho_w g\delta v d \quad (4.18)$$

In a finite element model, equilibrium is approximated by a finite set of equations by introducing interpolation functions. The interpolation is assumed to be based on material coordinates in the material skeleton (a "Lagrangian" formulation, Zienkiewicz et al., 2006).

4.2.1.1.3. Poro-elasticity and Biot's coefficient. The presence of a freely moving fluid in a porous rock modifies its mechanical response. Two mechanisms play a key role in this interaction between the pore fluid and the porous rock (Detournay and Cheng, 1993);

a) Increase of pore pressure will cause rock dilation

b) Rock compression will cause a rise in pore pressure if the fluid is prevented from escaping

The initial theory for the influence of pore pressure was first developed by Terzaghi (Terzaghi, 1923) who developed a model for one-dimensional consolidation. Biot (Biot, 1935) was the first to develop a linear theory of poro-elasticity which considers both the pore pressure increase inducing rock dilation and rock compression causing the rise of pore pressure. The simple relationship between effective stress, total stress and pore pressure is (assuming tensile components of stress as positive and compressive pressure, p being positive):

$$\sigma'_{ij} = \sigma_{ij} + \alpha\delta_{ij}p \quad (4.19)$$

Where σ'_{ij} is the effective stress tensor, σ_{ij} is the total stress tensor, δ_{ij} is Kronecker delta. $\delta_{ij} = 1$, when $i = j$, and $\delta_{ij} = 0$, when $i \neq j$. For most of the soil mechanics problems, where the bulk modulus K_s of the solid particles is much larger

than the whole material, $\alpha \approx 1$ can be assumed and the above equation can be modified to:

$$\sigma'_{ij} = \sigma_{ij} + \delta_{ij} p \tag{4.20}$$

4.2.1.1.4. Constitutive formulation and permeability. The constitutive behavior for fluid flow is governed by Darcy's law or Forchheimer's law. Darcy's law is generally applicable to low fluid flow velocities, whereas Forchheimer's law is commonly used for saturations involving higher fluid flow velocities. Darcy's law can be considered as a linearized version of Forchheimer's law.

Forchheimer's law describes pore fluid flow as:

$$v_w = -\frac{1}{sng\rho_w(1+V_c\sqrt{v_w.v_w})}\hat{k}.(\frac{\delta u_w}{\delta X} - \rho_w g) \tag{4.21}$$

$\hat{k}$ is the permeability of the porous medium with units of length/time, v_w is the average velocity of the wetting liquid (seepage velocity), and V_c is a velocity coefficient. Darcy's law is obtained by setting $\phi = 0$. It is seen that, as the fluid velocity drops to zero, Forchheimer's law approaches Darcy's law.

The permeability depends on the saturation of the fluid and on the porosity of the medium. Assuming that these dependencies are separable:

$$\hat{k} = k_s k \tag{4.22}$$

Where $k_s(s)$ gives the saturation dependency, with $k_s(1) = 1.0$ and k is the fully saturated permeability. For isotropic materials, $k = kI$.

4.2.1.2. Physical process identification and description. After the governing equations are initialized then it is important to have a conceptual perspective of the problem. This provides an initial estimate of the expected behavior under imposed conditions. Predicting the physical process, stress and displacement fields play a pivotal role in finite-element analysis. Several questions and/or concerns should be asked when identifying physical processes (Figure 4.4). For example: Is the process linear or non-linear or combination of both? Non-linear behavior of solids can take two forms: geometric non-linearity or material non-linearity (Zienkiewicz and Taylor, 2006). Typical material non-linearity can be modeling fluid flow into porous medium which does not

obey linear process. After identifying the behavior type in the model, the next question will be what kind of material model to be used? Typical material models can include elastic-plastic, poro-elastic, thermo-elastic, thermo-poro-elastic, visco-elastic, and visco-elasto-plastic. It is often required to add additional features to the model when certain material models are used. For instance, using poro-elastic or thermo-poro-elastic requires using pore pressure and temperature solid elements. This also influence initial and boundary conditions in the model.

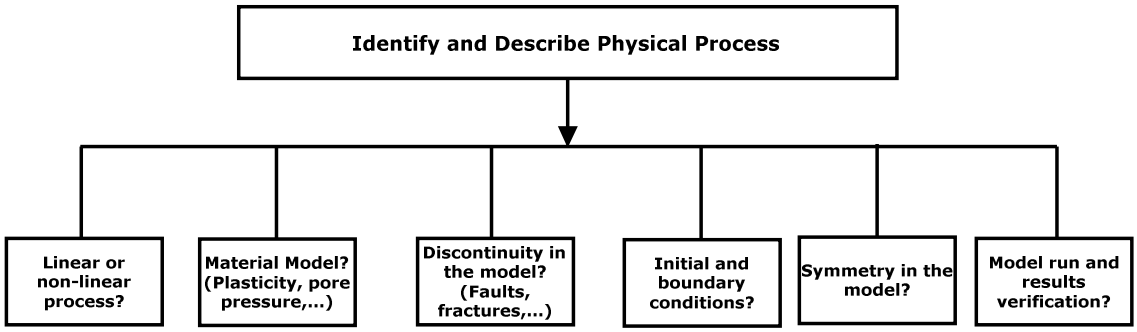

Figure 4.4. Major issues to be considered for describing physical process in a finite element model

Another concern can be existence of discontinuities in the model. Typical discontinuities can be joints, fissures, fractures and faults. Special features are required to have discontinuities in the numerical model. For instance, Figure 4.5 shows a two-dimensional model of a geological structure with a fault in which contact surfaces are used to model discontinuity. Having discontinuity in the model often leads in more complexity, numerical errors and convergence problems.

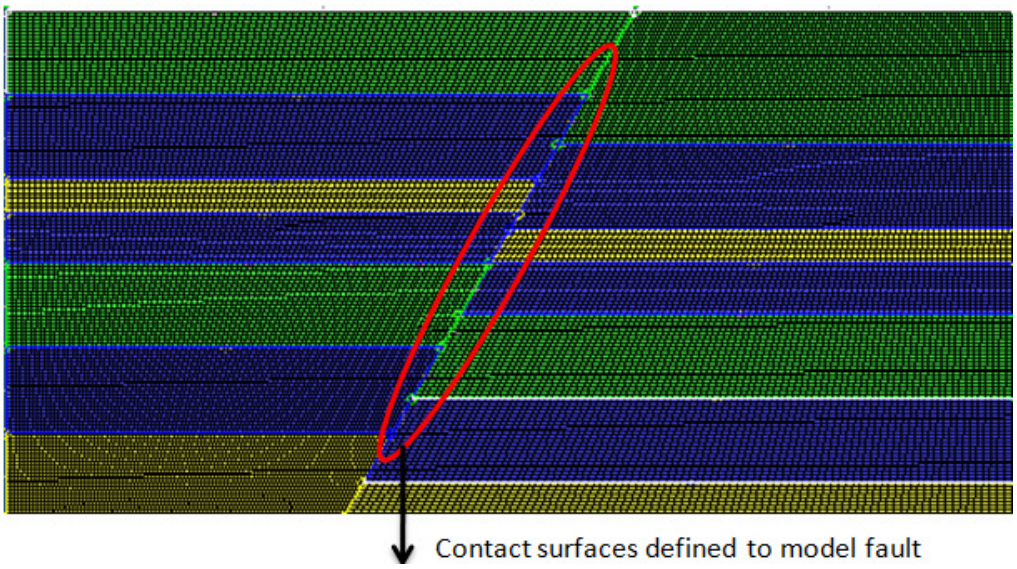

Figure 4.5. Two dimensional model of a fault in a geological structure- contact surfaces defined in the model

Initial and boundary conditions of a numerical model are very critical. Numerical simulation's results can vary significantly if correct conditions are not assigned in the model. Another challenge in assigning these conditions is selecting the best method to apply them in the model. Figure 4.6 shows a finite-element model for the near wellbore cement integrity study with three stress boundary conditions at the model top and sides, and initial pressure and temperature boundary conditions in cement elements. Having symmetry in the model also helps to reduce computation time and complexity of the model. As shown in Figure 4.6 because of the symmetry around a wellbore only half of the wellbore is modeled.

The last, but not the least, step in identifying a physical process is numerical results verification. Analytical equations, lab experiments, field observations and the analysis of natural analogues are often used to verify numerical results (de Pater et al., 1996, P.Hignett et al., 2007, Salehi et al., 2010). Analytical solutions are often not available when modeling complex physical problems. Conducting laboratory experiments can also be time-consuming and costly. Figure 4.7 shows the results from numerical simulations for a wellbore stability analysis in under-balanced drilling operations.

Appropriate ECD (equivalent circulating density) to prevent wellbore shear failure was predicted by numerical simulations verified with field observations.

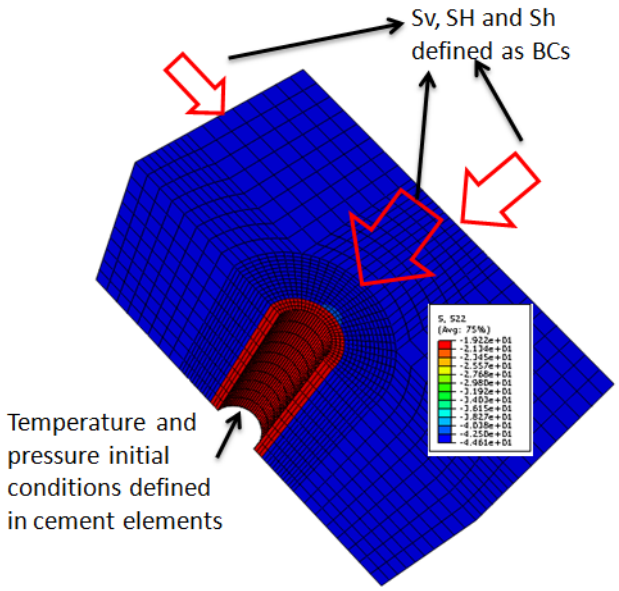

Figure 4.6. Boundary and initial conditions defined for a near wellbore finite-element study of cement integrity under dynamic conditions (Modified from Nygaard et al., 2011)

Figure 4.8 illustrates the details of the physical process for this study. As demonstrated, creating hydraulic fractures in the near wellbore is the main physical process. The process is non-linear since hydraulic fractures are created through injecting fluid through the porous media. This also described through non-linear governing equations. The material model defined for this process is poro-elastic which enables fluid flow and pore pressure build up in the model.

A source of discontinuity in the model is tensile fractures, and the methodology used for fracture creation is based on cohesive zone modeling. Because of the existing symmetry for wellbore, only half of the wellbore is modeled. Finally, near-wellbore fracture experiments are conducted to verify numerical simulations results.

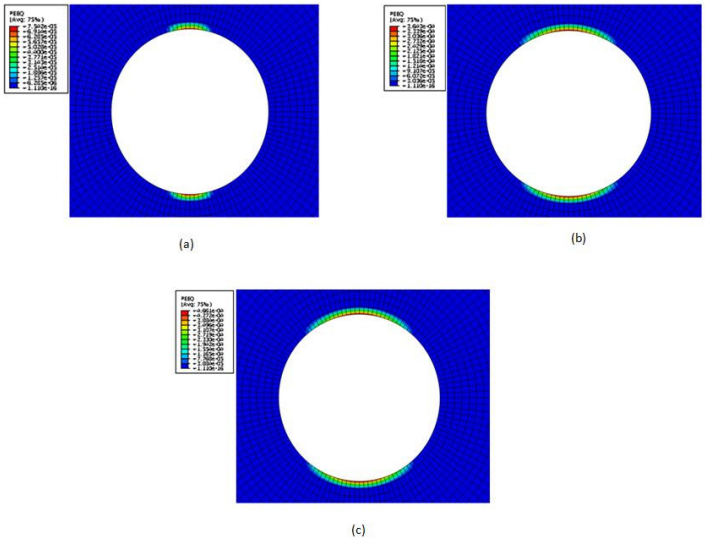

Figure 4.7. Appropriate ECD to prevent shear failure predicted by numerical simulations verified by field observations (a. 0.2 ppg pressure difference, b. 0.3 ppg pressure difference, c. 0.4 ppg pressure difference; from Salehi et al., 2010)

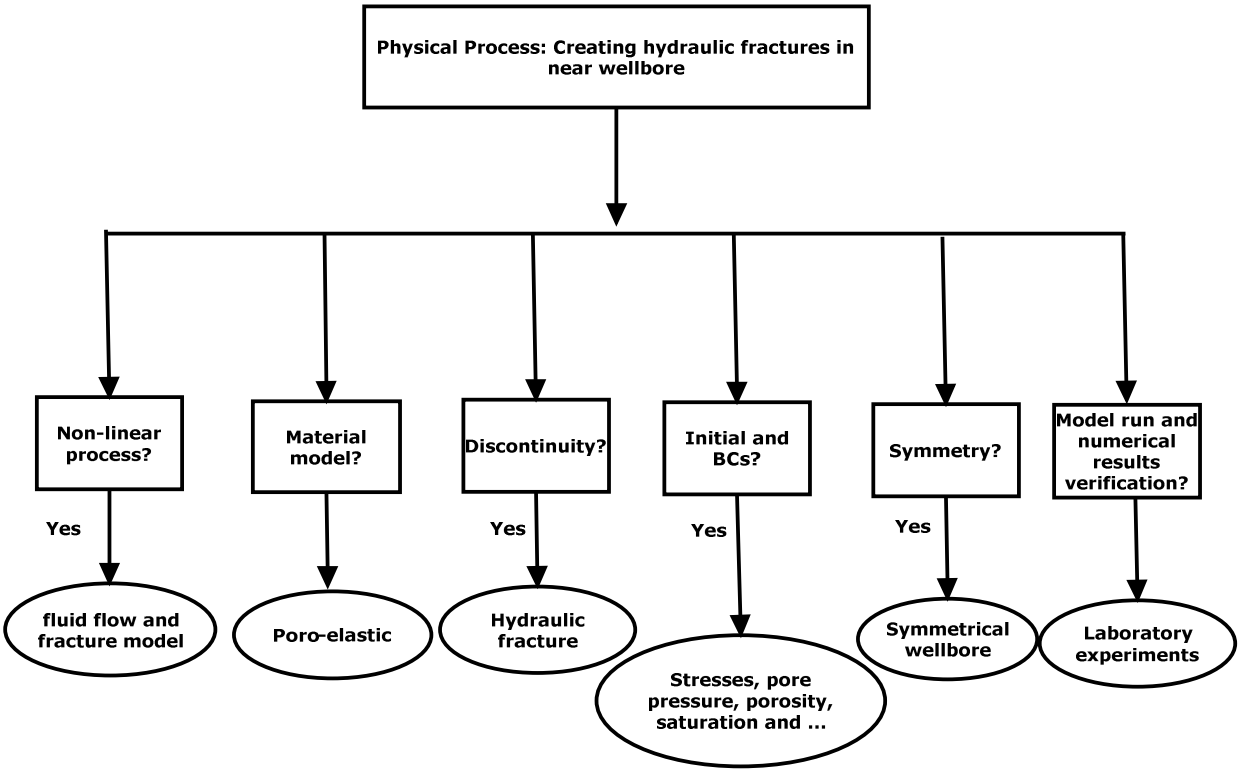

Figure 4.8. Schematic of physical process and related issues in this dissertation

4.2.1.2.1. Cohesive zone modeling. Cohesive finite elements were primarily developed by Barenblatt (1962) and Hilberborg et al., (1976) to be used for modeling discontinuities. These models were initiated as preferred methods for studding fracture problems in composite and monolithic materials systems (Shet and Chandra, 2002). Cohesive models have been used to simulate a fracture process under static, dynamic and cyclic load conditions (Camacho and Oritz, 1996 and Needleman, 1990). Table 4.1 reviews the most common cohesive models.

Table 4.1. Summary of cohesive modeling literature (Modified from Shet and Chandra, 2002)

Author	Problem Conditions	Comments
Barenblatt (1959, 1962)	Perfectly brittle materials	The first to propose cohesive zone concept
Dugdale (1960)	Yielding of thin ideal elastic-plastic steel sheets containing slits	Cohesive stress equated to yield stress of material
Needleman (1987)	Particle-matrix decohesion	Phenomenological model. Predicts normal separation.
Rice and Wang (1989)	Solute segregation	Considers normal separation and ignores shear separation
Needleman (1990)	Decohesion of interface under hydrostatic tension	Periodic shear traction to model shear stress due to slip
Tvergaard (1990)	Interfaces of whisker reinforced metal matrix composites	Quadratic model
Tvergaard and Hutchinson (1992)	Crack-growth in elasto-plastic material, peeling of adhesive joints	Claims shape of separation law are relatively unimportant
Xu and Needleman (1993)	Particle-matrix decohesion	Predicts shear and normal separation
Camacho and Oritz (1996)	Impact	Predicts failure by both shear and normal separation in tension and compression
Geubelle and Bayler (1997)	Delamination by low-viscosity impact	Bilinear model

In all of the cohesive models (Table 4.1), except for Dugdale's and Camacho models, a traction-separation law exists whereby increasing separation, traction reaches a maximum value then decreases. Figure 4.9 shows a typical softening behavior (Traction vs Separation) in cohesive zone when type I fracturing occurs. A high initial stiffness (penalty stiffness) was assigned between the layers before fracturing. After applying the loads on the material, interfacial normal tractions exceed the tensile strength. The stiffness will THE gradually drop to zero (Point 2 in Figure 4.9). Once the fracture is unable to transfer any further load, all the penalty stiffness will revert to zero (Point 5 in Figure 4.9).

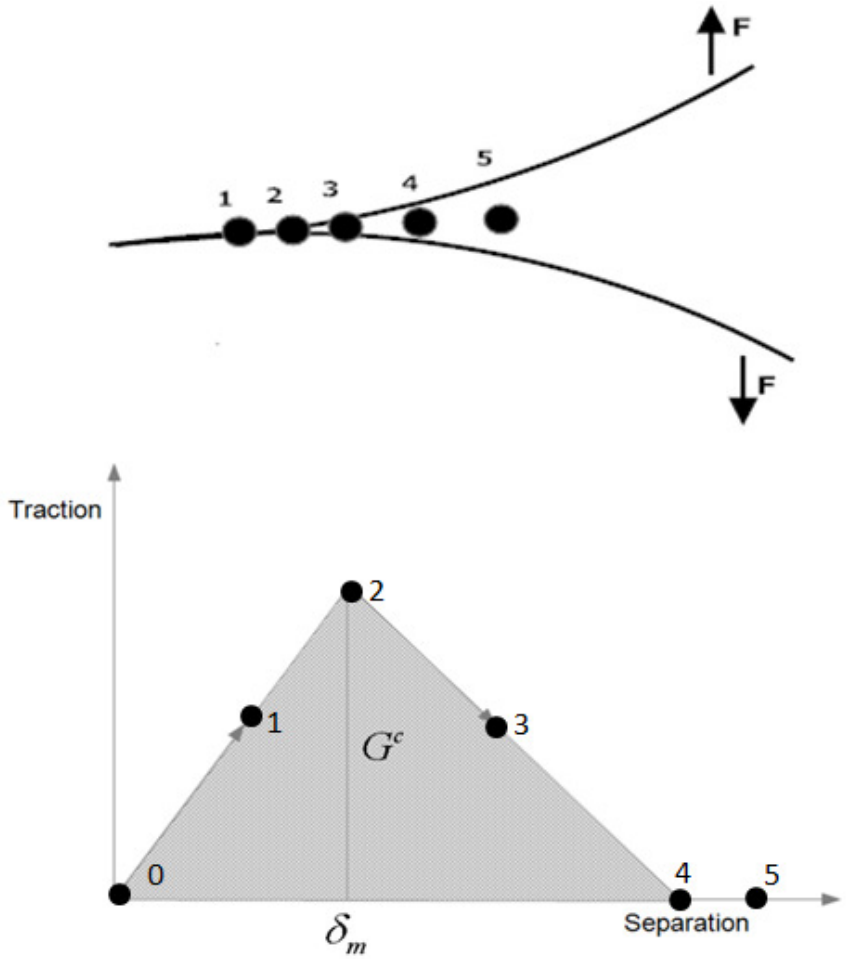

Figure 4.9. Traction-separation law for Mode I fracture

It has been shown that the cohesive zone can be related to Griffith's theory of fracture if the area under the traction-relative displacement relation is equal to the corresponding fracture energy (Rice, 1968). By the final displacement (δ^f), the following relationship exists:

$$\int_0^{\delta^f} \sigma d\delta = G_C \tag{4.23}$$

The nominal traction vector, σ consists of three components: σ_n in the normal direction, σ_s and σ_t in two shear directions (Figure 4.10). The corresponding separations are denoted by δ_n, δ_s, and δ_t.

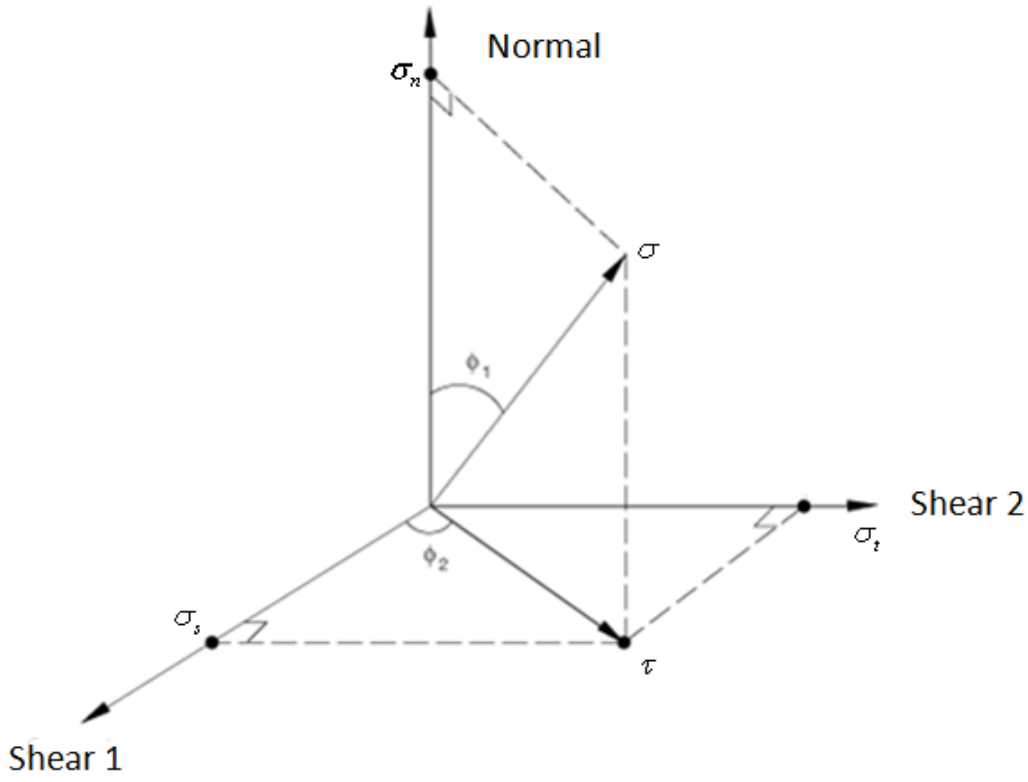

Figure 4.10. Normal and shear traction components

If t_0 is defined as the original thickness of the cohesive element, the nominal strains can be defined as:

$$\varepsilon_n = \frac{\delta_n}{t_0},\ \varepsilon_s = \frac{\delta_s}{t_0},\ \varepsilon_t = \frac{\delta_t}{t_0} \tag{4.24}$$

And, finally, elastic matrix can then be represented as:

$$\sigma = \begin{bmatrix} \sigma_n \\ \sigma_s \\ \sigma_t \end{bmatrix} = \begin{bmatrix} L_{nn} & L_{ss} & L_{nt} \\ L_{ns} & L_{ss} & L_{st} \\ L_{nt} & L_{st} & L_{tt} \end{bmatrix} \begin{bmatrix} \varepsilon_n \\ \varepsilon_s \\ \varepsilon_t \end{bmatrix} = L_t \varepsilon \tag{4.25}$$

Where L_t can be defined as the cohesive elastic stiffness or the penalty parameter.

4.2.1.2.1.1. Principle of virtual work for cohesive elements. Cohesive modeling for a quasi-brittle material assumes that a process zone exists at the crack tip where a constitutive relation is assumed to exist between the tensile normal stress and crack displacement on the crack wall (Jiang, 2010).

In order to follow a finite-element analysis based on the law of cohesion, it is necessary to explain the principle of virtual work in the cohesive zone. A pair of virtual crack surfaces exists in the potential crack path. These crack surfaces are subjected to separating forces which are called cohesive traction forces. These tractions target both inner and outer crack surfaces. The mechanical equilibrium equation considers the contribution of the cohesive tractions to be (Roe and Siegmund, 2003):

$$\int_V \overline{\sigma} : \delta\vec{F} d\Omega = \int_{S_{\text{int}}} \vec{T}_{CZ} . \delta\vec{\Delta} dS + \int_{S_{ext}} \vec{T}_{ext} . \delta\vec{u} dS \tag{4.26}$$

$\overline{\sigma}$ is the nominal stress tensor, $\overline{F}$ is the deformation gradient, Ω, S_{int} and S_{ext} represent the specimen volume, the internal/cohesive surface and the external surface, respectively. $\vec{T}_{CZ}$ denotes the cohesive traction vector and $\vec{T}_{ext}$ the external traction vector, $\vec{u}$ is the displacement vector and $\vec{\Delta} = u^+ - u^-$ represents the displacement jump across the two adjacent cohesive surfaces. The total deformation force on the fracture surface, given as

the volume integral on the left side of Equation 4.26 equals the traction integral over the cohesive zone inner surface (i.e. crack and the cohesive zone in front of the crack tip) and the tractions on the cohesive zone external surface). Evolution of the fracture is either defined by specifying effective displacement at complete failure or the evolution based on fracture energy. The other component to the definition of fracture propagation is the specification of the nature damage and final failure. This can be done by either defining linear or exponential softening laws (Jiang, 2010).

4.2.1.2.1.2. Fracture initiation criteria for cohesive elements. Fracture initiation refers to the beginning of the degradation when stresses or strains satisfy a certain fracture initiation criterion (Camanho and Davila, 2002). In order to model fracture initiation in the simulations, suitable criterion must be assigned. Criteria based on maximum nominal stress, maximum nominal strain and quadratic nominal stress were available for fracture initiation. However, previous investigations using quadratic nominal stress resulted in superior convergence rates and more accurate results (Camanho and Matthews, 1999; Davila and Johnson, 1993; and Cui et al., 1992). For this reason, quadratic nominal stress was used (Camanho and Davila, 2003):

$$\left\{\frac{<\sigma_n>}{\sigma_n^0}\right\}^2+\left\{\frac{\sigma_s}{\sigma_s^0}\right\}^2+\left\{\frac{\sigma_t}{\sigma_t^0}\right\}^2=1 \tag{4.27}$$

Where σ_i and *i= n, s, t,* represent the normal and two shear directions, respectively. $\sigma^0 i$ ^ *i= n, s, t* represent the tensile strength and shear strength in the corresponding directions, respectively. The symbol <> indicates that a pure compressive deformation or stress will not initiate damage. Damage is initiated when the above quadratic function involving the nominal stress ratio becomes unity.

4.2.1.2.1.3. Fracture propagation criteria for cohesive elements. The Fracture propagation law defines the rate of degradation for cohesive elements. Normally, when the fracture initiation criterion is satisfied, damage propagation begins. A fracturing ratio (F_r) will show the overall damage in the material; it has a value between 0 and 1. The traction vector components are affected by damage as follows:

$$\begin{aligned}\sigma_n &= \begin{cases}(1-F_r)\overline{\sigma}_n, & \overline{\sigma}_n \geq 0\\ \overline{\sigma}_n, & \end{cases}\\ \sigma_s &= (1-F_r)\overline{\sigma}_s,\\ \sigma_t &= (1-F_r)\overline{\sigma}_t\end{aligned} \tag{4.28}$$

Fracture propagation criteria is an important factor determining the extension and geometry of induced fracture. It is difficult to find a suitable criterion that is applicable to complex conditions. The most widely used criteria for predicting propagation are the power law and the Benzeggagh-Kenane (BK) criterion. The power-law criterion predicts the failure of thermoplastic matrix composites (Camanho and Davila, 2003; Needleman, 1987) whereas the BK criterion best describes fracture propagation in rock and mineral composites. The latter is expressed as a function of the Mode I and Mode II fracture energy and a material parameter obtained from a fracture mechanics test. Since this work assumes the opening of a Mode I crack, fracture energy in the first and second shear directions is the same. Thus, this criterion best fits these simulations (Benzeggagh and Kenane, 1996):

$$G_n^C + (G_s^C - G_n^C)\left\{\frac{G_s}{G_T}\right\}^J = G_C \tag{4.29}$$

An output variable shows how much damage each element has undergone. This information facilitates identification of the degradation factor in each simulation.

4.2.1.2.1.4. Fluid flow into cohesive elements. The fluid flow into the fracture can consider both tangential flow and normal flow (Figure 4.11). Tangential flow is the fluid flow in the cohesive elements gap, which can be modeled with either a Newtonian or Power law model. Normal flow is the fluid flow across the cohesive elements gap, this normally reflects resistance due to caking or fouling effects. Drilling fluid properties (viscosity and mud cake permeability) were used in the simulations.

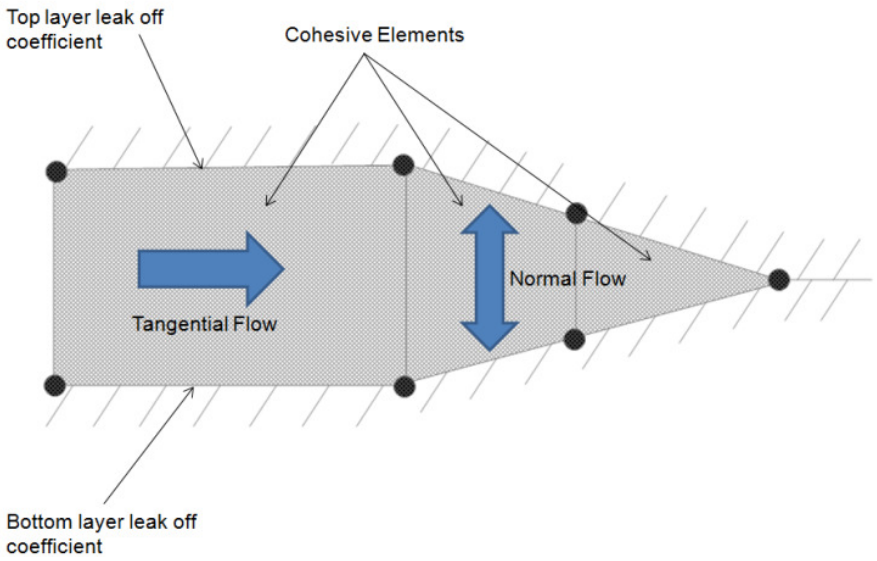

Figure 4.11. Fluid flow into cohesive elements simulated considering both tangential flow and normal flow

4.2.1.2.1.5. Newtonian fluid. If the fluid flow was simulated by Newtonian flow, the flow rate density can be given by the following equation:

$$qd = -k_t \nabla p \tag{4.30}$$

where k_t is the tangential permeability (the resistance to fluid flow), ∇p is the pressure gradient along the cohesive element, and d is the gap opening given as (Abaqus Documentation, 2009):

$$d = t_{curr} - t_{orig} + g_{init} \tag{4.31}$$

t_{curr} and t_{orig} are the current and original cohesive element thicknesses, respectively; and g_{init} is the initial gap opening. Tangential permeability can be defined according to Reynolds's equation:

$$k_t = \frac{d^3}{12\mu} \tag{4.32}$$

where μ is the fluid viscosity.

4.2.1.2.1.6. Power law fluid. If the fluid flow is simulated by Power law, the constitutive relationship is defined as:

$$\tau = f_c \gamma^y \tag{4.33}$$

where τ is the shear stress, γ is the shear strain rate, f_c is the fluid consistency, and y is the power law coefficient (flow behavior index). Tangential volume flow rate density can be defined as:

$$qd = -(\frac{2y}{1+2y})(\frac{1}{f_c})^{\frac{1}{y}}(\frac{d}{2})^{\frac{1+2y}{y}} \left\|\nabla p\right\|^{\frac{1-y}{y}} \nabla p \tag{4.34}$$

If the power law model is used in the simulations, it is required to have the fluid consistency and flow behavior index. Rheological properties of injecting drilling fluids are obtained from viscometer readings and then used for predicting input parameters in the models.

4.2.1.2.1.7. Normal flow across the cohesive elements. If normal flow is permitted in simulations, it is required to define fluid leak off coefficients (mud cake permeability) across the cohesive elements (Figure 4.12).

The normal flow can be defined as:

$$\begin{aligned} q_{top} &= c_{top}(p_i - p_{top}) \\ q_{bot} &= c_{bot}(p_i - p_{bot}) \end{aligned} \tag{4.35}$$

Where q_{top} and q_{bot} are the flow rates into the top and bottom faces. P_i is the pressure inside the cohesive element. P_{top} and P_{bot} are the pore pressures on the top and bottom surfaces. Leak off values can be obtained from mud cake permeability measurements in the drilling lab.

4.2.1.3. Input data collection. Collecting input data is a critical task when conducting numerical simulations. According to this study, rock mechanical properties and fracture mechanics input are required. Different sources of data can be used for collecting input parameters, these include:

- Published data in literature related to similar problems; including fracture mechanics and rock mechanic's lab tests, available well logs and/or geological information

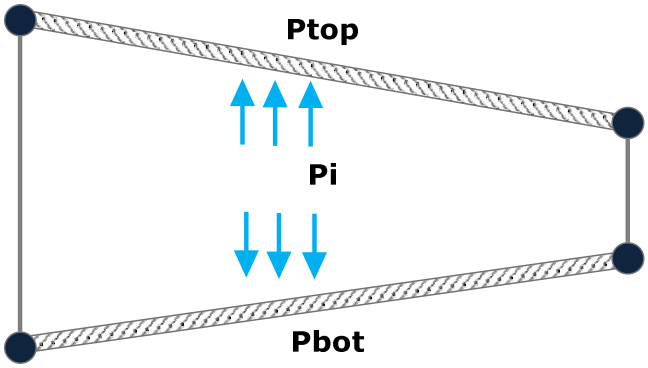

Figure 4.12. Normal flow defined in cohesive layers by assigning leak off coefficient at top and bottom layers

- Simultaneous lab experiments and/or field tests

Regarding this study, fracture mechanics input data were obtained from published papers and books. Parametric studies were performed for uncertain inputs which are presented in the next section. Regarding numerical results verification, input data such as rock mechanical properties and drilling fluids rheological properties were collected from experiments and tests were performed at Missouri S&T.

Fracture mechanics tests are required to find cohesive material properties; including cohesive fracture energy and material strength which are the most important parameters. These parameters are measured directly from experiments and reflect the actual heterogeneous material (Turon et al., 2007). Single-edge notched beam tests (SENB) are typical fracture mechanic tests used for predicting cohesive material properties determination. Normally, the objective in these tests is to obtain a load versus crack opening displacement (COD) that is used to determine fracture properties of materials. After the test is done and the load versus crack opening displacement is recorded, this information will be used to calculate fracture energy. The fracture energy is calculated based on the area under the crack opening and the displacement curve.

Fracture properties for sedimentary basin rocks have been published in the literature (Atkinson, 1987). For the purpose of simulations in this dissertation, published

data in the literature were used in fracture simulations. Appendix A shows fracture property data for different rocks using various fracture test set ups.

The other important property in rock fracturing is tensile strength. Rocks are much weaker under tensile conditions as compared to compressive or shear conditions. The tensile strength of a rock is thus one of the important mechanical criterions relevant to calculations involving rock deformability, fracture, crushing and fragmentation. The Brazilian test is often carried out to find the tensile strength of the rock samples. Figure 4.13 shows the Brazilian set up at Missouri S&T. The apparatus consists of a testing frame, loading apparatus consisting of loading pump and piston, load sensor and the Brazilian test rig.

Brazilian tensile strength can also be used for calculating fracture toughness. One simple correlation between tensile strength and fracture toughness is (Zhang, 2002):

$$T_0 = 6.88K_C \tag{4.36}$$

Table 4.2 reports the required parameters when cohesive elements are used. Generally, there are two ways to define the propagation of a fracture. The first method includes specifying the effective displacement at complete failure or the effective displacement at the initiation of damage. The second method includes introducing the fracture energy dissipated due to failure G^c or the propagation based on fracture energy. The latter method was used for simulations in this study. Since only Mode I fracture (opening mode) is simulated, the parameters in first and second shear directions are not required.

4.2.1.4. Mesh generation, discretization and verification. Mesh quality remains an important issue in generating accurate results for Finite-Element Analysis (FEA). Literature covering mesh optimization includes many different techniques and procedures for mesh refinement and smoothing (Freitag et al., 1995, Pardhanani and Carey, 1988, Zavattieri, 1996 and Knupp, 2000).

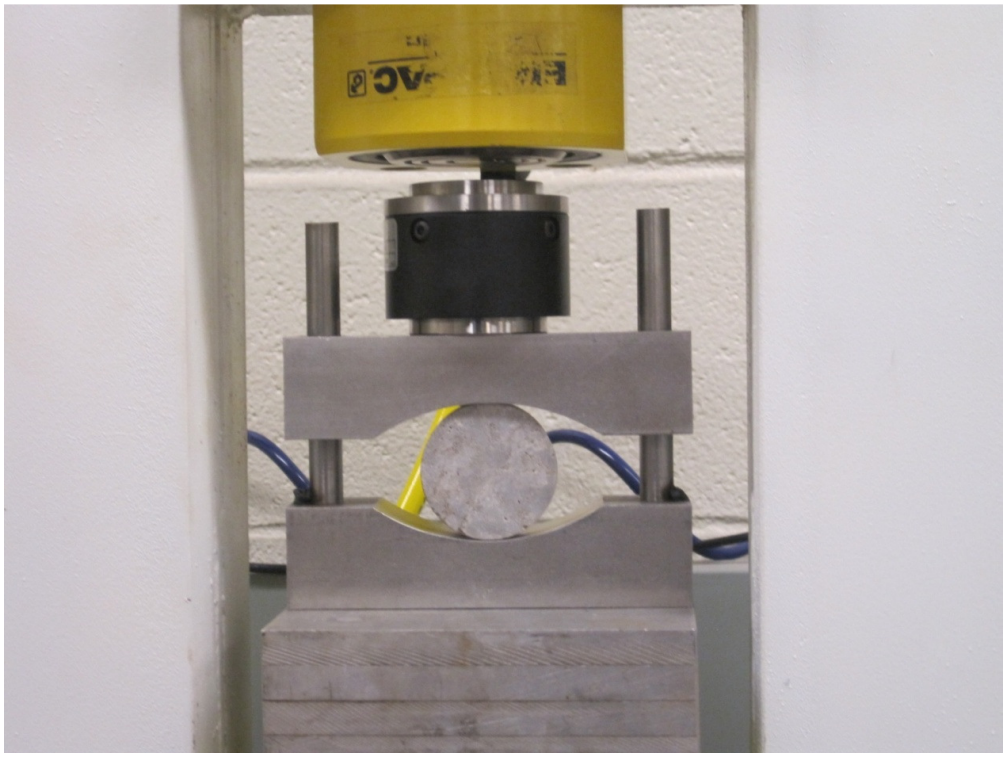

Figure 4.13. Brazilian test set up at Missouri S&T for measuring rock tensile strength

The mesh model size needs to be selected so that end effects are avoided. Further mesh refinement is required in the near wellbore region and other zones of interest. This decision is even more critical when three-dimensional models are used. Increasing the number of elements with additional degrees of freedom significantly adds to the complexity of the model. Further, adding more complexity to the models like including non-linear cohesive elements creates convergence problems, especially with a high number of integration points. For this research, mesh calibration results compared with analytical Kirsch solution derived for stresses outside a circular hole in an infinite elastic solid medium.

Table 4.2. Required parameters for using cohesive elements to model fracture in simulator

Input Parameter	Description
L_{nn}	Cohesive element stiffness value in the normal direction
L_{ss}	Cohesive element stiffness value in the first shear direction
L_{TT}	Cohesive element stiffness value in the second shear direction
$\sigma_n^0, \sigma_s^0, \sigma_t^0$	Maximum nominal stress in the normal, first shear and second shear direction respectively
$\varepsilon_n^0, \varepsilon_s^0, \varepsilon_t^0$	Maximum nominal strain in the normal, first shear and second shear direction respectively
G_n^C	Normal Mode critical fracture energy
G_S^C	Shear mode critical fracture energy in the first shear direction
G_t^C	Shear mode critical fracture energy in the second shear direction
C	Leak off coefficient
$y \& f_c, \mu$	Power law fluid model exponent and consistency or viscosity when modeling Newtonian fluid model

4.2.1.4.1. Meshing guidelines and algorithm. Appropriate meshing guidelines are required in order to achieve accurate results from finite-element models. These guidelines can be summarized as (Mac Donald, 2007; Practical Stress Analysis with Finite Elements):

1. Using quadratic elements in model in order to increase results accuracy and avoid artificial stress effects
2. Selecting sufficiently small element size to minimize the error of approximation within acceptable bounds
3. Assigning element's aspect ratios less than five in order to avoid degradation of numerical performance

Using finer mesh for near-wellbore region since it was the major region of interest for results extraction

4.2.1.4.2. Selecting element type. Three dimensional meshes for this study were created in Hyper Mesh™ software then they were imported to FE solver (ABAQUS™). Figure 4.14 and Figure 4.15 show different types of elements used in FE models to see which one concludes the most accurate results. Figure 4.16 shows the simulated results of hoop stress around the wellbore when compared with the Kirsch solution. Using 8-node quad elements resulted in the most accurate solution. Using second order triangle elements also resulted in less than 5 % error; however, the hoop stress results fluctuated with changing angle around the wellbore which makes it less intuitive to interpret the simulation results (Figure 4.16 and 4.17). The maximum error is recorded around 23 % for first order triangle elements. Comparing results from different element types revealed that using second order quad elements in simulations results in less error.

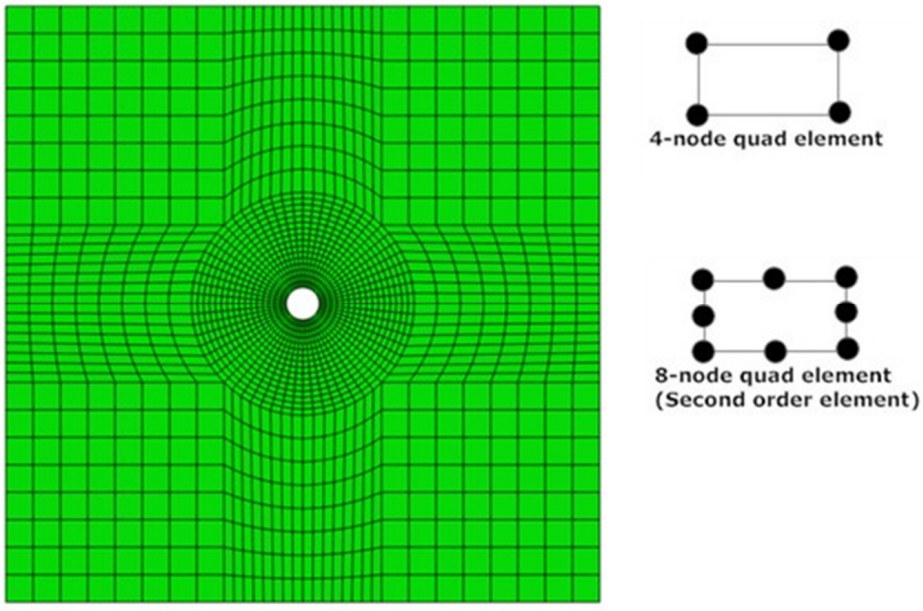

Figure 4.14. Four and eight-node quadratic finite element types

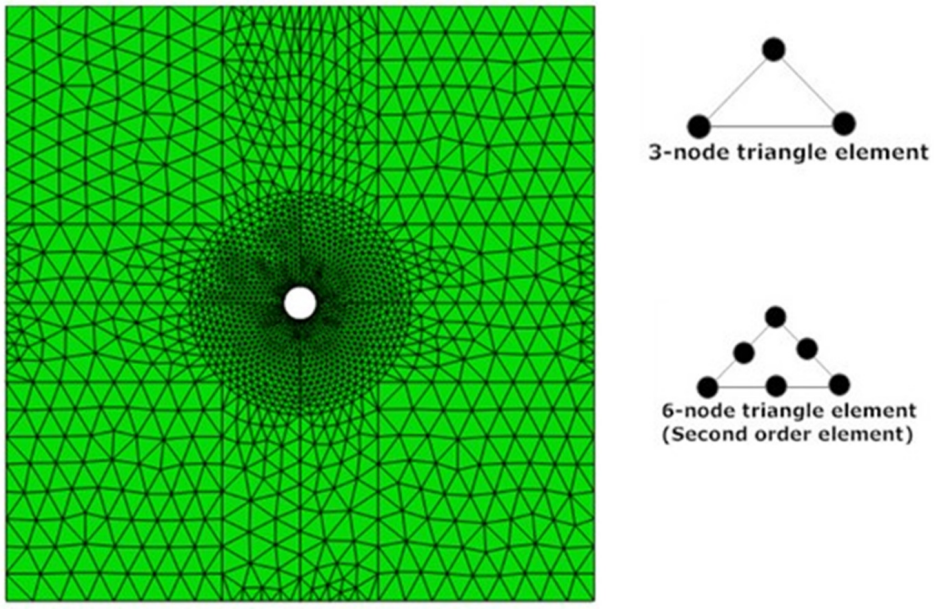

Figure 4.15. Three and six-node triangle finite element types

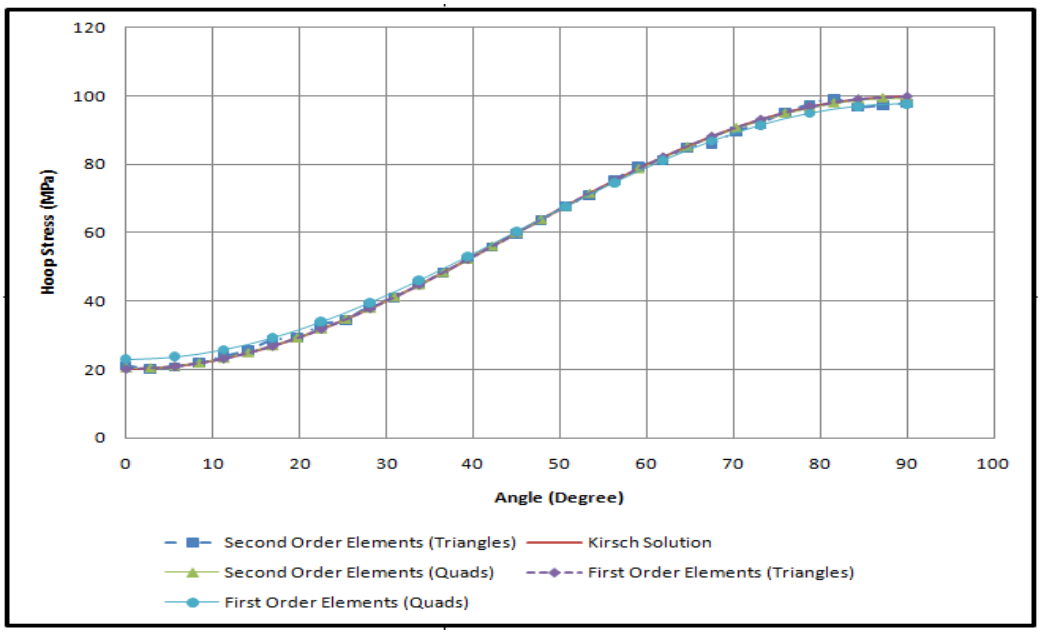

Figure 4.16. Wellbore hoop stress around wellbore compared with Kirsch solution for different element types

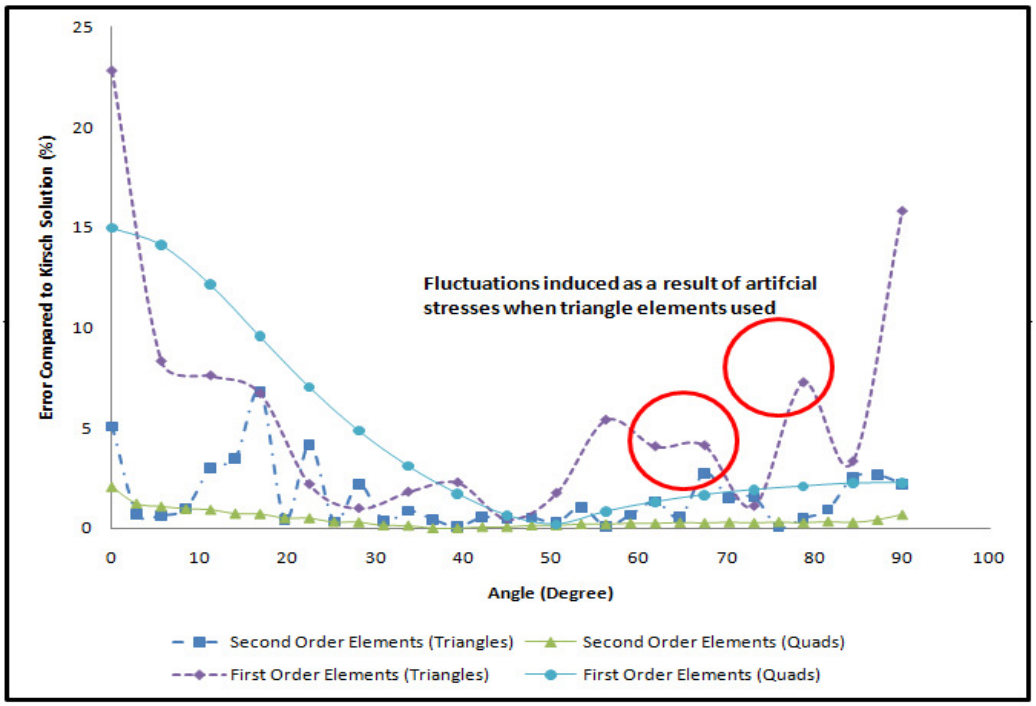

Figure 4.17. Calculation error for simulations with different element types compared to analytical solution

4.2.1.4.3. Model size effects. Using an appropriate number of elements and model size to eliminate the artificial effects in stress distribution is also very critical. First, models with different element density and compared with radial stresses calculated from Kirsch solution. Table 4.3 shows the results of using three different element densities in the models. The selected mesh for simulations has negligible error when compared with analytical solution.

Table 4.4 and Figure 4.18 show the results of choosing different ratio of model size over borehole diameter and compared with analytical solution. Since far field stresses are considered in the simulations, it is required for the model to show these stresses at an appropriate distance from the wellbore. Max difference from the Kirsch solution in Table 4.4 is 3.19 MPa which can be decreased to 0.11 MPa with increasing the ratio of model size to wellbore diameter.

Table 4.3. Number of elements used at one-quarter of borehole and error from Kirsch radial stress

Num of elements at one-quarter of borehole (2D Model)	Max difference from Kirsch radial stress (MPa)
10	1.1
20	0.5
30	0.14

Results indicated that any model bigger than four times the borehole size will yield results in an acceptable range.

Table 4.4. Ratio of model size over borehole diameter and max error from Kirsch radial stress

Ratio of Model size over borehole diameter	Max Difference from Kirsch Radial (MPa)
2	3.19
4	0.66
6	0.39
8	0.11

4.2.1.4.4. Cohesive zone mesh refinement. Cohesive model results are highly sensitive to element size vs. fracture zone size. For this reason, a rough estimate of the fracture zone size (based on elasticity and fracture parameters) is needed. It is often observed that finite-element results become distorted when the mesh size is not correlated with enough number of elements in the cohesive zone.

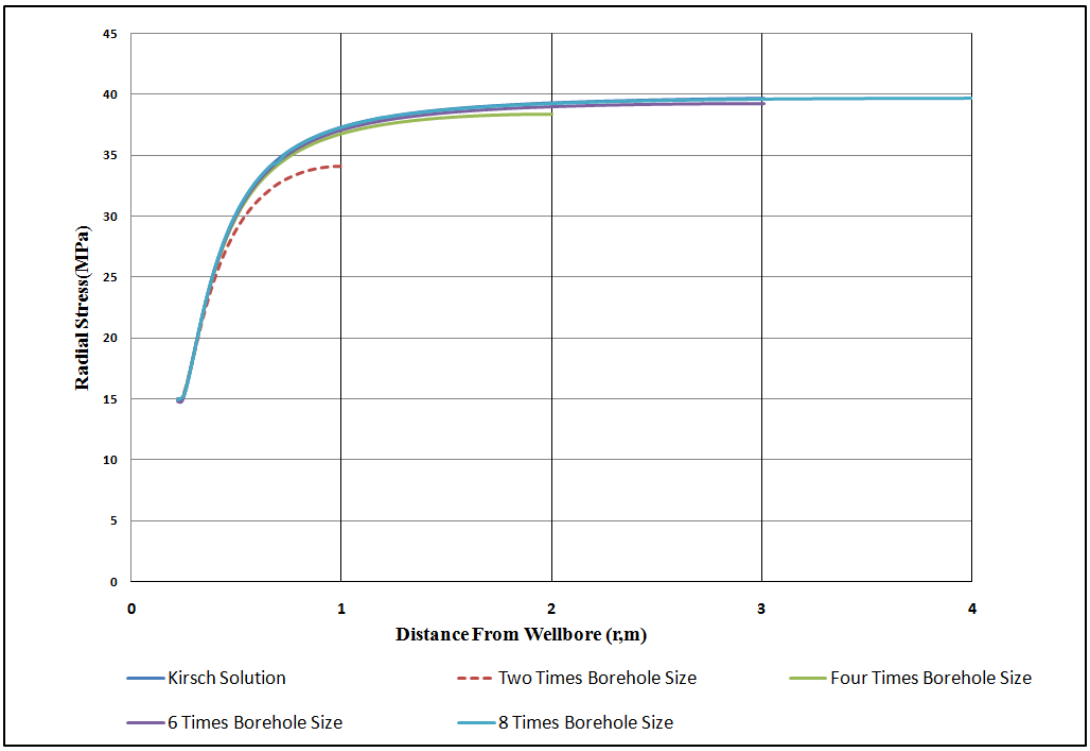

Figure 4.18. Radial stress versus distance based on different ratios of model size over borehole diameter

Different models exist in literature to predict the cohesive zone length (Turon et al., 2007). The general form in all the models predicts cohesive length proportional to the fracture energy (Gc) and inverse square of the material strength. The most commonly used models are Hillerborg's (Hillerborg et al., 1976) and Rice's model (Rice, 1968). The Rice model was used for cohesive zone mesh calibration in this study.

4.2.1.4.5. Summary of mesh sensitivity analysis. Based on mesh sensitivity analysis results, it is recommended to divide the mesh into four regions as illustrated in Figure 4.19. The circle size should be at least 2-3 times the borehole diameter and should be meshed by finer elements regarding the results extraction at the borehole wall and the near wellbore region. The rest of the mesh from circle to boundary should have a size of 4-6 times the borehole diameter so that the far field stress can be touched in the model. It is also recommended to use quadratic over triangle elements everywhere in the model, however, it gets difficult in complex geometries. The aspect ratio of the elements should

be kept less than five to secure accurate results. When using cohesive elements, converging issues are very important due to the non-linearity nature of the cohesive modeling. There is no fixed algorithm existing for mesh guidelines when these types of elements are used especially when near wellbore fractures are simulated. For this reason, it is recommended to consider both aspects of accuracy and easy to converge for these types of simulations.

4.2.1.5. Assigning material model. Using linear elastic material model is the easiest approach for geomechanical simulations. However, results of published numerical simulations revealed that this model in SEVERAL cases does not provide realistic results when compared with results from lab experiments and/or field trials (Mclellan, 1996, Salehi et al., 2010). Also the presence of a freely moving fluid in a porous rock modifies its mechanical behavior and makes the rock to RESPOND in a poro-elastic way (Detournay and Cheng, 1993). For these reasons, all the FE models in this study considered poro-elastic material properties including rock permeability, porosity and pore pressure.

Different types of cohesive elements are available in the FE software library including three dimensional cohesive elements with and without pre pressure (COH3D6, COH3D6P, COH3D8, COH3D8P). These elements are also described in Table 4.5. For poro-elasticity applications, only COH3D6P and COH3D8P elements can be used. COH3D6P elements are more appropriate when triangle fracture elements are used in the model. Therefore, it was decided to select 12-node displacement pore pressure type cohesive elements (COH3D8P) in fracture zone to match with other continuum three-dimensional elements (C3D8RP) used in other parts of the model. The active degrees of freedom for cohesive elements are 1,2,3 and 8 on the top and bottom faces and 8 at nodes on the middle face (Degrees of freedom are sets of independent displacement and/or rotations that specify completely the displaced or deformed position and orientation of the body or system). Figure 4.20 shows the schematic of elements and where in the model used.

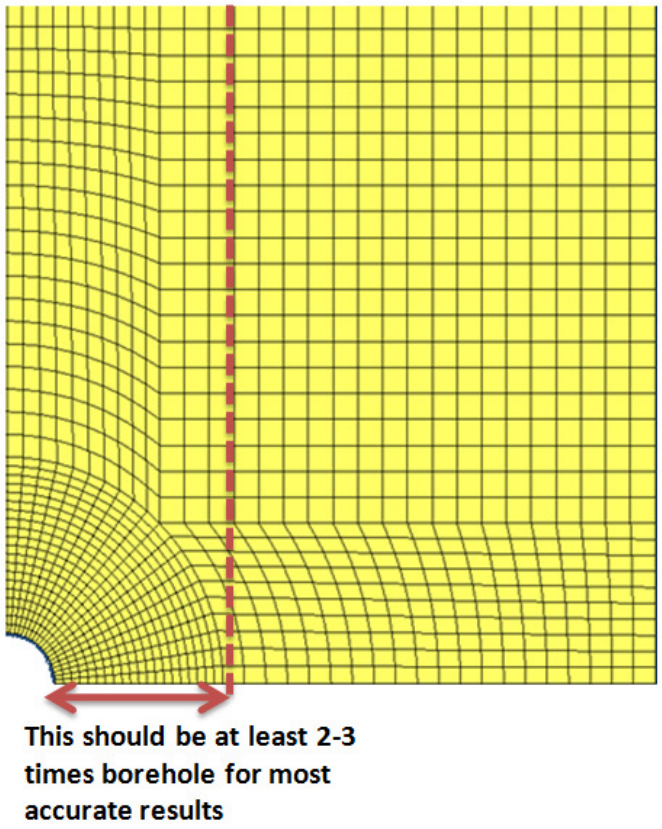

Figure 4.19. Sketch of the typical mesh used for near wellbore models

Table 4.5. Two and three dimensional cohesive elements library

Cohesive Element	Description
COH3D6	6-node three dimensional cohesive element
COH3D6P	9-node displacement and pore pressure three-dimensional cohesive element
COH3D8	8-node three-dimensional cohesive element
COH3D8P	12-node displacement and pore pressure three-dimensional cohesive element

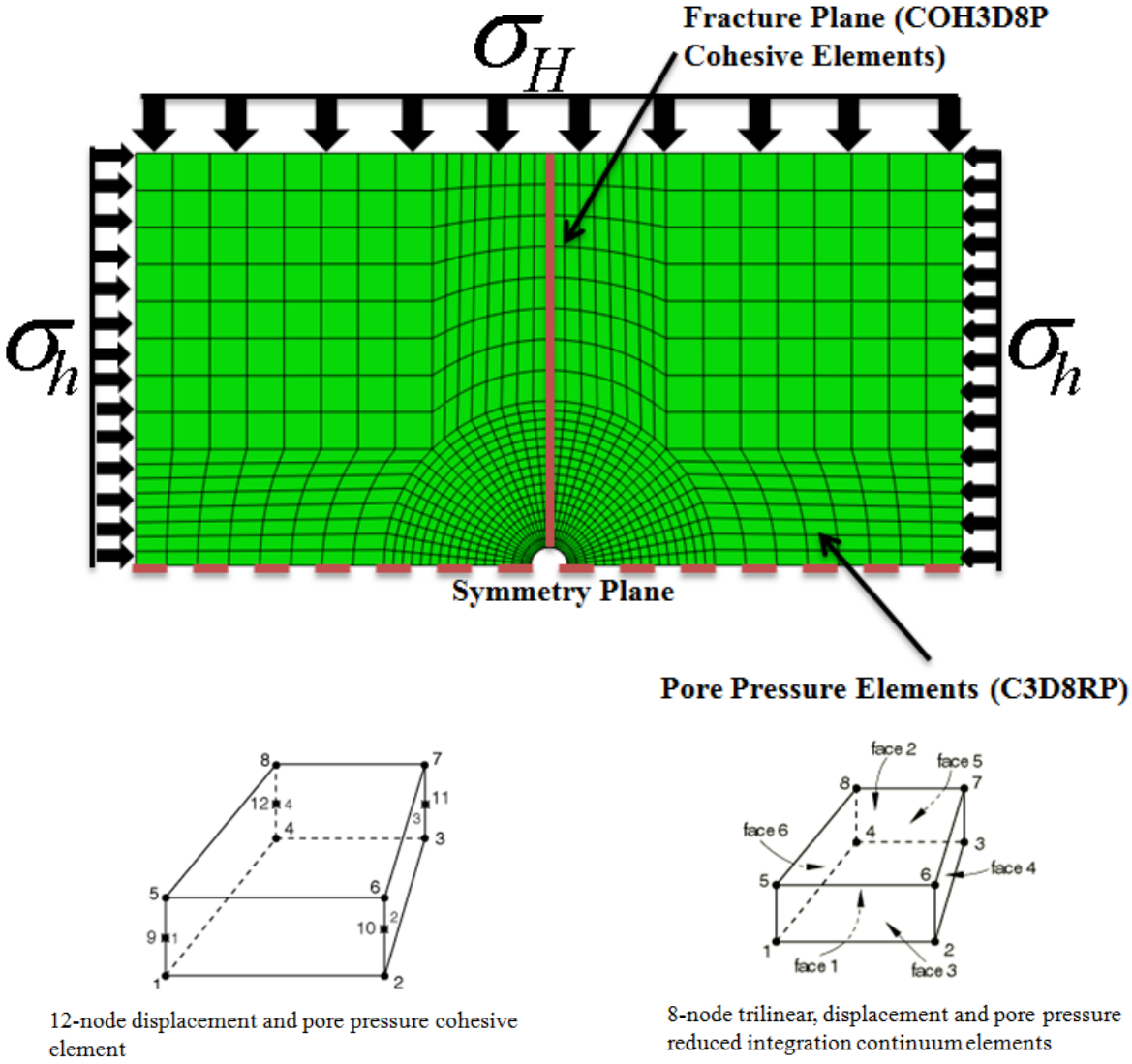

Figure 4.20. Type of continuum pore pressure and cohesive pore pressure elements used for poro-elastic simulations

4.2.1.6. Loads, initial and boundary conditions. Generally, all the loads, initial and boundary conditions have to be identified before they were applied into the model. This helps in constructing the model sketch and conceptualizing the problem. After they are collected, it should be decided what type of methodology is appropriate to apply those

into the model. For instance, boundary conditions can be applied in different ways such as putting them as displacements on the model boundary. Stress boundary conditions directly applied to model boundaries or they can be applied through adding and removing elements in excavation or drilling process.

Boundary conditions include subsurface stresses such as overburden stress, maximum and minimum horizontal stresses. These boundary conditions were implemented in the simulations through removing wellbore elements (Drilling step). Symmetry boundary condition was also used in the model since only half of the wellbore is modeled.

Before drilling takes place, the formation is under subsurface stresses (overburden and horizontal stresses). Once drilling occurs, a cylindrical volume of the formation will be removed, and this will change the stress regime in the near wellbore. This step is modeled by removing wellbore elements at the beginning of the simulations and applying far-field boundary conditions simultaneously (Figure 4.21).

FE models in this study are also affected by mud weight, injection loads, initial boundary conditions such as pore pressure, porosity (void ratio), permeability, initial fracture gap opening and in-situ stresses. Mud weight was simulated by defining distributed surface loads on the wellbore face. Furthermore, injection loads were modeled as concentrated fluid flow on the injection node.

4.2.1.7. Simulations run. When all the previous steps were accomplished, it would be more efficient to run simple test models first, before running detailed models. This will provide further insight for understanding model limitations. It is always tempting to increase complexities of the models, because it makes it more realistic. However, in some cases, adding complexities will have little influence on the model response, so they should be eliminated. Simple runs can also provide shortcomings than can be fixed before any significant effort can be invested in the analysis. For instance, starting with linear-elastic models always helps to observe and judge model response, and they are very simple to be implemented. Advanced material models can be added to simulations when other issues such as appropriate boundary conditions, element type and time increment were finalized.

Regarding this study, FE models were run in ABAQUS SIMULIA™ finite-element software. The code includes advanced material models for geotechnical/geomechanical applications, including modern failure/fracture capabilities and intensive elements library.

Simulations were run in multiple stages including equilibration and fluid flow (injection). In the equilibration phase, all the loads (except injection) and/or boundary conditions will be applied to the model to mimic downhole conditions. In the next step, other loads will be applied in order to initiate and propagate fracture.

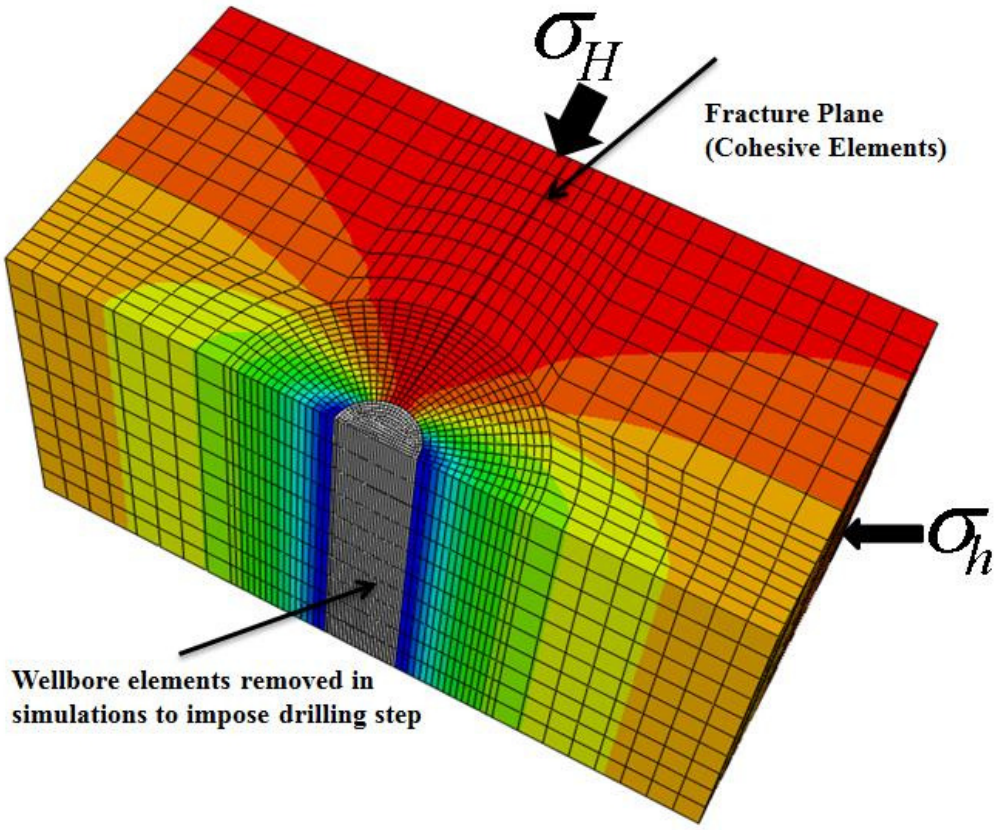

Figure 4.21. FEA poro-elastic model details including boundary conditions- Cohesive elements were aligned in maximal horizontal stress orientation

There are two distinctive steps for simulations in this study. The first step (Geostatic) aims to verify that the initial geostatic stress field is in equilibrium with applied loads and boundary conditions. This is, normally, the first step of a geomechanical analysis which can be followed by a coupled pore fluid diffusion/stress analysis. It is ideal to see complete equilibration which produces zero deformation after this step; however, this is very difficult when complexities of the model increase. It is also important to correctly establish initial conditions such as initial pore pressure, saturation, any geostatic stresses and porosity; otherwise, the results will be unreliable and unrealistic.

In the next step fluid is injected into the porous medium through a coupled pore fluid diffusion/stress procedure (Soil option). The mechanical part of the model is based on the effective stress principle which was described earlier in this section. Fully saturated fluid flow was used in simulations which is typically the general procedure for a geotechnical/ geomechanical analysis. It was critical to define correct time increments in this step; a simple guideline for calculating the minimum usable time increment is explained in Appendix B.

For verification of hoop stress in an intact case and sealed fracture, the following steps in Figure 4.22 are considered.

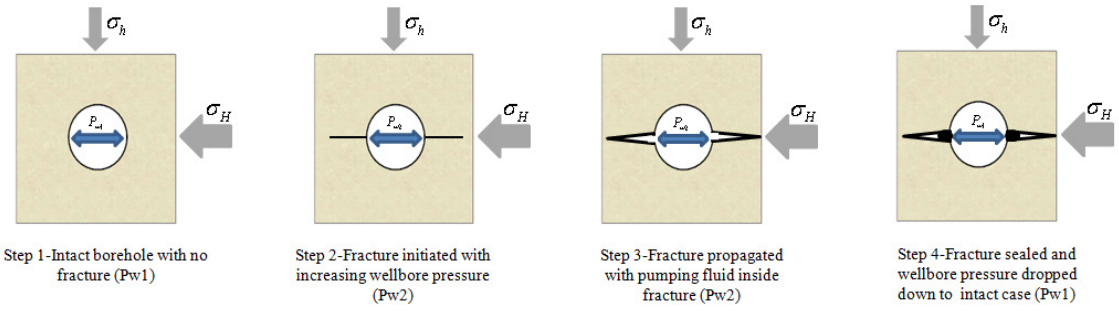

Figure 4.22. A schematic of steps required for a detailed wellbore strengthening study (Taken from Salehi et al., 2011)

4.2.1.8. Results extraction and analysis. The final stage of numerical simulations is the result extractions and analysis. Since the hoop (tangential) stress around a wellbore is a primary factor whether a wellbore is strengthened, investigating hoop stress is pertinent. Cartesian stress results were exported from the FE solver to MATLAB in order to calculate hoop stresses on different orientations around and by the distance from the wellbore. In addition, pore pressure, displacement, fracture width, length and propagation were extracted at each time step for further analysis. A detailed presentation of the results is provided in the next section.

Vectors and tensor quantities are expressed using indicial notation with respect to a fixed rectangular Cartesian coordinate system. SI units are used to illustrate the parameters and dimensions of the variables. Table 4.6 summarizes systems of SI units used for different parameters. Solver assumes negative stresses as compressive stresses and positive stresses as tensile stresses. However, due to common convention in the drilling industry, compressive stresses are positive and tensile stresses are negative.

Table 4.6. SI units required for simulations in solver

Parameter	**SI Unit**
Length	Meter (m)
Force	Newton (N)
Time	Seconds (S)
Mass	Kilogram (Kg)
Pressure	Pascal (Pa)
Density	Kg/m3
Fracture Energy	Joules/m2
Permeability	m/s
Viscosity	Pa.s

4.2.1.9. Model assumptions. It is critical to mention the assumptions considered for this study. Without making these assumptions, the problem becomes very complex and cannot be easily solved with the methodologies described in here:

Normal Faulting Stress Regime. As mentioned in the introduction section, the narrow pore-fracture window is also very common in highly deviated and horizontal wellbores. In addition, existence of different stress regimes affects fracturing criteria when drilling vertical wells. For simplicity, this study only considers vertical wellbores with normal faulting regime where overburden stress is the principle stress. Although it is believed that these assumptions do not change the overall conclusions from this study, it is recommended that future wellbore strengthening studies consider different stress regimes and deviated wellbores.

Mode I fracture. As discussed in Section 2.1.1.1, three modes of fracture displacement exist which are also knows as Mode I, II and III. For simplicity and also because of the lack of input data on the two other fracture modes, only Mode I is considered for simulations in this study.

4.2.2. Research Methodology for Task 2-Investigation of Fracture Resistance Increase. The objective for this section is to predict fracture propagation pressure when hydraulic fractures are sealed. Three analytical solutions for predicting fracture propagation pressure will be reviewed in this section.

4.2.2.1. Abe et al., solution. Abe et al., (1976) derived an analytical solution for a sealed penny-shaped crack in an infinitely extended medium. As shown in Figure 4.23, the crack is subjected to minimum far field stress (σ_h) and a non-invaded zone exists close to the fracture tip in which fracturing fluids cannot reach further. The fracture length is R, and the length of invaded zone is R1, pressure between the non-invaded zone and fracture tip is equal to the pore pressure. The solution can be used for the case of drilling fluids when a non-invaded zone exists close to the tip of the fracture (Figure 4.24).

The relationship between different terms is written in the following equation; the details of all equations have been reported in the original paper (Abe et al., 1976).

$$\frac{P_{fp}-\sigma_h}{\sigma_h-P_p}=\frac{1}{1-\sqrt{1-(\frac{R_1}{R})^2}}\times[\sqrt{1-(\frac{R_1}{R})^2}+\frac{\pi}{\sqrt{2R}}\times\frac{K_c}{(\sigma_h-P_p)}] \tag{4.37}$$

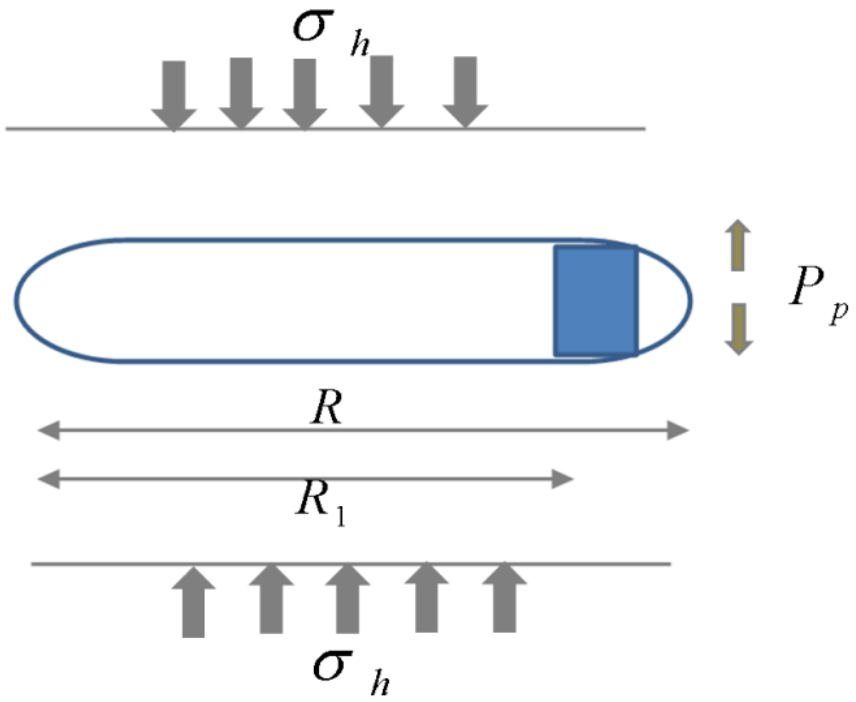

Figure 4.23. Penny-shaped fracture and existing boundary conditions

Effect of the second term in brackets is very small regarding fracture toughness in sedimentary basins and it can be completely ignored for large size fractures. Parameter λ is defined as sealing efficiency factor:

$$\lambda=\frac{1}{1-\sqrt{1-(\frac{R_1}{R})^2}}\times\sqrt{1-(\frac{R_1}{R})^2} \tag{4.38}$$

And the final equation can be summarized as follow for different values of λ :

$$P_{fp}=(\lambda+1)\sigma_h-\lambda P_p \tag{4.39}$$

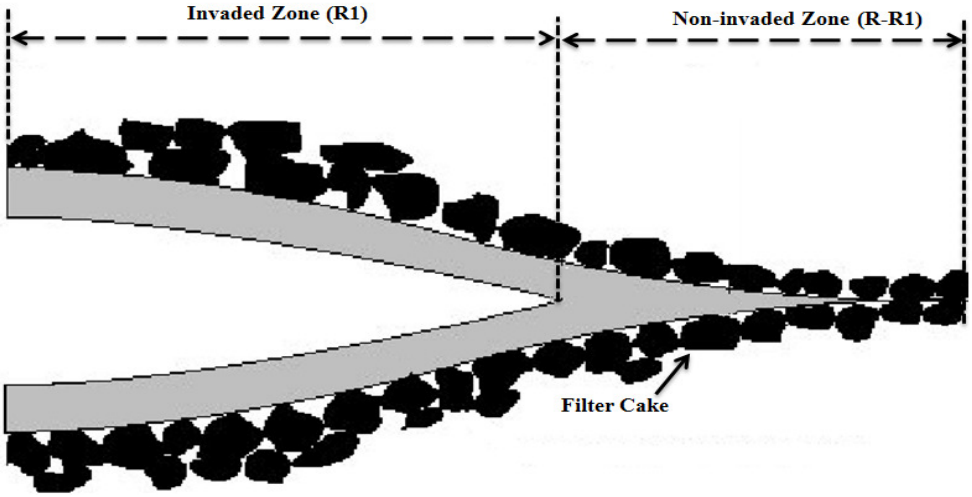

Figure 4.24. Invaded and non-invaded zone for a typical water-based drilling fluid

Equation 4.39 is very similar to the Kirsch solution, except for the term λ ; as this term increases, fracture propagation pressure increases as well. As shown in Figure 4.25, λ can be in range from 0 to 1.5.

As demonstrated by Figures 4.25 and 4.26, for the case of fully penetrating fluids, λ will be zero and fracture propagation pressure will be equal to the minimum far field stress. Also, when the ratio of σ_h / P_p goes higher, fracture propagation pressure increases. If the fracture is near the wellbore wall, the horizontal stress term in equation can be replaced with hoop stress. The sealing efficiency factor is a function of the length of the non-invaded zone at the tip of the fracture. This effect is verified in hydraulic fracturing experiments which showed that the fracture reopening pressure depends upon the amount of mud cake left on the wellbore wall (Morita et al., 1990, Morita et al., 1996, Oniya, 1994 and van Dam et al., 1998). Since water based mud develops a larger mud cake, they it normally have a higher reopening pressure than oil-based muds as observed in laboratory experiments.

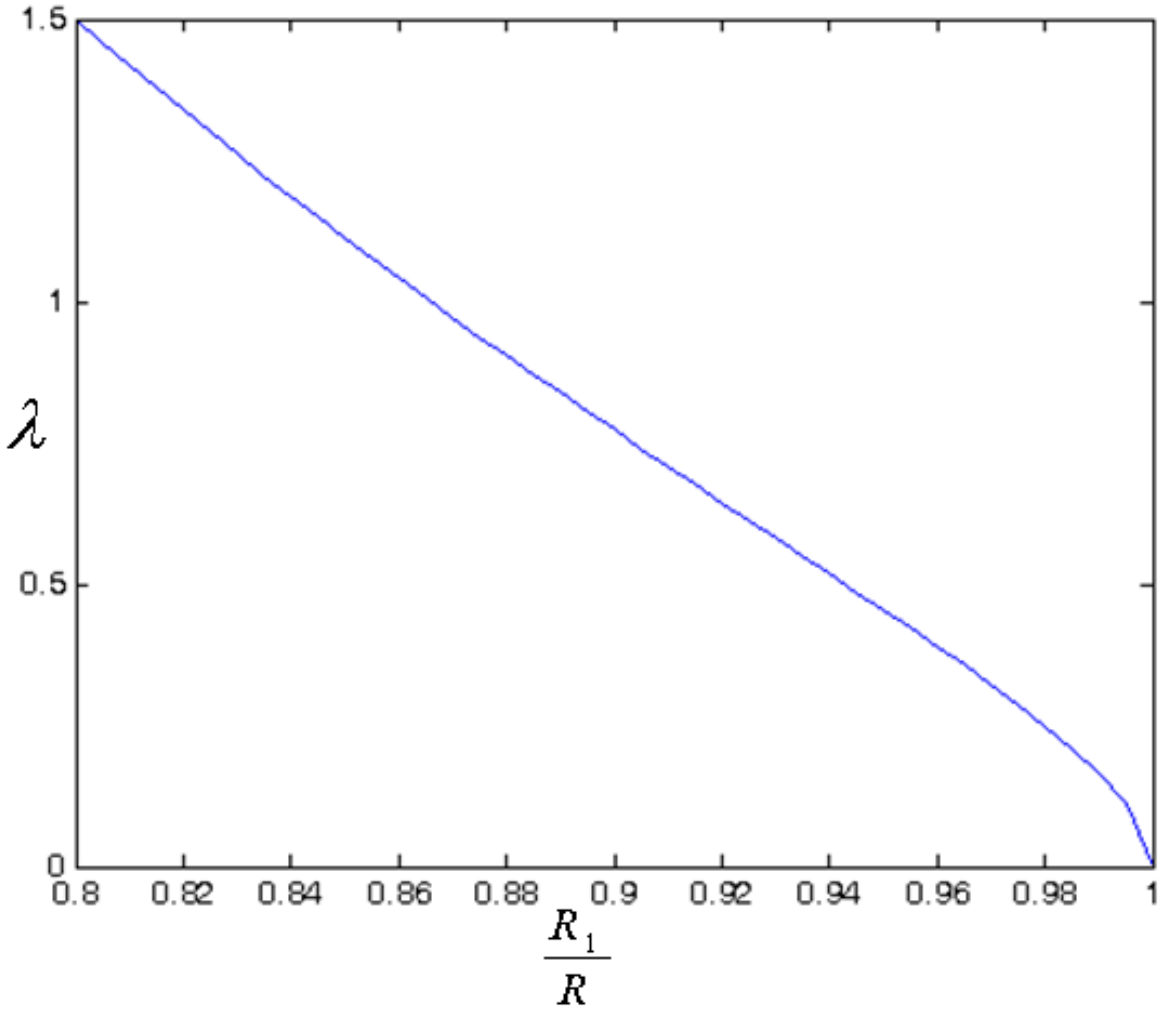

Figure 4.25. Sealing efficiency factor plotted versus ratio of the invaded zone. Note that non-invaded zone higher than 20 % is very unlikely to form

4.2.2.2. Morita et al., solution. The second equation for the sealed fracture is reported by Morita et al., 1988 and Fuh et al., 1992. The equation was derived from linear-elastic fracture mechanics (LEFM):

$$\Delta P_{fp} = \frac{1}{\sqrt{\pi h_{1/2}}}\left[\left(\frac{K_c}{2}\right)^2 + \sqrt{\left(\frac{K_c}{2}\right)^2 + \frac{E w_c(\sigma_h - P_p)}{2(1-\upsilon^2)}}\right] \tag{4.40}$$

The idea behind this equation was the existence of bridging solids in drilling fluids which acts as loss circulation control agents. These bridging materials form a stable barrier near the fracture tip which artificially impose pseudo-fracture toughness.

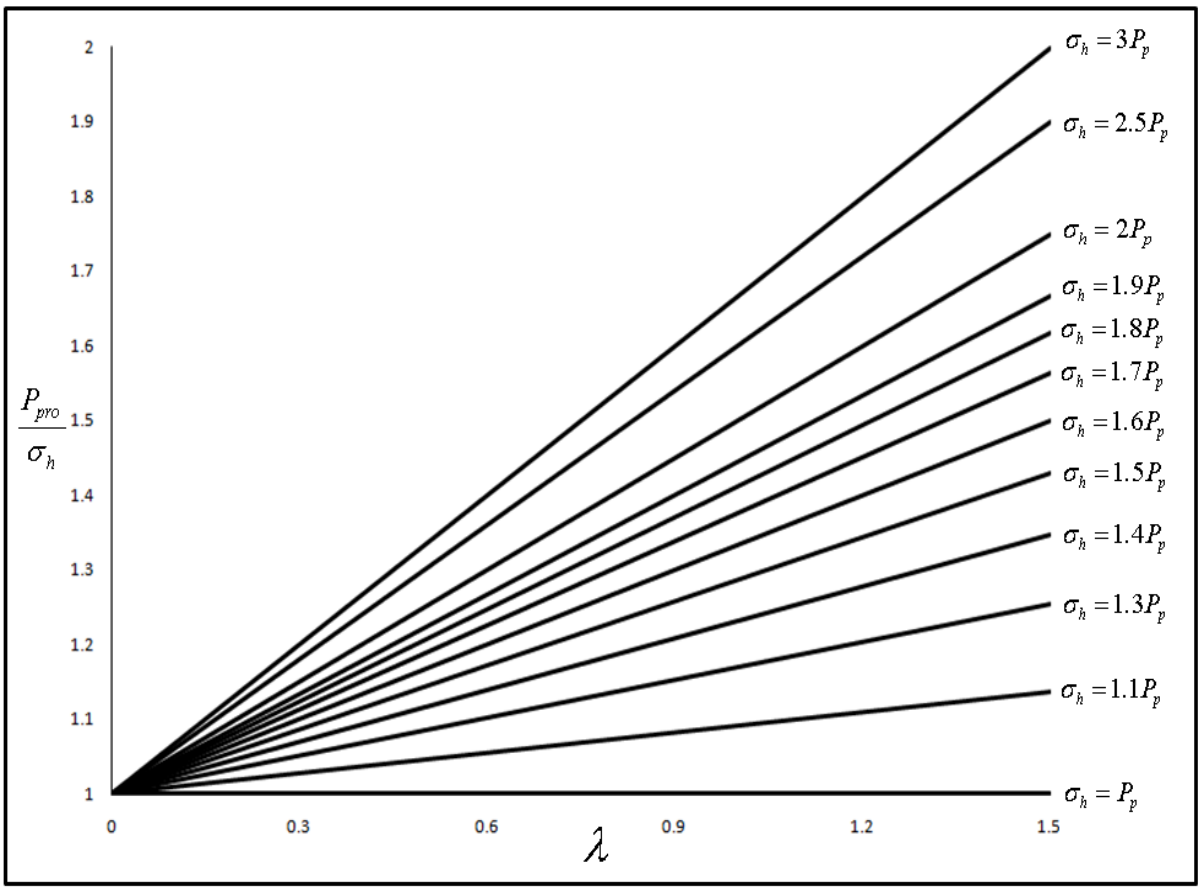

Figure 4.26. Variations of fracture propagation pressure versus sealing efficiency factor for different ratios of minimum far field stress to the pore pressure

4.2.2.3. Aadnoy and Belayneh solution. Aadnoy and Belayneh (2008) presented an alternative explanation of how fracture gradient can be increased above the theoretical Kirsch model value. The model developed is valid for non-penetrating fluids used during drilling operations. Their laboratory experiments on hollow cylinder tests demonstrated that fracturing resistance can be significantly improved by changing mud composition, especially the particles forming the barrier are key factors. According to them, the reason for the higher fracture pressure is that when a fracture opens, the mud cake does not split up but deforms plastically, maintaining the barrier. Their solution is very analogous to the one derived by Abe in terms of having a drilling fluid related parameter:

$$P_{fp} = \eta(3\sigma_h - \sigma_H - P_p) \tag{4.41}$$

η is defined as the barrier efficiency factor, and its value has been estimated to range from 1.23 to 3.89 determined by lab experiments. When the barrier efficiency is 1, the equation matches the linear-elastic Kirsch solution. Table 4.7 reports typical efficiency factors measured by laboratory experiments. According to Aadnoy and Belayneh, highest sealing efficiency factor is reported for Feldspar with particle sizes from 125 micron to 250 micron. The second highest number is for calcium carbonate with the same particle size distribution.

Table 4.7. Reported barrier efficiency for different LCMs (Taken from Aadnoy and Belayneh, 2004)

Particle type and sorting (Micrometer)	Reopening Pressure (MPa)	Fracture Pressure from linear elastic model	Yield strength correction in new elasto-plastic model (MPa)	Barrier efficiency
SiC (125-250)	10.5	8	2.5	1.31
SiC (125-250)	11	8	3	1.38
CaCO3 (125-250)	9.8	8	1.8	1.23
CaCO3 (125-250)	23.2	8	15.2	2.9
CaCO3 (63-250)	14.4	8	6.4	1.8
Feldspar (125-250)	31.1	8	23.1	3.89
Feldspar (125-250)	9.3	8	1.3	1.62
Feldspar (63-250)	19.1	8	11.1	2.39

4.2.3. Research Methodology for Task 3– Laboratory Experiments. The final task for this research is near wellbore fracture experiments which are accomplished by using the designed triaxial pressure cell at Missouri S&T. The main objectives for conducting experiments is to support finite-element modeling results. The detailed objectives are:

i. Observe fracture breakdown and propagation pressure for water-based muds
ii. Observe fracture reopening pressure and study the strengthening effect using water-based muds
iii. Compare wellbore breakdown pressure and fracture initiation time from numerical models with laboratory experiments

Sandstone and dolomite core samples were collected from nearby quarries in the Missouri. These rocks were the most common and abundant rocks in Missouri which are also good analogous to hydrocarbon bearing rocks. Figure 4.27 shows typical rock blocks collected which have average dimensions of one foot in length, height and width.

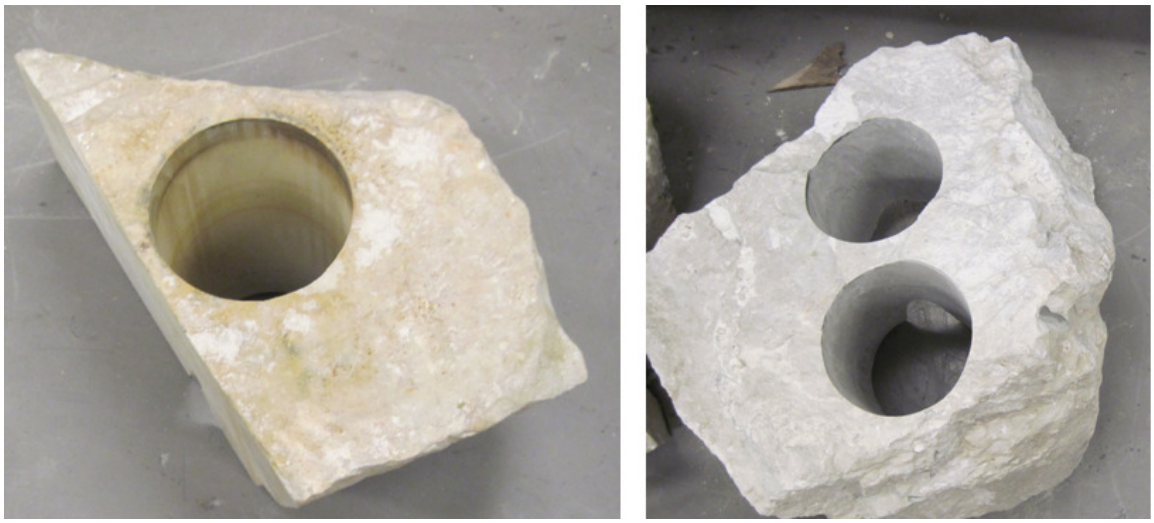

Figure 4.27. Dolomite and sandstone rock blocks collected from quarries (Right-Dolomite Left- Sandstone)

Workflow for the lab experiments includes preparation of 5.7 inches diameter and varying length from 8 to 12 inches core samples and testing them in a fracturing cell apparatus. The following detailed steps are followed for conducting the experiments:

Core Preparation

a) Pick up rock blocks from quarries
b) Drill out cores in Missouri S&T core lab
c) Cut and square core ends at the Missouri S&T Rock Mechanics Center
d) Drill out 0.5 inch wellbore in prepared core samples
e) Cement top and bottom caps
f) Vacuum and saturate cores

Fracturing tests

a) Place the core in the fracture machine
b) Connect pressure lines and spacers
c) Apply loads (overburden and confining)
d) Fill up accumulator with drilling fluid
e) Fill up wellbore with drilling fluid
f) Build up injection pressure and run the experiment

Core drilling was done at Missouri S&T core lab located in McNutt Hall. Then, cores were carried to Missouri S&T Rock Mechanics Center for ends squaring and smoothing. Details of the process will be explained by Liberman, 2012. After the cores were squared and smoothed, a 0.5 inch wellbore was drilled in core samples for injecting drilling fluids. After drilling out the wellbore, top and bottom caps with two inch casings were cemented to seal leakage path at top and bottom of the cores. Core samples were then vacuumed and saturated before testing. Figure 4.28 shows a dolomite core sample when the top cap is cemented.

After core preparation was finalized, core fracture experiments were conducted at the Drilling Fluids Lab located in McNutt Hall at Missouri S&T (Figure 4.29). The fracturing cell apparatus was specifically designed to conduct wellbore strengthening experiments.

The pressure ratings for confining and injection pressures are 2000 and 4500 Psi, respectively.

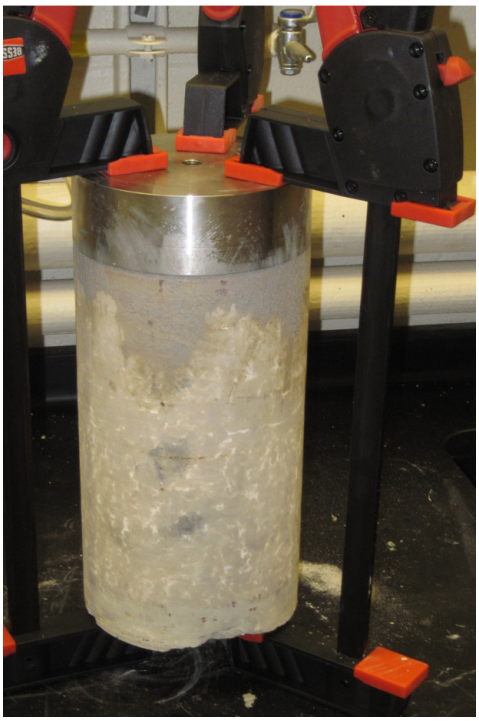

Figure 4.28. Dolomite core sample with top cap cemented

Figure 4.30 illustrates a schematic of the fracturing cell apparatus. Two injecting pumps are used to apply confining and injection pressure. One hand pump is used for building overburden stress on the cell top. All the data are recorded and plotted using LabView software. An accumulator unit also is used for injecting and circulating drilling fluids into the core samples. Using spacers inside the cell also helps to adjust different core lengths. These spacers are normally placed on the top injection cap.

Next, the core sample was saturated and placed in the cell where confining and overburden pressures applied before injection starts. The following step was to build up

injection pressure until the breakdown pressure is observed and continued to propagate the induced fractures. Injection pressures were monitored by connecting the pumps to a computer system during tests.

Figure 4.29. Fracturing cell apparatus fully designed and manufactured at Missouri S&T

Finally, when the fracturing test was completed, the fractured core sample was broken down to observe the fracture shape. Using big core size (6”) allows for longer fractures before reaching cell boundaries. This helps to study fracture propagation and sealing mechanisms both at fracture tip and mouth.

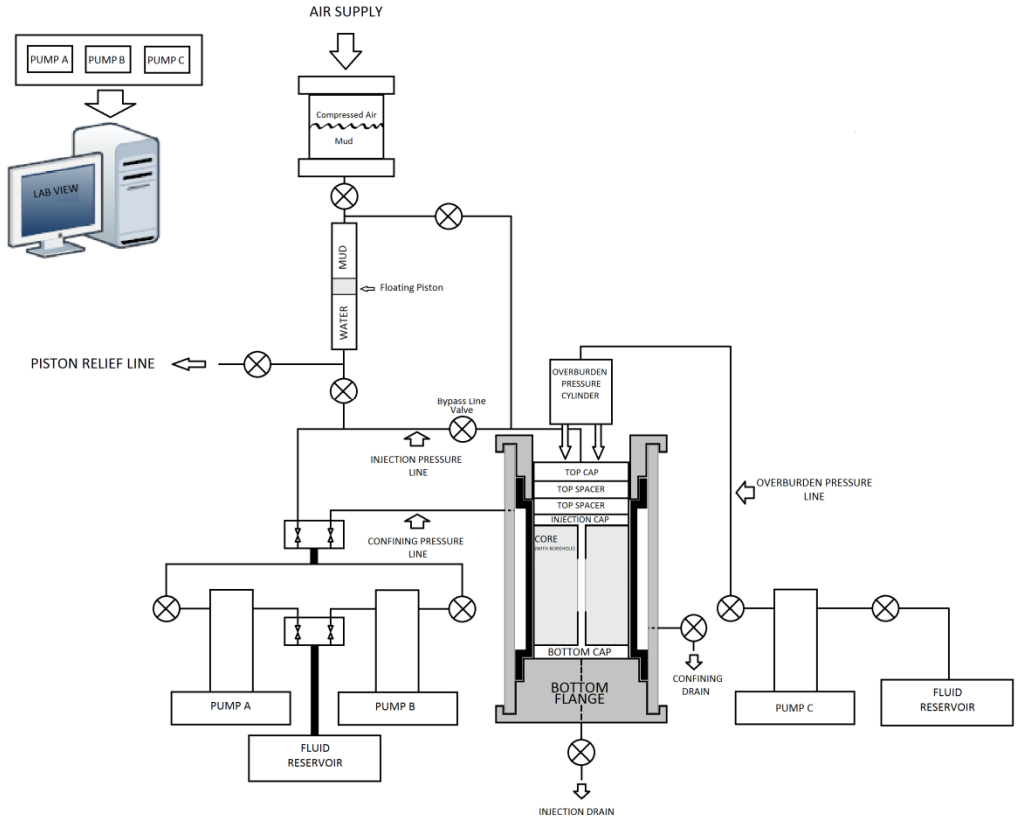

Figure 4.30. A schematic of fracturing cell designed at Missouri S&T

4.3. SUMMARY

In this section, the methodology for numerical modeling, analytical models and laboratory experiments were explained. The detailed method for initiating and propagating near wellbore fractures by finite-element models was also described.

Governing equations presented in this section includes the equations for fluid flow into porous media, permeability and poro-elastic terms. Identifying the physical process for the finite-element model is a very critical step, including all the details of discontinuities, initial and boundary conditions, material model and results verifications.

Input data used for this dissertation were obtained from combinations of sources; data published in related publications and data obtained from laboratory experiments conducted at Missouri S&T.

Three dimensional meshes built for this study were verified by the Kirsch analytical solution for accuracy. All the simulations were conducted in poro-elastic conditions where pore pressure elements were used in the models. Post-processing of the results were done in a Matlab code since the results obtained from the solver had to be converted from Cartesian coordinate to Cylindrical coordinate.

Three analytical solutions were reviewed in this section for predicting fracture propagation pressures. One of these solutions will be used for calculating the fracture gradient in the field case studies presented in the next section.

Laboratory experiments include preparation of 6 inch diameter core samples from dolomite and sandstone rock blocks collected from nearby quarries (Lieberman, 2011). The main goals of these tests are to verify some of the numerical simulations results, and also to study the strengthening effect of different drilling fluids system.

5. RESULTS

This section presents results obtained from numerical simulations, analytical models, field case studies and laboratory experiments. The numerical simulations cover both fracture geometry predictions and parametric study results and simulations of fracture initiation, propagation and sealing to test the wellbore strengthening hypothesis caused by increased wellbore hoop stresses. After presenting the numerical simulations results, field case studies from different oil producing basins with a narrow pore-fracture window and severe lost circulation problems were investigated. Finite-element models were used to analyze fracture gradient improvements through fracture sealing. The same field cases were also analyzed by Abe et al., which was presented in Section 4.2.2.1. This solution was used to test the second hypothesis of wellbore strengthening caused by fracture sealing and the effect of non-invaded zone on the fracture propagation pressure. Finally, in this section, results from fracture experiments will be presented and compared with numerical simulations.

5.1. FINITE-ELEMENT APPROACH

As mentioned in the previous section, cohesive elements are used for modeling fractures in this study. One key feature of these elements and the numerical solver is to observe the fracture opening in each element at any step of the fracture propagation. This will help in predicting the final fracture volume and length in order to design LCM pills.

A three-dimensional mesh was built and is illustrated in Figure 5.1. The input data for the model is based on Berea sandstone properties which were also been used in the DEA-13 fracture experiments (Morita et al., 1990, Morita et al., 1996, and Onya, 1994).

Table 5.1 shows the DEA-13 input data used in this study. This work has extended the DEA-13 experiment studies by modeling several scenarios with varying rock and filter cake permeabilities.

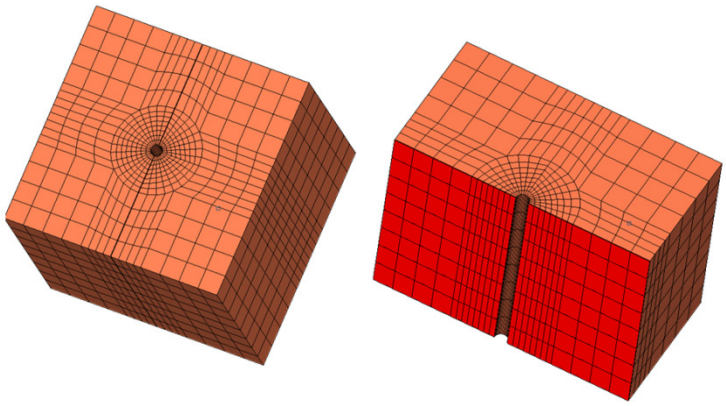

Figure 5.1. Three-dimensional mesh used for simulations (left) - Cohesive elements shown by red color (right)

Table 5.1. DEA-13 fracturing tests input data for Berea sandstone rock

Model Dimensions (inch)	30*30*30
Hole Size (inch)	1.5
Overburden stress (Psi)	3000
Max Horizontal Stress (Psi)	2200
Min Horizontal Stress (Psi)	1800
Young Modulus (MMPsi)	1.5
Poisson's Ratio	0.2
Rock Permeability (Darcy)	0.1
Fracture Toughness (Psi*inch^(0.5))	900

The initial and boundary conditions and loading steps were explained in the previous section.

5.1.1. Simulations Results. With the mechanical properties defined for both the rock and the cohesive layer, a fracture was initiated and propagated in the maximum horizontal stress direction equal to the direction of the cohesive layer. Figure 5.2 illustrates the crack growth around the wellbore, and Figure 5.3 shows the stress profile in the y-axis direction (the model shown in Figure 5.3 is oriented 90 degrees to the model in Figure 5.2). Fracture initiation created a tensile state of stress in the fracture plane. Fluid injection into the fracture and the initiation of fracture propagation increases the pore pressure in the flowing nodes and changes stress distribution. In the first set of simulations, permeability was increased from 100 milli-Darcy (mD) to 450 (mD). The run results show that crack growth has a strong relationship with permeability. Among the simulations in low-permeable to high-permeable rocks, the maximum difference in the fracture opening was 10 microns.

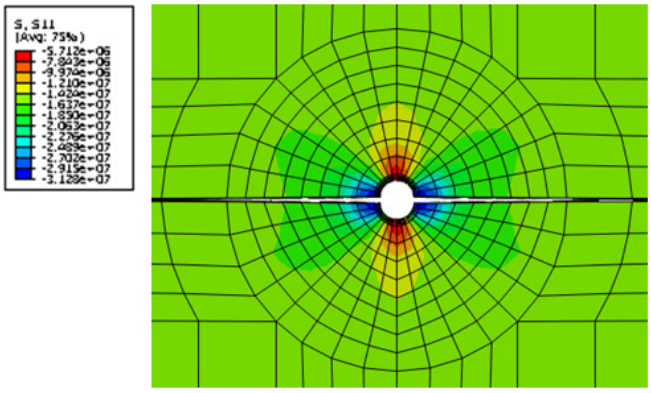

Figure 5.2. Crack forming parallel to the maximum horizontal stress direction

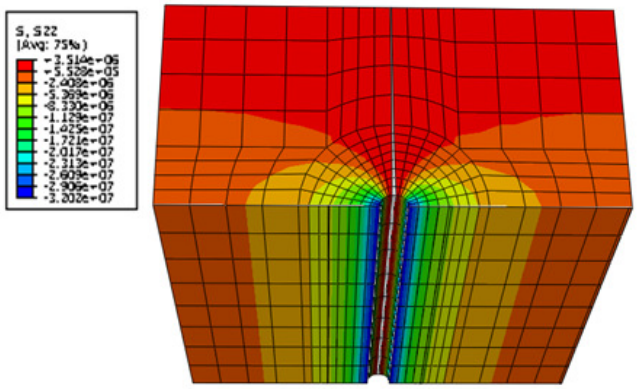

Figure 5.3. Half of the actual run model is cut off to show the stresses around the wellbore and the tensile stress in the fracture plane (parallel to the maximum horizontal stress)

Figure 5.4 shows the crack openings for various permeabilities; it indicates that the crack opening widens more over the time of injection which also will represent fracture length. Figure 5.5 illustrates crack growth as a function of time for several scenarios. As the permeability increased, the fracture length increased; results confirm length increase of 25 cm when the permeability was increased by 350 mD. The method for finding fracture length is based upon whether fracture initiation occurred in a cohesive element which means the fracture initiation criteria should have been satisfied for that element. The damage ratio during fracture propagation gradually evolves from a minimum value of 0 to 1. Table 5.2 shows the maximum damage ratio for each simulation as expected cracks propagate most in high-permeable rocks.

As shown in the table, the maximum damage ratio of 0.891 is reported for simulation case with 450 mD permeability. The lowest ratio of 0.722 is reported for simulation case with 100 mD permeability. It can be concluded from the table, as permeability of the rock increases, the damage ratio increases as well. Higher permeability of the rock allows for more leak off through the fracture face.

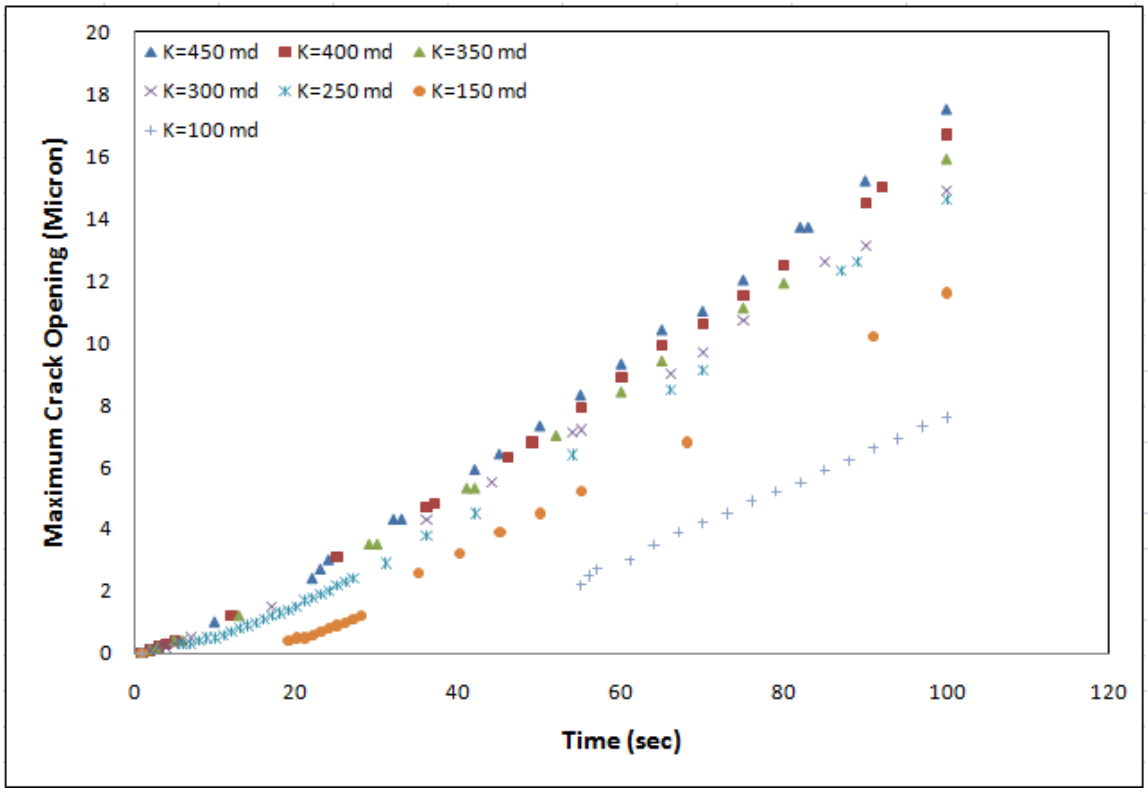

Figure 5.4. Crack opening versus time for rock with different permeability

Based on the crack width in each cohesive element, a fracture geometry model was built for the final crack formed around the wellbore. As shown in Figure 5.6, the terms w_c to w_m were assigned to crack openings from narrowest to widest; it must be noticed that Figure 5.4 is roughly showing the fracture opening through its length and the illustrated fracture tip is not representing the actual shape of the tip. Table 5.3 summarizes the details of crack geometry for each scenario. It was interesting to observe that the width near the tip of the fracture has changed from 0.1 micron to 1 micron for various scenarios. This also has been plotted in Figure 5.7. As illustrated in Figure 5.7, for different permeabilities, the fracture opening differs more at the fracture mouth than at the fracture tip. These observations distinguish these fractures from traditional wing shaped fractures calculated through traditional 2D hydraulic fracturing models.

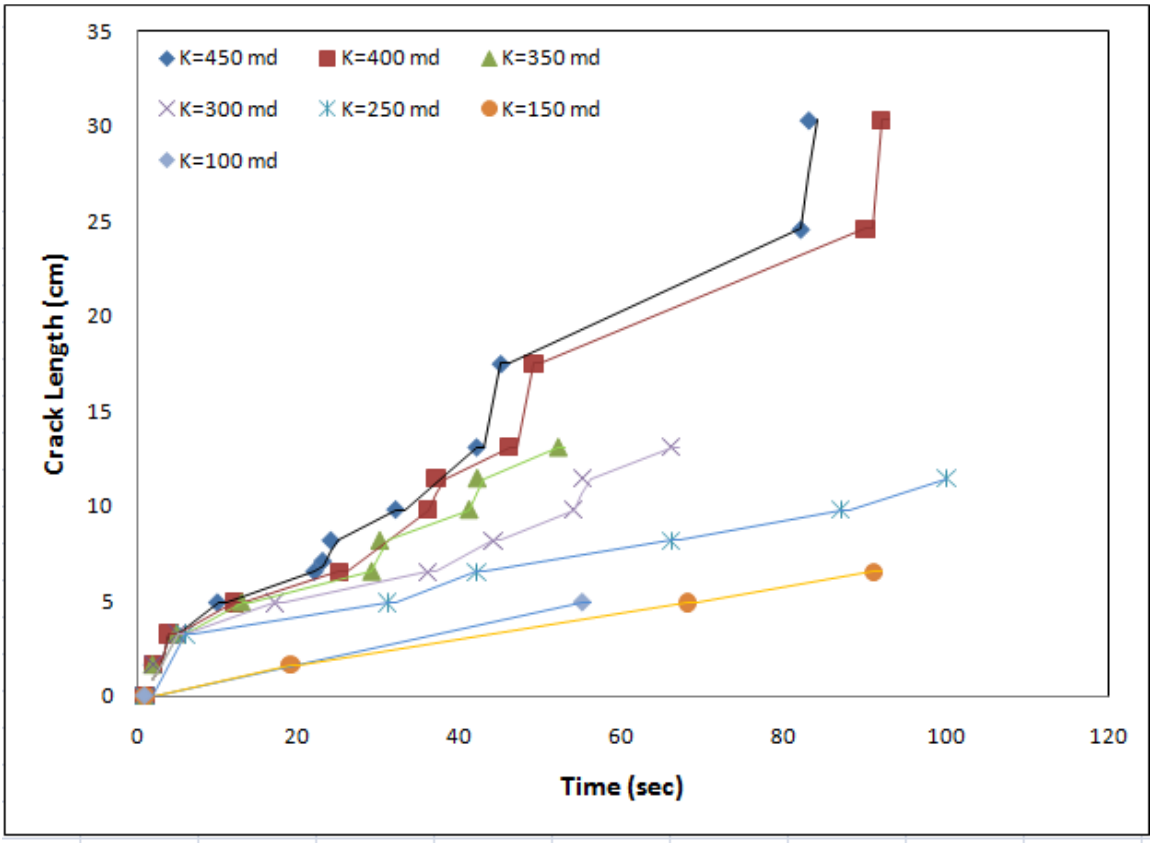

Figure 5.5. Crack length versus time for rocks with different permeability

Table 5.2. Maximum damage ratio as a function of permeability

K (mD)	**SDEG**
100	0.722
150	0.749
250	0.843
300	0.871
350	0.879
400	0.886
450	0.891

Based on the widths of the cohesive elements, the fracture volume can be predicted. More significantly, these results confirm that the size of the propping particles is important for effective crack sealing. Figure 5.8 shows two cracks with mouths of different widths. A change in particle size appears to be necessary to seal the crack mouth in each model. However, it may be feasible to use the same size particles for sealing the crack tips in both cases. This is a debating issue when different techniques of wellbore strengthening are used. For instance, in the Stress Cage technique the main target is to seal the fracture close to its mouth. In this case, formation permeability must be considered when designing sealing materials.

Table 5.3 shows that fracture geometry formed in the formation must be considered when calculating material sizes if the goal is to seal off the mouth in wellbore strengthening operations. There will be significant changes in materials volume especially when long fractures are induced in the wellbore.

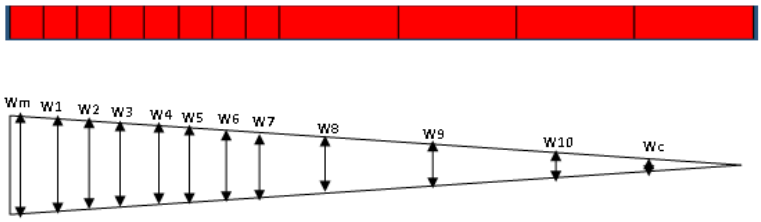

Figure 5.6. Crack geometry model in cohesive layer (Left side: cohesive elements close to wellbore, right side: cohesive elements at the end of the model)

Table 5.3. Details of crack geometry changing with rock permeability

Crack Opening (Micron)	K1, 100 mD	K2, 150 mD	K3, 250 mD	K4, 300 mD	K5, 350 mD	K6, 400 mD	K7, 450 mD
Wm	7.6	11.6	14.6	14.9	15.9	16.7	17.5
W1	2.5	5.5	7.6	7.9	8.5	9.2	9.7
W2	0.2	2.4	3.9	4	4.4	4.8	5.2
W3	0	1	2.7	3.1	3.5	3.8	4.1
W4	0	0	1.6	2.5	2.9	3.2	3.5
W5	0	0	0.8	2.4	2.8	3.1	3.3
W6	0	0	0.1	2.1	2.5	2.8	3.1
W7	0	0	0	2	2.4	2.6	2.9
W8	0	0	0	0.1	1.8	2.1	2.3
W9	0	0	0	0	0.2	0.3	0.4
W10	0	0	0	0	0	0	0.1
Wc	0	0	0	0	0	0	0

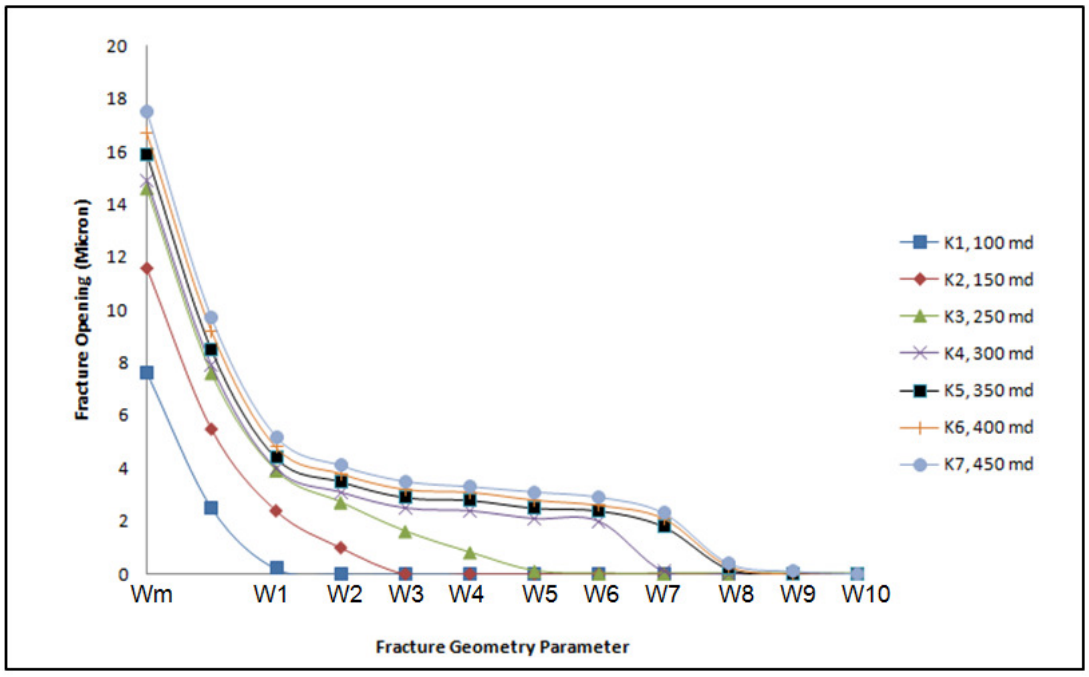

Figure 5.7. Comparison of fracture geometry in all models

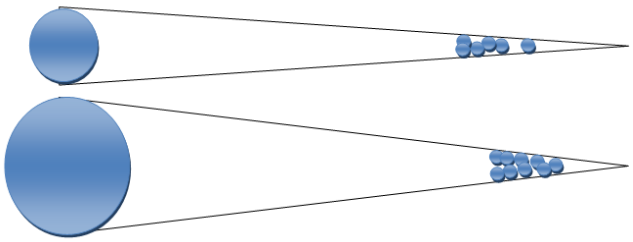

Figure 5.8. Particle size for sealing crack tip and mouth in two different cases

5.1.2. Parametric-studies of Hydraulic Fractures. The objective of this section is to present results of parametric studies in hydraulic fracturing to identify the most important parameters in determining fracture shape. This will be critical for wellbore strengthening applications when designing pills and LCM materials for the drilling fluid system. Proper design of sealing materials will prevent further fracture extension and may help to increase fracture propagation pressure. This is especially essential when conducting wellbore strengthening in unconsolidated formations where traditional hydraulic fracturing models cannot accurately predict fracture properties (Fett et al., 2008). Further, availability of input data is sometimes limited when conducting field operations. For this reason, knowing the weight of different inputs will lead in better design of the process and interpretation.

The parameters studied in this section are rock properties such as Young's modulus, Poisson's ratio, permeability, fracture toughness, and injecting fluid properties such as viscosity and injection rate carried out for both Newtonian and Power law fluid models.

Finally, the effect of all parameters has been illustrated in a normalized chart which shows weight of each parameter on fracture width which is a critical parameter in wellbore strengthening. These results can be used as a further guideline for designing wellbore strengthening pills and/or stimulations operations.

5.1.2.1. Model geometry. The three-dimensional mesh is illustrated in Figure 5.9. A wellbore with 0.22 meter (8.5 inch) diameter is modeled where total height and diameter of the circular mesh are 30 (98 ft) and 300 (984 ft) meter respectively. Figure 5.9 shows the three-dimensional mesh built for this section using approximately 5500 poro-elastic quadratic elements. Because the objective here is to run parametric studies, using small scale models causes convergence issues especially when the fractures reach the outer boundary of the model.

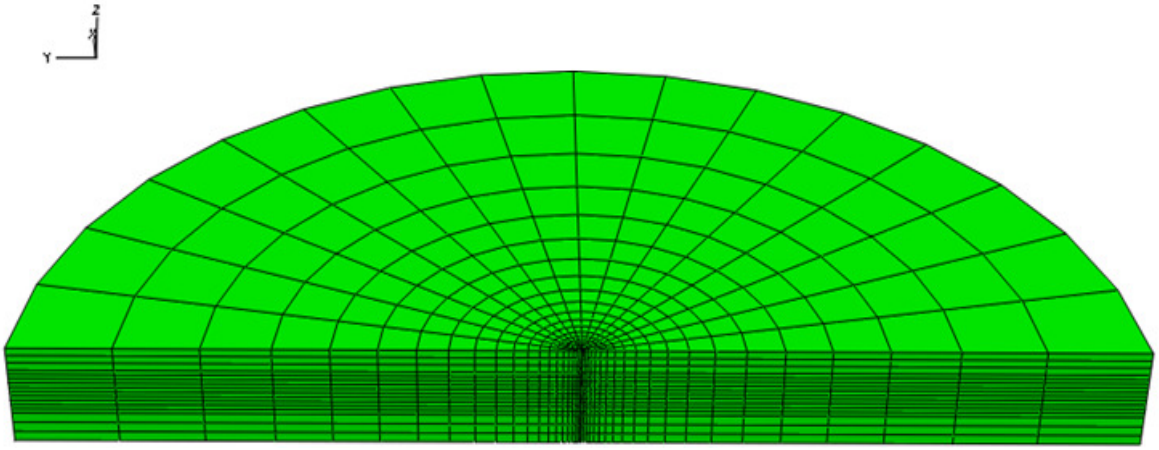

Figure 5.9. Three dimensional mesh created with 3D Hyper Mesh, pore fluid elements were used in entire model for fluid flow simulations

5.1.2.2. Fracture propagation in high permeable rocks. Table 5.4 shows the input data used for simulations. In the first run of simulations, base case properties were used, then parametric studies were carried out with keeping the permeability constant and changing other properties such as Young's modulus, Poisson's ratio, drilling fluid viscosity, fracture toughness and injection ratio. Later, rock permeability was lowered and similar simulations were conducted.

With the mechanical properties defined for both the rock and the cohesive layer, a fracture was initiated and propagated in the maximum horizontal stress direction, which is the direction of the cohesive layer. Simulation results when injected into highly permeable rock for 800 seconds is shown in Figure 5.10 which illustrates the extension of the fracture at the end of this step. Figure 5.10 also indicates fracture propagated out of the near wellbore and into far field. Figure 5.11 and Figure 5.12 show the fracture extension at the end of 20 and 100 Sec, respectively. As the Figures indicate, propagated fractures are much wider at the fracture mouth and narrow down more smoothly at the fracture tip. This is consistent with what was observed in Section 5.1.1.1. In addition, using cohesive elements enabled the prediction of the fracture opening at each element which can be used for predicting the final volume of the fracture. Maximum fracture

width at the end of 20 sec, 100 sec and 800 sec are 5.18 mm (0.2 inch), 5.88 mm (0.23 inch) and 6.13 mm (0.24 inch) respectively. Figure 5.13 illustrates cohesive zone openings at the end of 100 seconds.

Table 5.4. Base input data used in simulation

Hole Size (inch)	8.5 inch
Young Modulus (MMPsi)	1.5
Poisson's Ratio	0.225
Rock Permeability (Darcy)	0.1
Fracture Toughness (Psi*inch^(0.5))	1
Injecting fluid consistency index (K)	0.15
Power law coefficient (n)	0.86

After conducting the base case simulations, rock Young's modulus was decreased to 6 GPa (0.9 MMPsi) in the simulations to see the effect of changing rock stiffness. More than 2 mm (0.08 inch) increase in the maximum fracture opening was observed when rock stiffness changed. Figure 5.14 compares the fracture width profile in both higher and lower Young's modulus. Fracture opening through its length was also increased when Young's modulus decreased in the model (Figure 5.15). One important observation from Figure 5.14 is that maximum fracture openings widen more at early times of propagation when fracture is not stable and then grow more smoothly until the end of fracture propagation. This is also evident when decreasing or increasing rock's stiffness where Young's modulus affects the fracture opening significantly at the start of fracture propagation. This starts within a few seconds of fracture propagation as illustrated in Figure 5.14. In the next set of simulations, Poisson's ratio was increased from 0.225 to 0.3. Figure 5.16 compares the maximum fracture width in both cases. Figure 5.16 alos indicates that increasing Poisson's ratio will decrease the maximum

fracture opening which is also evident from the analytical hydraulic fracturing equations in Section 2. Similar trends are also achieved during hydraulic fracturing field operations where fracture width decreases as formation Poisson's ratio increases (Nierdoe, 1985). Figure 5.17 shows the fracture opening changes by its length for both cases. Comparing Figure 5.14 to Figure 5.16 indicates strong effect of Young's modulus on the fracture propagation behavior as where Poisson's ratio slightly affects fracture propagation. Initial implication from these results is the fracture propagation behavior in multi-layered formations where rock mechanical properties change from one layer to another. In addition, having uncertainty in Young's modulus values can significantly affect the calculated fracture geometry.

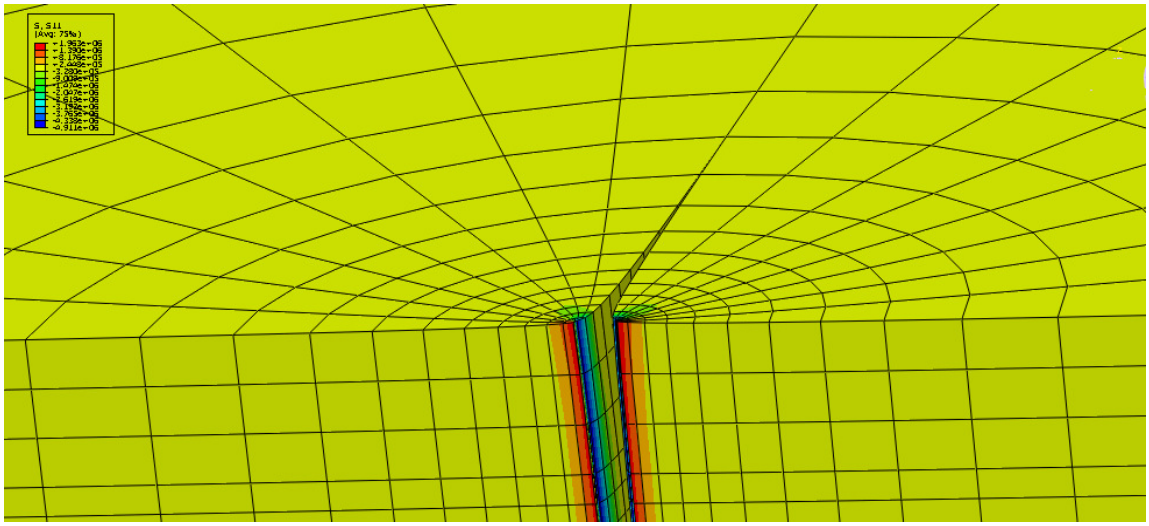

Figure 5.10. Sketch showing fracture propagation and geometry after 800 Sec
(Deformation magnified 300 times)

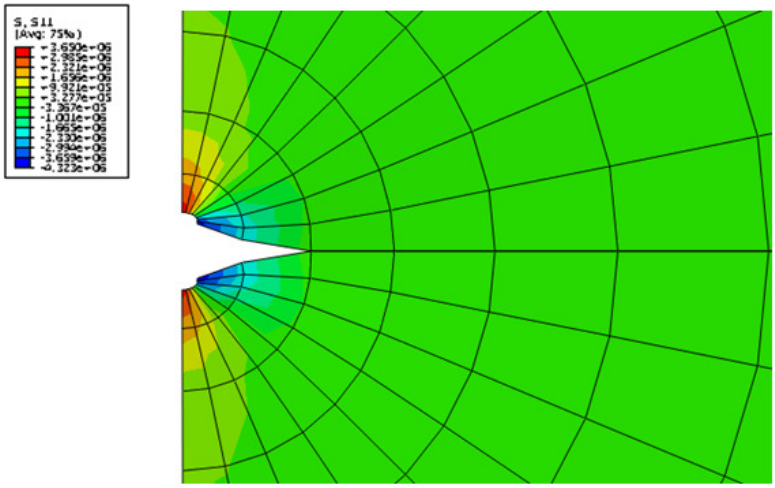

Figure 5.11. Fracture propagation after 20 Sec (Deformation magnified 300 times)

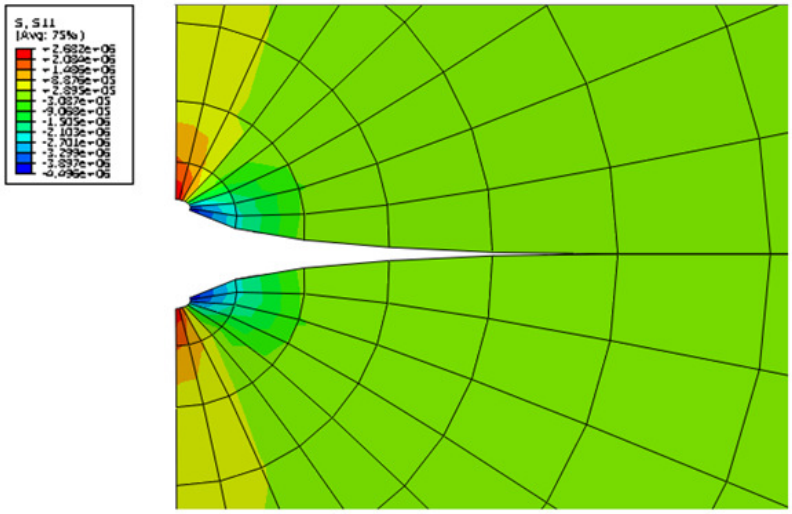

Figure 5.12. Fracture propagation after 100 Sec (Deformation magnified 300 times)

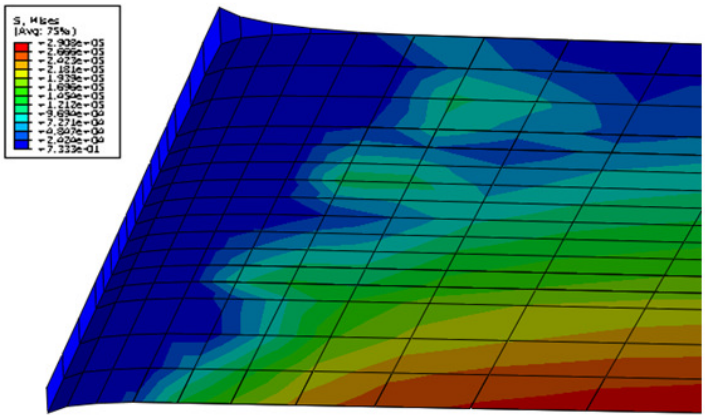

Figure 5.13. Cohesive elements (wedge) opening used to predict fracture geometry

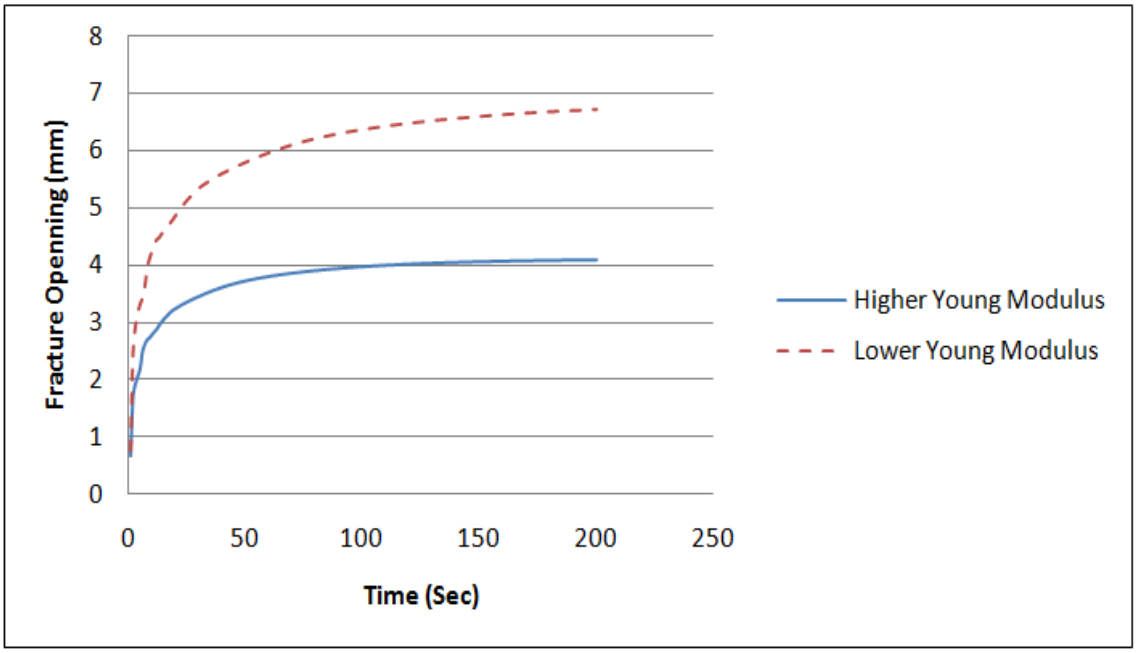

Figure 5.14. Effect of Young's modulus changes on maximum fracture width (Permeability=100 mD)

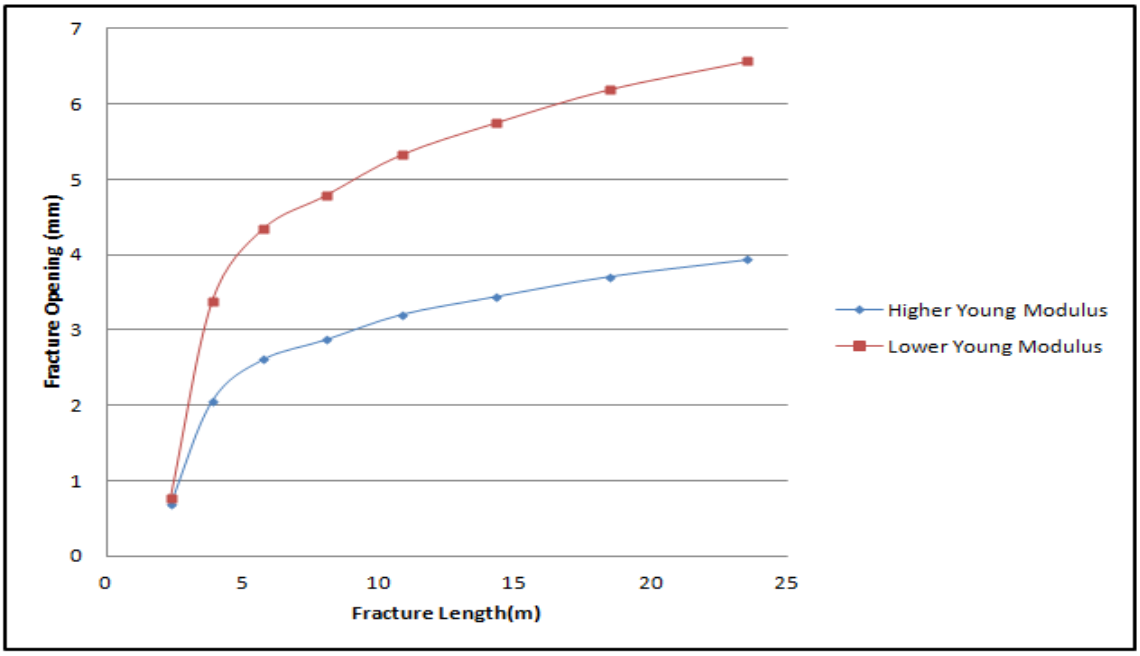

Figure 5.15. Effect of Young's modulus changes on maximum fracture opening through its fracture length

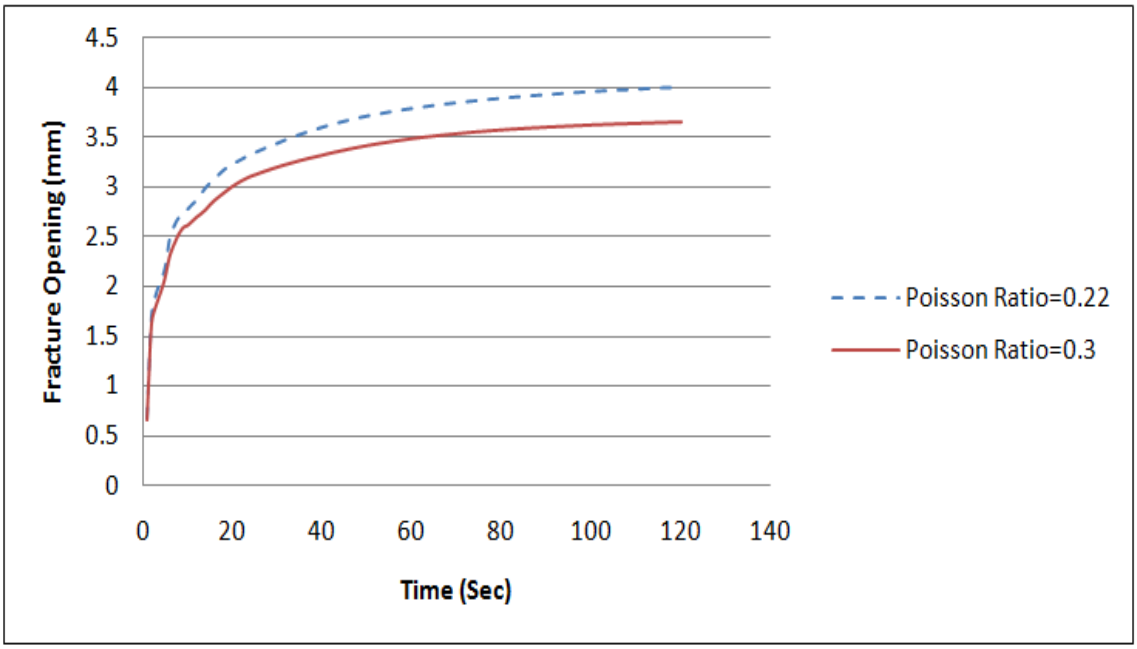

Figure 5.16. Effect of Poisson's ratio changes on maximum fracture opening (Permeability=100 mD)

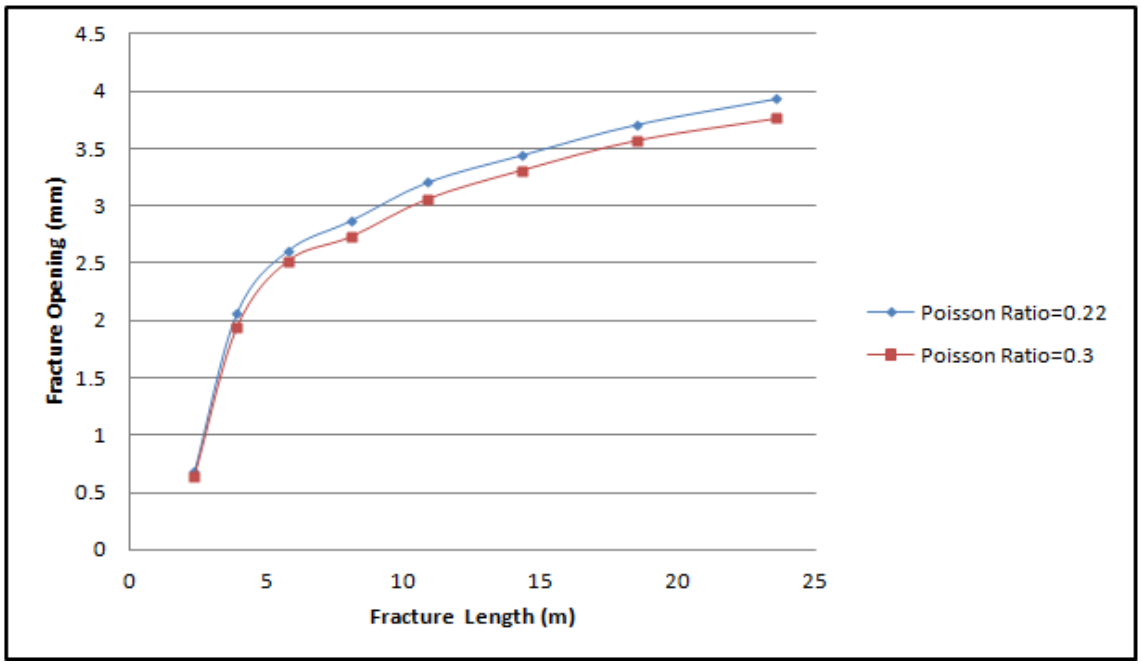

Figure 5.17. Effect of Poisson's ratio changes on fracture opening through its length

5.1.2.3 Fracture propagation in low permeable rocks. To study the effect low permeability had on the parametric study simulations of 1 mD and 0.001 mD rock samples were carried out. Similar results to the high permeable sample were observed when Young's modulus and Poisson's ratio were decreased in the simulation's run. Figure 5.18 shows the maximum fracture openings for the case of changing Young's modulus to 6 GPa (0.9 MMPsi), and Figure 5.19 shows that fracture opening profile when Poisson's ratio increased ($\nu = 0.3$). Figure 5.19 also shows the effect of Poisson's ratio more at the early time of fracturing simulations; but later on, the fracture width becomes similar in both cases. This indicates that the extent at which Poisson' ratio affects fracture width is less in low permeable rocks. It can be attributed to lower leak off from inside the fracture to the formation in low permeability formations; however, more simulations and validation with experiments are required to confirm this.

Fracture openings for all the samples with different permeabilities(100mD, 1mD and 0.001mD) are illustrated in Figure 5.20. This implies that formation permeability is

an important factor affecting the fracture width. This fact was not been reflected in Griffith's equation (Valco and Economides, 1995) for hydraulic fracturing since these operations are mostly executed in very low permeable rocks. This finding is very important for this study because wellbore strengthening applications are applied both for low and high permeable formations and sealing particles are designed to effectively bridge the induced fracture. Results of this study confirm that rock permeability needs to be considered in wellbore strengthening applications, since using this approach for different permeability rocks will form different fracture geometries.

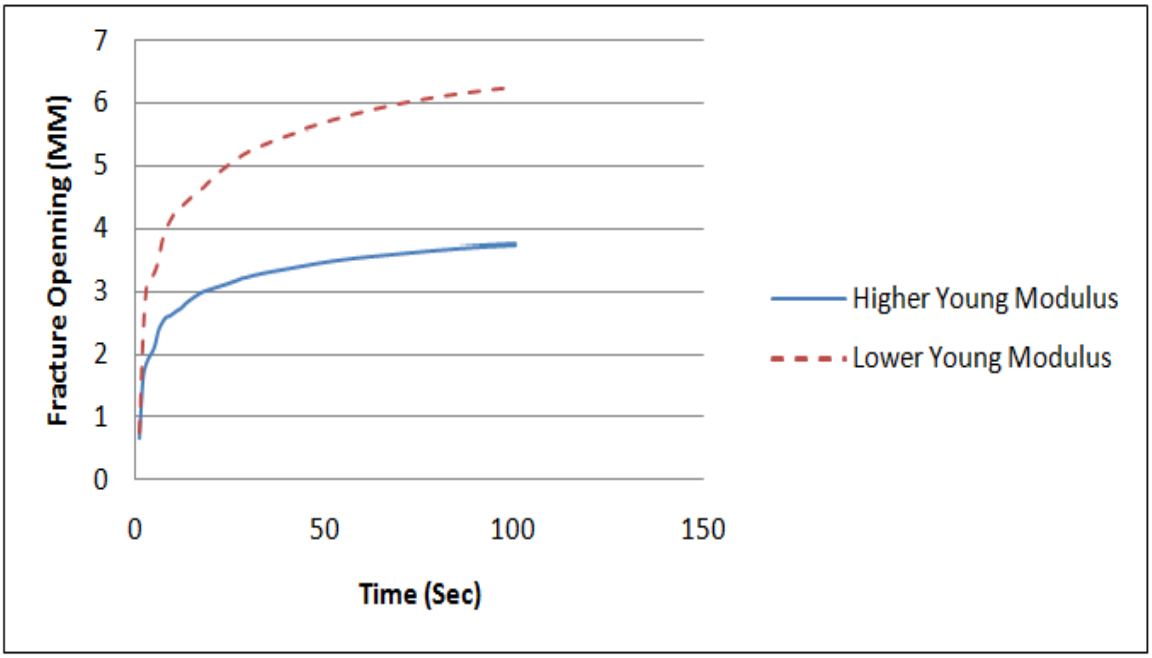

Figure 5.18. Effect of Young's modulus changes on maximum fracture opening (Permeability=1mD)

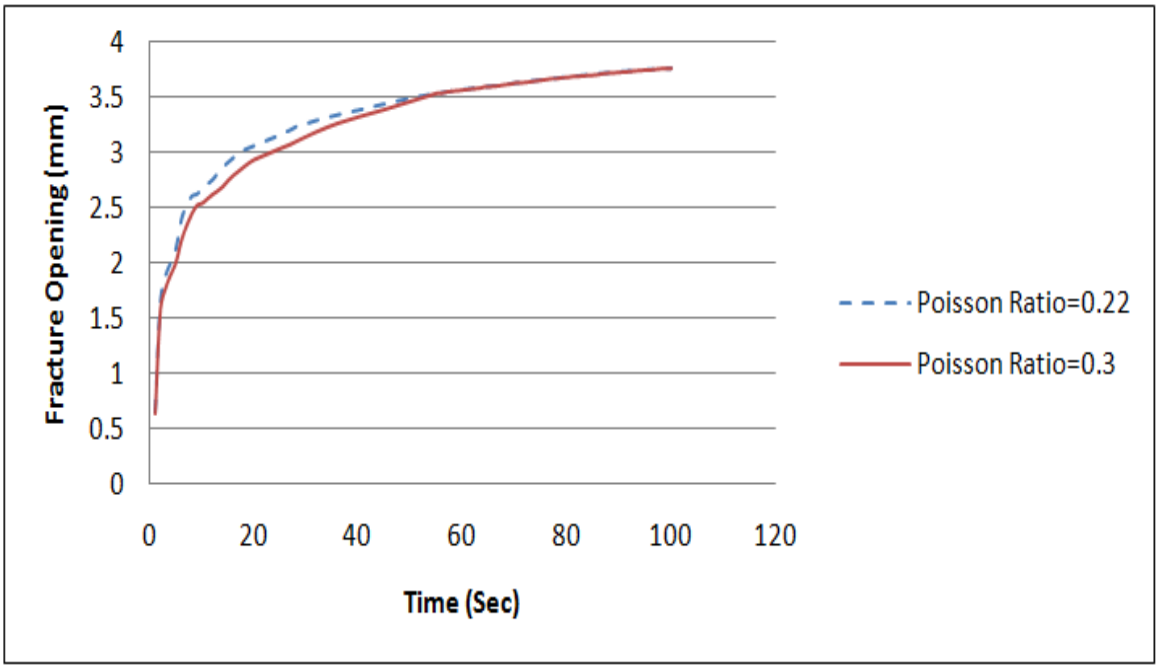

Figure 5.19. Effect of Poisson's ratio changes on maximum fracture opening (Permeability=1mD)

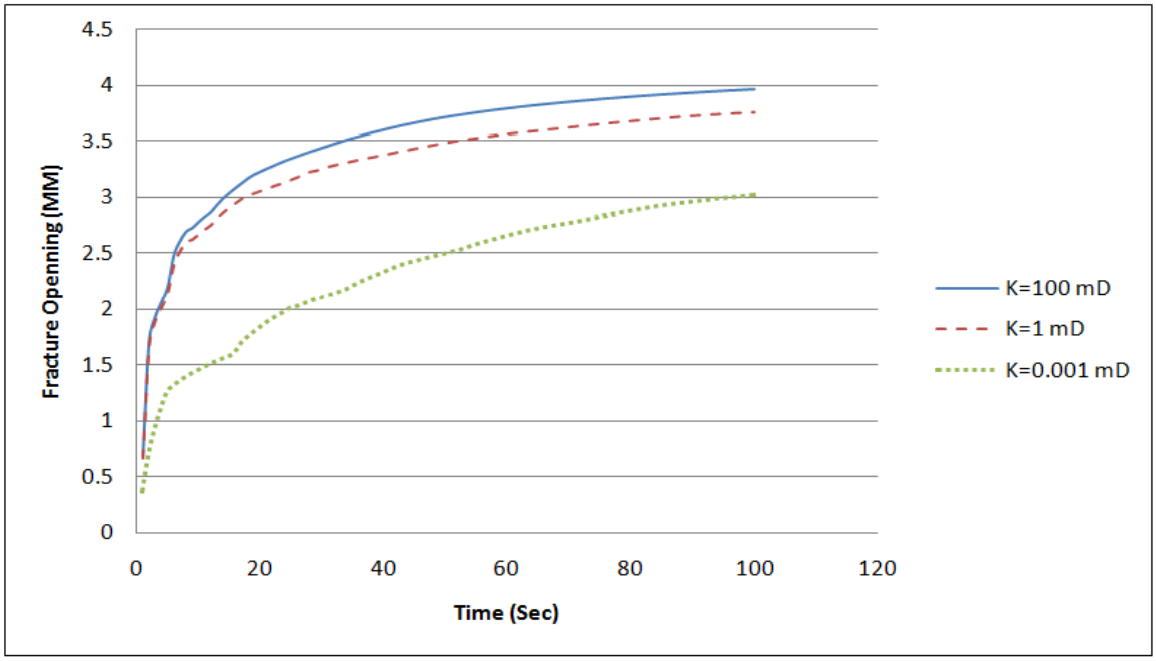

Figure 5.20. Effect of permeability changes on maximum fracture width

5.1.2.4 Effect of viscosity with Newtonian model. In this set of simulations, a Newtonian rheological model was used. Different fluid viscosities from 1cp to 120 cp were used in both high and permeable rock samples. Figure 5.21 shows the effect of increasing viscosity in the permeable sample (100mD). Further, when fluid viscosity increased, fracture width decreased at early times (up to 100 Sec) but later (250 Sec), it catches up. High fluctuations in the fracture opening were also confirmed in early times due to high fluid exchange until an impermeable cake forms. Similar observations have been reported in the literature (Bunger et al., 2005); the effect of viscosity was significant in the beginning which resulted in strong coupling between the fluid and solid mechanics. This causes the existence of a significant lag zone when injecting in permeable rocks. Published results of laboratory scale hydraulic fracturing experiments (van Dam et al., 1998) revealed that up to 0.001 meter fluid lag length is observed with a fracture radius of 0.1 meter. Fluid leak-off in permeable formations will change the propagating regime at the tip of the fracture where a pressure-dropped zone is observed.

Figures 5.22 and 5.23 illustrate the effect of increasing viscosity on the 1 and 0.001 mD rock samples, respectively. As expected, increasing fluid viscosity will increase the fracture width over time. Comparing results from low permeable samples (1 mD and 0.001 mD) to the high permeable ones (100 mD) indicates a strong effect of viscosity in the low permeable samples. This can be attributed to having higher energy which widens the fracture more when using high viscous fluids in low permeable rocks. This approach is used in hydraulic fracturing operations for opening the hydraulic fractures wider. These results indicate that no fluid lag region or very negligible one exists when fracturing in low permeable formations. This observation can also explain the difficulty of sealing fractures for wellbore strengthening applications in low permeable formations where no lag exists between fluid front and fracture tip.

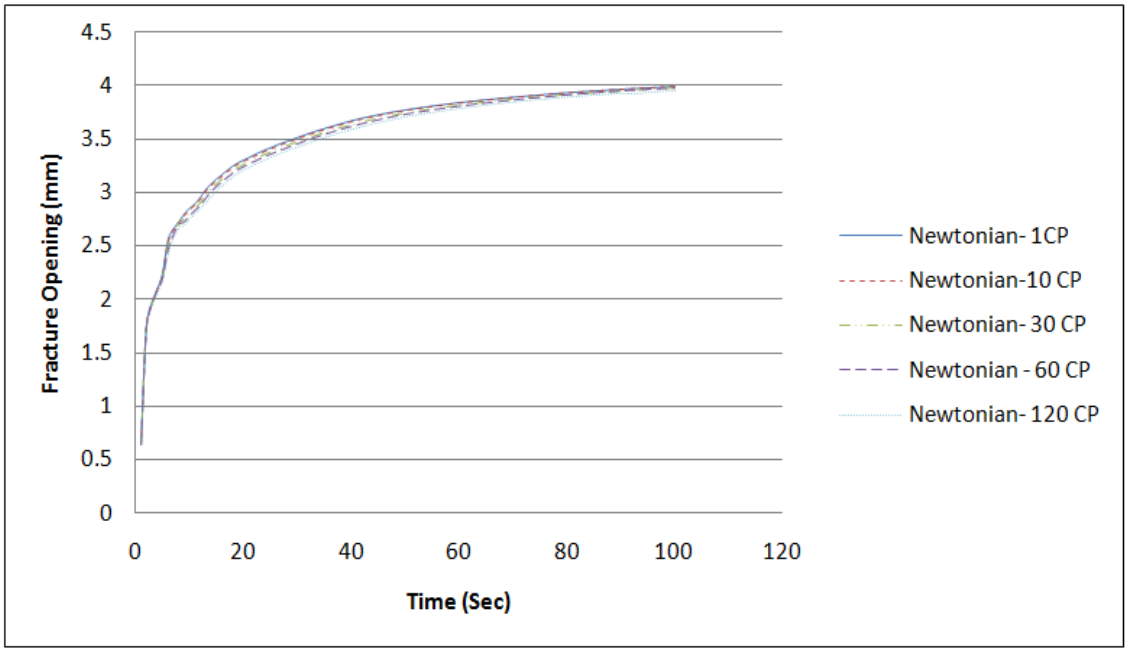

Figure 5.21. Effect of fluid viscosity changes on maximum fracture width (Permeability=100 mD)

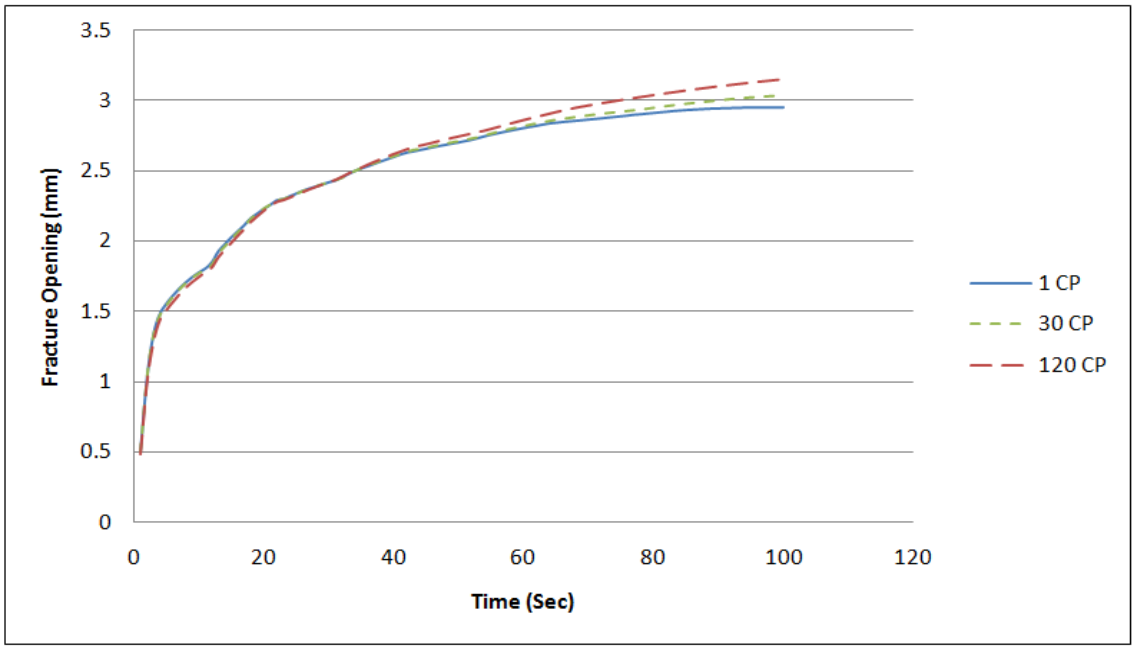

Figure 5.22. Effect of fluid viscosity changes on maximum fracture opening difference (Permeability=0.001 mD)

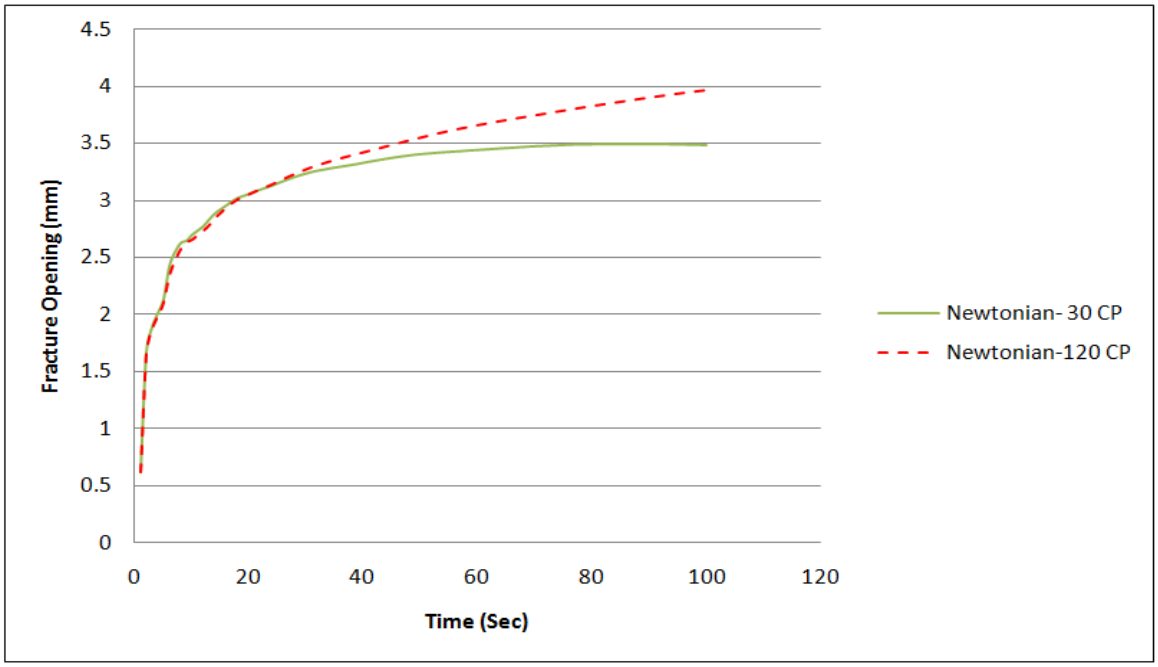

Figure 5.23. Effect of fluid viscosity changes on maximum fracture width (Permeability=1 mD)

5.1.2.5 Effect of injection rate. Injection rate is a controllable parameter in hydraulic fracturing operations. Some forms of analytical equations for hydraulic fracturing include the term of injection rate (where fluid within the crack will be in laminar, Perkins and Kern, 1961):

$$w = 0.38[\frac{Q\mu R}{E}]^{\frac{1}{4}} \tag{5.1}$$

According to the analytical equation, crack width is proportional to the fourth root of injection rate (Q). Similar observation was achieved from simulations where increasing injection rate increased the fracture width. Simulations show that increasing injection rate from 0.01 m^3/Sec to 0.08 m^3/Sec will increase the crack width up to 200 micron (0.008 inch). Figure 5.24 illustrates the fracture opening over time when injection rate was increased. Figure 5.24 also indicates the sensitivity of the fracture opening in the later injecting time where the fracture opening for both high and low injection rates are almost similar at early time.

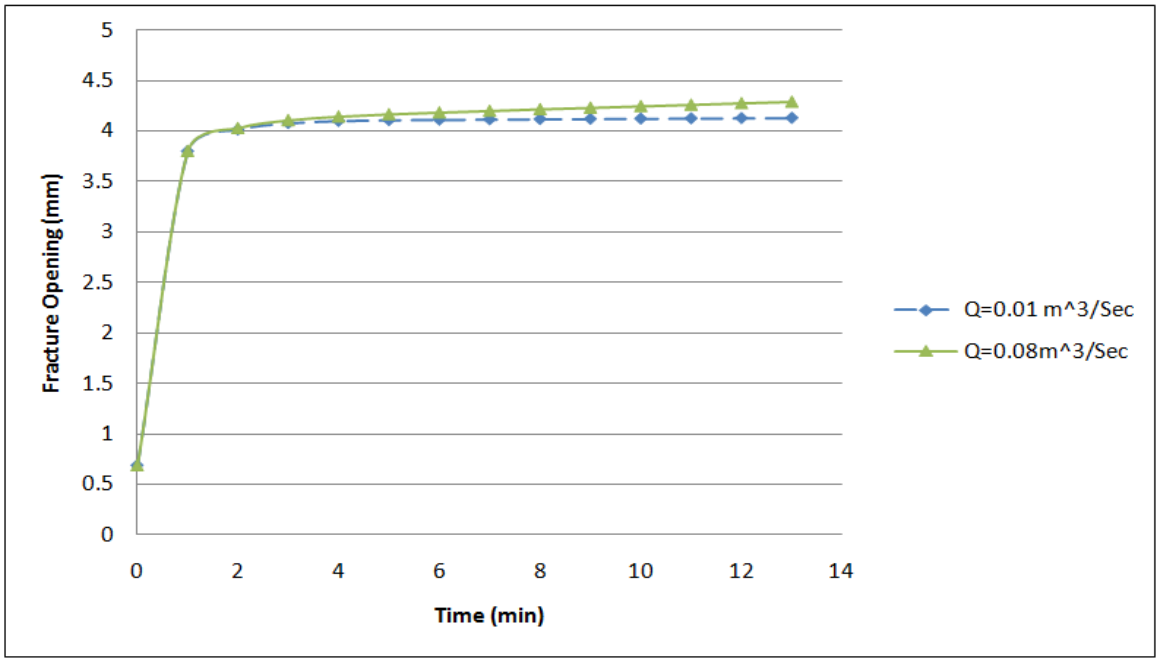

Figure 5.24. Effect of increasing injection rate on maximum fracture width (Permeability=100 mD)

Several simulations were carried out to identify the weight of all parameters on fracture width, based on changing only one parameter each time. Results were normalized and illustrated in Figure 5.25. It shows that changing the value for the rock Young's modulus has a significant effect on the fracture opening compared to other parameters. Changing the rock permeability from very small values in shales to higher values in sandstones will increase the fracture opening significantly. Poisson's ratio has a similar trend on the fracture opening as Young's modulus but with less overall effect. Slight changes were observed for increasing values for injection rate and fracture toughness of the rock compared to other parameters. Figure 5.25 helps to classify the affecting parameters into primary and secondary ones, where rock mechanical parameters are the primary factors.

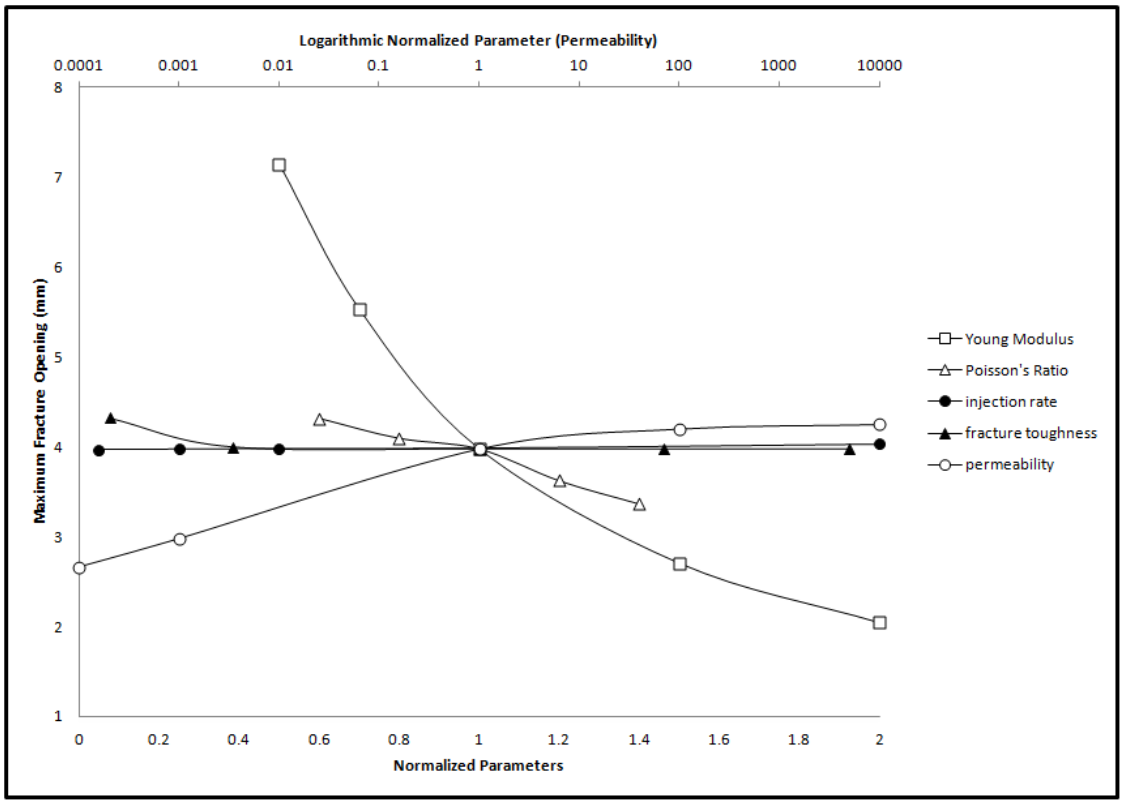

Figure 5.25. Effect of different parameters on maximum fracture opening based on normalized values

5.1.3. Fracture Geometry and Parametric Study Discussion. Knowing fracture geometry is an essential part of designing an effective wellbore strengthening pill. Arresting fractures early (shorter fracture length), from the time they start initiation is very critical in wellbore strengthening. However knowing fracture length is not as critical as fracture width (Wang et al., 2008). According to parametric studies conducted by Wang et al., 2008, fracture length has minor effects and only at the fracture location where stress anisotropy exists.

It is generally observed in hydraulic fracturing treatments, that higher rock permeabilities reduce cracks growth; because as the permeability of the rock increases, more fluids will dissipate from the fracture and this leaves less energy to pressurize the crack to grow further. However, according to the simulations, it was found that another

mechanism taking place which makes the higher permeability rocks to widen up more comparing to lower permeability rocks. State of effective stress around the fracture boundary is a key point in controlling the fracture width and growth; when there are more fluids leaking from the fracture, this makes the fracture face to be in higher mode of tensile strength according to Terzaghi's principle. This results in the existing fracture to widen up more.

This effect might on the other hand be reduced when higher injection rates are used or pumping time increased as the case would be in hydraulic fracturing operations. Since the point of interest in this study is the early time short fractures created during drilling, the objective is to arrest these fractures as quick as possible. These fractures might lead to massive loss circulations if not properly controlled.

As mentioned in Section 2, Stress Cage (SC), Fracture Closure Stress (FCS) and more recently Fracture Propagation Resistance (FPR) are the techniques used to elevate the fracturing pressure. Although particle size and strength have been the debating issues in these techniques, to date, no study has determined decisively the sealing effect of particles shape, geometry, and distribution. The fracture model presented here can predict the fracture geometry based on a pre-defined orientation. Contrary to the general belief that fracture width decreases uniformly from the mouth of the fracture to its tip, the results of the present study show that fractures are wider at the mouth, and they become narrow in a non-linear fashion along their length.

Fracture width data in Table 5.4 confirm that material shape may also be an important issue in sealing fractures. Maintaining bridge stability at the mouth should be harder than pushing bridges inside the crack, and this is the case reported in some Stress Cage operations (Alberty, 2004). As discussed by the results, formation permeability must be considered when using this technique. Other solutions may be speculated can be to design bridging materials based on sealing the tip of the fracture rather than keeping them at the mouth. This is similar to the practice used for the Fracture Closure Stress (FCS) technique.

Predicting fracture geometry is another result from the simulations that can help to calculate the necessary materials volume. For instance, normal practice in the Stress Cage technique is to calculate the volume of the fracture based on a triangular prism

shaped the height and width of the target aperture (Alberty, 2004). Then particle size distribution (PSD) is predicted based on the calculated fracture volume. The presented model confirms that this volume cannot represent the true volume of the induced fracture and it is necessary to estimate particle size distribution based on widths from aperture to the tip of the crack.

The practice in the Fracture Closure Stress (FCS) technique is different. Normally, the size of the materials is relatively unimportant and it is believed that "any pill will develop into an immobile mass if it can be made to lose its carrier fluid" (Dupriest, 2005). The research reported here demonstrates that if pills are not designed based on the size and shape of a fracture, they cannot effectively seal the fracture. In other words, there is always a risk that the solid materials in the wellbore strengthening pills are made too large to penetrate the induced fractures. In such cases, the pill will fail once drilling practice continues.

This work also conducted a parametric study to investigate the effect of rock properties such as Young's modulus, Poisson's ratio and permeability and different fluid properties including viscosity and injection rate on fracture propagation. Rock samples with permeabilities of 100 mD, 1mD and 0.001 mD were modeled in this study.

The simulations indicate that fracture opening is a strong function of Young's modulus and permeability. Simulations indicate that crack width is affected also by rock Poisson's ratio, where up to 400 micron decrease was observed in the fracture width when increasing Poisson's ratio to 0.3. For this reason, in executing the wellbore strengthening approach, rock stiffness should be considered as the primary parameter controlling fracture width.

Results of simulations studies conclude same trend as the analytical equations presented earlier. A recent study from the Daqing Oilfield in China also confirmed fracture opening increased when rock Young's modulus was reduced (Zhang, et al., 2010). Their results also indicate that fracture opening for 2mD rock permeability will be higher when the viscosity of the injecting fluid increased.

5.2. NUMERICAL SIMULATIONS OF FRACTURE INITIATION, PROPAGATION AND SEALING

The main objective of this section is to present results for the numerical simulations of the investigation of hoop stress changes after fracture initiation, propagation and sealing. As mentioned in the previous section, one of the existing wellbore strengthening hypotheses is the increase of wellbore hoop stress more than the ideal wellbore without fracture when fractures are sealed. In order to test this hypothesis, it is required to know hoop stress values at each step of simulation. Previous numerical studies for wellbore strengthening did not include the fracture propagation step and are based on wedging an assumed fracture with a pre-defined width and length. It is believed that the key to understand wellbore strengthening is to include the complete wellbore strengthening process in a continuous simulation. These steps were illustrated in Figure 4.22 of previous section.

The first two simulation steps of fracture initiation and propagation resemble a typical leak off test (Figure 5.26). With assuming no initial fractures exist around the wellbore, the first step will be to look at the state of stress around the borehole when no fractures are formed. The second step will be to increase the wellbore pressure untill the hoop stress around the borehole drops down and fractures start to initiate. Then the drilling fluid starts to gradually enter the fracture, fracture breakdown happens and it starts propagating. It is very critical to precisely record stress changes around the borehole in each step. The final step will be the fracture sealing and to see whether wellbore strengthening has actually increased the wellbore hoop stress. The stress condition in the last step should be compared with the initial condition which both having the same mud weight. Previous studies have failed to model the problem with all the steps involved. It is not clearly understood why wellbore strengthening is successful in some occasions and not in others.

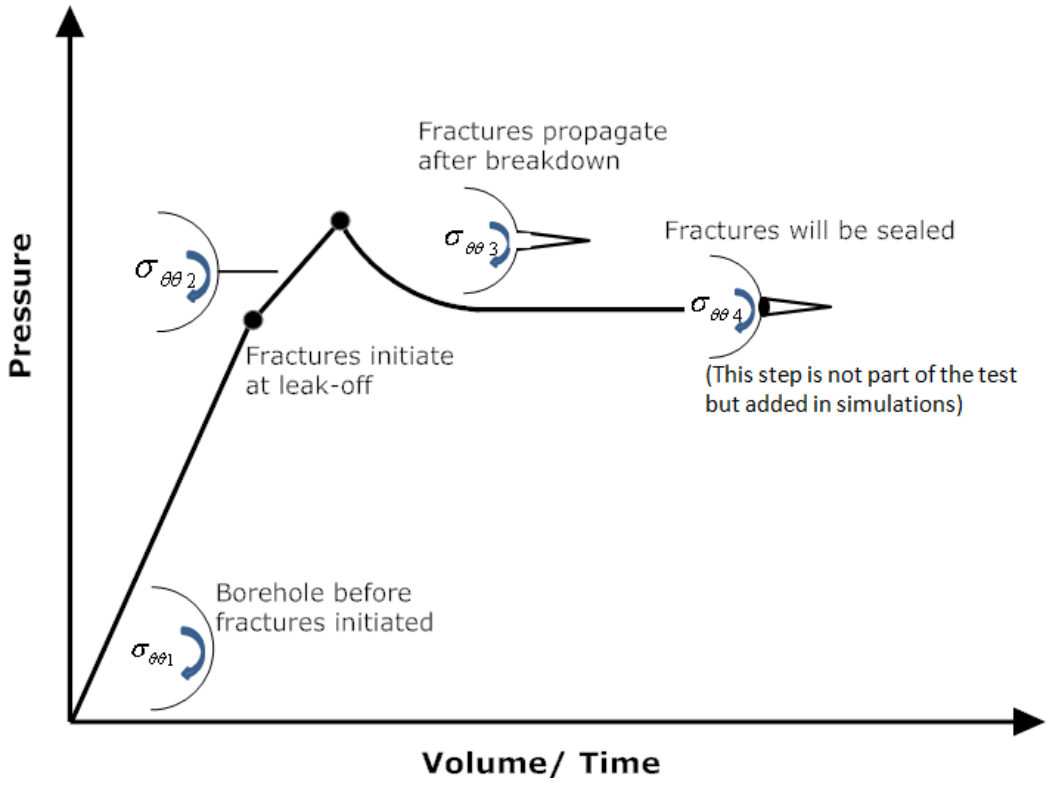

Figure 5.26. A schematic of the steps required in the simulations for fracture sealing based on a typical LOT

The simulation model for fracture initiation, propagation and sealing includes three meters of open hole with one meter of sandstone between two layers of shales with different rock properties. Geomechanical properties of the sand and shales were imported regarding field initial and boundary conditions. Table 5.5 shows the input parameters used for the sand layer in the simulations.

Table 5.5. Geomechanical input parameters for sand layer used for simulations

Young's modulus (MMPsi)	3.6
Poisson's Ratio	0.25
Maximum Horizontal Stress (Psi)	1160
Minimum Horizontal Stress (Psi)	725
Rock Permeability (mD)	40
Porosity	0.2

Figure 5.27 shows the hoop stress around the wellbore when no fractures have been initiated. Zero degree is aligned parallel to maximum horizontal stress orientation and 90 degree is aligned parallel to minimum horizontal stress orientation.

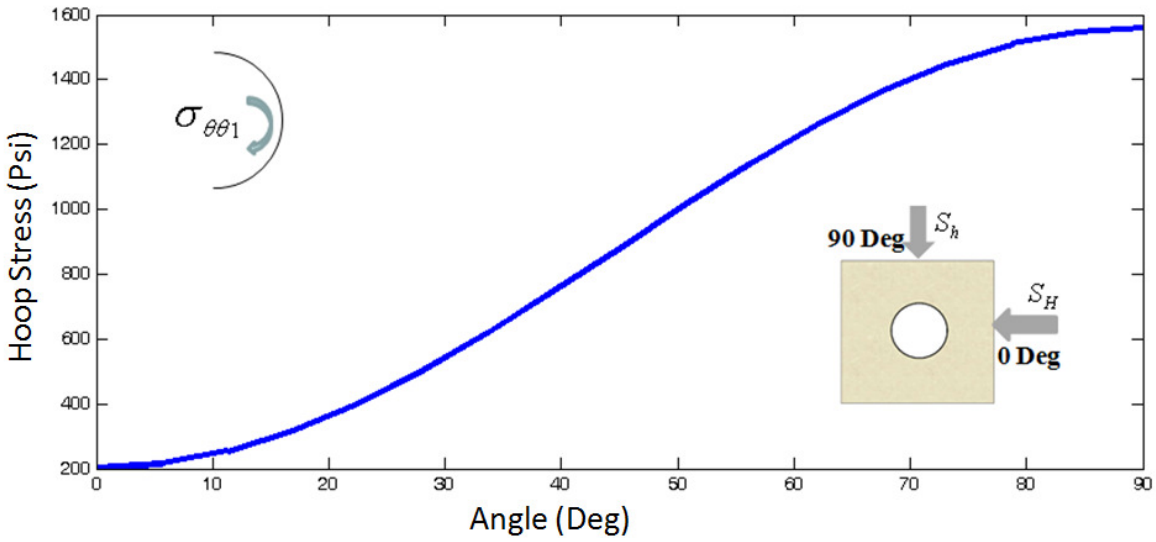

Figure 5.27. Hoop stress around the wellbore when no fracture exists (Zero degree: Maximum horizontal stress orientation, 90 degrees: Minimum horizontal stress orientation)

Predicting the lost circulation zone is often hard in field operations. It is often believed that the lost zone is located at the bottom of the well which is not always true. A wellbore might have a very long open hole which makes it hard to identify the exact lost location (Wang, 2007).

In the next step of simulations, the mud weight was increased until fractures start to initiate. Figure 5.28 demonstrates the extension of the tensile zone appearing in the model. The results indicate that the upper and lower boundary between the sand and shales are more prone to have tensile failures which are due to the changes in material properties and in-situ stress contrasts.

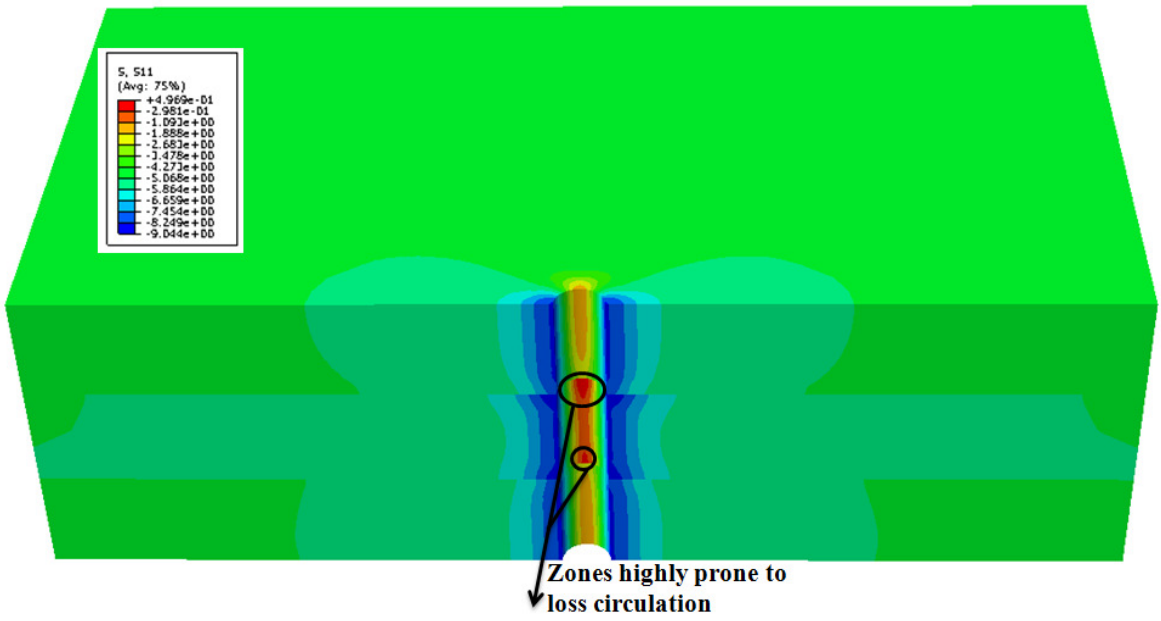

Figure 5.28. Loss circulation zones predicted using finite-element analysis

Figure 5.29 shows hoop stresses around the wellbore when the fracture has been initiated (broken green line), and hoop stresses were compared to the hoop stresses when the mud weight is elevated. The hoop stress in maximum horizontal stress orientation has dropped to zero. Since tensile stress of the formation was neglected in the simulations,

fractures will be initiated when the hoop stress drops to zero according to the Kirsch solution. Hoop stresses also dropped in all orientations around the wellbore.

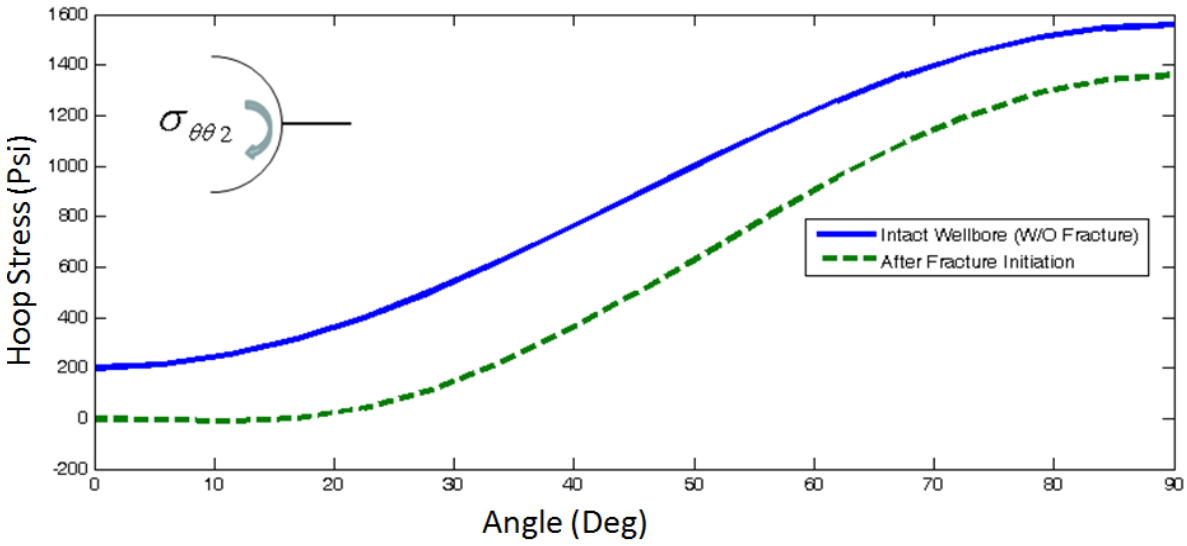

Figure 5.29. Hoop stress around the wellbore after fracture initiated (broken green line) and for intact wellbore (blue line)

In the next step of the simulation, tensile fractures propagated by injecting fluid into the fracture. Fracture propagation starts with further injection into the initiated fracture, and this creates a tensile state of hoop stress in the fracture plane. Figure 5.30 shows the propagated fracture after the propagation step is completed. Figure 5.30 indicates that fracture propagated from the near wellbore into the far field. Different stress profiles in each layer are caused by different rock properties which creates stress concentration at the layer boundaries. Figure 5.31 shows the hoop stress results around the wellbore after propagation, and it was plotted together with the results for the two previous steps. As shown in Figure 5.31, the hoop stress dropped at the maximum horizontal stress orientation because of the injection. Figure 5.32 shows pore pressure distribution in the model during fracture propagation. As shown in Figure 5.32, pore pressure has higher values at injection points and then smoothly distributes into the

formation. Pore pressure distribution shows a strong relationship with formation permeability, wherein high permeable formations pore pressure dissipates faster than in low permeable formations.

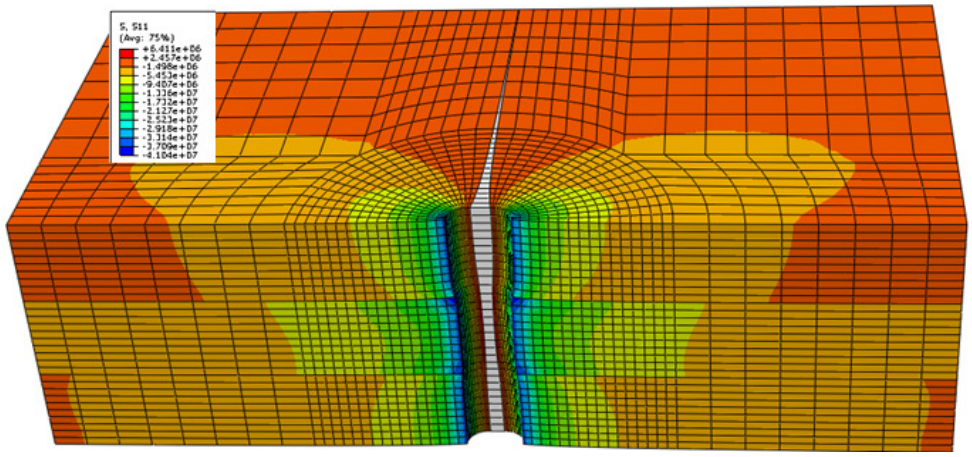

Figure 5.30. Tensile fracture propagated in the max horizontal stress direction (deformation magnified)

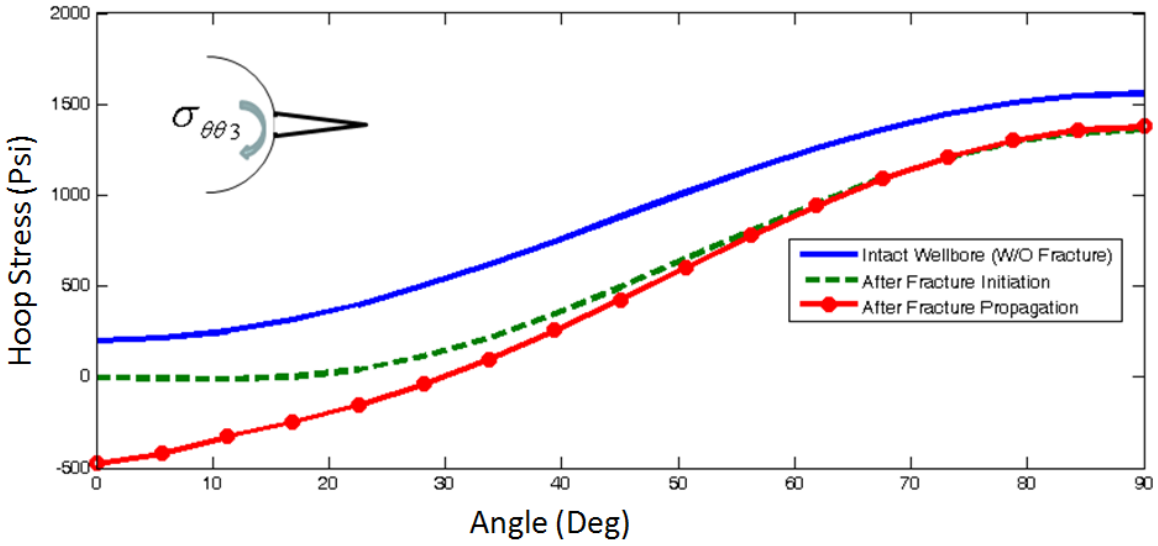

Figure 5.31. Hoop stress around the wellbore after fracture propagated (red line), after fracture initiated (broken green line) and for intact wellbore (blue line)

Other poro-elasticity parameters (saturation and void ratio) are also included in Figure 5.33. Since only fluid flow for fully saturated flow has been modeled, no changes in saturation happen during fracture propagation.

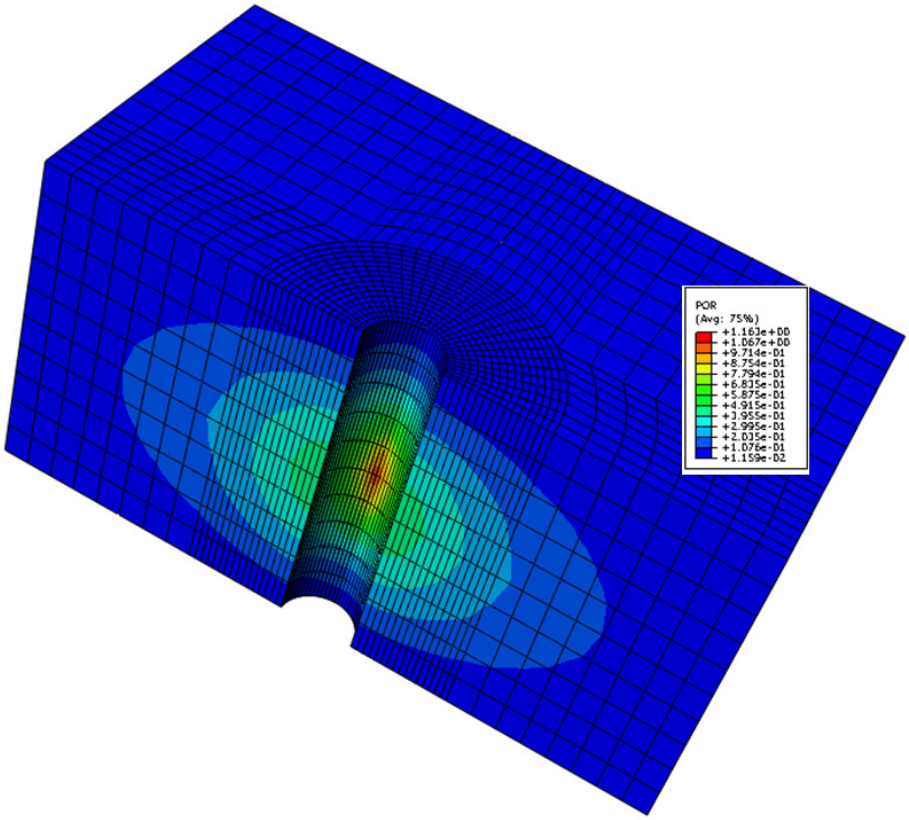

Figure 5.32. Pore pressure plum in the model during fracture propagation

Final step was simulated by using pressure boundary conditions inside the propagated fracture in order to seal it. This step isolates the fracture pressure from the wellbore pressure and makes the fracture pressure constant. Mud weight was also lowered to the initial condition in order to compare hoop stress results at the end of this step and hoop stress results in intact wellbore. Figure 5.34 shows that wellbore hoop

stress, when fractures were sealed, shifts from tensile to compressive mode, but they do not exceed original hoop stress existing around the wellbore before fractures initiated.

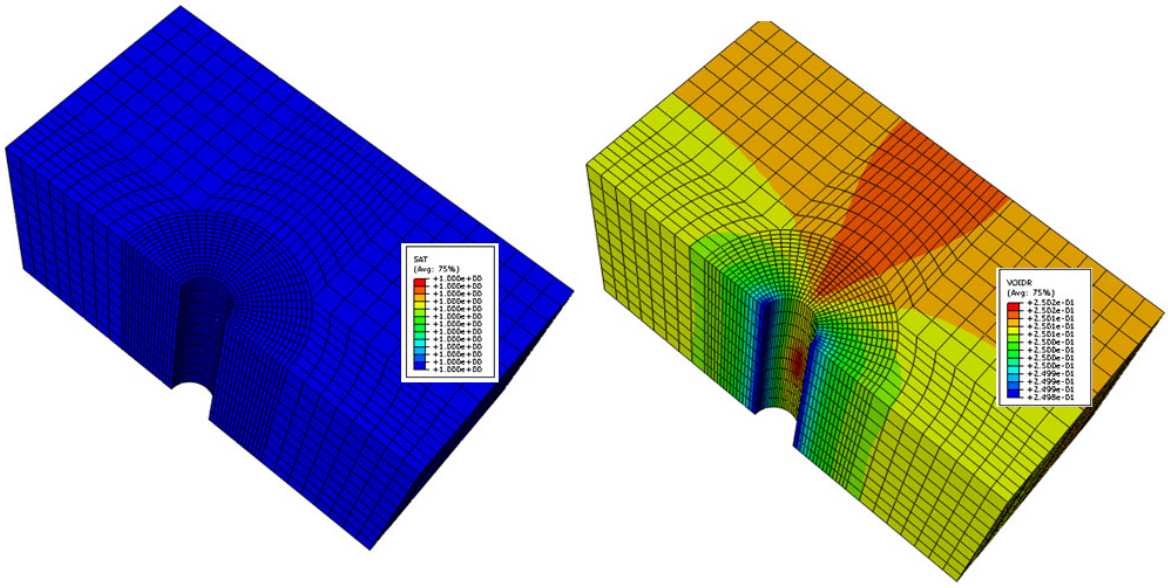

Figure 5.33. Saturation profile (left) and void ratio (right) in the model

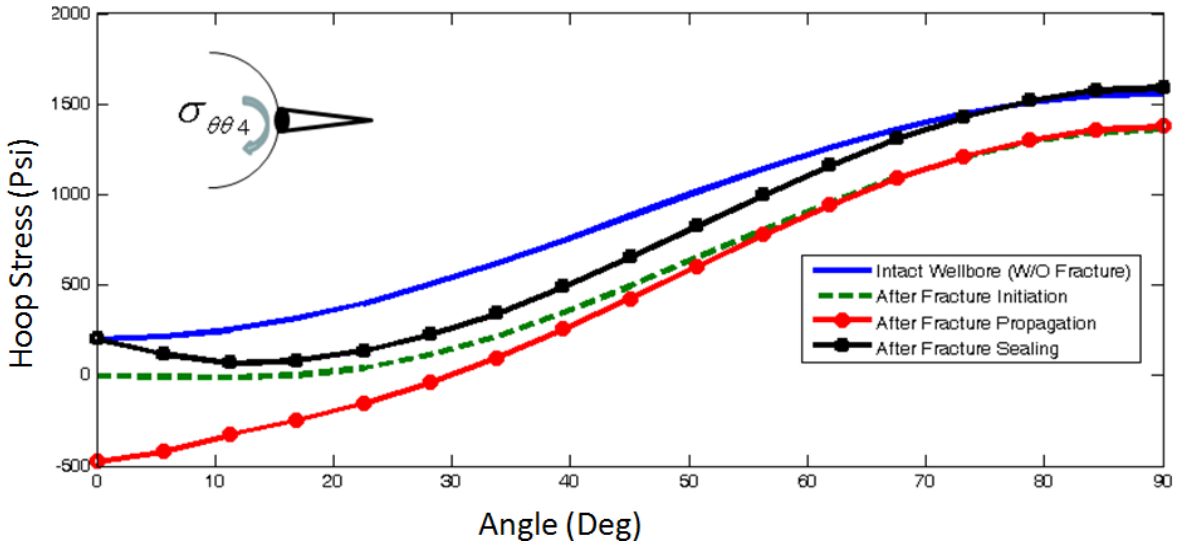

Figure 5.34. Hoop stress around the wellbore after fracture sealed (black line), after fracture propagated (red line), after fracture initiated (broken green line) and for intact wellbore (blue line)

This result indicates that wellbore strengthening has the capability to restore the hoop stress, but it is not actually able to strengthen the wellbore by increasing stress more than its ideal state, which can also be defined by the Kirsch's analytical solution. Some other studies (Alberty and Mclean, 2004, Wang et al., 2007a) argue that propping the fracture will significantly increase wellbore hoop stress which can be higher than its ideal wellbore pressure containment (WPC). This might be due to using linear-elastic analysis which does not take into effect porous elasticity of the rocks, and also comparing the stress state just before and after sealing rather than comparing it with the intact wellbore. No lab data has been reported so far to confirm increased hoop stress above the intact Kirsch solution hoop stresses or even replicate this mechanism. The results from the poro-elastic geomechanical model do not support the mentioned hypothesis; although, fracture sealing deliberately restored the wellbore hoop stress.

5.3. FIELD CASE STUDIES

Lost circulation has been reported as the number one geomechanical problem which has resulted in large non-productive time while drilling. The objective here is to present numerical and analytical simulations results to investigate lost circulation incidents and remediation in several oil producing fields from different sedimentary basins. The models were built based on reported input data in published papers.

The methodology followed in the numerical simulations was to build a geomechanical model for the depth of the lost circulation incident reported and model fracture propagation and sealing. The hoop stress results were compared after each step. Hoop stress after fracture sealing is considered to be the new fracture gradient achieved for the specific formation. Results for fracture gradient increase were also calculated based on Abe et al., solution for sealed fractures (Section 4.2.2.1). Here, it is assumed that five percent of the fracture is filled by a non-invaded zone (R-R1). This can be an upper estimate for the non-invaded zone inside the fractures (van Dam et al., 1998).

5.3.1. Offshore Caspian Sea. The first field example is from Shah Deniz field which was discovered in 1999 and is located 100km south of Baku. Maximum water depth is 600 meters (1960 ft) in the Caspian Sea. This field is characterized by a complex

pore and fracture pressure profile, and the Balakhany sands are associated with a major pressure regression immediately below the regional high pressure seal (Alberty and Mclean, 2001). The depth of the structure plus the elevation from the crest to the flank and the water depth complicated the prediction of pore and fracture pressures. This led to very severe mud losses and wellbore stability issues in this field. Previous offset wells results indicate up to 20 % reported NPT (non-productive time) which is a significant number compared to other problems.

Major risks are primarily related to the pressure regime, in overpressured sandstones interbedded with overpressured mudstones. These conditions provide a limited PP-FG window, with the potential for wellbore breathing and the possibility of wellbore breakouts. Figure 5.35 shows one of the offset wells pore-fracture pressure windows, which indicates a very narrow window in 21000 ft depth. The high fracture pressure which exceeds overburden stress at the lower depth is a result of regional tectonic stresses.

A FEA sub model was built regarding the rock mechanical properties and stress regime in this field to observe feasibility of using the wellbore strengthening approach to widen the window at the mentioned depth. Results of simulation are presented in Figure 5.36. Complete hoop stress restoration occurred at a 90 degrees angle at the fracture causing losses, but the final hoop stress at the wellbore after fracture sealing did not go further than its ideal state when no fractures exist. This example clearly shows that plugging and/or sealing fractures does not increase the wellbore hoop stress beyond its ideal state which can also defined by the Kirsch solution. Several parameters including rock mechanical properties, stress anisotropy and injecting fluid properties affect hoop stress restoration which need to be identified.

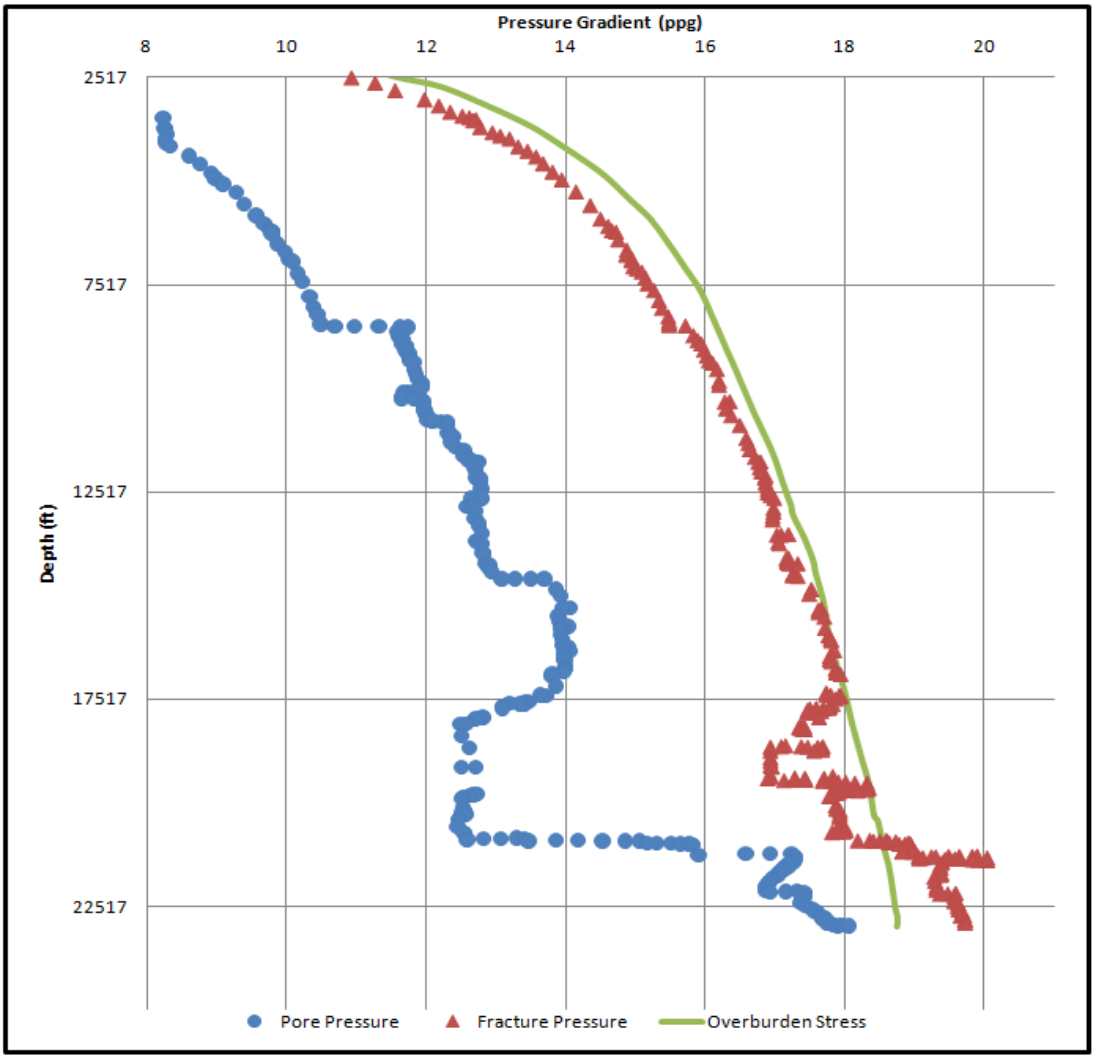

Figure 5.35. Pore- fracture pressure window for the offset well in Caspian Sea, very tight operational window exists below 20000 ft

5.3.2. Offshore Persian Gulf (12-1/4" section). The second field example is a wellbore strengthening operation in a 12 1/4" wellbore section of the offshore Persian Gulf. Previous offset wells provide the pore-fracture pressure window shown in Figure 5.37. Lost circulation, differential sticking across the loss zone, wash-outs and salt water kicks were reported to be the major challenges in offset wells.

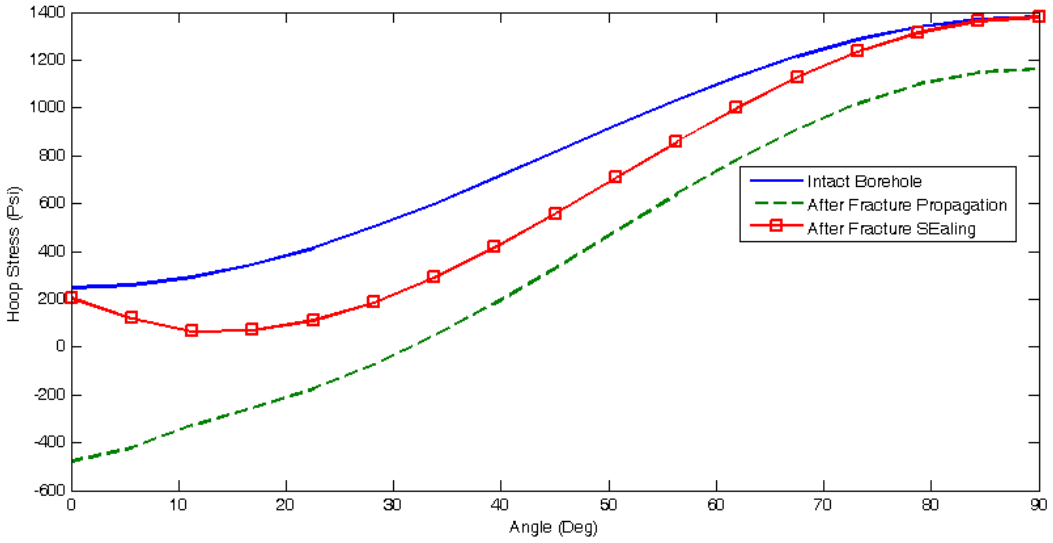

Figure 5.36. Wellbore hoop stress for intact borehole, after fracture propagation and sealing for Caspian Sea offset well

Although a KCL mud with the LCM concentration summarized in Table 5.6 was used to mitigate high loss rates in this section, loss circulation caused large non-productive time. A FEA geomechanical model was built for the target zone at a depth of 9350 ft in which field reports showed severe losses. The objective for the geomechanical model is to observe how wellbore strengthening is able to raise the fracture gradient in this interval.

Hoop stress for intact borehole, fracture propagation and sealing results are given in Figure 5.38. Similar to the previous case, sealing the fractures in this field is able to restore most of its hoop stress within 90 degrees from the fracture direction, but it is not able to completely restore hoop stress in other areas around the wellbore.

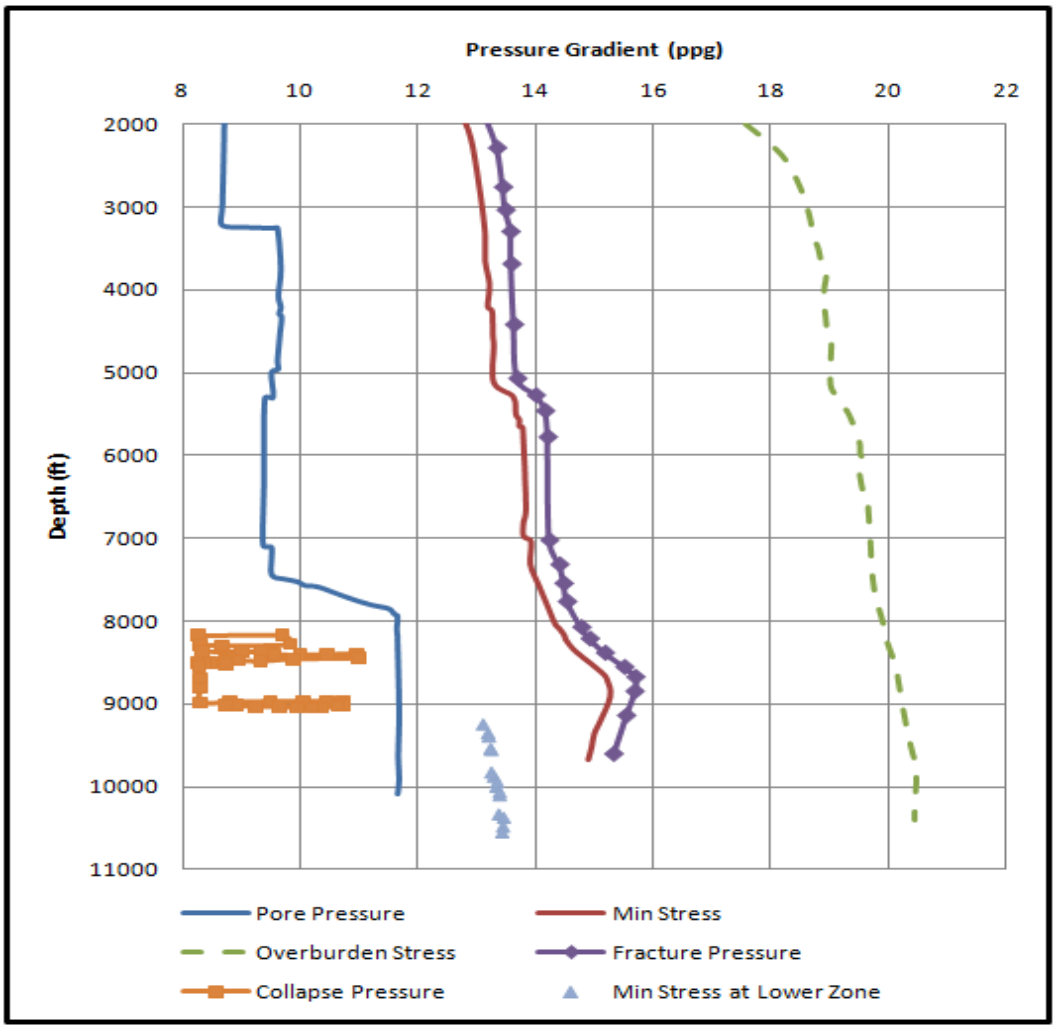

Figure 5.37. Pore- fracture pressure window for offset well in Persian Gulf

Table 5.6. LCM type and concentration used for decreasing loss rate

LCM	Concentration (lb/bbl)
CaCo3 F	7
CaCo3 M	7
Mix II F	7
Mix II M	7
Mica F	1.8
EPI Seal XF	8.8
Kwik Seal F	1.8

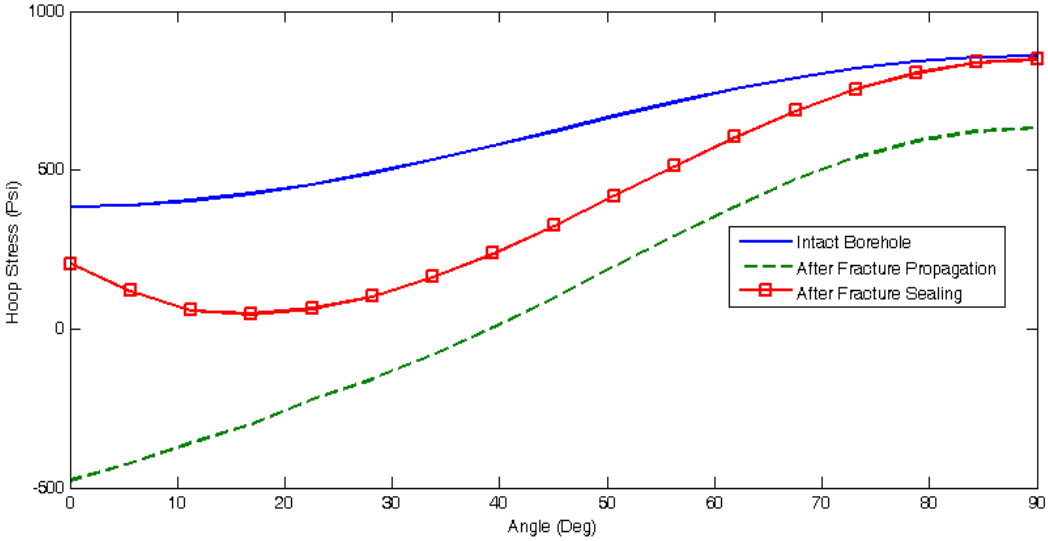

Figure 5.38. Wellbore hoop stress for intact borehole, after fracture propagation and sealing for Persian Gulf well

5.3.3. Nile Delta (Offshore Mediterranean Sea). As outlined by Sanad et al., (2004), drilling in the offshore Nile Delta of the Mediterranean Sea is quite challenging regarding the existence of geo-pressured shale-bound sands that can narrow down a pore-fracture pressure window (Figure 5.39). The target zone from 14698 ft to TD has the narrowest window between pore-fracture pressures. The exploration well in this field experienced lost circulation below 15000 ft with a 16.4 ppg mud weight. It is known that LCM pills containing 40 to 60 ppb and also 40-bbl cross-linked polymer pills were pumped but little success was achieved. Using a fracture gradient enhancement squeeze system (FGESS), wellbore pressure containment integrity increased to 17 ppg measured by a FIT test (Sanad et al., 2004).

FGESS treatments were used as the wellbore strengthening pill application. These materials typically develop into the sealant when mixed with mud and evolve into a moldable, ductile and non-brittle seal when used as LCM. Geomechanical properties were imported in the existing FEA model to simulate the effect of fracture sealing on the hoop stress in the target zone. Figure 5.40 shows the simulation results for this case where the hoop stresses after sealing, did not exceed the ideal condition.

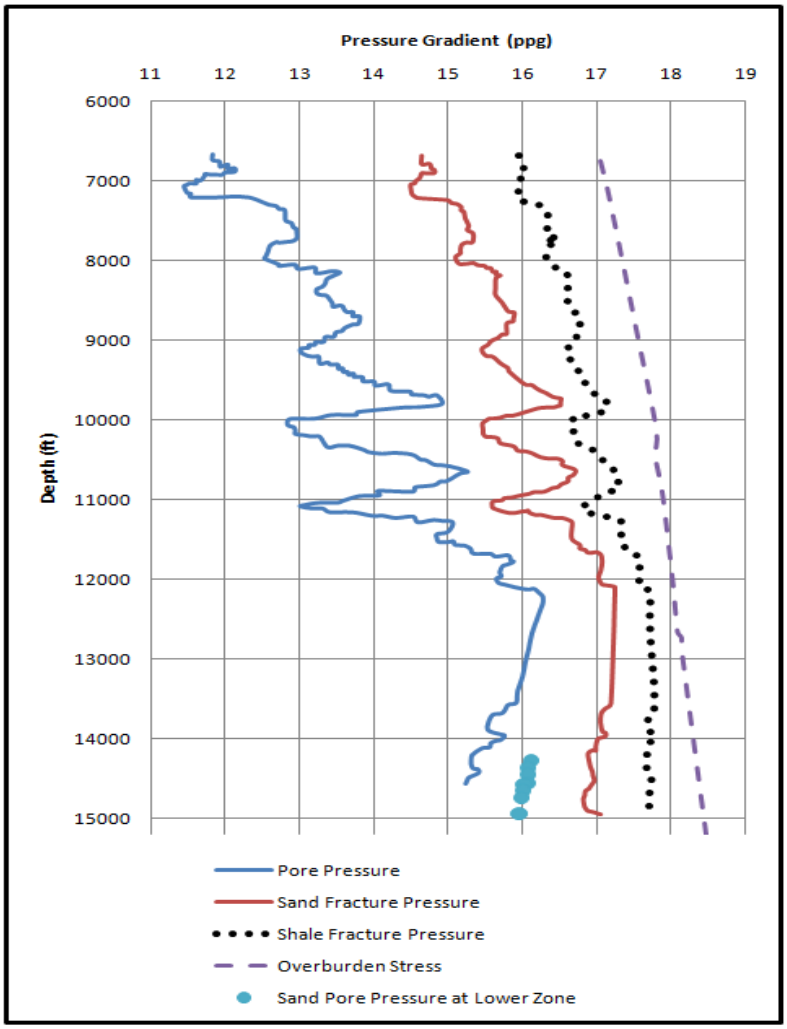

Figure 5.39. Pore- fracture pressure window program for offset well in Nile Delta

Hoop stress restoration in the Nile Delta offset well is smaller than the other cases due to the high Poisson's ratio (0.33) of the sandstone. As mentioned by Aadnoy and Belayneh (2009), the borehole is pressurized in the radial direction by increasing the mud weight which will cause tension in the tangential direction. This effect is mainly controlled by the Poisson's ratio and will be more pronounced with lower Poisson's values. In the case of fracturing, increasing the mud weight from the equilibrium state results in Poisson's effect on the stresses as presented in Section 3.3.1 and Equation 3.27.

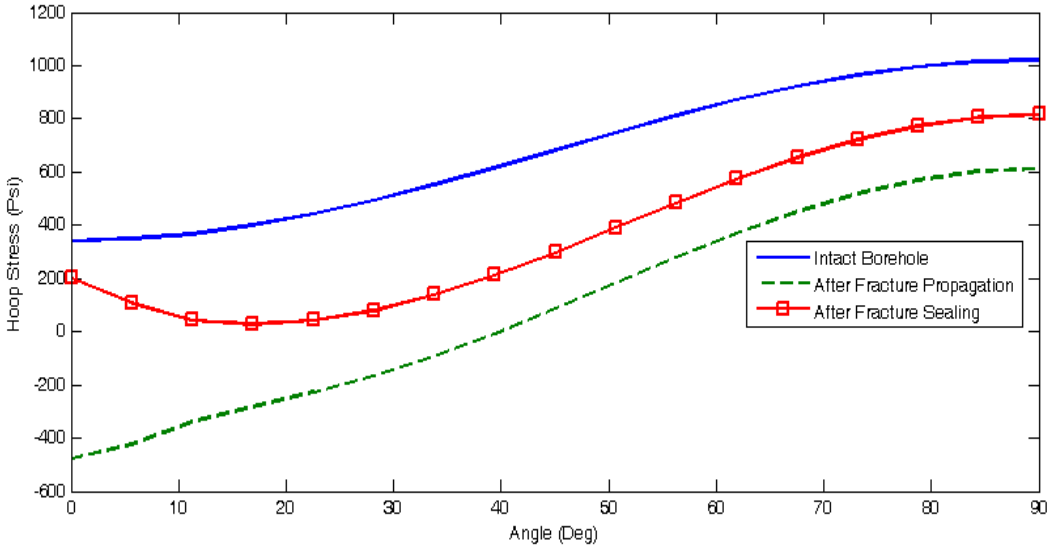

Figure 5.40. Wellbore hoop stress for intact borehole, after fracture propagation and sealing for Nile Delta offset well

As illustrated in Figure 5.41, this factor increases as Poisson's ratio decreases. The maximum number for scaling factor is 1 which occurs when Poisson's ratio drops to zero which is an unrealistic number. For rocks with average 0.25 Poisson's ratio, the scaling factor is around 0.6.

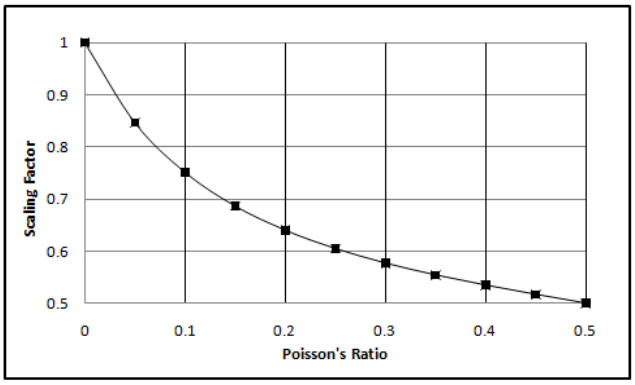

Figure 5.41. Poisson's ratio scaling factor decrease as Poisson's ratio increases

5.3.4. Offshore North Sea (Visund Field). Visund is an oil and gas field in blocks 34/8 and 34/7, 22 kilometers north-east of the Gullfaks field in the Tampen area of the Norwegian North Sea (Zobak et al., 2003). FMS/FMI log runs in several wells in this field revealed extensive drilling-induced tensile fractures which can be minimized by raising the fracture propagation pressure (Figure 5.42). Observation indicates that tensile cracks formed on the borehole wall almost continuously from 7380 to 9285 ft TVD (Wirput et al., 1997). Figure 5.43 shows the predicted formation pore pressure from RFT, values of the fracturing pressure predicted by leak off test and the maximum horizontal stress in the field determined from the analysis of drilling the induced tensile fractures in the field (Zoback et al., 2003). A similar numerical approach was executed at a depth of 9300 ft.

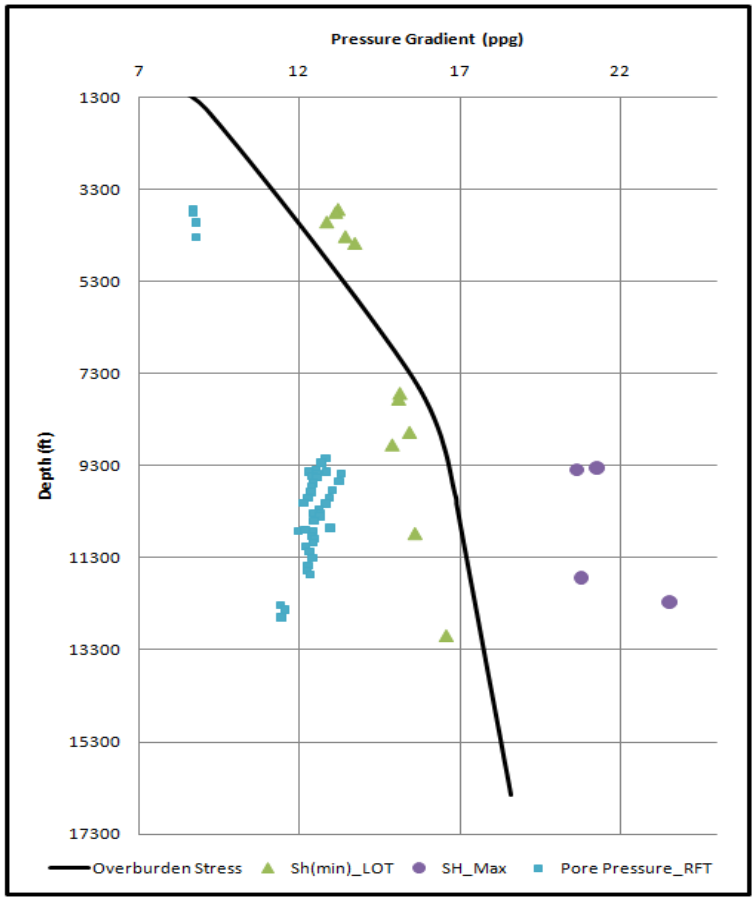

Figure 5.42. Pore- fracture pressure window for Visund field

Figure 5.44 shows the FEA result of sealing the loss zone for this well. Similar observations to other field cases were seen in which fracture sealing only restores some of the wellbore hoop stress but cannot increase it more than the ideal case in the direction of the tensile fractures. Poisson's ratio of 0.2 considered in the simulations which gives a higher Poisson's scaling factor on hoop stresses, especially on 90 degrees away from the fracture zone. This gives 0.16 ppg increase of the hoop stress gradient than its intact case at 90 degrees. Wellbore breakout analysis must be run to analyze the risk of break outs when wellbore strengthening is executed at this depth.

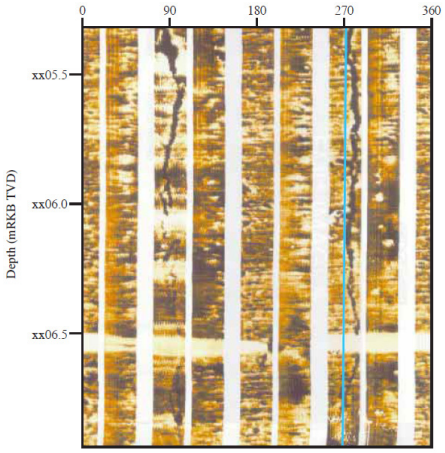

Figure 5.43. FMI image of offset well in Visund field showing drilling-induced fractures (Zobak et al., 2003)

5.3.5. Fracture Propagation Pressure Enhancement (Analytical Solution). The second objective was to evaluate the fracture propagation increase by sealing and/or propping fractures for the field cases studied. Abe et al., fracture equation (Section 4.2.2.1) was used by considering a 5% non-invading zone existing in the fractures. Results for new fracture gradients are plotted from Figures 5.45-48. The original casing program for the well in the Caspian Sea shows the use of excessive casing strings as a result of a tight PP-FG window. However, taking into account 5% of the fracture is filled by non-invaded zone (R-R1), gives fracture gradient increase up to 1.3 ppg (Figure 5.45).

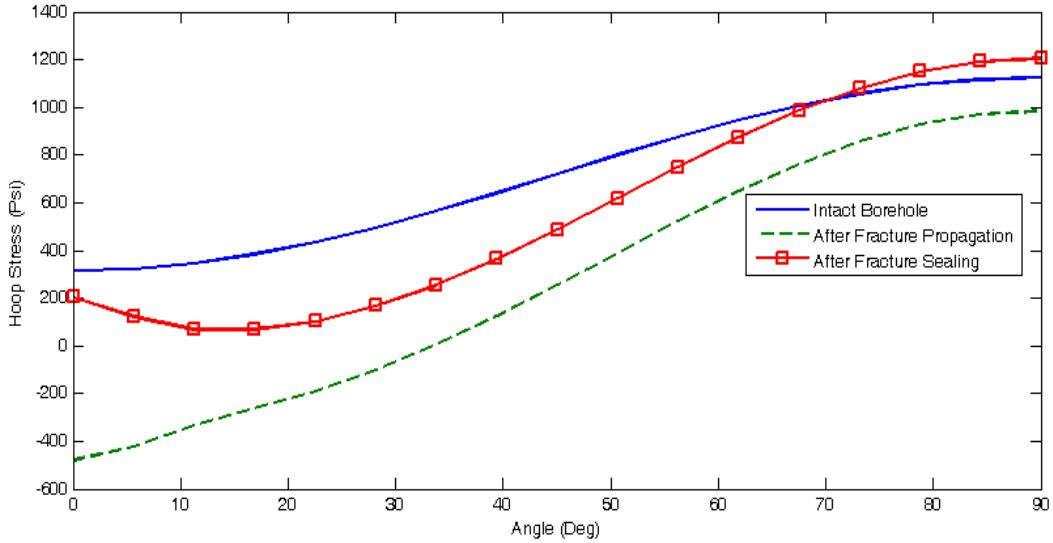

Figure 5.44. Wellbore hoop stress for intact borehole, after fracture propagation and sealing for Visund field well

With the same procedure for the well in the Persian Gulf (Figure 5.46), fracture gradient can be increased up to 16.55 ppg which is around 3.5 ppg higher than the current fracture gradient in the loss zone. These results are very consistent with some field data reported by Fuh et al., (1992, 2007). Conditions in the Visund field are different where strike-slip faulting regime exist; maximum horizontal stress is very high for this field. Figure 5.47 shows that new fracture gradient can be close to overburden stress. An intensive wellbore stability study is required for this field which considers conditions in highly deviated wellbores with different orientations and potentials for break outs (Takatoshi et al., 2001).

Pore pressure was very high in the well drilled in the Nile Delta and the potential for the loss circulation during drilling is more serious. The analysis for this case indicates a fracture gradient increase of 1.3 ppg for the zone of interest (Figure 5.48). The actual field report indicates that using the loss circulation squeeze system increased the fracture gradient by 0.5 ppg which can be a lower limit for wellbore strengthening.

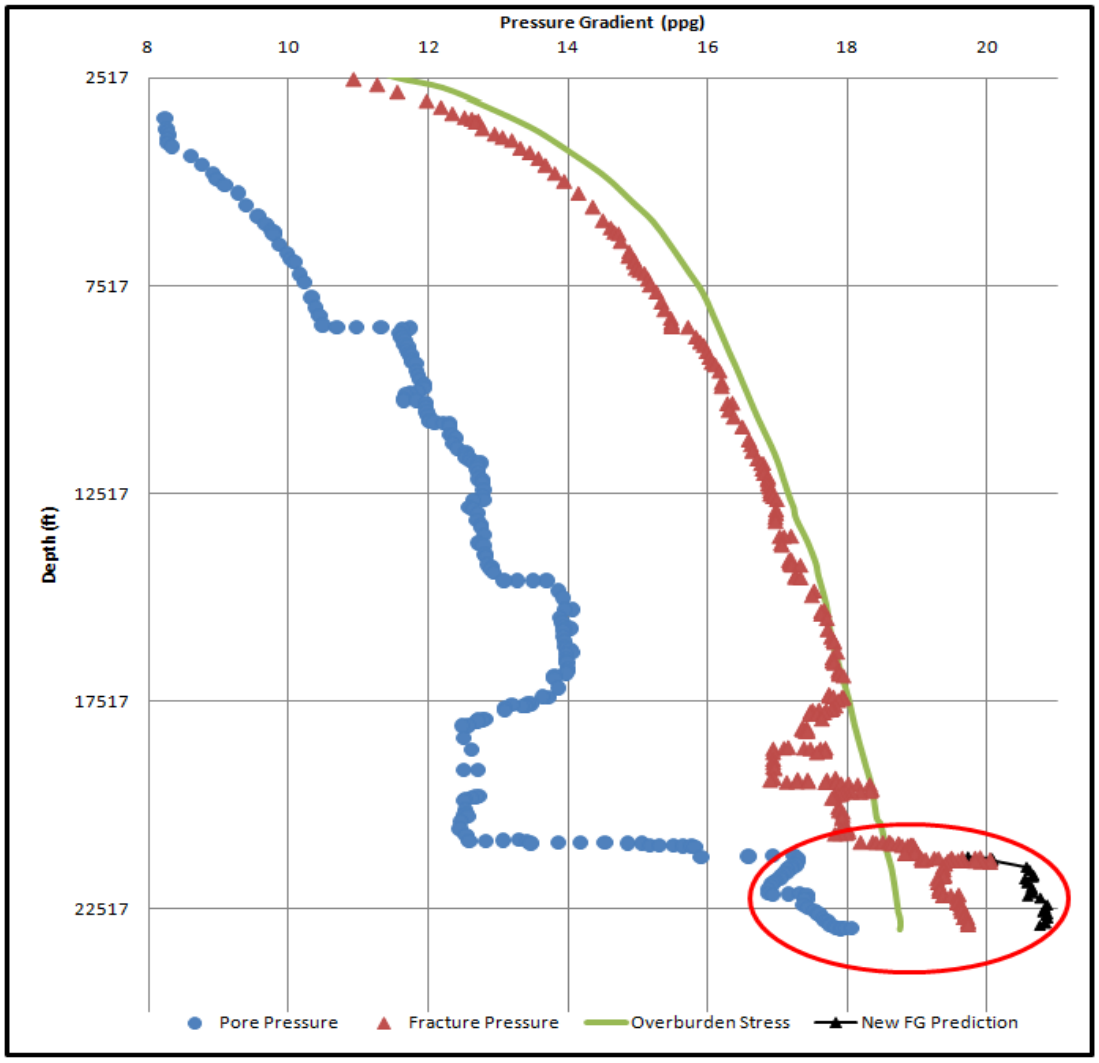

Figure 5.45. New fracture gradient predicted for lost circulation episode in Caspian Sea offset well

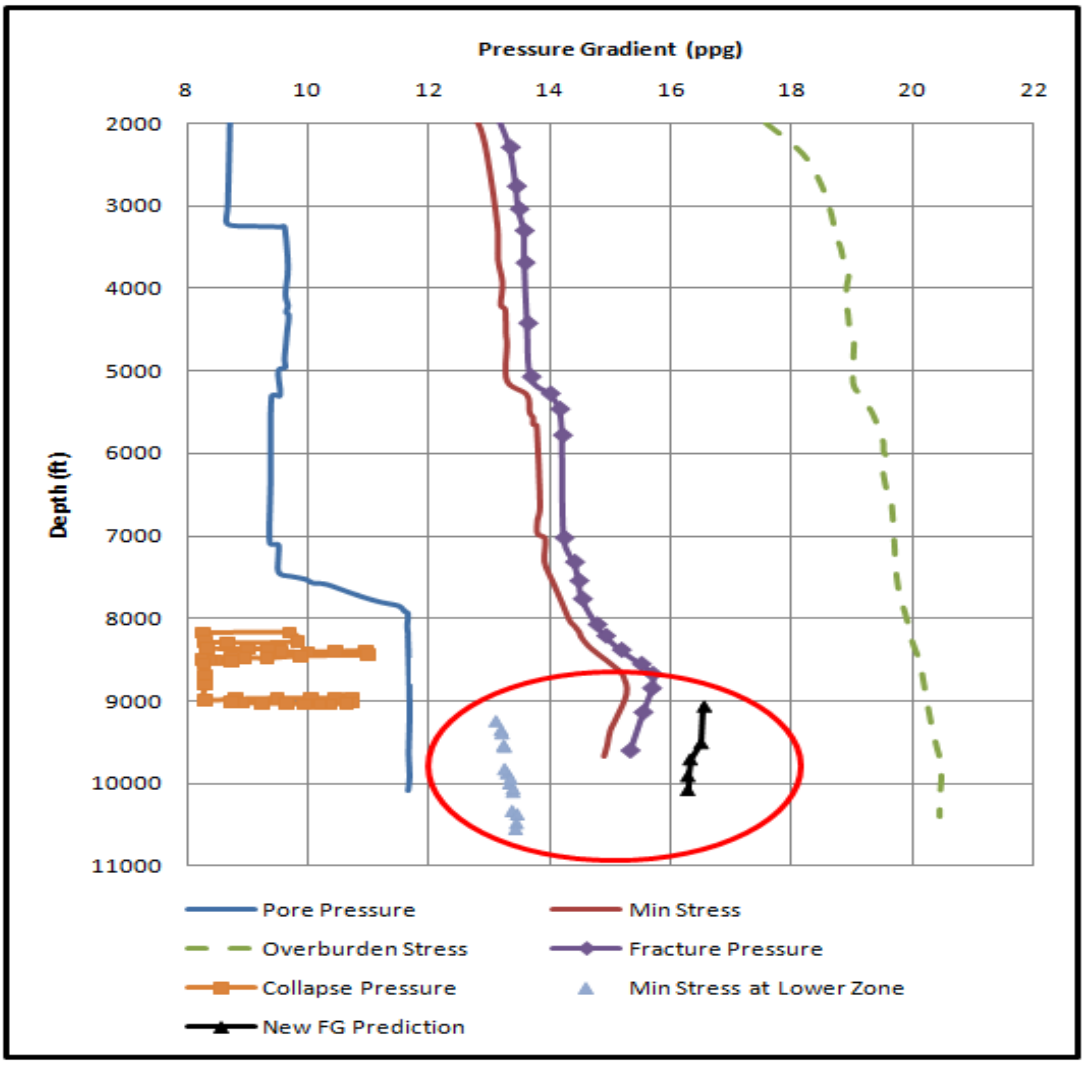

Figure 5.46. New fracture gradient predicted for lost circulation episode in Persian Gulf offset well

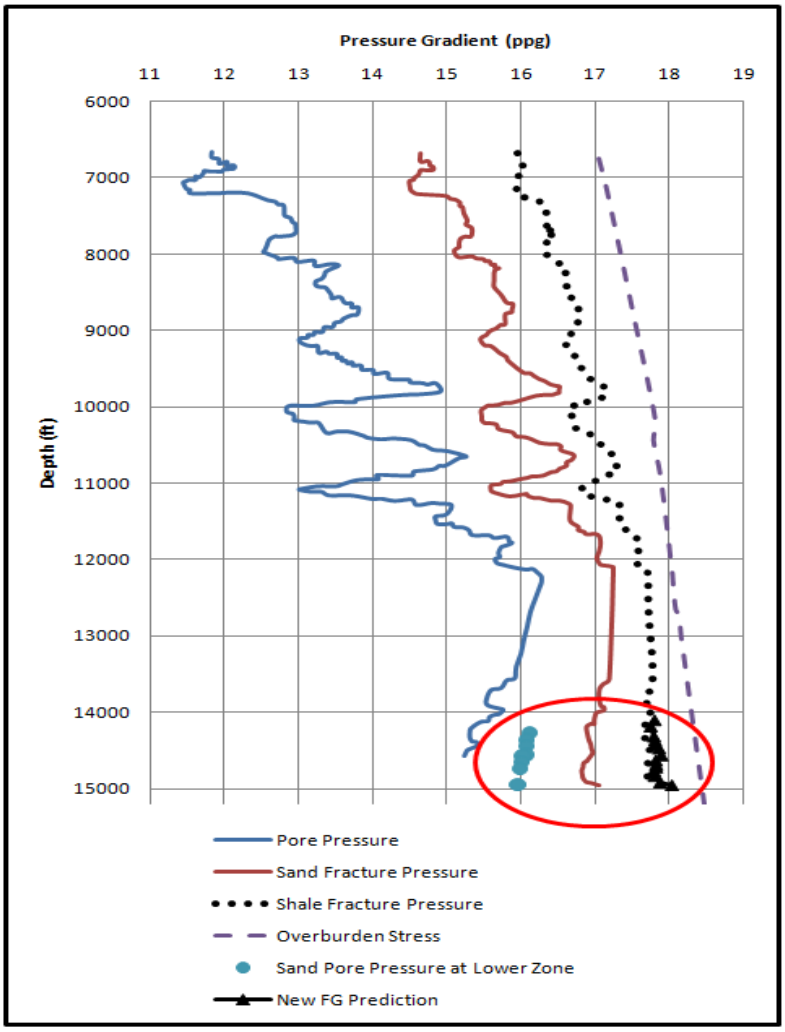

Figure 5.47. New fracture gradient predicted for lost circulation episode in Nile Delta offset well

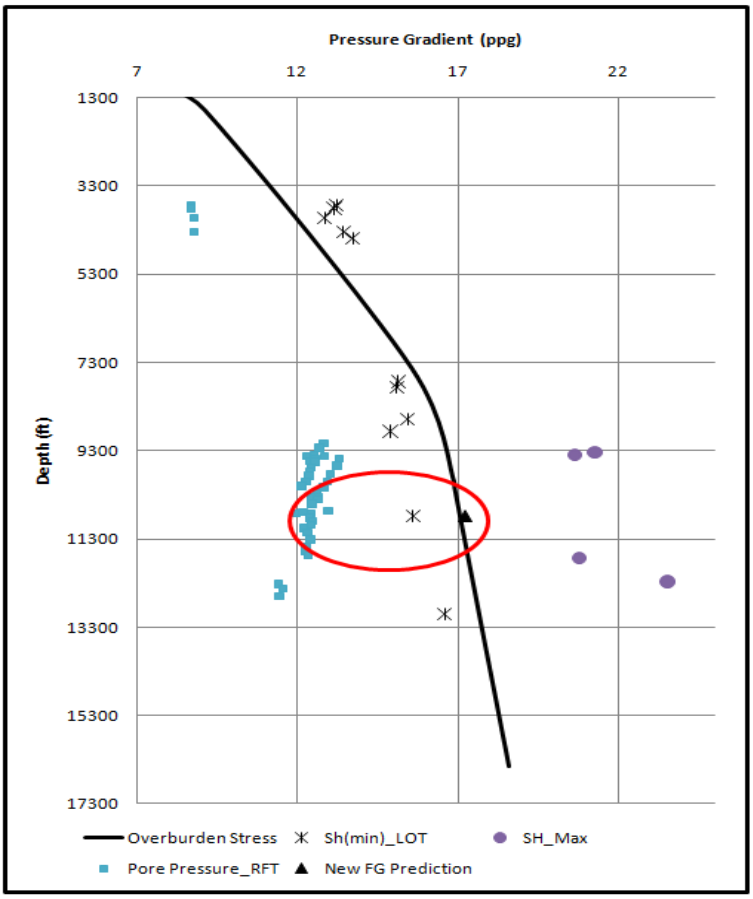

Figure 5.48. New fracture gradient predicted for lost circulation episode in Visund field offset well

5.4. EXPERIMENTS RESULTS

The aim of this section is to present results obtained from fracturing experiments. Both sandstone and dolomites fractured using water-based muds.

5.4.1. Test 1-Dolomite (Water). The first fracture test was conducted on a dolomite core sample using water for injection (Figure 5.49). Overburden and confining pressures were kept at 400 and 200 Psi respectively. Figure 5.50 shows injection pressure versus time for this test. Fracture breakdown pressure for this test occurred at 1222 Psi. As illustrated in Figure 5.50, a sharp breakdown did not happen in this test due to pre-existing natural fractures in the sample which are also visible in the figure. These pre-existing fractures will lower the breakdown pressure and will inflate the breakdown curve.

Figure 5.49. Dolomite core sample used for water test

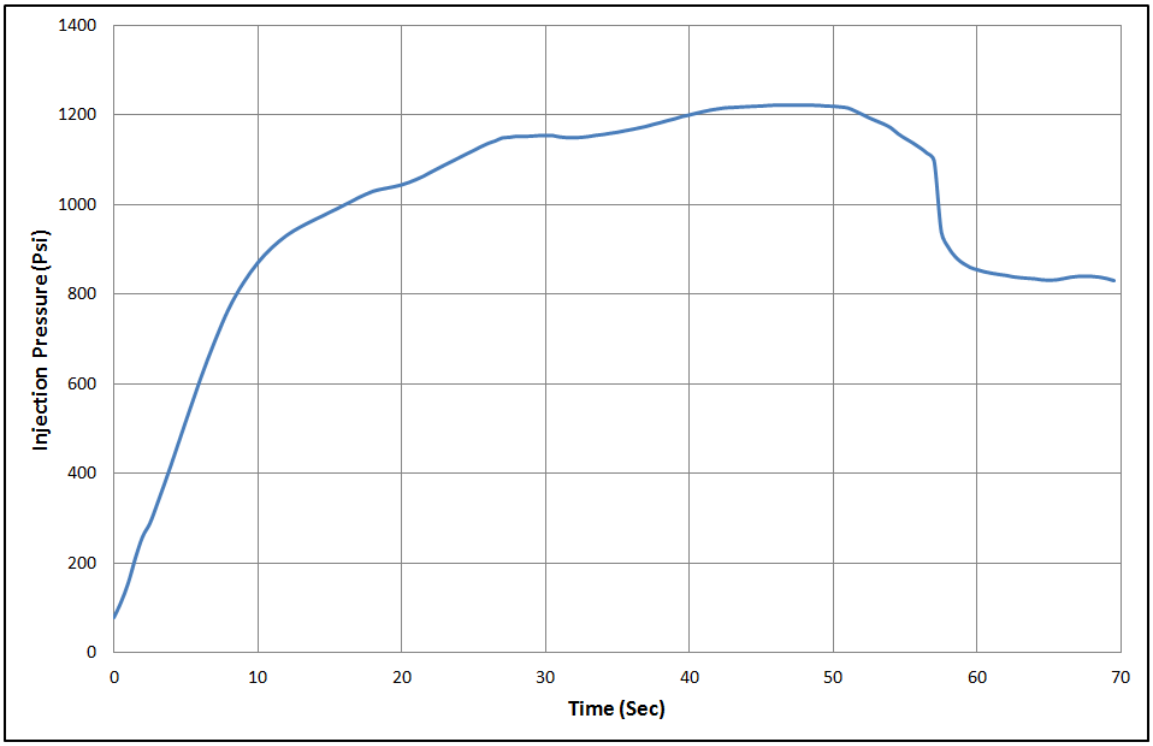

Figure 5.50. Injection pressure versus time for the first dolomite test

5.4.2. Test 2-Dolomite (8% Bentonite). The second fracture test was also conducted on the dolomite core sample using 8 % Bentonite mud (Figure 5.51). Overburden and confining pressures were kept similar to the previous test. A second reopening cycle was also conducted for this test right after the releasing pressures in the first cycle. Figure 5.52 shows the result of injection pressures versus time for the two test cycles. Unlike the first test with water, a sharp breakdown pressure was observed in this test. This is because of fewer pre-existing natural fractures in the sample as shown in Figure 5.51. As shown in Figure 5.52, fracture initiation pressure happened at 3405 Psi, and the pressure continued until ultimate breakdown at 3700 Psi. After ultimate breakdown, the pressure dropped to around 1650 Psi. In the reopening cycle, breakdown pressure occurred at 2059 Psi.

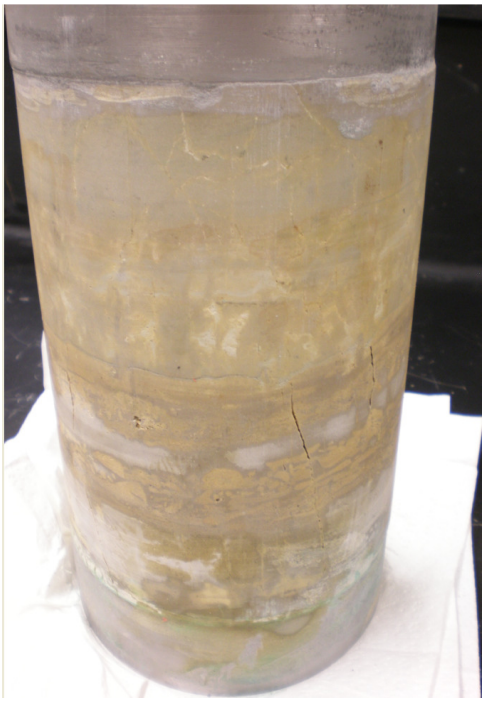

Figure 5.51. Dolomite core sample used for 8% Bentonite mud

The 400 Psi pressure difference between the reopening and propagating pressure at the first cycle is due to fracture healing and mud gelling of 8% Bentonite mud which is in agreement with the DEA-13 experiment results. The higher breakdown pressure in this test (3700 Psi) compared to the previous test with water (1222 Psi) is also due to using mud as a non-penetrating injection fluid. One important observation is the huge difference between the laboratory fracture pressure and the pressure obtained from the theoretical Kirsch solution, $P_{breakdown} = 2 \times 200 = 400 + T_0$ (Psi). This difference comes from a variety of sources including the size and end effect of the laboratory set up. These effects were also observed in the fracture test results from the DEA-13 and the GPRI experiments (Morita et al., 1996 and Dudley et al., 2001).

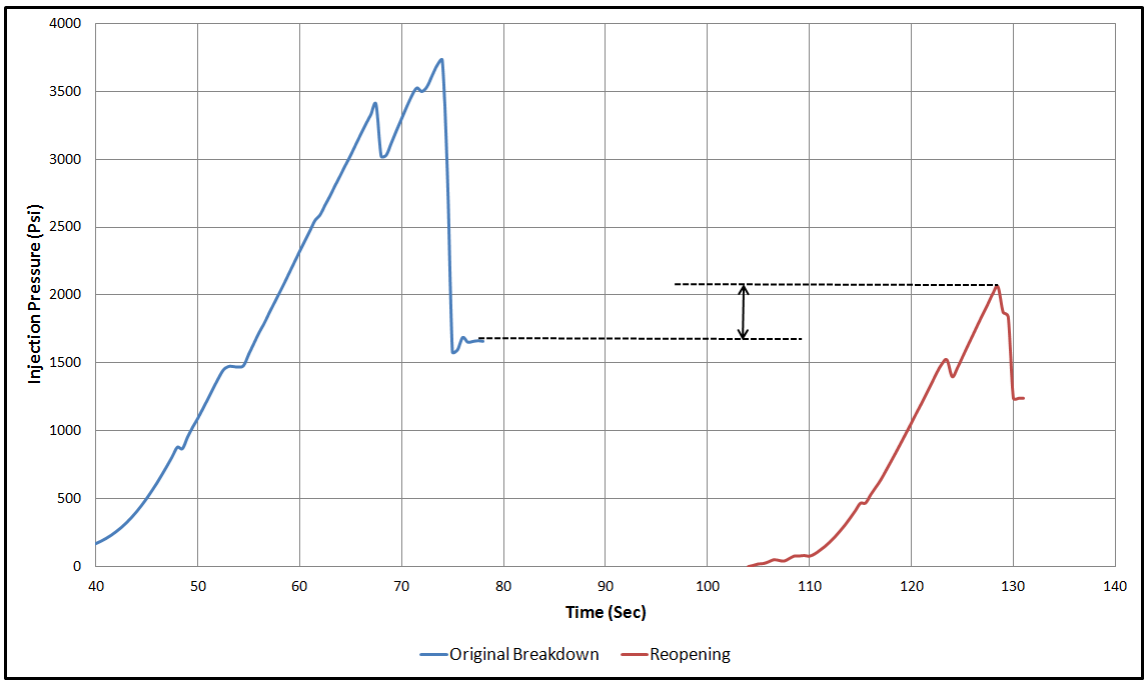

Figure 5.52. Injection pressure versus time for the second dolomite sample using 8% Bentonite mud

As shown in Table 5.7 for the DEA-13 fracture experiments, the breakdown pressure ratio between the laboratory and theoretical solution for the 1.5 inch borehole is more than three times when using drilling fluids.

Table 5.7. Comparison of borehole breakdown pressure between theoretical and laboratory results for different injecting fluids (from Morita et al., 1996)

Injecting Fluid	σ_h (Psi)	σ_H (Psi)	$P_{breakdown}$ Theoretical	$P_{breakdown}$ Laboratory
Muds (Ave)	1800	2200	**3350**	**11500**
Muds (Ave)	300	2500	1450	4300
Water	900	1100	1229	4000
Oil	900	1100	1229	5600

Furthermore, the borehole diameter has a significant difference in borehole breakdown pressure. Whereas the borehole radius increases, the breakdown pressure decreases. Results from DEA-13 experiments (Figure 5.53) for the breakdown pressure on the 1.5 inch and 4 inch boreholes showed 2310 pressure difference (10300 Psi for 1.5 inch and 7990 Psi for 4 inches).

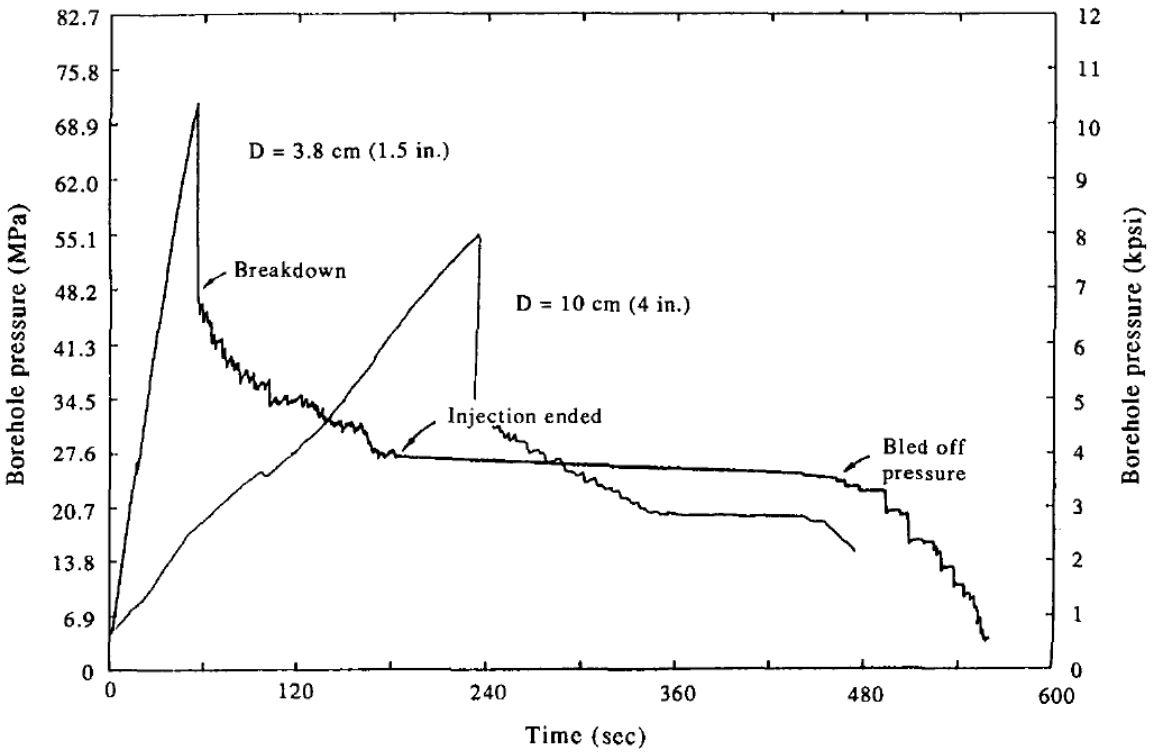

Figure 5.53. Wellbore breakdown pressure using 16 ppg mud for 1.5 inch and 4 inch wellbore sizes of Berea sandstone (from Morita et al., 1996)

In order to accurately predict breakdown pressure at field conditions, a correlation (scaling law) is required between the wellbore radius and breakdown pressures (Figure 5.54).

Figure 5.54 illustrates the relationship for the borehole breakdown pressure based on the borehole diameter in the DEA-13 experiments; although having two data points and a linear relationship is not enough to draw a firm conclusion. However, this can be used as a rough approximation when scaling up laboratory results to field conditions.

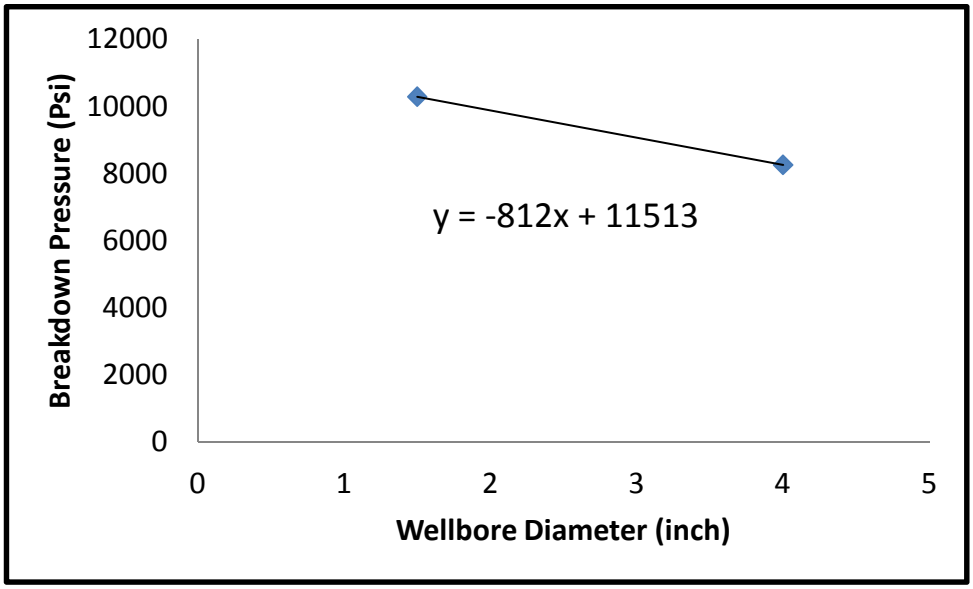

Figure 5.54. Linear correlation for wellbore breakdown pressure versus wellbore size based on DEA-13 experiments

5.4.3. Test 3-Dolomite (Horizontal Fracture). In this test, the goal was to create the horizontal fracture in the sample using water and also to measure the breakdown pressure. For this reason, values for confining and overburden pressures were swapped for this test and injection pressure versus time was recorded. Figure 5.55 shows the core sample before fracturing (left) and horizontally split core after the fracture test (right).

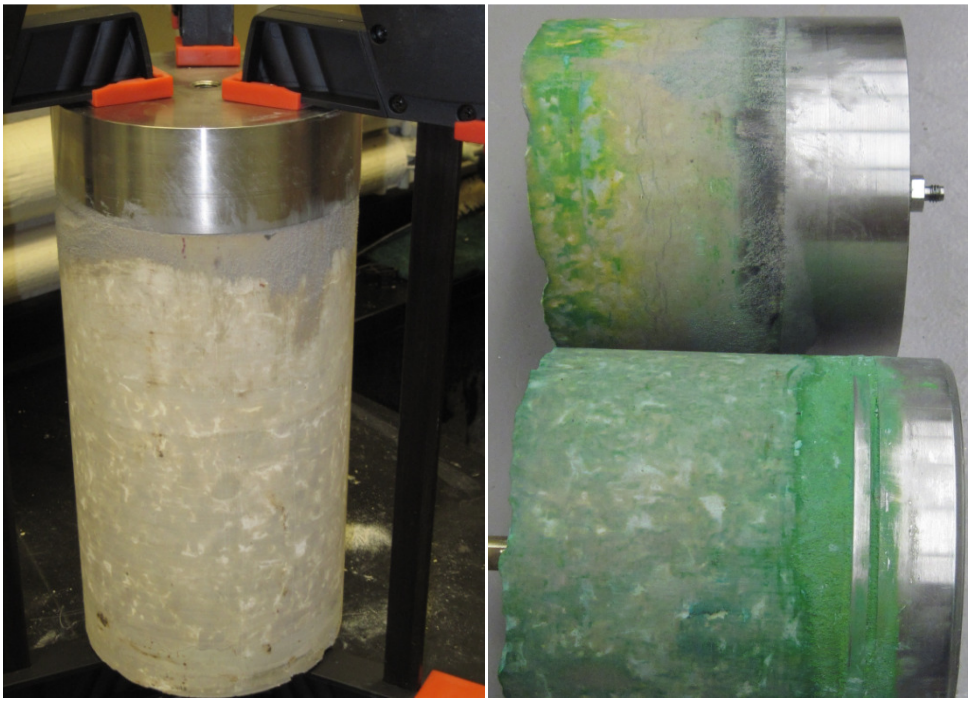

Figure 5.55. Dolomite core sample horizontally fractured with water

Figure 5.56 shows the injection pressure versus time for this test. Fracture breakdown pressure occurred at 2224 Psi for this sample. It was attempted to run the reopening test on this sample; but due to horizontal fracture occurrence in the first cycle, increasing injection pressure led to overburden pressure increase. This increase occurred due to lifting up the split core in the test apparatus and pushing on the overburden pad. Similar to previous tests, higher than theoretical breakdown pressure was recorded for this test due to borehole size and core end effects.

5.4.4. Test 4-Sandstone (8% Bentonite). The first fracture test on the sandstone sample was conducted using 8% Bentonite mud. Unlike the dolomite core samples, the sandstone had no pre-existing natural fractures (Figure 5.57). Figure 5.58 shows injection pressure versus time for this test. Similar to the test on dolomite with 8% Bentonite, the reopening cycle was also conducted for this test.

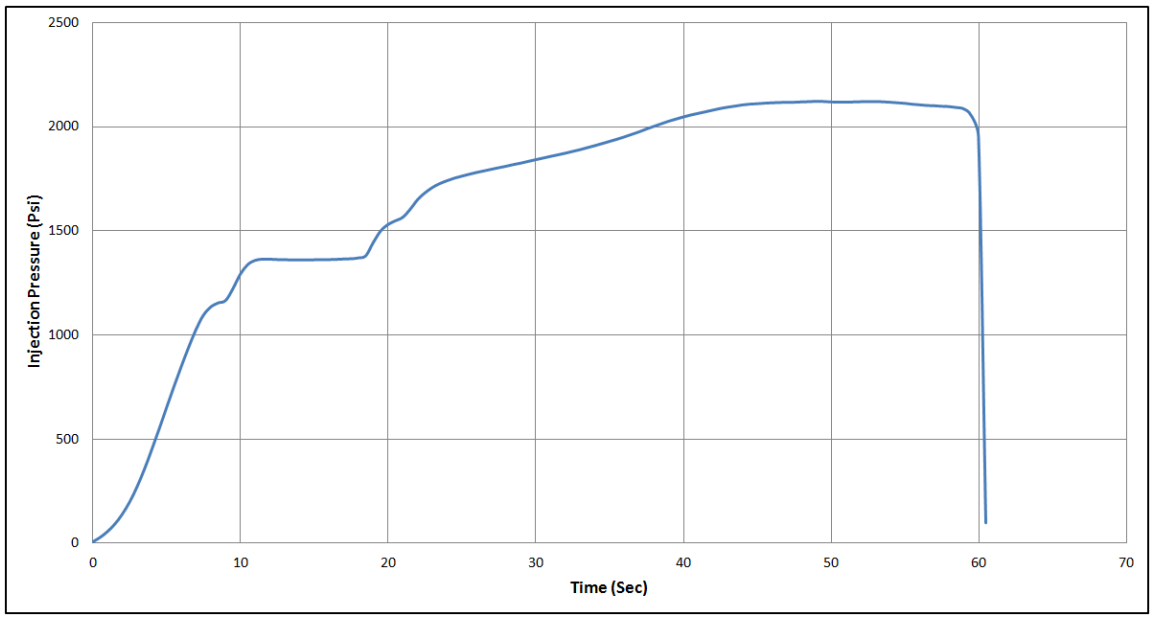

Figure 5.56. Injection pressure versus time for the third dolomite sample using water

Figure 5.57. Sandstone core sample used for fracturing test with 8% Bentonite

Fracture initiation pressure for this sample occurred at 1850 Psi and pressure increased until ultimate breakdown which happened at 1928 Psi pressure. Shortly after the first cycle, the second injection was conducted shortly and ultimate reopening pressure was recorded at 1794 Psi. The pressure difference between the two peaks can be explained by the tensile strength of the sandstone; the average value from conducted Brazilian tests reported to be 377 Psi. According to the theoretical equation, it was expected to observe the reopening pressure at 1551 Psi (tensile strength subtracted from original pressure breakdown).

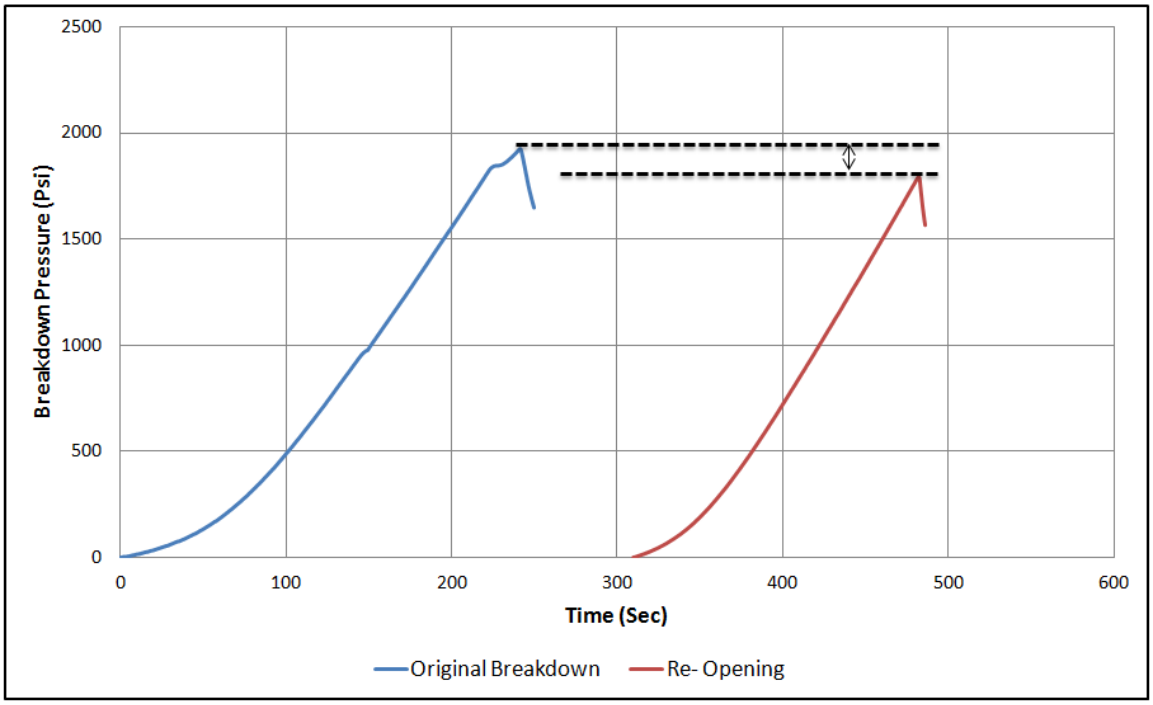

Figure 5.58. Injection pressure versus time for the first sandstone sample using 8% Bentonite mud

However, due to fracture healing caused by 8% Bentonite, higher reopening pressure can be justified. This indicates using only 8% Bentonite (without any LCM) can

result in about a 243 psi strengthening effect. In addition, lower pressure breakdown was observed for sandstone when compared with dolomite using similar mud. This is due to much lower permeability in dolomite compared to sandstone which provides a perfect non-penetrating condition in the dolomite sample.

Another important observation is the difference between the breakdown pressures by the theoretical Kirsch solution similar to the test on the dolomite sample. The pressure obtained from the theoretical Kirsch solution ($P_{breakdown} = 2\times200+T_0 = 400+377 = 777$ Psi). This is much lower than what was obtained from the laboratory experiments (1928 Psi). To justify pressure difference affected by wellbore size, the scaling relationship from DEA-13 experiments was used.

Figure 5.59 illustrates the wellbore breakdown pressure obtained from the previous numerical linear elastic model for the 8.5 inch wellbore, breakdown pressure obtained from the laboratory experiment for the 0.5 inch wellbore and the scaled up result for 0.5 inch wellbore based on DEA-13 experiments.

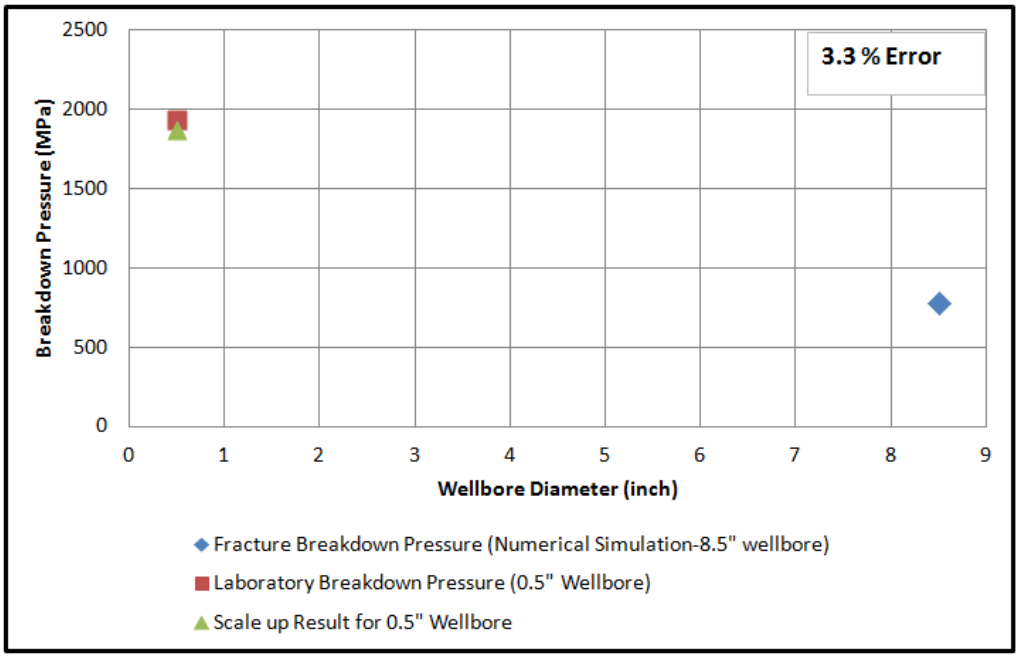

Figure 5.59. DEA-13 correlation has been used for scaling up fracture breakdown pressure in larger borehole diameters

A very good agreement between lab and correlated results exists (3.3 % error). This is a very important observation in predicting the accurate fracture breakdown pressure based on wellbore diameter and explains very well why smaller borehole sizes have less stability problems compared to larger borehole diameters (van den Hoek et al., 1994).

Similar observations have been reported by others for predicting rock strength from laboratory experiments (van den Hoek et al., 1994 and Collins, 2002). They have examined the scale effect on a hollow cylinder. For a rock friction angle of $\phi = 30^o$, the scale effect was:

$$\sigma_f \propto (2*R_W)^{-m} \tag{5.2}$$

where σ_f is the confining stress at failure and m=0.3333 or 0.2667, depending on the failure mode. For a wellbore diameter of 8.5 inches, this will result in a drop to 39% to 47% of the failure stress of the 0.5 inch inner diameter specimen. Figure 5.60 shows borehole collapse results on Castlegate, Berea and Red Wilmore sandstones, which clearly indicates smaller borehole diameters have higher collapse strengths. Although a size effect is quite common in rock mechanics testing, not much work conducted in studying the size dependency of the wellbore breakdown pressure.

5.4.5. Collecting Input Data. Input data for a finite-element model includes Young's modulus, tensile strength, porosity, permeability, fracture toughness, injection rate, and drilling fluid rheological properties. Table 5.8 shows the input data obtained for Sandstone. Young's modulus was obtained from correlation existing between UCS and Young's modulus (Nygaard et al., 2007):

$$UCS = 9.4E^{0.7} \tag{5.3}$$

The UCS value was measured by the triaxial cell setup existing in the McNutt Hall drilling lab and the average value of UCS is reported in Table 5.8. Fracture toughness was calculated from the empirical correlation existing between Brazilian tensile strength and the fracture toughness given the Equation 4.35 in the previous section.

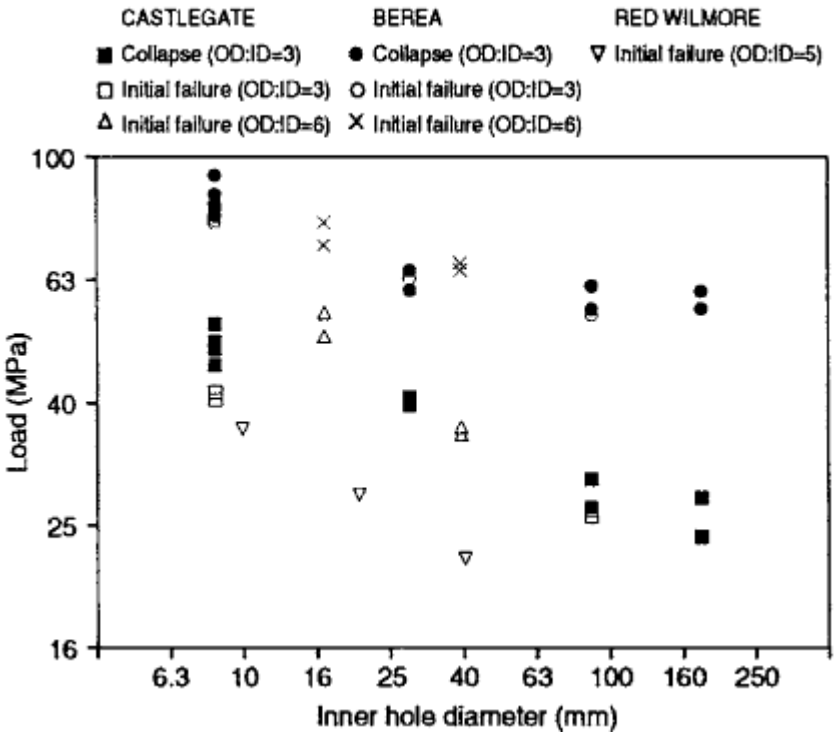

Figure 5.60. Hollow cylinder collapse strength and initial failure for different inner borehole diameters in sandstones (Taken from van den Hoek et al., 1994)

Table 5.8. Sandstone rock properties measured by laboratory experiments

Roubidoux Sandstone Properties	
Permeability (mD)	63
Porosity (%)	15
Average UCS (Psi)	12325
Young Modulus (MMPsi)	3.32
Poisson's Ratio	0.25
Fracture Toughness (Psi*inch^(0.5))	387
Average Brazilian Tensile Strength (Psi)	377

Table 5.9 shows drilling fluid properties of 8 % Bentonite used for the fracture test on the sandstone sample.

Table 5.9. Rheological properties of 8% Bentonite mud

8% Bentonite Mud							
θ_{300}	θ_{600}	Mw (ppg)	f_c (eq cp.)	y	Filtrate (30 min, ml)	PV (CP)	YP Lbf/100ft2
29	50	8.7	111	0.78	11	21	8

5.4.6. Finite-element Model. Three-dimensional finite-element models (FE models) were constructed with the similar dimensions compared to the core samples using quadratic elements and increasing mesh density in the near wellbore region (Figure 5.61). Due to symmetry conditions, the model was cut in half and symmetry boundary conditions were used (Figure 5.62). Similar to previous models, near wellbore stresses were imposed by removing wellbore elements and having overburden and confining pressures applied to all elements in the FE model.

Data obtained from laboratory experiments (Table 5.8) was used in the numerical model. The fluid flow model in the cohesive elements was based on the power law drilling fluid model in Table 5.9. Filter cake permeability was defined and calculated based on the results from the filter-press test.

The goal here is to compare the results obtained from the last experiment on the sandstone sample with numerical simulations. Since tensile strength of the sandstone has been measured in lab tests, this information can be used for defining fracture initiation criteria in the model. No laboratory experiment was conducted for the tensile strength of the dolomite sample.

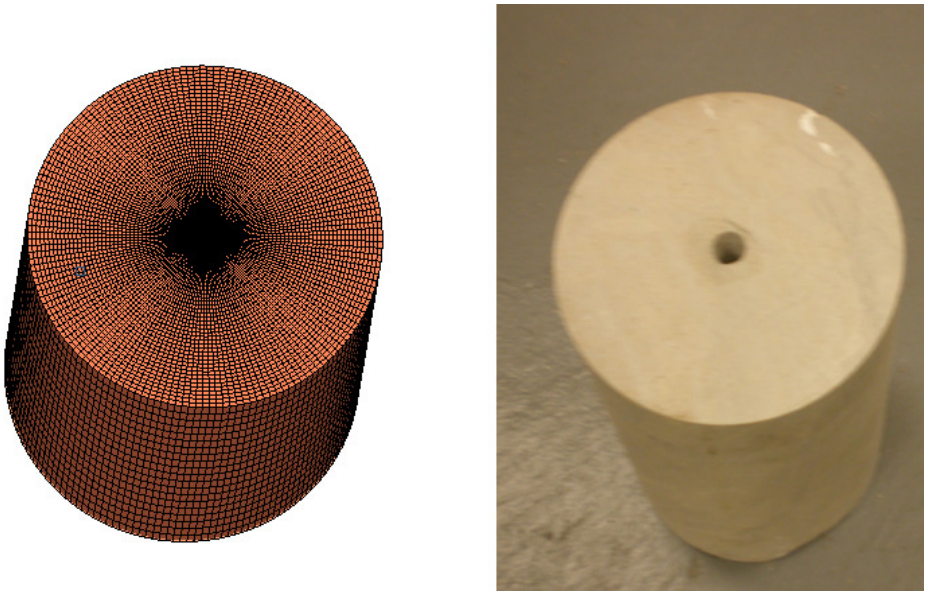

Figure 5.61. FE models were constructed with the similar dimensions compared to core samples

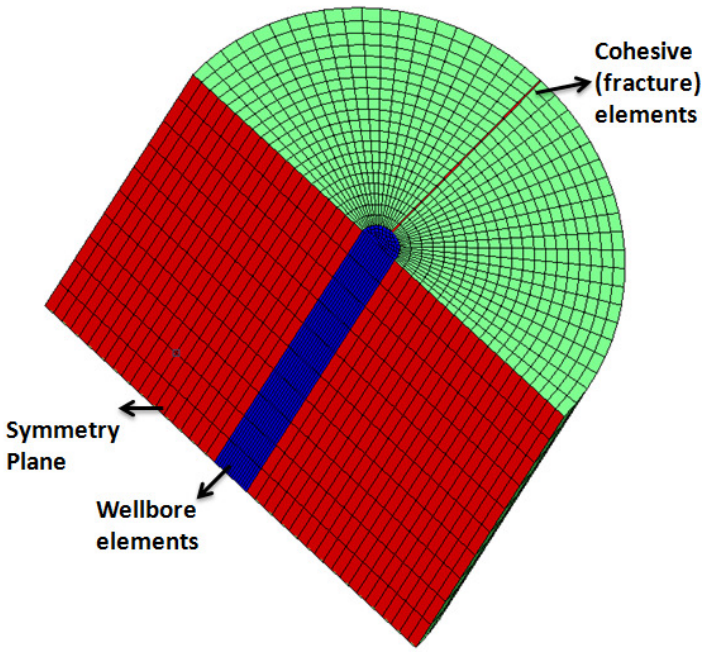

Figure 5.62. Half model used in simulations because of symmetry conditions

The time to reach tensile strength of the rock and fracture initiation can be predicted from the numerical results. This information then can be compared with the wellbore breakdown time which is 242 sec (4 min) with 5ml/min injection rate (Figure 5.58).

5.4.7. Simulation's Results. As mentioned in the previous section, fracture initiation refers to the beginning of the degradation of the response of a material. Specifically, when normal stress in fracture elements reach the tensile strength of the rock, the fracture starts to initiate in the model. Figure 5.63 shows that at t=345 sec, normal stress in the wellbore wall's cohesive element reach the tensile strength value (377 Psi or 2.6 Mpa). At this point, as more fluid is pumped into the fracture, it starts to propagate and the width of fracture enlarges.

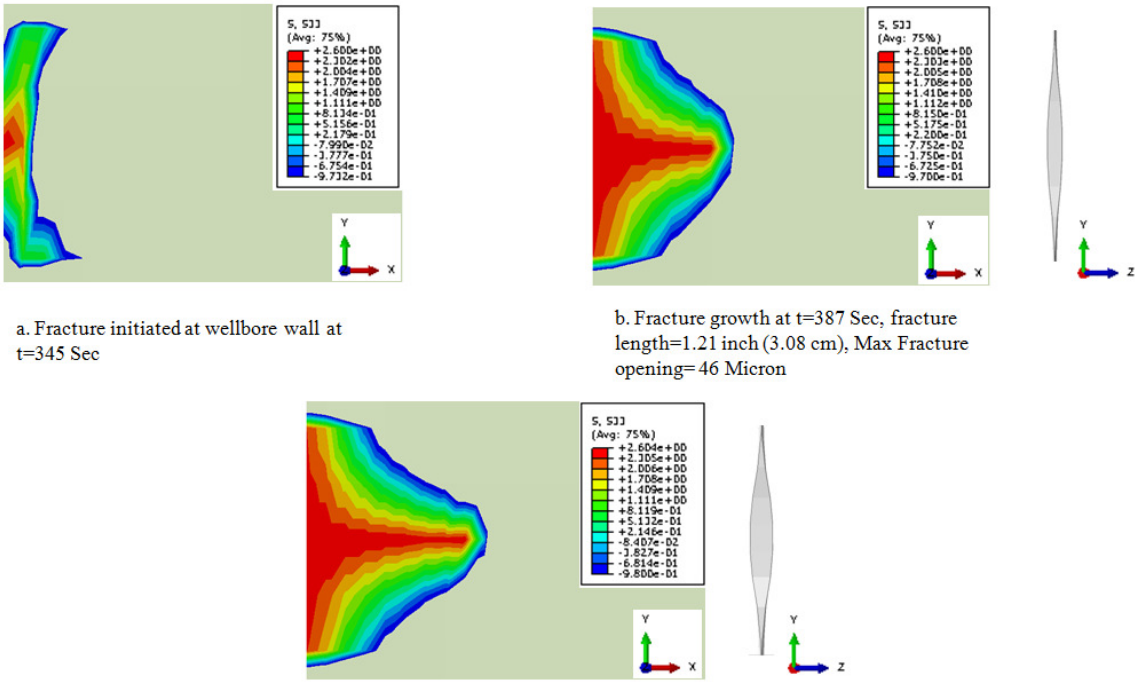

a. Fracture initiated at wellbore wall at t=345 Sec

b. Fracture growth at t=387 Sec, fracture length=1.21 inch (3.08 cm), Max Fracture opening= 46 Micron

c. Fracture growth at t=413 Sec, fracture length=1.49 inch (3.78 cm), Max Fracture opening= 56 Micron

Figure 5.63. a. Fracture initiation at t=345 Sec, b and c. Propagation of hydraulic fracture in simulated sample at t=387 Sec and t=413 Sec, respectively

The second shot is taken at t=387 sec, when fracture has a fracture length of 1.21 inch and the maximum width of the fracture is 46 Micron. And the final shot was taken at t=413 sec, where the fracture length reached 1.49 inch and the maximum fracture opening is 56 micron. Figure 5.64 shows pore pressure profile and the maximum fracture opening at injection zone.

The time required for fracture initiation and breakdown from the numerical simulation is 103 seconds more that what actually was observed from laboratory experiments. The difference in time is because of two uncertainties in the values used in the numerical simulations. These uncertainties are related to the lab experiments:

- Actual permeability of the near wellbore
- Actual injection rate inside the wellbore

These uncertainties rise from the experiment set up and procedure. Before running each experiment using drilling fluid, the procedure was to flush and circulate mud into the wellbore in order to build up an impermeable filter cake in the wellbore. This occurred before starting the fracture test. This phenomenon was not reflected in the simulations, because it is not clear to which order of magnitude permeability should be reduced in the near-wellbore region of the model. Furthermore, this effect only has to be included as a very thin layer on the borehole wall to consider the effects of the initial mud cake.

Due to the uncertainty in permeability, the amount of drilling fluid's leak off into the formation in the numerical simulations is higher than in the actual experiment. This condition will increase the time required for the fracture initiation in the model.

The other uncertainty is the injection rate which is read at the pump outlet before going through the accumulator unit and injection lines. Having 5ml/min injection rate at pump outlet may not be the exact injection rate into the wellbore. Friction effects caused by pumping mud through accumulator pads and injection lines might change the rate of injection inside the wellbore.

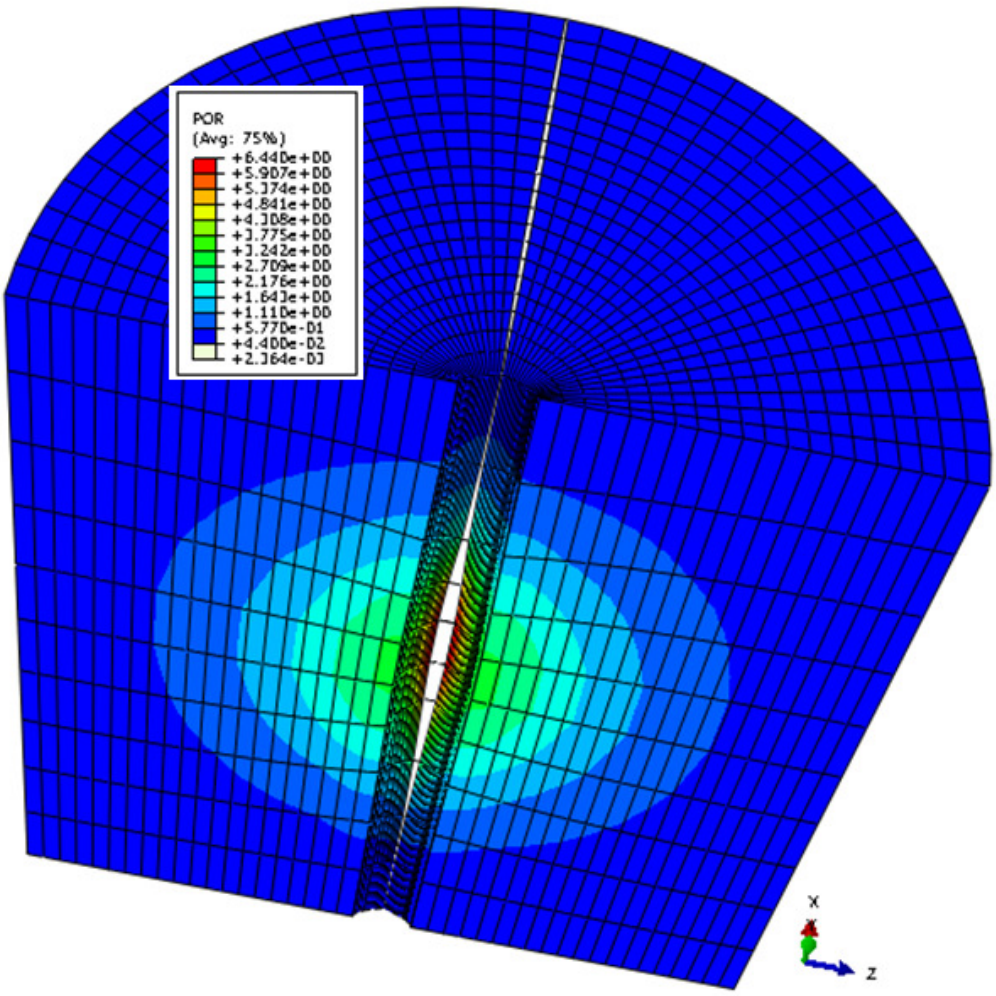

Figure 5.64. Pore pressure in the model at the end of simulation (t=693 Sec) and maximum fracture opening (95 Micron) at wellbore wall (Magnified deformation)

In order to get more accuracy from numerical models, two modifications should be made. First, one extra flow sensor should be placed at the wellbore inlet in order to accurately read the injection rate inside the wellbore. Second, surface elements should be included in the numerical model defining lower permeability at the wellbore wall as illustrated in Figure 5.65. Further simulations must be conducted defining permeability values in the near wellbore and to verify fracture initiation time.

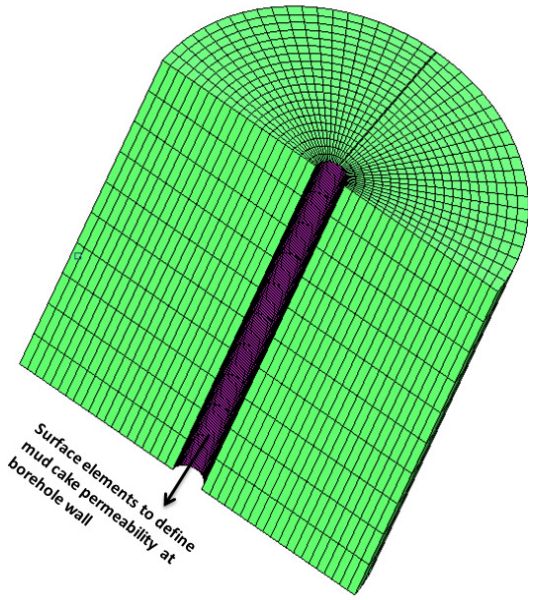

Figure 5.65. Surface elements should be defined at borehole wall in order to define mud cake permeability for future work

5.5. SUMMARY

This section can be summarized into three main sections:

- Predicting fracture geometry and fracture parametric studies
- Hoop stress changes after fracture initiation, propagation and sealing
- Laboratory experiments and lab finite-element models

Results from fracture parametric studies indicated the importance of Young's modulus and permeability as the most important parameters affecting fracture width. It was also found that knowledge of fracture width at the wellbore wall is very critical since fractures in different samples show similar width at fracture width.

Results from hoop stress changes at each step presented in this section indicate that wellbore strengthening is not able to increase wellbore hoop stress more than its ideal condition defined by the Kirsch solution. However, analytical solutions confirm that the

existence of sealant in the fracture is able to enhance fracture propagation pressure when reopening induced fractures.

Simulations results also indicate strong effects of Poisson's ratio and stress anisotropy on hoop stress restoration. Using analytical solutions indicate the importance of having a suitable non-invaded zone in the fracture in order to prevent further propagation of the fracture. This should be considered in current wellbore strengthening applications which rely on the proactive mud program and particles to wedge into the fracture mouth in order to increase wellbore hoop stress.

The laboratory experiment's results gave the following observations. Scaling effect is very significant; borehole breakdown pressure from laboratory experiments are much higher than what was predicted from the Kirsch solution. Using the scaling law from DEA-13 experiments gives a good approximation between the theoretical value in the 8.5 inch wellbore and 0.5 inch wellbore lab experiments.

Permeability of the formation can significantly change the wellbore breakdown pressure. Results from fracture tests on the dolomite sample were much higher than sandstone samples. Furthermore, having pre-existing fractures in the formation can significantly lower the wellbore breakdown pressure. So, naturally existing fractures is one of the primary reasons for having lost circulation unexpectedly.

Results from finite-element simulations to match laboratory experiments are close. However, it takes more time in simulations to reach fracture initiation than actual experiments. Two important uncertainties govern this difference: permeability of the filter cake at the wellbore wall and actual injection rate in the wellbore. Some modifications in the laboratory set up and the numerical model are required in order to accurately match the results.

6. DISCUSSION

Numerical results verified hoop stress restoration by fracture sealing as shown in Figure 5.34 and field cases presented in Section 5.3. However hoop, stress increase more than the ideal case (wellbore without fracture) was not verified (as seen in Figure 5.34). The important concept here is to find or establish the ideal hoop stress or the ideal fracture gradient represented as the Kirsch solution for a non-fractured material a wellbore can have and then compare it with the fracture gradient achieved after conducting wellbore strengthening. This is especially critical in an operational sense when the upper limit or ideal fracture gradient is unknown due to the unavailability of extended leak off tests (XLOT). Often the results published for a successful wellbore strengthening operation consider the ideal fracture gradient based on leak off tests (LOT) or mini-frac results (as seen in Section 5.3). To better understand this misconception, this section will begin with a discussion on leak off tests and/or extended leak off tests which give valuable information on the wellbore condition and how this will change the practical implications of wellbore strengthening. Two field case examples for wellbore strengthening in the Gulf of Mexico will be presented wherein the first case shows how results from LOT can mislead in establishing an ideal fracture gradient and the wellbore condition. In the second example, the results after conducting wellbore strengthening are compared with the Kirsch solution for the ideal fracture gradient.

In addition, a new methodology to identify the lost circulation type is presented when having limited geomechanics input data. This is followed by relevant field case examples.

6.1. LEAK OFF TEST

To identify the fracture pressure gradient in the formation leak off tests, extended leak off tests (XLOT) or mini-frac tests can be conducted. These tests are normally conducted after a cement job to ensure the pressure integrity of the shoe. For a leak off test, a volume is pumped slowly with a constant flow rate into a few feet of formation below the casing shoe. The pressure and volume readings are plotted until the linear

pressure versus volume response shows a distinct break in the curve (Figure 6.1). If a mini-frac or XLOT (Figure 6.2 and Figure 6.3) test is conducted pumping is continued until a clear formation breakdown is seen and pumping is continued to identify fracture propagation pressure before pumping is stopped. When the pressure is stopped, the frictional dynamic loss for the pumping fracture is lost and pressure is bled off. The instantaneous shut in pressure and fracture closure pressure can be recorded (Raaen et al., 2006 and Warpinski et al., 1998). For a mini-frac or extended leak off test, the instantaneous fracture pressure or fracture closure pressure can be used to estimate the least horizontal stress value. See Fjaer et al., (2009) for a review of the different methods to interpret the minimum horizontal stress from XLOT and mini-frac tests.

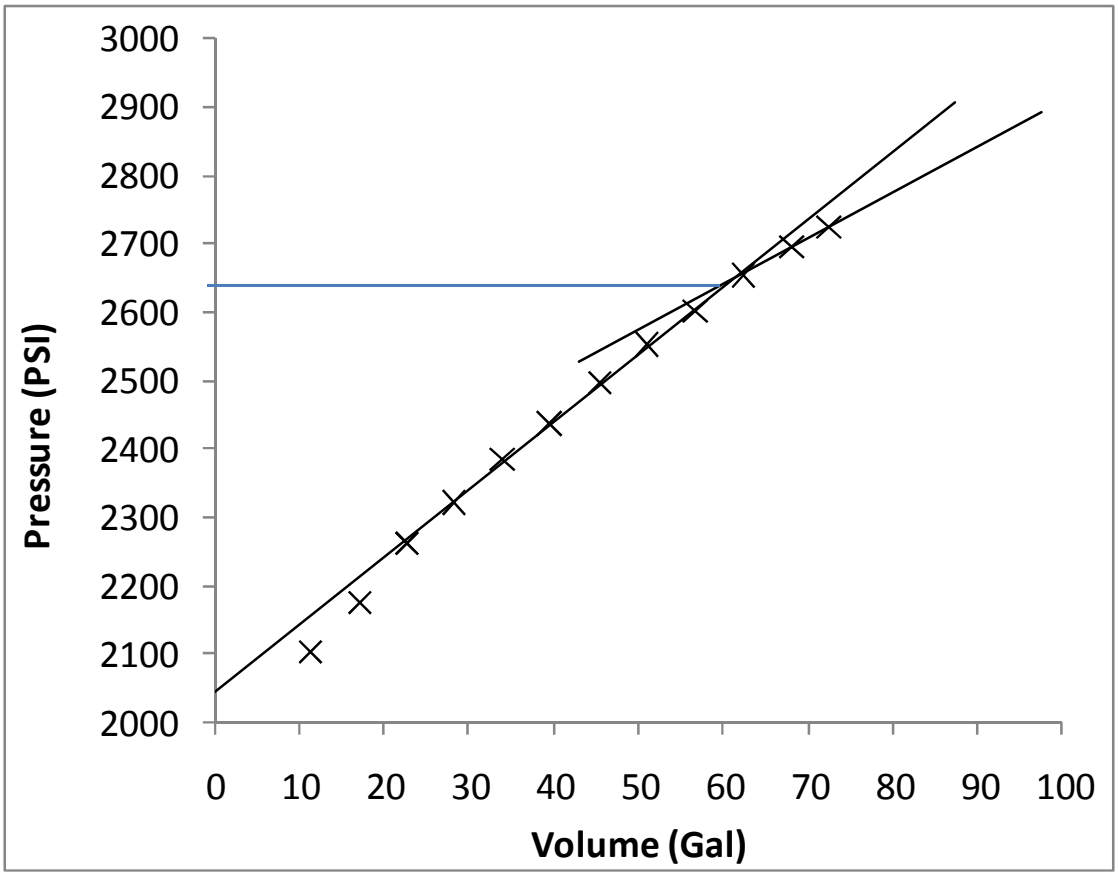

Figure 6.1. Leak off test from Southern North Sea

The break in the linear trend seen in the leak off test in Figure 6.1 at 2653 psi is the leak off point (LOP). The leak off point is the onset of fracture initiation and not where the ultimate fracture breakdown pressure is reached as determined by the Kirsch solution (for non-penetrating fluid):

$$P_{frac} = 3\sigma_h - \sigma_H - P_p + T_0 \tag{6.1}$$

The onset of fracture initiation can be influenced by drilling induced fractures, breakout of parts of the wellbore, chemical reactions occurring between drilling fluids and formations, fluid pressure drop in filter cake, filter cake plasticity and drilling fluid type, formation plasticity (Aadnoy and Belayneh, 2008, Morita et al., 1990). Actually, the fracture model given in Equation 6.1 assumes that there should not be any LOP. The model estimates a deformation to appear linear elastically until fracture point is reached. Figure 6.2 shows an extended leak off test where the ultimate fracture strength is reached without any leak off point to be determined. The ultimate fracture strength occurs at 1855 psi. When the fracture propagates further, the fracture has overcome the hoop stresses close to the wellbore, and 1285 psi is required to further propagate the fracture. The least horizontal stress can be estimated based on the ISIP or change of slope in the bleed back phase of the XLOT test.

Figure 6.3 shows an extended leak off test where the fracture initiation pressure is 3400 psi and ultimate fracture strength is 3625 psi (Oekland et al., 2002). For the second pressure test cycle, fracture initiate pressure is significantly less than the initial maximum fracture pressure. When the fracture is reopened in the second pressure cycle, the tensile strength in the rock is destroyed. Further, a clearer leak off point is seen in the second curve before reaching the maximum fracture pressure of 3045 psi. The difference of 580 psi will be an upper measure of the tensile strength of the rock. In addition to breaking down the tensile strength of the rock, an existing fracture might be hydraulically open and to further propagate the fracture, the pressure needs only to be bigger than the least horizontal stress (when neglecting friction and fluid losses). Figure 6.4 shows the XLOT test from the next well drilled, where the fracture initiation pressure is around 2975 psi, which is significantly less than the fracture breakdown pressure of the first well in Figure 6.4. The fracture initiation pressure is approximately the same as the fracture reopening

for the second fracture cycle and comparable to the fracture reopening pressure of the first well. The leak off test from well 10-8 in Figure 6.4 shows clearly that the leak off tests can represent a value close to the fracture propagation pressure in an already damaged formation with preexisting fractures. The fracture initiation pressure value from LOT tests can be controlled by fractures or weakness planes and give significantly lower values than expected.

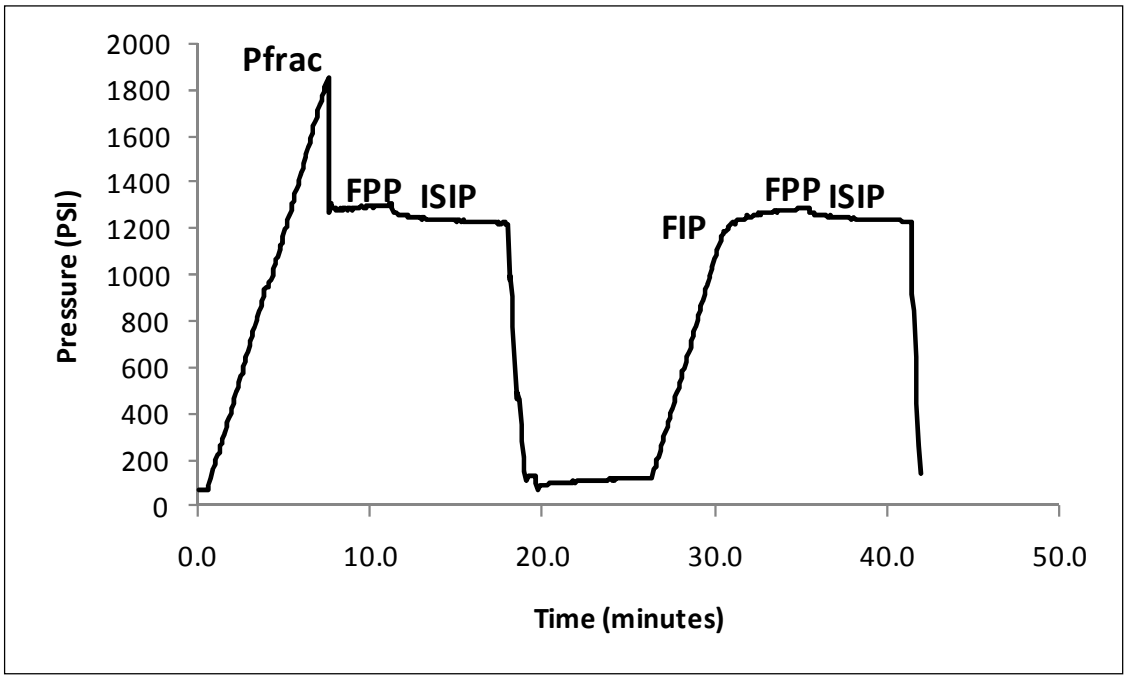

Figure 6.2. XLOT test from Southern North Sea (Oekland et al., 2002)

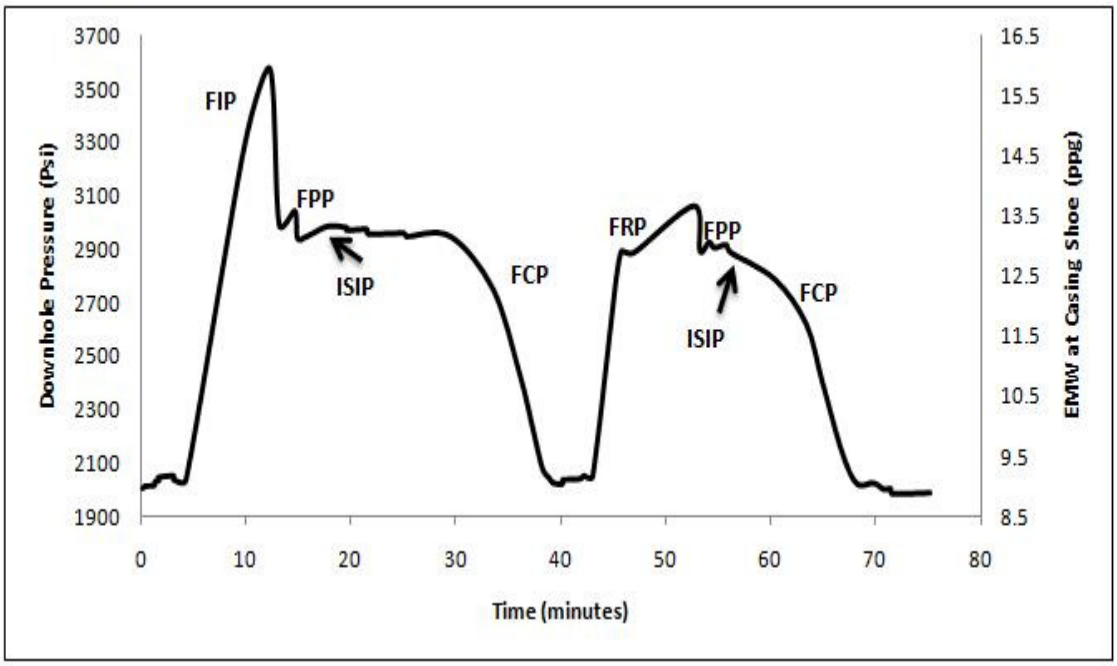

Figure 6.3. XLOT test well 10-7 in the Norne field (Oekland et al., 2002)

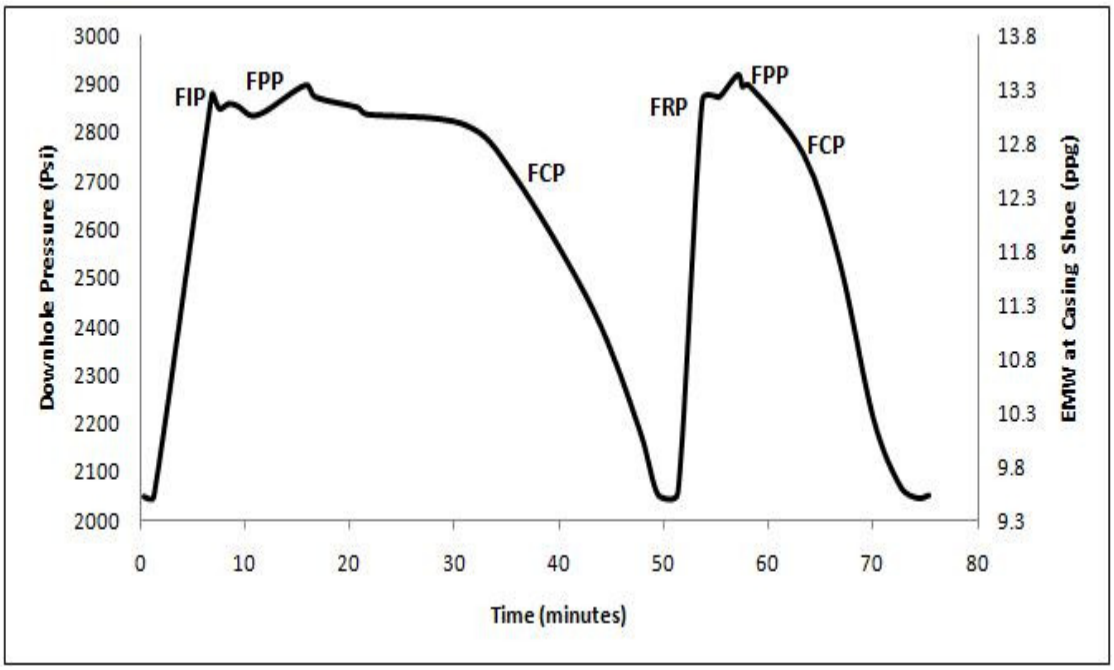

Figure 6.4. XLOT test well 10-8 in the Norne field (Oekland et al., 2002)

As seen above, the wellbore condition will greatly control what a leak off test will measure. If an extended leak off test is performed, it is easier to identify the actual physical condition of the wellbore. Figure 6.5 summarizes the different wellbore conditions and what measurement can be obtained from a LOT or XLOT. For an intact borehole, the leak off test has to exceed the elevated effective hoop stress and tensile strength before fracture propagation starts. If a small fracture appears at the wellbore wall, the tensile strength has been overcome, but hoop stresses still prevent fractures to propagate. However, for a situation where a large fracture exists around the wellbore, the hoop stress reduces to the least horizontal stress perpendicular to the fracture far away from the wellbore. In this situation, the LOT test will break off when the fracture starts to propagate; and therefore, the LOT is measuring the least horizontal stress. The last wellbore condition in Figure 6.5 is when a fracture has propagated to intersect with vugs and / or natural fractures. In this situation, LOT measures only the pore pressure gradient. The upper limit of the fracture gradient for the intact wellbore where both hoop stress and tensile strength contributes to the fracture resistance is given by Equation 6.1.

Naturally, existing fractures intersecting the wellbore will reduce the leak off gradient as seen in Figure 6.5. However, in most drilling operations XLOT is not performed and which of the situations in Figure 6.5 the LOT test represents is not easily determined. If LOT results are available from nearby wells, comparing the results can help in determine the wellbore integrity. When losses are experienced in a situation with larger fractures (the two lower situations on Figure 6.5), sealing off the fracture and void space with LCM material will stop losses. However, if drilling commences and losses continue because of the added pressure from annular friction pressure, the LCM material has to be placed so that the fracture is sealed off close to the wellbore wall. Near the wellbore wall the hoop stresses rise which can significantly increase the fracture pressure.

Figure 6.6 shows that for a 8.5 inch wellbore about one foot into the formation most of the hoop stress is gone. Therefore, it is required that the LCM material has a size distribution comparable to the fracture width of the fracture close to the wellbore wall.

Wellbore Condition	Leak Off Test Measurement
Intact Borehole 	$\sigma_{\theta\theta} - P_p + T_0$
Borehole with a very small fracture 	$\sigma_{\theta\theta} - P_p$
Borehole with a large propagated fracture in far field zone 	S_h
Borehole with a large propagated fracture which has cut vugs and natural fractures 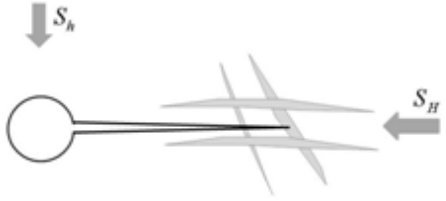	P_p

Figure 6.5. Effect of how different wellbore conditions change the interpretation of LOT

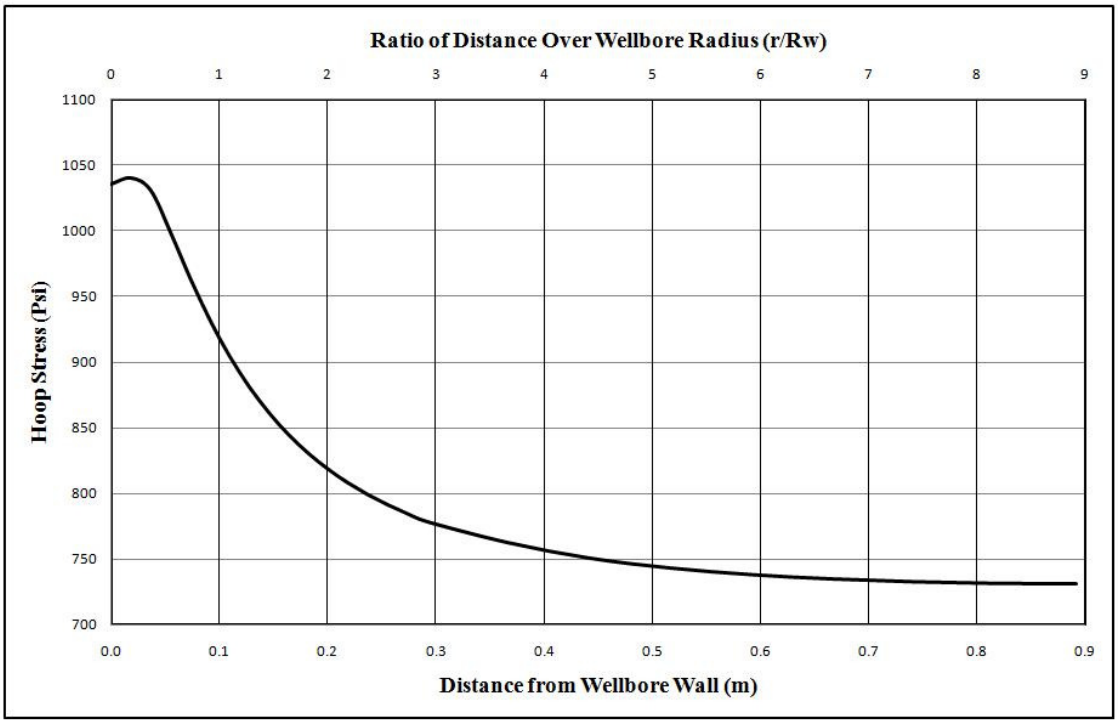

Figure 6.6. Wellbore hoop stress as a function of distance from the borehole wall (Poro-elastic conditions)

6.2. CRITICAL REVIEW OF WELLBORE STRENGETHENING (FIELD CASE STUDIES)

The aim of this section is to present two relevant field cases for wellbore strengthening. In the first case, the LOT results can mislead in establishing ideal fracture gradient and wellbore condition. In the second case, the fracture gradient achieved by wellbore strengthening is compared with the fracture gradient obtained from the Kirsch solution in an ideal wellbore with no fracture.

6.2.1. Case I- Western Shelf, Gulf of Mexico. The western shelf in the Gulf of Mexico is one of the most challenging areas in the world to drill due to HP/HT conditions, faulted formations, and depleted reservoirs. Lost circulation has been reported as one of the major problems in this region (Traugott et al., 2007).

A well has been drilled in this area to explore deep HPHT gas reservoirs. The well name and exact location has not been disclosed by the operators. Severe losses and kicks were encountered in the original drilling plan and before reaching target depth.

After unsuccessful sidetracks to pass the lost zone, it was decided to conduct wellbore strengthening or WPCI (wellbore pressure containment integrity) treatments in order to increase wellbore integrity.

Two weak zones were clearly identified before the wellbore strengthening job: One below the shoe at 17628 to 17710 ft measured depth (16038 TVD), and the other at 18480 to 18520 ft measured depth (16679). Before treatments, maximum mud weight of 18 ppg was not enough to hold back the lower producing sand; and as the mud weight increased, the well started to lose mud in the upper weak zone (Traugott et al., 2007).

Two treatments were planned and used in the weak zones, and the wellbore pressure integrity was increased from 18.26 to 19.1 ppg. No losses were reported after treatments and when reached TD (Total depth). Figure 6.7 shows the LOT results before treatments, after first treatment, and after the second treatment. The analysis is based on pressure readings for the entire 852 ft open hole before and after treatments.

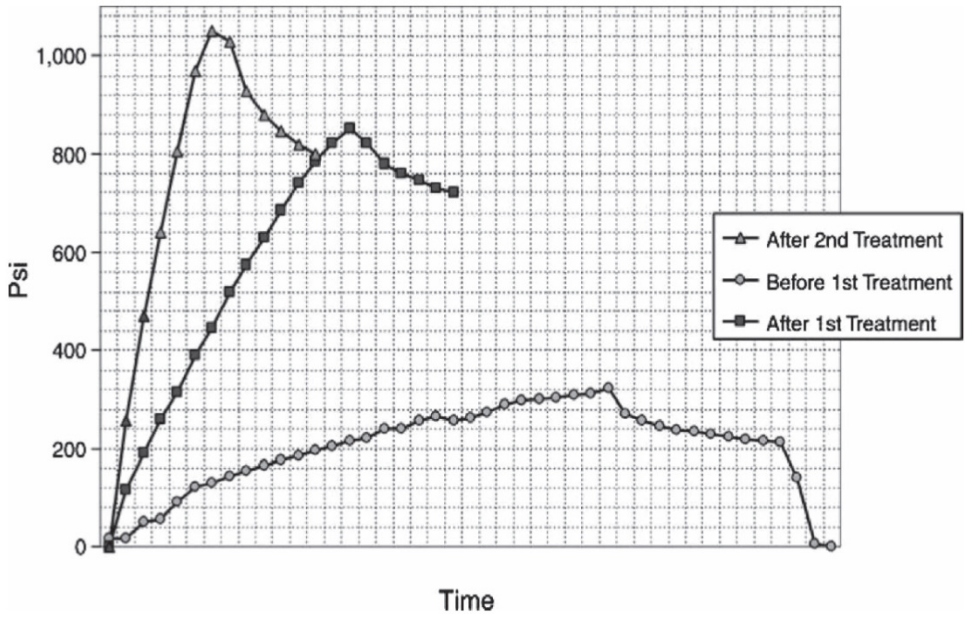

Figure 6.7. LOT data for open hole section before treatment, after the first treatment, and after the second treatment (Taken from Traugott et al., 2007)

Further analysis of Figure 6.7 indicates that LOT after the first treatment cannot be representative of the fracture gradient for the intact wellbore and which of the situations in Figure 6.5 the LOT test represents is not easy to determine. The misconception here is to consider these results as a proof for the wellbore strengthening operation to increase wellbore hoop stress beyond its ideal value. Increase in the fracture gradient after treatments might have been achieved by restoring wellbore hoop stress where the upper limit is not clear. Unfortunately, no geomechanical data was reported in order to calculate the ideal fracture gradient by using analytical solutions.

6.2.2. Case II- Mississippi Canyon, Gulf of Mexico. In 2008, Total E&P USA sidetracked a well in the Mississippi Canyon (Fett et al., 2008). Figure 6.8 shows the mud weight window for this well. A geomechanical study indicated that a 10.3 ppg mud weight is required to prevent borehole breakout in order to drill the reservoir section. As shown by Figure 6.8, because of depletion in this field, the fracture gradient has significantly dropped at depth 7200 ft. Using predicted mud weight would have greatly increased lost circulation in this zone, both while drilling the 8.5 inch hole and cementing 7 inch liner.

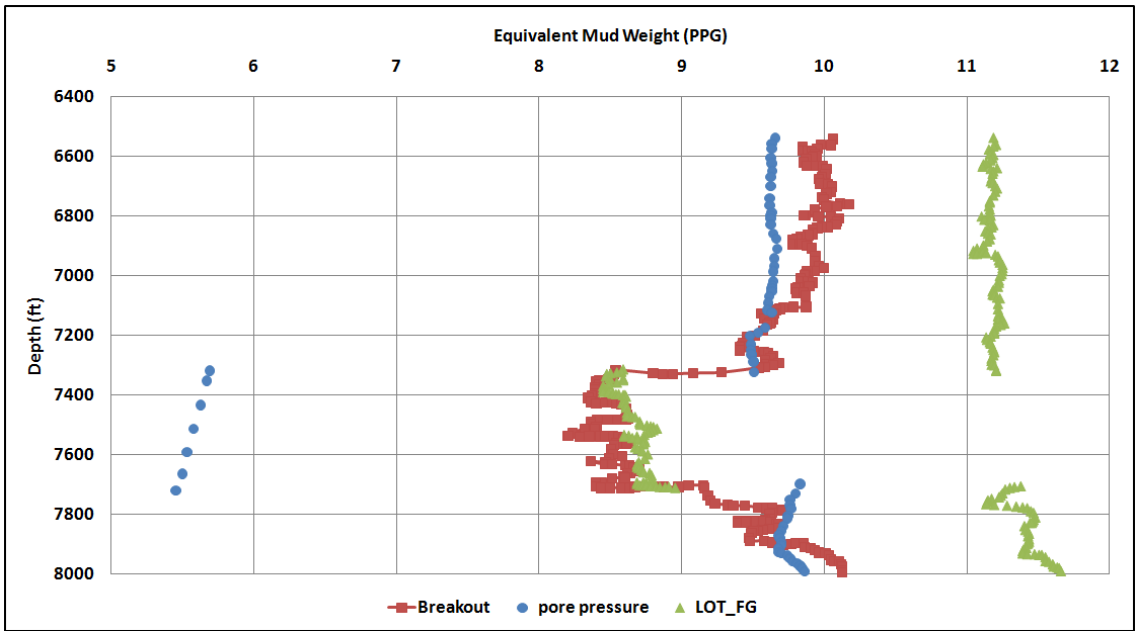

Figure 6.8. Reported pore pressure, fracture gradient and break outs for deep water well in Gulf of Mexico (Modified from Fett et al., 2010)

Laboratory tests from cores taken from offset wells indicated highly porous and permeable sands which are poorly consolidated. The idea of using SBM muds (synthetic based muds) using LCMs was bypassed to prevent formation damage into the producing reservoir. It was then decided to use a wellbore strengthening pill in order to strengthen the unconsolidated sand.

This was sidetracked in 8.5 inch hole and before reaching to the top of the sand reservoir; the drilling fluid system was treated with wellbore strengthening package. Figure 6.9 shows the ECD recorded when drilling the reservoir section. As shown by Figure 6.9, the maximum recorded ECD was approximately 11.1 ppg which is above the previous break down pressure estimated for this field. No losses were recorded while drilling this section. This proved that the wellbore was successfully strengthened.

A follow up geomechanics study was conducted for this well to calculate the theoretical breakdown pressure using the Kirsch solution. The calculated fracture gradient has been illustrated by the black line in Figure 6.9. Results indicate that this ideal fracture gradient (for intact wellbore without any fracture) is still higher than what was achieved by the wellbore strengthening application.

Although more field cases are required to draw a conclusion for the true upper limit of wellbore strengthening, these results, so far, support the conclusion from the numerical results where wellbore hoop stress after wellbore strengthening did not exceed ideal hoop stress for the intact wellbore. In addition, analysis based on LOT results cannot be reliable for predicting the achievable upper limit for wellbore strengthening.

6.3. IDENTIFYING FRACTURE TYPE

For pre-existing fractures it will be important to distinguish between mechanically open or closed fractures or hydraulically open or closed fractures. The formation can be brittle, so an existing fracture can stay hydraulically open even if there are normal forces acting above the fracture plane (Nygaard et al., 2006). When fractures are hydraulically open, losses might occur if the mudweight is higher than the pore pressure gradient. The mud will then displace the pore fluid in the open fracture volume.

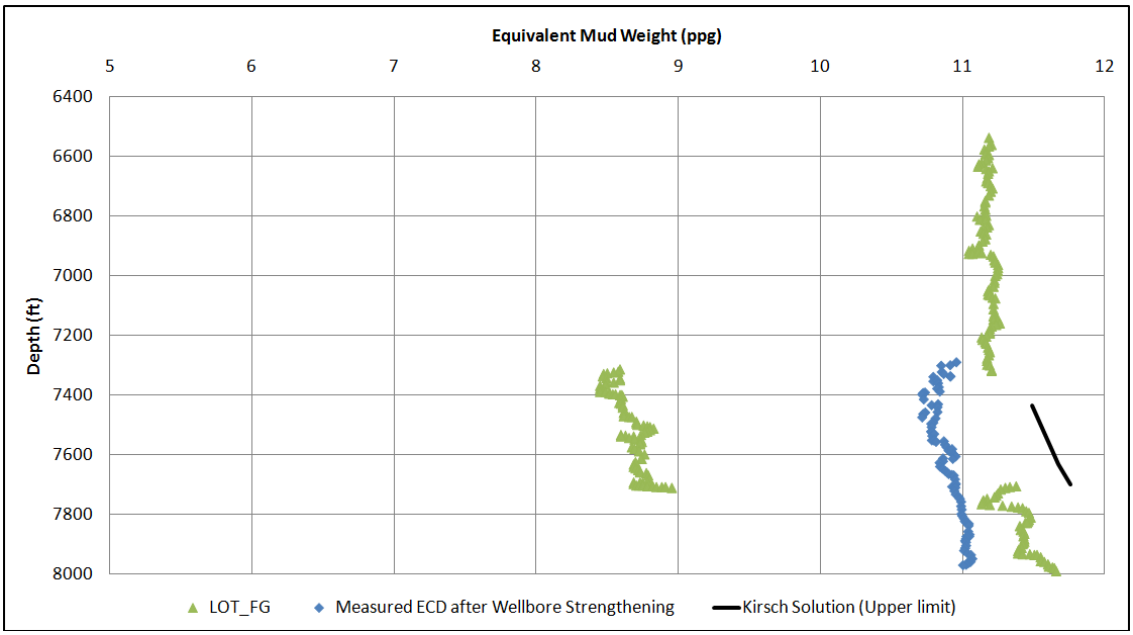

Figure 6.9. Measured ECD after wellbore strengthening application and fracture gradient calculated from the Kirsch solution

A simple criterion to evaluate if there is risk for experiencing hydraulically open fractures and experience losses with mud weights above pore pressure gradient is given as:

$$OCR = \frac{80.75 UCS^{0.55}}{\sigma_V - P_p} \tag{6.2}$$

Where OCR is overconsolidation ratio and UCS is unconfined compressive strength. OCR is a concept taken from soil mechanics which tells us how brittle the rock will be under current effective stresses. Details about OCR can be found for instance in Lambe and Whitman, 1979. If fractures naturally exist hydraulically open fractures are to be expected for OCR values above 2.5. UCS can be estimated from well logs, and numerous correlations have been developed between well logs and UCS (Chang et al., 2006). When experiencing losses in hydraulically open fractures, losses will continue until the fracture volume is filled up. To propagate or widen these fractures, the mudweight has to be above the least horizontal stress. Therefore, these losses will often

stop after some time, even if no lost circulation material is added or not. To better understand the concept above, some relevant field cases are presented.

In Appendix C some field cases with lost circulation incidents are presented. The main reason for lost circulation has been cited to be natural fractures or induced tensile fractures connected to open natural fractures.

7. SUMMARY, CONCLUSIONS, AND FUTURE WORK

This study developed finite-element simulations for modeling the fracturing process including fracture initiation, propagation and sealing. In addition, analytical models, field case studies and laboratory experiments were conducted to further support numerical simulations results. The main conclusions of this study can be summarized below.

The analysis presented in this dissertation concludes that the wellbore strengthening approach is not able to increase the wellbore hoop stress more than its ideal or intact case in the fracture zone. Hoop stress restoration is the main mechanism happening during fracture sealing, which, in none of the cases studies goes above the ideal wellbore hoop stress. This finding helps to know the limit of this technology in current and future field deployments. The maximum fracture gradient enhancement obtained from wellbore strengthening should not be expected to exceed the theoretical limit from the non-penetrating Kirsch solution. It is plausible that having an appropriate non-penetrating zone in a fracture helps to elevate the fracture propagation pressure when using enhanced water-based muds. However, it is very challenging to keep a sustainable fracture gradient increase above the theoretical limit by increasing fracture propagation pressure. The main issue is to keep the stable non-invaded zone (LCM) inside the fracture without them failing.

When planning and evaluating results of the lost circulation treatments or wellbore strengthening treatments, it is important to understand how the limitation of data is controlling the interpretation and understanding of the results. For instance, leak off tests do not give a good indication if the LOP represents the fracture breakdown pressure or fracture propagation pressure. Therefore, conducting XLOT tests where a more accurate reading of the minimum horizontal stress and the intact fracture breakdown pressure is imperative for understanding the type of losses occurring. In addition, well logs can be used to estimate if large losses are likely at low mud weights. If the OCR is above 2.5, losses should be planned for even when drilling with mud weights at or below minimum horizontal stress.

Fracture width is a critical data for wellbore strengthening application. Simulations of anticipated fracture width should be conducted so the particle size distribution of the lost circulation or wellbore strengthening material can be designed to seal off the fracture at the wellbore wall to take full effect of the elevated wellbore hoop stresses near the wellbore. The actual strength or stiffness of the particulate material seems to be of a lesser importance to change hoop stress restoration beyond the Kirsch solution. However, the material should be strong enough to withstand the pressure drop between the fracture and wellbore. In addition, sufficient strength is required to withstand the load when the formation collapses on the material. Furthermore, fracture tip is associated with high stress concentration. Effectively sealing this zone will be one of the primary mechanisms involved in increasing the fracture propagation pressure, which was also concluded using the analytical solution.

Parametric studies of fracture propagation indicate the strong effect of Young's modulus and rock permeability on fracture width. The fracture model presented here can predict the fracture geometry based on a pre-defined orientation. Contrary to the general belief that fracture width decreases uniformly from the mouth of the fracture to its tip, the results of the present study show that fractures are wider at the mouth; and they become narrow in a non-linear fashion along their length. Parametric studies of hoop stress restoration based on conducted field case studies indicate a strong effect of stress anisotropy and rock's Poisson's ratio. In the case of fracturing, increasing the mud weight from the equilibrium state might result in Poisson's effect on the stresses which has an effect on the amount of hoop stress restoration.

Results from laboratory experiments conducted for this study are in very good agreement with DEA-13 and GPRI laboratory experiments. Higher wellbore breakdown pressure rather than the theoretical prediction was observed in laboratory experiments due to scaling effects. Using the DEA-13 experiments correlation for the Berea sandstone sample resulted in a very good approximation. However, more work is required to develop a robust scaling law for current experiments. More than 200 Psi strengthening effect was observed in the sandstone sample when comparing the initial borehole breakdown pressure and the reopening pressure when considering average rock tensile strength. This may approve the fracture propagation pressure improvement by having a

non-invaded zone inside the fracture for water-based muds which, alternatively, explains wellbore strengthening mechanism.

A very high breakdown pressure was observed in the dolomite due to very low permeability, high tensile strength and the non-penetrating condition on the borehole wall. The experimental pressure test results from the sample with the pre-existing fracture had a lower breakdown pressure which did not occur sharply.

Results reported from laboratory experiments in this study are limited. Future work should include more experiments on sandstone using oil-based and synthetic based muds and different LCM materials in water-based muds to study fracture breakdown and reopening pressures. Furthermore, as mentioned in the first section, the wellbore strengthening effect has not been reported for shales due to their low permeability. Therefore, lab experiments should be extended for different shales.

The scaling relationship between laboratory experiments and field conditions should be developed. This requires drilling different borehole diameters on the sandstone and dolomite and fracture testing at similar conditions. It is expected to observe a similar trend to DEA-13 experiments on sandstone; however, the shape of the scaling's curve can be different in dolomite or shales due to permeability effects.

The current numerical model does not consider thermal effects in the simulations. Thermal effects caused by various drilling operations can significantly impact near wellbore stresses. For instance, in deep water drilling, temperature changes of the drilling fluid in the riser result in lower drilling fluid temperature at the bottom hole. Figure 7.1 shows results of the leak-off tests conducted at various drilling fluid temperatures (Gonzalez et al., 2004).

Tests were performed in an onshore well drilled in South Texas at the depth of 3000 ft. The water-based mud was first cooled down by ice and circulated until the bottom hole temperature reached 92 Degree Fahrenheit (F). The first test was conducted and LOT was 2435 Psi. In the next run, the mud was heated and circulated until BHT was 133^{o} F and the LOT was 2563 Psi, about 128 Psi difference from first test. For the final test, BHT was 153^{o} F and the LOT was 2675 Psi which is 240 Psi difference from the first test. These results indicate that thermal effects can be very significant especially if a narrow pore-fracture window exists or when drilling high temperature wells.

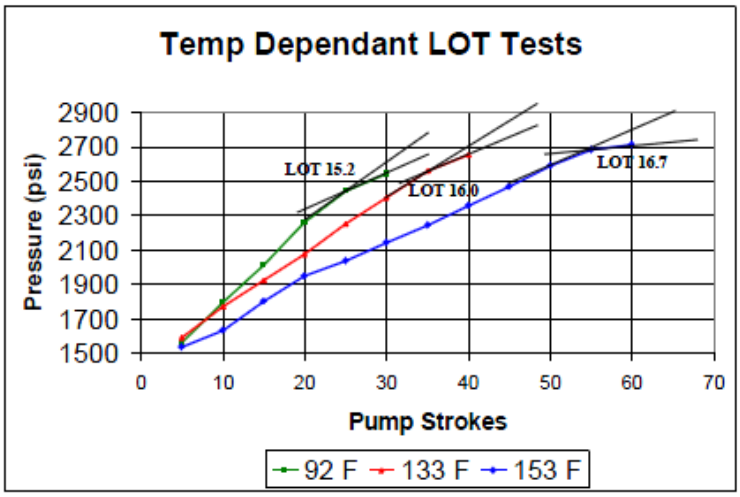

Figure 7.1. Leak off test results for various drilling fluids temperature at onshore Texas (Taken from Gonzalez et al., 2004)

It is highly recommended that future wellbore strengthening studies include thermal options in the numerical models and also, if possible, in near wellbore fracture experiments. The thermo-poro-elastic material model can be used in numerical simulations if thermal properties are also available.

Chemical and time-dependant effects in shales were not considered in this study. The chemical interactions can happen between drilling fluids and shale due to capillary effects, osmosis, convection, diffusion and ion flow (Mody and Hale, 1993, van Oort, 1997). These phenomenon can significantly affect near wellbore stresses which is the key for wellbore strengthening applications. Time-dependent effects may also happen due to filter cake build up and filter cake properties variation with time which again affects near wellbore stresses (Tran et al., 2010). Having an impermeable mud cake around the borehole will help to gain strengthening effect due to changes in effective stress concentrations around the wellbore (Abousleiman et al., 2007).

Another line of future work for wellbore strengthening will be wellbore breathing which is a lost circulation/well control related problem in the drilling industry, and the identification and treatment of this problem is still a critical issue (Ozdemirtas et al.,

2007). A limited number of studies has been published about the mechanism behind this phenomenon; not even a single study has linked this problem with wellbore strengthening technology. Field practices reported wellbore breathing as a common phenomenon when naturally fractured formations were intersected by the wellbore. Intensive numerical simulations studies with potential laboratory experiments design are required to investigate this effect in wellbore strengthening context.

Using nano-particles as LCM in the mud system have great potential to mitigate the lost circulation problem and emerge as an alternative wellbore strengthening approach. One main advantage with these particles is that they can be made as strong as steel due to their size, shape and chemical interactions (Singh and Ahmed, 2010 and Phuoc et al., 2009). Therefore, it is recommended to test these materials in the fracture experiments in order to verify the strengthening effect achieved.

Despite the limitations noted, the current poro-elastic model presented in this study could successfully investigate the physical mechanisms of wellbore strengthening. As noted in the literature, the chemical mechanisms of wellbore strengthening are still underutilized, and no successful field deployment has been reported. The model in this study was also capable to report fracture geometry (width, length and height) in wellbore strengthening applications. The developed model provides insight on critical parameters tied with strengthening applications. Furthermore, the conducted laboratory experiments, analytical models and field cases support the results obtained from numerical simulations.

APPENDIX A

ROCK FRACTURE PROPERTIES

Rock fracture mechanic tests are required to measure fracture properties. The following table represent reported values of fracture energy resistance in different rock samples.

Table A.1. Energy rate resistance for different rocks

Material	Energy rate resistance (Jm^{-2})	Method	Reference
Alpnach Sandstone	94	CENBB	Cooper (1977)
Arizona Sandstone	273	DCB	Perkins and Bartlett (1963)
Cardium Sandstone	105	WDCB	Peck et al. (1985b)
Berea Sandstone	20	RBT	Krech (1974)
Boise Sandstone	87	DCB	Perkins and Bartlett (1963)
Chilhowee Quartzite	62-126	SENB	Friedman et al. (1972)
Coconino Sandstone	50	SENB	Friedman et al. (1972)
Colorado Sandstone	192	DCB	Perkins and Bartlett (1963)
Fontainebleau Sandstone	15-54	DT	Darot et al. (1985)
Milsap Sandstone	227	DCB	Perkins and Bartlett (1963)
Portland Sandstone	73-81	WDCB	Barton (1981)
Sioux Quartzite	180-210	WDCB	Peck and Gordon (1982)
Tennessee Sandstone	76	SENB	Friedman et al. (1972)
Torpedo Sandstone	122	DCB	Perkins and Bartlett (1963)
Valdilliez Sandstone	98	CENBB	Cooper (1977)
Witwatersrand Quartzite	615	DynSENB	Dor et al. (1978)
Woodbine Sandstone	19	DCB	Perkins and Bartlett (1963)
Austin Limestone	15	DCB	Perkins and Bartlett (1963)
Carrara Marble	71	CENBB	Cooper (1977)
Carthage Limestone	78	DCB	Perkins and Bartlett (1963)
Danby Marble	80-100	SENB	Forootan-Rad and Moavenzadeh (1968)
Ekeberg marble	69		Lindqvist et al. (1984)

APPENDIX B

PREDICTING STABLE TIME INCREMENT FOR FULLY SATURATED FLOW

A simple guideline can be used for predicting the minimum stable time when simulating fluid flow in the fully saturated flow (Abaqus documentation):

$$\Delta t > \frac{\gamma_w (1+\beta V_w)}{6Ek}(1-\frac{E}{K_g})^2 (\Delta L)^2$$

Where

Δt : Time increment

γ_w : Specific weight of the wetting liquid

E : Young's modulus of the soil and/or rock

k : Permeability of the soil

V_w : Magnitude of the velocity of pore fluid

β : Velocity coefficient (zero in case of Darcy flow)

K_g : Bulk modulus of the solid grains

ΔL : Typical element dimension

APPENDIX C

USING OCR TO IDENTIFY HYDRAULIC FRACTURE TYPE

To identify whether the fractures are hydraulically open or closed, OCR values are calculated. Table C.1 shows the input value used for the OCR calculation and more details about lost circulation incident.

Table C.1. Lost circulation occurrence and calculated OCR

Field/Formation	**Depth of Lost (ft)**	**UCS (Psi)**	σ_V **(Psi)**	σ_H **(Psi)**	σ_h **(Psi)**	**Pp (Psi)**	**OCR**	**Hydraulic Fracture**
Indonesia (Gunung Kembang)	3280	1000	2855	3186	2400	1279	2.29	Closed
Offshore Nigeria (Intra-Biafra Shale)	6695	2974	5949	5176	4816	3447	2.63	Opened
Venezuela (San Joaquin Field)	9180	4500	9180	13495	7711	1700	1.1	Closed
North Sea Block 9/13 (Ness Field)	8750	6000	7400	6500	6000	4400	3.22	Opened

Gunung Kembang Field (Indonesia)

The Gunung Kembang Field, located in the South Extension area of Indonesia working areas, is a carbonate reservoir containing an oil column about 43 feet thick (Hudya et al., 2007). The thin oil column is positioned between a gas cap approximately 117 feet thick and a water aquifer. Evidence of natural fractures was found during early field development. While drilling well GK-6 HW by sidetracking already existing vertical well GK-6, severe losses to natural fractures were observed. During drilling of the pilot hole in the 8 ½ inch hole section, mud losses of approximately 45 bbl/hr occurred while using a mud weight of 11 ppg. Major losses occurred in the 6 inch hole section at a depth of ~4090 ft (3280 ft TVD).

Losses in the GK-6 Pilot wells were attributed to drilling with high Equivalent Circulating Densities (ECDs). In the Gunung Kembang Field, losses were common in wells drilled with ECDs ~12 ppg due to critically stressed natural fractures. Fluid losses in wells drilled with lower mud weights and ECDs, such as GK-6 HW, may have been caused due to overbalanced drilling in a depleted reservoir or drilling into large cavities or highly porous fault-breccia zones. *Calculated overconsolidation ratio (OCR) for the Gunung Kembang Field was 2.29, verifying the natural fractures were hydraulically closed.*

Intra-Biafra Shale (Offshore Nigeria)

Geology of the Niger River delta consists of unconsolidated sands of the Pleistocene Benin Formation, overlying the Pliocene Agbada Formation (Lowrey and Ottesen, 1995). The Qua Iboe member is predominately weak shale, whereas the Biafra members are firmer. Both formations are susceptible to mechanical instability. Normal faulting, with a major fault system of ENE-WSW represents the structural geology of the area.

Vertical well Oso 16B was planned to be drilled through the Intra-Biafra shale from 6,500 ft TVD to 10,700 ft TVD, using mud weights ranging from 12.5 ppg to 13.8 ppg. On a trip made at 7,581 ft MD, the well packed off and returns were lost at 7,109 ft MD (6695 ft TVD). Mud weight was reduced from 12.5 ppg to 11.5 ppg to regain full returns. After full returns were regained, mud weight was gradually increased to 13.8 ppg to reach TD.

Maximum hole enlargements of 19 inches through the Intra-Biafra occurred down to a depth of 9,000 ft TVD. Below this depth, hole size remained near gauge. Fluids were most likely lost due to the jarring and pumping process used while trying to free stuck pipe, which is a common issue in this area. Extreme pressures exerted on the wellbore during efforts to free pipe caused tensile fracturing, which led to lost returns. *Calculated OCR for Niger River delta was found to be 2.63, implying hydraulically opened fractures.*

San Joaquin Field (Venezuela)

The San Joaquin Field is located in the eastern part of Venezuela, in the central part of the state of Anzoátegui (Azeemuddin et al., 2006). This area is composed of high

compressive and tensile stresses that create significant rises and folds in the structure. Oficina Formation consists of gray to brownish-gray shales, light gray, fine to coarse-grained sandstones and siltstones, with thin lignites, ligntic shales, green to light-gray claystones, glauconitic sandstones, and thin limestones. Merecure Formation is made up of large, whitish-gray to pinkish-gray, quartizitic sandstones, with layers of light-colored shales and brownish siltstones. The San Juan Formation is mostly very hard, gray to light gray, fine to medium-grained, well-sorted sandstone beds ranging from 1 to 3 feet thick. The stress regime for both Merecure and San Juan was found to be strike slip.

Mud losses were recorded while drilling through the San Juan Formation at 9180 ft, while using a mud weight of 10 ppg. Losses were believed to have occurred due to tensile fractures that were created due to insufficient mud weight (Figure C.1). The drilling induced fracture shown in Figure C.1 is considered to be associated with a natural fracture present in the formation, causing lost circulation at that location. Losses did not occur when mud weight was decreased. *Calculated OCR was 1.1, indicating hydraulically closed fractures.*

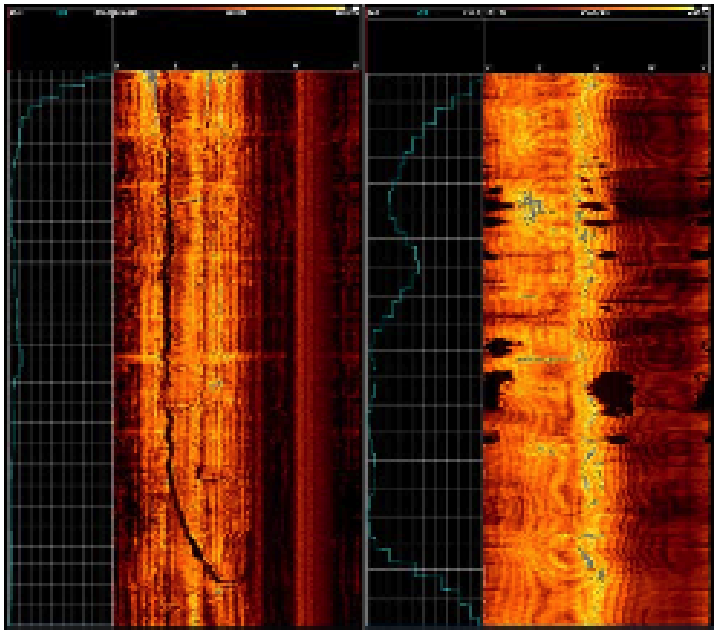

Figure C.1. Borehole image showing drilling induced fracture (left) and breakouts (right) from Azeemuddin et al., 2006

Ness Field (North Sea Block 9/13)

Block 9/13 is located in the west-central part of the Viking Graben in the U.K. sector of the North Sea (Ottesen and Kwakwa, 1991). The wellbore instability problems of Block 9/13 are related to the Paleocene and Jurassic shales present in the area. Structural geology of the area shows NNE oriented horst with westward tilted fault blocks.

Lost returns were experienced during cementing in some wells but not others, most likely because of the variation in the fracture gradient, as well as the depletion of the reservoir. With the depletion of the normally pressured reservoir and the need for a higher mud weight to stabilize the formation, the casing design was altered to better suit the conditions (Figure C.2). The new casing design allows the use of lower mud weights for most of the 12 ¼ inch hole section. *Calculated OCR for Block 9/13 was 3.22, signifying hydraulically opened fractures.*

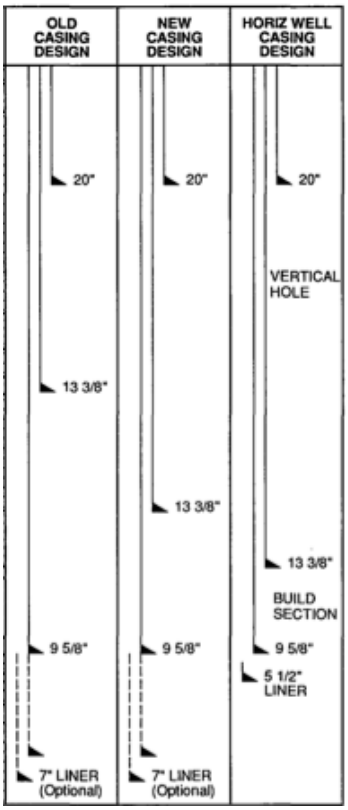

Figure C.2. Casing Design for well in Block 9/13 North Sea
(Ottesen and Kwakwa, 1991)

BIBLIOGRAPHY

Aadnoy, B. S., and Chenevert, M. E. 1987. Stability of Highly Inclined Boreholes. SPE Drilling Engineering, pp. 364- 418.

Aadnoy, B. S., and Belayneh, M., 2008. Design of Well Barriers to Combat Circulation Loss. SPE Drilling and Completion, 295-300.

Aadnoy, B. S.; Cooper, I.; Miska, S.Z.; Mitchell, R.F., and Payne, M. L. 2009. Advanced Drilling and Well Technology, SPE publications.

Aadnoy, B. S., and Belayneh, M. 2009. A New Fracture Model that Includes Load History, Temperature, and Poisson's Effects. SPE Drilling and Completion, pp. 452-455, September 2009.

Aadnoy, B.S., 1988. Modelling of the stability of highly inclined boreholes in anisotropic rock formations. SPE Drilling Eng., 259–268.

Aadnoy, B. S., Rogaland, U., and Chenevert, M. E. 1987. Stability of highly inclined boreholes. SPE/IADC 16052, SPE/IADC Drilling Conf., New Orleans, LA, Mar. 15–18.

Aadnoy, B. S., and Belayneh, M. 2004. Elasto-plastic fracturing model for wellbore stability using non-penetrating fluids. Journal of Petroleum Science and Engineering, 45, 179-192

Alberty, M. W., and McLean, M. R. 2004. A Physical Model for Stress Cages. SPE 90493, SPE Annual Technical Conference, Houston.

Alberty, M. W., and McLean, M. R. 2001. Fracture Gradients in Depleted Reservoirs-Drilling Wells in Late Reservoir Life. SPE/IADC 66740, Netherlands

Abousoleiman, N. Y., Nguyen, V., and Hemphill, T., M. Y. 2007. Time-Dependant Wellbore Strengthening in Chemically Active or Less Active Rock Formations. Paper AADE-07-NTCE-67 presented at the 2007 AADE National Technical Conference and Exhibition, Houston, 10-12 April.

Abou-Sayed, A. S., Brechtel, C. E., and Clifton, R. J. 1987. In Situ Stress Determination by Hydrofracturing: A Fracture Mechanics Approach, J. Geophys. Res., 83, 2851-2862.

Abaqus Documentation Manual, version 6.9, 2009.

Abe, H., Mura, T., and Keer, L.M. 1976. Growth Rate of a Penny-Shaped Crack in Hydraulic Fracture of Rocks. J. Geophys. Res., 81, No. 29, 5335-5340.

Advani, S. H., and Lee, J. K., 1982. Finite element simulations associated with hydraulic fracturing, SPE 8941.

Adachi, J., Siebrits, E., Peircec, A., and Desroches, J. 2007. Computer simulation of hydraulic fractures, International Journal of Rock Mechanics & Mining Sciences 44, pages: 739–757.

Anderson, T. L., 1995. Fracture Mechanics: Fundamentals and Applications. Second edition, CRC Publications, United States.

Aston, M. S., Alberty, M. W., Duncum, S., Bruton, J. R., Friedheim, J. E., and Sanders, M.W., 2007. A New Treatment for Wellbore Strengthening in Shale. SPE 110713, SPE Annual Technical Conference, Anaheim, California.

Atkinson, B. K. 1987. Fracture Mechanics of Rock. Academic Press publications (Academic press geology series).

Azeemuddin, M., Maya, D., Guzman, E. A. and Ong, S. H. 2006. Underbalanced Drilling Borehole Stability Evaluation and Implementation in Depleted Reservoirs, San Joaquin Field, Eastern Venezuela. IADC/SPE 99165. Presented at IADC/Drilling Conference, Miami, Florida, 21-23 February 2006.

Bannister, M., Shercliff, H., Bao, G., Zok, F., and Ashby, M. F. 1992. Toughening in brittle systems by ductile bridging ligaments. Acta Metallurgica et Materialia. Vol. 40, No. 7, 1531-1537.

Barenblatt, G. 1962. The mathematical theory of equilibrium of cracks in brittle fractures. Advanced Applied Mechanics; 7:55-129.

Benaissa, S., Bachelot, A., and Ong, S. 2006. Preventing Mud Losses and Differential Sticking by Altering Effective Stress of Depleted Sands. SPE 103816, Presented at the IADC/SPE Asia Pacific Technology Conference and Exhibition, Bangkok, Thailand, 13-15 November.

Benzeggagh, M. L., and Kenane, M. 1996. Measurement of Mixed Mode Delamination Fracture toughness of Unidirectional Glass/Epoxy Composites With Mixed-Mode Bending Apparatus. Composites Science and Technology 56:439-49

Biner, S. B. 1994. The role of interfaces on fracture and creep deformation behavior of brittle matrix composites with ductile discontinuous reinforcements, Control of interfaces in Metal and Ceramic Composites, eds. R. Y. Lin and S. G. Fishman, TMS, 149-164.

Biot, M. A. 1941. General theory of three-dimensional consolidation. J. App. Phys., 12, pp. 155-164, 1941.

Blair, S. C, and Cook, N .G. W. 2000. Analysis of compressive fracture in rock using statistical techniques: Part II. Effect of microscale heterogeneity on macroscopic deformation. International Journal of Rock Mechanics and Mining Science, Vol. 35, pp. 849-861.

Boulanger, R. W., and Duncan, J. M., 2000, Geotechnical Engineering Photo Album: University of California at Davis, accessed March 15, 2006, at http://cee.engr.ucdavis.edu/faculty/boulanger/geo_photo_album/index.html

Bordelon, A. 2010. Manual for Three-Point Bending Single-Edge Notched Beam (SENB) Fracture Test for Plain or Fiber-reinforced Concrete. Three Point Bending Fracture Test Manual, updated September 2010.

Bradley, W. B., 1979. Failure of inclined borehole. J. Energy Resour. Technol., Trans. ASME 101, 233–239.

Brege, J. J., Christian, C. F., Quintero, L., and Clark, D. E. 2010. Improving Wellbore Strengthening Techniques by Altering the Wettability of Nan-Aqueous Fluids Lost to Drilling Induced Fractures. AADE-10-DF-HO-43, presented at 2010 AADE Fluids Conference and Exhibition, Houston, Texas, April 6-7.

Cao, J. W, and Sakai, M. 1996. Crack-face fiber bridging: Finite element analysis, analytical model, and experimental results. Journal of Materials Research. Vol. 11, No. 6, 1537-1544.

Camacho, G. T., and Oritz, M., 1996. Computational Modeling of Impact Damage in Brittle Materials. Int. J. Solids Structure., 33, pp. 2289-2938

Camanho, P. P., and Davila, C. G. 2003. Mixed Mode Decohesion Finite Elements for the Simulation of Delamination in Composite Materials. Nasa/TM., Journal of Composite Materials, Vol. 37, No. 16, 1415-1438.

Camanho, P. P., and Matthews, F. L. 1999. Delamination onset prediction in mechanically fastened joints in composite laminates. Journal of Composite Materials, 33, pp. 906-927.

Cardwell, B. J., and Yee, A. F. 1998. Toughening of epoxies through thermoplastic crack bridging. Journal of Materials Science. Vol.33, 5473-5484.

Clegg, R. E., and Paterson, G. D. 2004. Ductile Particle Toughening of Hydroxyapatite Ceramics Using Platinum Particles. Structural Integrity and Fracture International Conference (SIF'04), Brisbane, 47-53.

Clifton, R. J., Simonsen, E. R., Jones, A. H., and Green, S. J. 1976. Determination of the critical stress intensity factor, KIC, from internally pressurized thick-walled vessels, Exp. Mech. Vol.16, 233-238.

Chang, C., Zoback, M. D., and Khaksar, A. 2006. Empirical relations between rock strength and physical properties in sedimentary rocks." J. Pet. Sci. Eng. Vol 51, 223–237.

Cook, R. D. 1995. Finite Element Modeling For Stress Analysis. Published by John Wiley and Sons, pp. 8, USA.

Collins, P. M. 2002. Geomechanics and wellbore stability design of an offshore horizontal well. SPE/CIM/CHOA 78975, International Thermal Operations and Heavy Oil Symposium and International Horizontal Well Technology Conference, Canada, 2002.

Cui, W., Wisnom, M. R., and Jones, M. 1992. A Comparison of Failure Criteria to Predict Delamination Unidirectional Glass/Epoxy Specimens Waisted Through the Thickness. Composites 23(3): 158-66.

Davila, C. G., and Johnson, E. R. 1993. Analysis of Delamination Initiation in Postbuckled Dropped-Ply Laminates. AIAA Journal 31 (4), pp. 721-727.

Deily, F. H., and Owens, T. C., 1969. Stress around a wellbore. SPE 2557, 44th SPE Ann. Fall Meeting of AIME held in Denver, CO, Sep. 28–Oct. 1.

Detournay, E., and Cheng, A. H-D. 1993. Fundamentals of Poroelasticity. Section 5 in Comprehensive Rock Engineering: Principles, Practices and Projects, Vol. II, Analysis and Design Method, pp. 113-171, 1993.

de Pater, C. J., Desroches, J., Groenenboom, J., and Weijers, L. 1996. Physical and Numerical Modeling of Hydraulic Fracture Closure. SPE Production and Facilities, May 1996, pp.122-128.

Dixon, J. R., and Strannigan, J. S. 1972. Determination of Energy Release Rates and Stress-Intensity Factors by the Finite-Element Method, Journal of Strain Analysis, Vol. 7, No. 2, pp. 125-131.

Dudley, J., Fehler, D. F., and Zeilinger, S. 2001. Minimizing Lost Circulation Problems with Synthetic Muds, GPRI Project 2000 DC 3, December, 2001.

Dupriest, F. E., 2005. Fracture Closure Stress (FCS) and Lost Returns Practices. SPE/IADC 92192, SPE/IADC Drilling Conference, Amsterdam.

Dupriest, F. E., Smith, M. V., Zeilinger, C. S., and Shoykhet, I. N., 2008. Method to Eliminate Lost Returns and Build Integrity Continuously with High-Filtration-Rate Fluid. SPE/IADC 112656. Orlando.

Dugdale, D. S., 1960. Yielding of Steel Sheets Containing Slits. J. Mech. Phys. Solids, 8, pp. 100–104.

Economides, M., and Valco, P. 2005. Hydraulic Fracture Mechanics. Published by John Wiley and Sons Ltd, USA.

E.Launey, M., and O.Ritchie, R. 2009. On the Fracture Toughness of Advanced Materials. Advanced Materials. Vol. 21, 2103-2110.

Engelder, T. 1993. Stress regimes in the lithosphere Princeton University Press, Princeton, New Jersey, U.S.A. 475 pp. (ISBN 0-691-08555-2.)

Evans, A. G. 1990. Perspective on the Development of High-Toughness Ceramics. Journal of American Ceramics Society. Vol. 73, No. 2, 187-206.

Fantner, G. E. 2005. Sacrificial bonds and hidden length dissipate energy as mineralized fibrils separate during bond fracture. Nature Materials. Vol. 4, 612–616.

Fett, D., Martin, F., Dardeau, C., Benaissa, S., Adachi, J., and Pastor, J. 2010. Case History: Successful Wellbore Strengthening Approach in a Depleted and Highly Unconsolidated Sand in Deepwater Gulf of Mexico. SPE Drilling and Completion, Vol. 25, No. 4, pp. 500-508, 2010.

Fjaer, E., Holt, R. M., Horsrud, A .M., Raeen, A. M., and Risnes, R., 2008. Petroleum Related Rock Mechanics. Second edition, Elsevier publishing.

Freitag, L., Jones, M., and Plassman, P. 1995. An Efficient Parallel Algorithm for Mesh Smoothing. In Proceedings of the Fourth International Meshing Round Table. Sandia National Laboratories, 1995, pp. 47-58

Freiman, S. W., Weiderhorn, S. M., and Mecholsky, J. 2009. Environmentally Enhanced Fracture of Glass: A Historical Perspective. J. AM. Ceram. Soc. 92(7), 1371-1382.

Fuh, G. F., Morita, N., Byod, P. A., and McGoffin, S. J. 1992. A New approach to preventing lost circulation while drilling. SPE 24599, 67th Annual Technical Conference and Exhibition, Washington

Fuh, G. F., Beardmore, D., and Morita, N., 2007. Further Development, Field Testing, and Application of the Wellbore Strengthening Technique for Drilling Operations. SPE/IADC 105809, SPE/IADC Drilling Conference, Amsterdam.

Gale, J. F. W., Reed, R. M., and Holder. J., 2007. Natural fractures in the Barnett Shale and their importance for hydraulic fracture treatments. AAPG Bulletin 91: 603–622.

Geertsma, J., and de Klerk, F., 1969. A rapid method of predicting width and extent of hydraulically induced fractures, Journal of Petroleum Technology, Vol. 21, pages: 1571–81 [SPE 2458].

Gill, I., Roegiers, J-C., and Moos, D. 2006. Wellbore Cooling as a Means to Permanently Increase Fracture Gradient. SPE 103256, presented at SPE Annual Technical Conference and Exhibition, 24-27 September, San Antonio, Texas.

Gonzalez, M E., Benjamin, J., E. Lofton, J., Pepin, G. P., Schmidt, J. H., Naquin, C. J., Ellis, S. T., and Laursen, P.E. 2004. Increasing Effective Fracture Gradients by Managing Wellbore Temperatures. 2004. IADC/SPE 87217, paper presented at IADC/SPE drilling conference, Dallas, Texas, 2-4 March 2004.

Griffith, A. A., 1920. The phenomena of rupture and flow in solids. Philosophical Transactions of the Royal Society of London, A 221, 163–198.

Grenet, L., 1899. Mechanical Strength of glass. Bull. Soc. Enc. Industry. Nat. Paris, (Ser.5), Vol. 4, 838-848.

Harrison, E., Kieschnick, W. F., and McGuire, W. J., 1954. The mechanics of fracture induction and extension, Petroleum Trans AIME, Vol. 201 pages: 252–63.

Hillerborg A., Modeer N., and Petersson PE. 1976. Analysis of crack formation and crack growth in concrete by means of fracture mechanics in finite elements. Cement and Concrete Research; 6:773-782.

Howard, G. C., and Scott, P. P. 1951. An Analysis and the Control of Lost Circulation. Trans. AIME, p. 171.

Hubbert, M. K., and Willis, D. G., 1957. Mechanics of hydraulic fracturing, Journal of Petroleum Technology, 9(6), pages: 153–68.

Hudya, D. F., Natalia, S., and Castillo, D. 2007. The Effect of Pressure Depletion on Geomechanical Stress and Fracture Behavior in Gunung Kembang Field. Proceedings, Indonesian Petroleum Association, Thirty-first Annual Convention and Exhibition, May, 2007.

Irwin, G. R., and Kies J. A., 1954. Critical Energy Rate Analysis of Fracture Strength, Weld. J. 33, Welding Research Supplement, 193-198.

Jaeger, J., Cook, N. G. W., and Zimmerman, R. 2007. Fundamentals of Rock Mechanics. Fourth edition by Blackwell Publishing.

Jiang, H. 2010. Cohesive zone model for carbon nano-tube adhesive simulation and fracture/ fatigue crack growth. PhD dissertation. Graduate Faculty of the University of Akron.

Kaageson-Loe, N., Sanders, M.W., Growcock, F., Taugbol, K., Horsud, P., Singelstad, A. V., and Omland, T. H. 2008. IADC/SPE 112595, presented at 2008 IADC/SPE Drilling Conference in Florida, 2008.

Khristianovic S. A., and Zheltov, Y. P., 1955. Formation of vertical fractures by means of highly viscous liquid. In: Proceedings of the fourth world petroleum congress, Rome, pages: 579–86.

Kirsch. 1898. Die Theorie der Elastizitat und die Bedurfnisse der Festigkeitslehre. Zeitschrift des Vereines deutscher Ingenieure 42, 797-807.

Krstic, V. D. 1983. On the fracture of brittle-matrix/ductile-particle composites, Philosophical Magazine A, Vol. 48, 695-708.

Lavrov, A., and Tronvoll, J. 2005. Mechanics of Borehole Ballooning in Naturally-Fractured Formations. SPE 93747, 14th SPE Middle East Oil and Gas Show, Bahrain.

Lambe T. W. and Whitman, R. V. 1979. Soil Mechanics S.I. version, 2nd ed." New York: J. Wiley and Sons, Inc.

Liberman, M., 2012. Hydraulic fracturing Experiments to Investigate Lost Circulation, MSc. Thesis, Missouri University of Science and Technology.

Lockner, D. A., and M. Beeler, N. 2002. Rock Failure and Earthquakes. International Handbook of Earthquake and Engineering Seismology, Vol. 81A, pp. 505-537.

Lowrey, J. P., and Ottesen, S. 1995. An Assessment of the Mechanical Stability of Wells Offshore Nigeria. SPE Drilling & Completion, March 1995, pp. 34-41.

Messenger, J. U. 1981. Oil well drilling- Lost Circulation. PennWell Publishing Company, Tulsa Oklahoma, USA.

Morita, N., Black, A. D., and Fuh, G. F., 1996a. Borehole Breakdown Pressure with Drilling Fluids-I. Empirical Results. Int. J. Rock Mech. Min. Sci. & Geomech. , 39-51.

Morita, N., Black, A. D., and Fuh, G. F., 1996b. Borehole Breakdown Pressure with Drilling Fluids-II. Semi-Analytical Solution to Predict Borehole Breakdown Pressure. Int. J. Rock Mech. Min. Sci. & Geomech., 53-69.

Morita, N., Black, A. D., and Fuh, G. F. 1990. Theory of Lost Circulation Pressure. SPE 20409, presented at SPE Annual Technical Conference and Exhibition, 23-26 September 1990, New Orleans, Louisiana

Morita, N., L. Whitfill, D., and A. Wahl, H. 1988. Stress Intensity Factor and Fracture Cross-Sectional Shape Predictions From a Three-Dimensional Model for Hydraulically Induced Fractures.

Maiti, S., and Geubelle, P. H. 2006. Cohesive Modeling of Fatigue Crack Retardation in Polymers: Crack Closure effect. Engineering Fracture Mechanics. Vol.7 3, 22-41.

Mac Donald, B. J. 2007. Practical Stress Analysis with Finite Elements. Published by Glasnevin Publishing. Mclellan, P.J., May 1996. Assessing the risk of wellbore instability in inclined and horizontal wells. J. Can. Petrol. Technol. 35 (5), 21–32.

Mclean, A., Wilde, A., Zamora, M., and Rafferty, M. 2010. The Top 10 Mud-Related Concerns in Deepwater Drilling Operations- Revisited After 10 Years. Presented at 2010 AADE Fluids Conference and Exhibition, Houston, Texas.

Mitchell, J. 2001. Trouble-Free Drilling. Vol. 1, Stuck Pipe prevention, Drilbert Engineering Inc., Texas, US.

M. Knupp, P. 2000. Achieving Finite Element Mesh Quality Via Optimization of the Jacobian Matrix Norm and Associated Quantities. Part I- A Framework for Surface mesh Optimization. Int. J. Numer. Meth. Engng, 48, pp. 401-420.

Mody, F. K. and Hale, A. H., 1993, Borehole-Stability Model to Couple the Mechanics and Chemistry of Drilling-Fluid/Shale Interactions, Journal of Petroleum Technology, November, pp. 1093-1100, SPE Paper No. 25728.

Montilva, J., Fredricks, P., and Sesah, O. 2010. New Scaled-Down Automated Control System Manages Pressure and Return Flow While Drilling and Cementing Production Tubing in Depleted Onshore Field. SPE 128923, presented at IADC/SPE Drilling Conference and Exhibition, 2-4 February 2010, New Orleans, Louisiana, USA.

Needleman, A., 1990. An Analysis of Tensile Decohesion Along an Interface. J. Mech. Phys. Solids, 38, pp. 289-324

Needleman, A. 1987. A Continuum Model for Void Nucleation by Inclusion Deboning. Journal of Applied Mechanics 54:525-31.

Niihara, K. 1991. New Design Concept of Structural Ceramics—Ceramic Nanocomposite. J. Ceram. Soc. Jpn. Vol. 99, No.10, 974–82.

Nierode, D. E., 1985. Comparison of Hydraulic Fracture Design Methods to Observed Field Results. Journal of Petroleum Technology, October 1985, pp 1831-1839

Nordgren, R. P., 1972, Propagation of a vertical hydraulic fracture, SPE Journal, 12(8), pages: 306–14, SPE 7834.

Nordgren, R. P., 1972. Properties of a vertical hydraulic fracture. SPEJ. Trans., AIME, 253, 306-14.

Nygaard, R., Salehi, S., and Lavoie, R. 2011. Effect of Dynamic Loading on Wellbore Leakage for the Wabamun Area CO2 Sequestration Project. CSUG/SPE 146640, will be presented at the Canadian Unconventional Resources Conference held in Calgary, Alberta, 15-17 November 2011.

Nygaard, R., Gutierrez, M., and Bratli, R. K. Brittle-ductile transition mudrocks and shales it's implication for hydrocarbon migration and seal. Marine and Petroleum Geology, 2006.

Nygaard, R., Bjorlykke, K., Hoeg, K., and Hareland, G. 2007. The effect of digenesis on stress-strain behavior and acoustic velocities in sandstones. Rock Mechanics: Meeting Society's Challenges and Demands-Eberhardt, Stead and Morrison, 2007 Taylor & Francis Group, London, pp. 805-811.

Ohiji, T., Jeoong, Y. K., Choa, Y. H., and Niihara, K. 1998. Strengthening and Toughening Mechanisms of Ceramic Nanocomposites. Journal of American Ceramics Society. Vol. 81(6), 1453-1460.

Okland, D., Gabrielsen, G. K., Gjerde, J., Sinke, K. and Williams E. L. 2002. The Importance of Extended Leak-Off Test Data for Combatting Lost Circulation. SPE/ISRM Rock Mechanics Conference, Irving, Texas, 20-23 October 2002.

Onyia, E. C. 1994. Experimental Data Analysis of Lost-Circulation Problems During Drilling with Oil-Based Mud. SPE Drilling and Completion, March 1994, pp. 25-31.

Ouchterlony, F. 1983. Fracture toughness testing of rocks, Courses and Lectures on Rock Fracture Mechanics, No. 275, H.P. Rossmanith, (Ed.), Technical University of Vienna, Springer Verlag, 68-155.

Ouchterlony, F. 1986. A core bend specimen with chevron edge notch for fracture toughness measurements. Rock Mechanics: Key to Energy Production, Proc. 27th US Symposium on Rock Mechanics., H. L. Hartman, (Ed.), SME, Littleton, CO., 177-184.

Ottesen, S., and Kwakwa, K. A. 1991. A Multidisciplinary Approach to In-Situ Stress Determination and Its Application to Wellbore Stability Analysis. SPE/IADC 21915, presented at SPE/IADC Conference held in Amsterdam, 11-14 March, 1991.

Ozdemirtas, M., Babadagli, T., and Kuru, E. 2007. Numerical Modeling of Borehole Ballooning/Breathing- Effect of Fracture Roughness. Presented at the 8th Canadian International Petroleum Conference, Paper 2007-038, June 12-14, 2007.

Pardhanani A., and Carey, G. 1988. Optimization of Computational Grids. Numerical Methods for Partial Differential Equations, 4(2), pp. 95-117

Perkins, T. K., and Kern, L. R., 1961. Widths of hydraulic fractures, Journal of Petroleum Technology, 13(9), pages: 937–49 [SPE 89].

Peterlik, H., Roschger, P., Klaushofer, K., and Fratzl, P. 2006. From brittle to ductile fracture of bone. Nature Materials. Vol. 5, 52-55.

P. Hignett, A., White, A. A., Carter, R. D., N.Jackson, W. D., and Small, R. M. 2007. A comparison of laboratory measurements and numerical simulations of baroclinic wave flows in a rotating cylindrical annulus. Quarterly Journal of the Royal Meteorological Society, Vol. 111, pp. 131-154.

Phuoc, T., X., Soong, Y., Chyu, M., K., and Lee, J. 2009. Nanoparticles Applications for Controlling Drilling Fluid Rheological Properties at High Temperatures. AADE 2009NTCE-11-05, 2009 National Technical Conference and Exhibition, Louisiana.

Raaen, A. M., Horsrud, P., Kjoerholt, H., and Oekland, D. Improved routine estimation of the minimum horizontal stress component from extended leak-off tests. Int. J. Rock Mech. 7 min. Sci Vol. 43 37-48. 2006.

Ramos, G. G., Mouton, D. E., Wilton, B. S., and Leksmono. 1998. Integrating Rock Mechanics with Drilling Strategies in a Tectonic Belt, Offshore Bali, Indonesia. SPE/ISRM 47286, Presented at SPE/ISRM Eurock, Norway, July 1998.

Reid, P., and Santos, H. 2006. Ultralow Invasion Drilling Fluids: A Practical Route to Reduced Wellbore Instability, Reduced Mud Losses, Wellbore Strengthening, and Improved Productivity. SPE 101329, presented at the SPE/IADC Indian Drilling Technology Conference and Exhibition, Mumbai, India, 16-18 October.

Rice, J. R. 1968. Mathematical analysis in the mechanics of fracture, Fracture Academic Press, pp. 191-311.

Rice, J. R., 1968. A Path Independent Integral and Approximate Analysis of Strain Concentration by Notches and Cracks. ASME J. Appl. Mech., 35, pp.379–386.

Ritchie, R. O., Gilbert, C. J., and McNaney, J. M. 2000. Mechanics and mechanisms of fatigue damage and crack growth in advanced materials. International Journal of Solids and Structures. Vol.37, 311-329.

Ritchie, R. O. 1999. Mechanisms of fatigue-crack propagation in ductile and brittle solids. International Journal of Fracture. Vol. 100, 55-83.

Roe, K. L., and Siegmund, T. 2003. An irreversible cohesive zone model for interface fatigue crack growth simulations. Eng. Frac. Mech., 70, pp. 209-232.

Rolf, S. T., and Barsorm, J. M., 1977. Fracture and fatigue control in structures. New Jersey, Prentice-Hall, p. 562.

Rubinstein, A. A., and Wang, P. 1998. The fracture toughness of a particulate-reinforced brittle matrix. Journal of the Mechanics and Physics of Solids, Vol. 46, 1139-1154.

Salehi, S., Hareland, G., and Nygaard, R. 2010. Numerical simulations of wellbore stability in under-balanced-drilling wells. Journal of Petroleum Science and Engineering, Vol. 72, June 2010, pp. 229-235.

Salehi, S., and Nygaard, R. 2011. Evaluation of New Drilling Approach for Widening Operational Window: Implications for Wellbore Strengthening, SPE 140753, will be presented at SPE Productions and Operations Symposium, Oklahoma city.

Sanad, M., Butler, C., Waheed, A., Engelman, B., and Sweatman, R. Numerical models help analyze lost-circulation/flow events and frac gradient increase to control an HPHT well in the east Mediterranean Sea., IADC/SPE 87094, Dallas, 2004.

Santos, H., Reid, P., McCaskill, J., Kinder, J., and Kozicz, J. 2006. Deep-water Drilling Made More Efficient and Cost Effective: Using Microflux Control Method and Ultralow Fluid to Open the Mud-Weight Window. Paper OTC 17818 presented at the Offshore Technology Conference, Houston, 1-4 May.

Sepehr, K. and Stimpson, B. 1988. Potash Mining and Seismicity: A Time-Dependent Finite Element Method, International Journal of Rock Mechanics and Mining Sciences & Geomechanics Abstracts, Vol. 25, No. 6, pp. 383-392.

Shet, C., and Chandra, N. 2002. Analysis of Energy Balance When Using Cohesive Zone Models to Simulate Fracture Processes. Transactions of the ASME, Vo. 124, pp.440-450.

Shin, C. S., and Cai, C. Q. 2000. A model for evaluating the effect of fatigue crack repair by the infiltration method. Fatigue Fracture Engineering Materials Structure. Vol. 23, 835–45.

Sigl, L. S., Mataga, P. A., Dalgleish, B. J., McMeeking, R. M., and Evans, A. G. 1981. On the toughness of brittle materials reinforced with a ductile phase, Acta Metallurgica, Vol. 36, 945-953.

Singh, S., and Ahmed, R. 2010. Vital Role of Nanopolymers in Drilling and Simulations Fluid Applications. SPE 130413, SPE Annual Technical Conference and Exhibition, Italy, 19-22 September, 2010.

Song, I., Suh, M., Won, K. S., and Haimson, B. 2001. A laboratory study of hydraulic fracturing breakdown pressure in table-rock sandstone. Geosciences Journal, Vol. 5, No. 3, pp. 263-271.

Stolarska, M., Chopp, D.L., Moës, N., and Belytschko, T., 2001. Modelling crack growth by level sets in the extended finite element method, International Journal for Numerical Methods in Engineering, Volume 51, Pages 943-960.

Suyan, K. M., Sharma, V., and Jain, V. K. 2009. An Innovative Material for Severe Lost Circulation Control in Depleted Formations. SPE/IADC 125693, presented at SPE/IADC Middle East Drilling Technology Conference and Exhibition, Bahrain, 2009.

Swanson, P. L. 1984. Subcritical Fracture Propagation in Rocks: An Examination Using the Methods of Fracture Mechanics and Non-Destructive Testing. PhD Dissertation. Department of Geological Science. University of Colorado, CO.

Takatoshi, I., Zoback, M. D., and Peska, P. 2001. Utilization of mud weights in excess of the least principal stress to stabilize wellbores: Theory and Practical Examples. SPE Drilling & Completion, 2001.

Terzaghi, K. 1923. Die berechnung der durchlassigkeitsziffer des tones aus dem verlauf der hydrodynaischen spannungerscheinungen" Sitz. Akad. Wissen., Wien Math. Naturwiss. KI., Abt. IIa, 132, 105-124, 1923.

Torfs, K., and Van Grieken, R. 1997. Chemical relations between atmospheric aerosols, deposition and stone decay layers on historic buildings at the Mediterranean coast. Journal of Atmospheric Environment. Vol. 31, pp. 2179-2192.

Traugott, D., Sweatman, R., and Vincent, R., 2007. Increasing the Wellbore Pressure Containment in Gulf of Mexico HP/HT Wells. SPE Drilling and Completion, 16-25.

Turon, A.; Davila, C. G.; Camanho, P. P; and Costa, J. 2007. An engineering solution for mesh size effects in the simulation of delamination using cohesive zone models. Journal of Engineering Fracture Mechanics 74, 1665-1682.

Ur-Rehman, A., and Thomason, P. F. 1993. The effect of artificial fatigue-crack closure on fatigue-crack growth. Fatigue Fracture Engineering Materials Structure. Vol. 16(10), 1081–90.

US Department of Interior, 2011. REPORT REGARDING THE CAUSES OF THE APRIL 20, 2010 MACONDO WELL BLOWOUT, THE BUREAU OF OCEAN ENERGY MANAGEMENT, REGULATION AND ENFORCEMENT, Sep 2011, http://www.boemre.gov/pdfs/maps/dwhfinal.pdf

Van Oort, E., Friedheim, J., Pierce, T., and Lee, J., 2009. Avoiding Losses in Depleted and Weak Zones by Constantly Strengthening Wellbores. SPE 125093, SPE Annual Technical Conference and Exhibition held in New Orleans, Louisiana.

van Oort, E., 1997. Physico-Chemical Stabilization of Shales, Proceedings of SPE International Symposium on Oilfield Chemistry, 18-21, February, Houston, TX, SPE Paper No. 37263.

van Dam, D. B., de Pater, C. J., and Romijn, R. 1998. Analysis of hydraulic fracture closure in labratory experiments, SPE/IRSM 47380, Proc. of Eu-Rock 98, Rock Mechanics in Petroleum Engineering, Trondheim, Norway, 1998.

Van den Hoek, P. J., Smit, D.-J., Kooijman, A. P., Bree, Ph. De, Kenter, C. J., and Khodaverdian. 1994. Size dependency of hollow cylinder stability. SPE28051, Proceedings, urock'94 SPE/ISRM International Conference, Rock Mechanics in Petroleum Engineering, 29-31 August, Delft, pp.191-198

Wang, H., Soliman, M. Y., and Towler, B. F. 2009. Investigation of Factors for Strengthening a Wellbore by Propping Fractures. SPE Drilling and Completion, pp. 441-451.

Wang, H. 2007b. Near Wellbore Stress Analysis for Wellbore Strengthening. PhD dissertation, Department of Chemical and Petroleum Engineering, University of Wyoming.

Wang, H., Towler, B.F., 2007a. Fractured Wellbore Stress Analysis: Sealing Cracks to Strengthen a Wellbore. SPE/IADC 104947, SPE Drilling Conference, Netherlands.

Wanner, A., Rizzo, R., and Kromp, K. 1991. Toughening Mechanisms in Quasi-Brittle Materials, edited by S. P. Shah, Kluwer Academic Publishers, Dordrecht, The Netherlands, 405–423.

Wang, H., Sweatman, R., Engelman, B., Deeg, W., Whitfill, D., Soliman, M., and Towler, B. F. 2008. Best Practice in Understanding and Managing Lost Circulation Challenges. SPE Drilling & Completion, June 2008, pp. 168-175.

Warpinski, N. R., Peterson, R. E., Branagan, P.T., and Wolhart, S. L. In situ stress and moduli: Comparison of values derived from multiple techniques. SPE 49190. SPE Annual Technical Conference & Exhibition, Louisiana September 27-30, 1998.

Whittaker, B. N., Singh, R. N., Sun, G. 1992. Rock Fracture Mechanics: Principle, Design and Applications. Elsevier publishing.

Wirput, D., Zoback, M., Hanssen, T., and Peska, P. 1997. Constraining the full stress tensor from observations of drilling-induced tensile fractures and leak off tests: Application to borehole stability and sand production on the Norwegian Margin. Int. J. Rock Mechanics and Mining Sciences, 34, No. 3-4, 1997.

Woo, C. W., and Kuruppu, M. D. 1992. Use of Finite Element Method for Determining Stress Intensity Factors with a Coin-Section Simulation Model of Crack Surface, International Journal of Fracture, Vol. 20, No. 3, pp. 163-178.

Yanyan, W., Mingxu, Z., and Daqing, F. 1993. A study of retarding fatigue crack growth using an artificial wedge. Fatigue Fracture Engineering Materials Structure. Vol. 16, 363–76.

Zamora, M., and Broussard, M. P. S. 2000. The Top 10 Mud-Related Concerns in Deepwater Drilling Operations. SPE 59019, presented at SPE International Petroleum Conference and Exhibition in Mexico, 1-3 February 2000, Villahermosa, Mexico.

Zavattieri, P. 1996. Optimization Strategies in Unstructured Mesh Generation. International Journal for Numerical Methods in Engineering, 39, pp. 2055-2071.

Zhang, G. M., Liu, H., Zhang, J., Wu, H. A., and Wang, X. X., 2010. Three-dimensional finite element simulation and parametric study for horizontal well fracture. Journal of Petroleum Science and Engineering. doi:10.1016/j.petrol. 2010.03.032.

Zhang, Z. X. 2002. An empirical relation between mode I fracture toughness and the tensile strength of rock. Int. Jour. of Rock Mechanics and Mining Science, 39, pp. 401-406.

Zienkiewicz, O. C., Taylor, R. L., and Nithiarasu, P. 2006. The Finite Element Method For Fluid Dynamics. 6th edition published by Elsevier Butterworth-Heinemann.

Zienkiewicz, O. C., and Taylor, R. L. 2006. The Finite Element Method For Solid and Structural Mechanics. 6th edition published by Elsevier Butterworth-Heinemann.

Zoback, M. D., Barton, C. A., Brudy, M., Castillo, D. A., Finkbeiner, T., Grollimund, B. R., Moos, D. B., Peska, P., Ward, C. D., and Wirput, D. J. Determination of stress orientation and magnitude in deep wells. Int. J. Rock Mechanics and Mining Sciences, 40, 2003, 1049-1076.

VITA

Saeed Salehi was born on September 16, 1981. He recieved his Bachelor's degree from the Petroleum University of Technology in Iran (2003). Before starting his Master's at University of Calgary, he worked two years as field drilling engineer in Iran. He was responsible for daily drilling operations at on-shore rigs in Iran. He finished his Master's degree in University of Calgary in 2007. He worked on "ECD management for under-balanced drilling wells" during his Master's program. After finishing his Master, he worked again as a drilling engineer and geomechanics specialist for the wells drilled in the South Pars gas field in the Persian Gulf. He was involved in well planning, drilling program and wellbore stability issues. In January 2009, he began his PhD program in the Petroleum Engineering program at the Missouri University of Science and Technology.